Doctoral Dissertation

博士論文

Tests of Alternative Theories of Gravity through Gravitational-Wave Polarizations

(重力波偏極モードによる重力理論検証)

A Dissertation Submitted for the Degree of Doctor of Philosophy

December 2020

令和2年12月博士(理学)申請

Department of Physics, Graduate School of Science,

The University of Tokyo

東京大学大学院理学系研究科

物理学専攻

Hiroki Takeda

武田 紘樹

Contents

Abstract

The polarization mode search of gravitational waves from compact binary mergers, such as binary black holes and binary neutron stars, allows us to test the gravity theory in a strong gravity field. Gravitational waves are a phenomenon in which distortions of space-time propagate as waves. As light has polarization degrees of freedom, gravitational waves have the polarization modes, which exerts different effects on the free masses. In addition to the two tensor modes allowed in general relativity, four additional non-tensorial (vector and scalar) modes are allowed in the alternative theories of gravity. Therefore, we can probe into the nature of gravity by separating the polarization modes in the gravitational wave signal from the strong and dynamical system of compact binary coalescences. Furthermore, separation of polarization modes may be able to lead to the verification and elucidation of unknown gravitational nonlinear phenomena and the structure of the universe that can be observed only with the polarization tests.

So far in the observational tests using gravitational waves from compact binary mergers, the tensor, vector, and scalar modes have been explored separately. However, such a purely polarized mode search cannot test the realistic theories of gravity. In this thesis, first we revealed the polarization separability of the mixed polarizations with the ground-based detector networks with the waveforms including the factors independent of the theories of gravity. Second, we searched for non-tensorial polarization modes with real gravitational wave signal such as GW170814 (binary black hole merger) and GW170817 (binary neutron star merger). In the pure polarization tests, we reanalyzed the signal with the waveforms consistent with modified theories gravity and utilized the information about the binary neutron star source from the electromagnetic counterpart. As a result, we obtained Bayes factors supporting general relativity that outperform the LIGO-Virgo Collaboration results by a factor of 5 in the binary black hole and 32 orders of magnitude in the binary neutron star. In the scalar-tensor search, we searched for the mixed scalar-tensor modes with the amplitude and phase corrections from additional scalar radiation. Consequently, we found the first direct constraints on the ratio of the scalar mode amplitude to the tensor mode amplitudes in the strong gravitational field for GW170814 and GW170817, which support general relativity.

Notation

Here is summary for notation. The standard mathematical and physical notations are adopted. We basically adopt the notation in [1] and the abstract notation [2].

$\Rightarrow$	implication(semantics)
$\Leftrightarrow$	equivalence(semantics)
$\wedge$	logical conjunction(semantics)
$\vee$	logical disjunction(semantics)
$\neg$	negation(semantics)
$\forall$	universal quantifier(semantics)
$\exists$	existential quantifier(semantics)
$\in$	$p \in A$ denotes that p is an element of A
$\cup$	$A \cup B$ denotes the union of the set A and B
$\cap$	$A \cap B$ denotes the intersection of sets A and B
$\subset$	$A \subset B$ denotes tha A is subset of B
$-$	$B - A$ denotes the complement in B of the set A
$\{\|\}$	$\{p \in A \| Q\}$ denotes the set consisting of those elements p of the set A which satisfy condition Q
$\times$	Cartesian product; $A \times B$ is the set $\{(a,b) \| a \in A \text{and} b \in B\}$
$\emptyset$	the empty set
$\mathbb{R}$	the set of real numbers
$\mathbb{R}^n$	the set of n-tuples of real numbers
i	imerginary number
$\mathbb{C}$	the set of complex numbers
$\mathbb{C}^n$	the set of n-tuples of complex numbers

$: \to$	$f : A \to B$ denotes that f is a map from the set A to the set B
$\circ$	$f \circ g$ denotes the composition of maps $g : A \to B$ and $f : B \to C$, i.e., for $p \in A$ we have $(f \circ g)(p) = f[g(p)]$
[ ]	$f[A]$ denotes the image of the set A under the map f, i.e., the set $\{f(x)\|x \in A\}$
i	imaginary number
C^n	the set of n-times continuously differentiable functions
C^∞	the set of infinitely continuously differentiable (=smooth) functions
$x(t)$	the function of time, time series data
$\tilde{x}(s), \tilde{X}(s)$	the function in s region(Laplace transformed function)
$\tilde{x}(f), \tilde{X}(f)$	the function of frequency, frequency series data(Fourier transformed function)
f	frequency
$\mathcal{P}_x$	power spectral density of $x(t)$. When the dimension of x is U, the dimension of $\mathcal{P}_x$ is $\mathrm{U}/\sqrt{\mathrm{Hz}}$
c	speed of light $c = 2.99792458 \times 10^8$ m/sec
G	gravitational constants $G = 6.67408 \times 10^{-11}$ $\mathrm{m}^3/(\mathrm{kg\ sec}^2)$
h	Planck's constant $h = 6.626 \times 10^{-34}$ J$\dot{\mathrm{s}}$ec
e	elementary charge $e = 1.602 \times 10^{-19}$ C
k_B	Boltzmann constant $k_B = 1.381 \times 10^{-23}$J/sec

Abbreviation

Abbreviation list in this thesis.

2G	Second Generation
3G	Third Generation
AdV	Advanced Virgo
aLIGO	Advanced LIGO
BBH	Binary Black Hole
BNS	Binary Neutron Star
BS	Beam Spliter
CBC	Compact binary coalescences
CE	Cosmic Explorer
ET	Einstein Telescope
GR	General Relativity
GW	Gravitational Wave
LVC	LIGO-Virgo Collaboration
PD	Photo Diode, Photo Detector
PSD	Power Spectral Density
RMS	Root Mean Square
SNR	Signal to Noise Ratio
SPA	Stationary phase approximation

Chapter 1

Introduction

Gravity is a kind of force. It is known as the weakest of the four fundamental forces in modern physics. A familiar example of gravitational phenomenon would be two objects with mass or energy are attracted to each other. In 1687, Isaac Newton recognized the gravity as a force and postulated the inverse-square law of universal gravitation in his "Principia" [3]. In the 1910s, Albert Einstein theorized the general relativity (GR) as a theory of gravity [4]. Einstein's general theory of relativity is a nonlinear and dynamic theory of gravity that describes spacetime as a four-dimensional Lorentz manifold [2, 5, 6]. The effects of gravitation are described by distortion of space-time rather than a force in GR. Since GR has been verified by solar system experiments and binary pulsar observations with high accuracy under weak gravitational fields, GR is now widely accepted as a fundamental theory of gravity. For example, the Mercury-Sun system was used to observe perihelion precession predicted in GR [7, 8]. Equivalent principle tests have been done by lunar laser range experiments to track changes in lunar orbital distance and motion using a retroreflector placed on the lunar surface. [9]. By recording the trajectories of LAGEOS and LAGEOS2 by the laser ranging, the dragging effect of the inertial system was observed [10]. The Cassini spacecraft has tested the bending and delay of the photons by the measurement of the frequency shift of radio photons to and from the Cassini spacecraft near the Sun [11]. The double binary pulsar systems are also excellent laboratories for testing GR [12–14]. Pulsars are highly magnetized rotating neutron stars which emit a narrow radio beam along the magnetic dipole axis. Since the magnetic dipole axis is inclined to the rotational axis, the pulsar emits a radio pulse that can be detected once per rotational period when the beam is directed toward Earth.

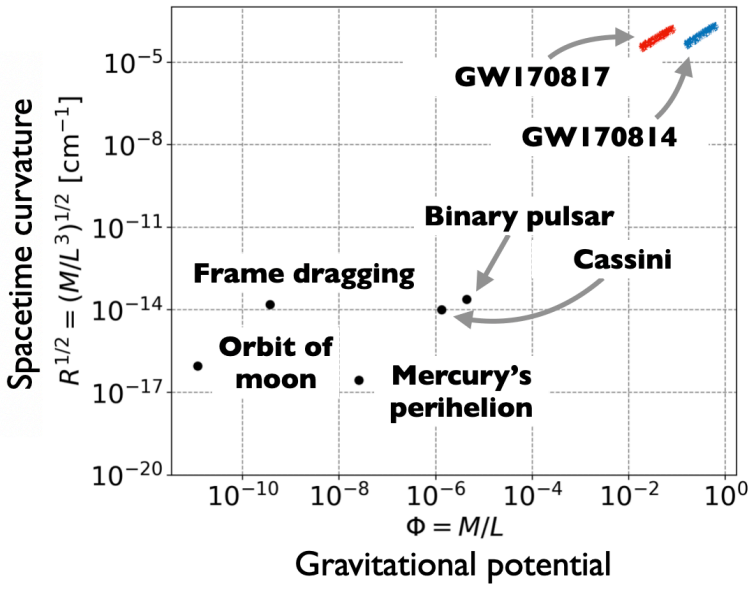

Figure 1.1: The region of the gravitational fields in testing GR. The characteristic gravitational potential $\Phi = M/L$ and the characteristic spacetime curvature $R = M/L^3$ with the characteristic mass scale M and the characteristic length scale L in the observations and the experiments for testing GR: orbit of moon [9], frame dragging [10], Mercury's perihelion [7, 8], Cassini [11], binary pulsar [12–14], GW170814 (binary black hole merger) [16], and GW170817 (binary neutron star merger) [17].

GR has been tested through the observations of orbital motion using pulsed signals delivered at very regular intervals. The mass and length scale of each system are summarized in [15]. Fig. 1.1 shows the characteristic gravitational potential $\Phi = M/L$ and the characteristic spacetime curvature M/L^3 where M and L are the characteristic mass and size of the system for the solar system experiments and binary pulsar observations. In spite of these many human attempts, no break in GR has been found even now, nearly 100 years after its proposal.

On the other hand, however, many alternative theories of gravity have been proposed [8]. The alternative theories of gravity are constructed by adding new fields or considering higher order, higher dimension, or non-locality. There are two main motivations to extend GR. One is the observational motivation to

explain the accelerated expansion of the universe or inflation. Second is more theoretical motivation to test GR as a low energy effective theory including unification of quantum theory and gravity theory. We can better understand GR by exploring the theories beyond GR, which may lead to solving various problems left in modern physics. Since GR is a nonlinear and dynamic theory, it is important to test it dynamically in a strong gravitational field where nonlinear effects are more effective. The first observation of the gravitational wave (GW) from a compact binary coalescence (CBC) with the GW detector Advanced LIGO (aLIGO) [18] in 2015 made it possible to test gravity theories by GWs [19]. GWs are a phenomenon in which the disturbance of space-time propagates as waves. GWs are radiated from the objects with any acceleration that is not spherically or cylindrically symmetric. In conventional astronomy, various observations have been carried out mainly using electromagnetic waves. The observation of GWs will reveal a new picture of the universe, such as the observation of celestial bodies that do not emit electromagnetic waves, which was not accessed with conventional electromagnetic wave observations. This means that humankind has acquired a new set of eyes: gravitational waves. The stretching and shrinking of space-time by GWs is so small, but to acquire these new eyes, humankind has made tremendous progress in science and technology, and realized GW observation 100 years after the proposal of the existence of GWs. GWs are classified into four major types depending on the waveform: chirp, continuous, burst, and stochastic [1]. In this thesis, we mainly deal with GWs from CBCs such as binary black holes (BBHs) and binary neutron stars (BNSs), which is called chirp signal. CBCs in which two compact objects, such as a black hole or a neutron star, merge into one produce the chirp GWs. The coalescence of a comparable mass binary system can be roughly divided into three phases: inspiral, merger, and ringdown [20–22]. At the inspiral phase, the compact objects are well-separated and the orbital velocity is much smaller than the speed of light. In the merger phase, the compact objects are so close to each other and then as the orbital velocity approaches the speed of light, the compact objects plunge into the other and coalescence. At the final ringdown phase, the highly distorted remnants formed after the merger are relaxed to a stationary state, vibrating and radiating deformation. As Fig. 1.1 also shows the gravity regime for the CBCs in which

the theories of gravity can be probed, it became possible to test the nature of gravity in stronger gravity field by the observations of GWs from CBCs.

After the first event, a lot of GWs from CBCs have been observed by the GW detector network with aLIGO and Advanced Virgo (AdV) [23]. The first observing run, O1, ran from 12 September 2015 to 19 January 2016 and the second observing run, O2, from 30 November 2016 to 25 August 2017. As for the latest third observing run, O3, the first half run O3a ran from 1 April 2019 to 1 October 2019 and the second half run 03b ran from 1 November 2019 to 27 March 2020. 11 GW event candidates (including one BNS candidate GW170817 [17]) have been reported in O1 and in O2 [24], and 39 GW event candidates (including two mass gap BBHs GW190412 [25] and GW190814 [26], one BNS candidate GW190425 [27], one BBH with the intermediate mass black hole remnant GW190521 [28], and one potential NSBH GW190426_152155 [29]) have been reported in O3a [29]. Several investigations to test GR by GWs from CBCs have been proposed and carried out for these detected GWs [30, 31]. One is the consistency tests in which the consistency of the data is evaluated. One way of the consistency test to test GR is to subtract the best-fit waveform from the observed data and compare the statistical properties of the residuals with those expected from instrumental noise [32]. Another is the inspiral-merger-ringdown consistency test in which the consistency of the low frequency part of the signal (corresponding to the inspiral phase) is checked with the high frequency part of the signal (corresponding to the post-inspiral phases) by comparing the estimated parameter values [33,34]. In addition, parametrized testing is also popular. Deviations from GR may emerge as changes in the evolution of binary dynamics, especially in the evolution of the orbital phase which is related to the GW phase. The usual waveform models are calculated analytically or numerically under the assumptions of GR. In the parametrized test of GW generation, the deviations from GR are evaluated by introducing shifts in the GW phase coefficients of the CBC waveforms [32,35–44]. The early inspiral phase of CBC is properly modeled by the post-Minkowskian (PM) and post-Newtonian (PN) approximation [45–48], which is accompanied by the expansion in terms of a small expansion parameter v/c. We shall use p_i to collectively denote the inspiral and post-inspiral parameters where i denotes the power of v/c. Deviations from GR for chirp

signals are expressed by the relative shifts $\delta\hat{p}_i$ as $p_i \rightarrow (1+\delta\hat{p}_i)p_i$ where the relative shifts are regarded as additional free parameters in the parametrized test of GR generation. GR can be also tested by evaluating the relative shifts based on the Bayesian inference for the observed signal. Similarly, it is possible to test the GW propagation parametrically by a phenomenological modification of the GW dispersion relation $E^2 = p^2c^2 + A_\alpha p^\alpha c^\alpha$ where E and p are the GW energy and GW momentum, and A_α and α represent the phenomenological modification parameters [49,50]. This phenomenological modification includes the theoretical predictions. $A_0 > 0$ corresponds to a massive graviton with a graviton mass $m_g = \sqrt{A_0}/c^2$ [51]. Furthermore, the values of 2.5, 3, and 4 for α correspond to the leading predictions of fractal spacetime [52], doubly special relativity [53], and Hořava-Lifshitz [54] and extra dimensional [55] theories, respectively. A leading contribution with $\alpha = 4$ is also predicted in the standard model extension with only the non-birefringent terms [56] . GR can be also tested by evaluating the modification parameters using the Bayesian inference of the waveforms with a phase correction derived from the modification of the dispersion relation for the observed signal. In addition, the speed bound of the GW from GW170817 and GRB170817A constrains alternative theories of gravity at the precision of 10^{-15}. A large class of theories as alternatives to dark energy have been ruled out by the constraint [57–66].

However, despite these tremendous efforts, no evidence for violations of GR has been reported so far. The polarization test is also one method to test GR. The polarization mode search of GWs from CBCs, such as BBH and BNS, also allows us to test the theory of gravity in a strong gravity field. As light has polarization degrees of freedom, GW also have polarization modes, which exert different effects on the test masses [7,8]. In addition to the two tensor modes allowed in general relativity [1,2], four non-tensorial (vector and scalar) modes are allowed in a general metric theory of gravity [7, 67–69]. In the gravity theory tests presented above, only two tensor modes and the modifications for the two tensor modes are considered. More specifically, GWs in scalar-tensor theory [70,71] and f(R) gravity [72–76] are allowed to have scalar polarizations in addition to tensor modes [7,8,68,77,78]. Up to six polarization modes are allowed [79] in bimetric theory of gravity [80,81] while up to five polarization modes are allowed [82] in massive gravity theory [83,84]. On the other hand,

GWs in a medium containing bounded subsystems would have anomalous polarizations [85]. Separation of polarization modes may be able to lead to the verification and elucidation of unknown gravitational nonlinear phenomena and the structure of the universe that can be observed only with the polarization tests, for example, in GW generation the screening mechanism works and causes little waveform correction, but non-tensorial modes are excited during propagation by nonlinear effects such as non-uniform galactic fields. The discovery of polarized modes beyond GR indicates the existence of additional degrees of freedom in the theory of gravity, the breaking of gauge symmetry or the unknown nonlinear phenomena of gravity, and can bring breakthroughs to modern physics such as gravity theory and cosmology. The restrictions on the polarization modes obtained in this study provide observational insights into theoretical studies such as the explanation of the accelerated expansion of the universe and the integration of quantum theory and gravity theory. Therefore, we can acquire insight into the nature of gravity, by separating the polarization modes in the GW signals from the strong and dynamic system of CBC.

However, there have been a few analytical and observational studies on the tests of GWs from CBCs unlike some other waveforms such as GW bursts, continuous GWs, and stochastic GWs so far. That is because the waveforms of the GWs from the CBCs depend on the binary parameters so that it is more difficult to analyze the observed signal. A few analytical attempts for distinguishing the polarizations were performed. For any sources, the detector signal appears as a linear combination of multiple polarization modes (see Chapter 3 for more details). [86] develops a method to reconstruct the polarizations of the GW bursts in time-series data. In the burst cases, since the signal time is short, it is reduced to a simple matrix inverse problem. We need the same number of detectors as the number of polarization modes to be verified. GW bursts have not yet been detected, so no observational constraints have been obtained. [87] studied a single detector measurement of a continuous GWs from a triaxial pulsar source. They developed methods to distinguish between the polarization modes in a model independent way through a matched filtering technique. In the case of the continuous GWs, the detector signal duration is long enough and the Earth's rotation and the change in time of the detector response functions can be utilized so that even a single ground-based

detector can separate the polarization modes. In [88], the authors rebuild the ideas of [87] in a Bayesian framework that achieve model-independent detection, model selection, and inference. Since continuous GWs have not yet been observed, no observational constraints have been obtained again. In [89], the detectability of additional polarization modes of a stochastic GW background with laser-interferometric detectors on the Earth was discussed and a component separation scheme was proposed. In the paper, the correlation analysis [90–92] was extended to the non-tensorial polarization modes. Rather than resolving the relative polarization content within each frequency bin [89], [93] assume a power-law model for the energy-density in each polarization mode. In [94], the LIGO-Virgo collaboration (LVC) searched for a stochastic background of generically polarized GWs using the data by aLIGO during O1 and the methodology presented in [93] and limited the energy densities of tensor, vector, and scalar modes.

As for the analytical attempts for GWs from CBCs, a simple analysis method using the sine-Gaussian wave packet waveform as a toy model was reported to probe polarizations from CBCs [95]. On the other hand, null stream based analysis method has been proposed [96–100]. The null stream is a time series constructed by taking a linear combination of the multiple detector signal such that the stream does not have specific polarization components (see Chapter 3). As for the observations, the LVC analyzed the several GWs in the O1 and O2 runs in the purely polarized models, in which the Bayesian model selection comparing GR with the theory having only scalar or vector polarizations was conducted [30, 44]. The idea of their search was to replace the detector response function of the tensor mode with those of the vector or scalar modes to evaluate which type of polarization modes purely reproduced the detected signal well. However, the waveforms must depend on the geometrical parameters as well as the specific parameters of the gravity theory, which are not considered in these works. In [31, 98, 100], polarization searches for the signal minus the tensor components have been conducted based on the null stream method. These tests give the constraints on the Bayes factors between GR and the artificial pure polarization theories allowing only vector or scalar polarization modes. In recent years, the polarization separability of dipole radiations has been discussed for supermassive black hole binaries with pulsar

timing arrays [101] and for massive black hole binaries with a space-based GW detector Taiji [102]. It has been reported that the observation of the multiple copies of the same GW signal by strong lensing would help the detector network to measure different combinations of the same polarizations [103].

However, while the utilization of appropriate waveform models is essential in obtaining the correct observational limits and has the potential to improve the sensitivity of tests, the waveforms of the CBCs are not assumed or the only simple substitution of the response function is considered in these previous works about polarization tests of GWs from CBCs. The waveforms must depend on the geometrical parameters, for example the inclination angle dependence, as well as the specific parameters of the gravity theory. The dependence of the specific parameters must depend on the specific theory of course. However, the geometrical patterns of the radiation are general among theories of gravity, which are determined by the geometry of the system [96]. Without the dependence independent of the theory of gravity, it should affect on the parameter estimation. Moreover, the standard alternative theories of gravity predict not the pure polarizations but the mixed polarization modes. Therefore, the accurate search for and the investigations of the polarization modes by the waveform model of GWs from CBCs with full polarization contents consistent with the alternative theories of gravity is required for testing gravity in realistic alternative theories of gravity beyond GR. The separation condition of a mixture of polarization modes of GWs from CBCs is still unknown, while it is known that we need the enough detectors more than or equal to the polarization modes for GW bursts, but the number of the detectors may less than the number of polarization modes for continuous GWs. Therefore, first of all it is crucial for observations to study the separability of the polarization modes and to reveal the separation conditions for mixed polarization modes of GWs from CBCs.

In this thesis, we study the separability of the polarization modes of the GWs from CBCs and search for the beyond GR polarization modes with the real data using the waveforms consistent with alternative theories of gravity. First of all, we reveal the polarization separability of the mixed polarizations with the current and future ground-based GW detectors based on the Fisher information matrix. Our polarization models include several non-tensorial po-

larization modes in addition to the tensor modes with the factors independent of the theories of gravity such as the detector response function and the geometrical patterns of the radiation. Second, we reanalyze the pure polarization tests of GW170814 (BBH) and GW170817 (BNS) in the improved polarization waveform models. GW170814 is a GW from a BBH coalescence observed by three detectors [16] and GW170817 is a GW signal from a BNS coalescence observed by three detectors [17]. Finally, we perform the first search for a scalar-tensor mixed polarization mode for GW170814 and GW170817 and give constraints on the additional polarization amplitude. We basically focus on the inspiral phase of CBCs, but we consider the inspiral-merger-ringdown in the pure polarization tests for comparison with [30,44]. This is because it is extremely difficult to model the plunge and merger even within GR from the lack of a numerical modeling of these phases in alternative theories gravity, although a large GR discrepancy is expected under the strong gravitational field such as post-inspiral phase. In order to make the studies robust, we basically consider the only inspiral phase. ‘‘Strong-field’’ here means the region of spacetime where the gravitational field is dynamical and nonlinear and the PN expansion well perturbatively models such strong dynamics and nonlinearities.

This thesis is organized as follows. Chapter 2 provides the basics of GWs in GR. In Chapter 3, we describe interaction of GWs with test masses and provide the GW detector signal with full polarization content, and then we present the classification of polarization modes and the parametrized waveforms with full polarization modes based on the inspiral waveforms in some alternative theories. Finally, we review the previous polarization tests regarding CBCs. Chapter 4 describes the GW data analysis techniques, in particular the Fisher analysis and the Bayesian inference, which are used in the latter analysis. In Chapter 5, we discuss the polarization separability with the current and the future ground-based detectors. In Chapter 6, we show the results of the pure polarization tests of GW170814 and GW170817. In Chapter 7, we search for an additional scalar polarization mode in addition to the tensor modes for GW170814 and GW170817 giving the first direct observational constraints on the amplitudes of the additional scalar polarization modes in a mixed polarization framework. Finally, we devote the last Chapter 8 to the conclusion of the thesis.

Chapter 2

Gravitational waves in general relativity

Space-time is regarded as a set of events and the gravity is expressed by the metric on the space-time manifold in the metric theories of gravity. GWs are the perturbations of metric propagating as waves in the space-time. In this chapter, we shall consider the gravitational waves in GR. The basics of variation are provided in Appendix A. The variational procedure is given in Appendix B in the context of GR.

2.1 Field equations

In GR, the gravitational action is given by,

$$S = S_E + S_M. \tag{2.1}$$

S_E is the Einstein action,

$$S_E := \frac{c^3}{16\pi G} \int R, \tag{2.2}$$

and S_M is the matter action. The Riemann tensor R_{abcd}, the Ricci tensor R_{ab}, and the Ricci scalar R are defined as mentioned in the notation section. The matter action is defined such that the variation of the action in terms of the metric gives the energy-momentum tensor T_{ab},

$$\delta S_M = \frac{1}{2c} \int T^{ab} \delta g_{ab}. \tag{2.3}$$

The Einstein field equations can be derived by the variation with respect to the metric g_{ab},

$$R_{ab} - \frac{1}{2} g_{ab} R = \frac{8\pi G}{c^4} T_{ab}. \tag{2.4}$$

2.2 Linearization

2.2.1 Curved space-time

We shall consider the linearization of the theory in some space-time. The metric are written as

$$g_{ab}(x) = \bar{g}_{ab}(x) + h_{ab}(x), \quad |h_{ab}| << 1 \tag{2.5}$$

where $\bar{g}_{ab}$ is the metric for the some curved and dynamical or flat background spacetime and h_{ab} is the perturbations. Roughly speaking, h_{ab} denotes the gravitational waves as we will see below. Here, it is assumed in the small amplitude conditions $|h_{ab}| << 1$ that on the region of spacetime of interest, a coordinate such that the diagonal element of $\bar{g}_{ab}$ are $O(1)$ is used. When considering the linearization around the flat space-time metric $\bar{g}_{ab} = \eta_{ab}$, the definition of gravitational waves is relatively clear. In this case, the background space-time is flat and the small perturbations around it are defined as gravitational "waves" because h_{ab} satisfies a wave equation in a suitable gauge. However, one sometimes need to consider the gravitational waves in some curved space-time, for example when studying whether gravitational waves curve the background space-time. In the most general situation, there is no reasonable way to separate the waves from the background because the x-dependent terms can be moved between $\bar{g}_{ab}$ and h_{ab} freely due to the dynamical property that is x-dependence of $\bar{g}_{ab}$. It becomes possible to distinguish perturbations from the background when a clear separation in scales exists. In space, the following distinction condition is a kind of clear separations in scales,

$$\lambda << L_B, \tag{2.6}$$

where L_B is the typical scale of spatial variation in $\bar{g}_{ab}$ and $\lambda\!\!\!^{-} := \lambda/2\pi$ is the reduced wavelength of small amplitude perturbations. [1] From this spatial perspective, h_{ab} can be regarded as small ripples on the smooth background $\bar{g}_{ab}$. Alternatively, in frequency space, the following distinction condition is a kind of clear separations in scales

$$f >> f_B, \tag{2.7}$$

where f_B is a maximum frequency that $\bar{g}_{ab}$ has and f is a peak frequency of the perturbations h_{ab}. From this frequency perspective, h_{ab} can be regarded as high frequency perturbations on a static or slowly varying background $\bar{g}_{ab}$. When the above conditions about clear separation in scales exist, one can identify the perturbed components, then we can split and define the GWs as perturbations Eq. (2.5) on the background. Since L_B and f_B are unrelated a priori in general, the above conditions are independent. It is sufficient that one of them is satisfied for a distinction between background and perturbations.

Therefore, provided that a clear distinctions of scales in space or in time, the metric can be written in the form Eq. (2). We shall expand the Einstein field equations around the background metric $\bar{g}_{ab}$. The typical amplitude $h := O(|h_{ab}|)$ and either $\lambda\!\!\!^{-}/L_B$ or f_B/f are two small parameters in the expansion. The contraction of Eq. (2.4) gives the following another form of the Einstein field equations,

$$R_{ab} = \frac{8\pi G}{c^4}(T_{ab} - \frac{1}{2}g_{ab}T). \tag{2.8}$$

where T is the trace of the energy-momentum tensor T_{ab}. We expand the Ricci tensor up to quadratic order $O(h^2)$ by applying the expression Eq. (2),

$$R_{ab} = \bar{R}_{ab} + R^{(1)}_{ab} + R^{(2)}_{ab} + \cdots \tag{2.9}$$

where $\bar{R}_{ab}$ is the Ricci tensor formed by $\bar{g}_{ab}$, $R^{(1)}_{ab}$ is linear in h_{ab} and $R^{(2)}_{ab}$ is quadratic in h_{ab}.

$$R^{(1)}_{ab} = \frac{1}{2}(\bar{\nabla}^c\bar{\nabla}_a h_{bc} + \bar{\nabla}^c\bar{\nabla}_b h_{ac} - \bar{\nabla}^c\bar{\nabla}_c h_{ab} - \bar{\nabla}_b\bar{\nabla}_a h) \tag{2.10}$$

[1] For a oscillating function $f(x) \propto e^{ikx}$, the typical length scale is the reduce wavelength in a sense that $|df/dx| = (1/\lambda\!\!\!^{-})|f|$.

$$R^{(2)}_{ab} = \frac{1}{2}\bar{g}^{ef}\bar{g}^{cd}\left[\frac{1}{2}\bar{\nabla}_a h_{ec}\bar{\nabla}_b h_{fd} + (\bar{\nabla}_e h_{bc})(\bar{\nabla}_f h_{ad} - \bar{\nabla}_d h_{af})\right.$$
$$+ h_{ef}(\bar{\nabla}_b\bar{\nabla}_a h_{fd} + \bar{\nabla}_d\bar{\nabla}_f h_{ab} - \bar{\nabla}_d\bar{\nabla}_b h_{af} - \bar{\nabla}_d\bar{\nabla}_a h_{bf}) \tag{2.11}$$
$$\left.+(\frac{1}{2}\bar{\nabla}_c h_{ef} - \bar{\nabla}_e h_{cf})(\bar{\nabla}_b h_{ad} + \bar{\nabla}_a h_{bd} - \bar{\nabla}_e h_{cf})\right]$$

Thus, $\bar{R}_{ab}$ contains only low frequency modes and $R^{(1)}_{ab}$ contains only high frequency modes, while $R^{(2)}_{ab}$ contains low and high frequency modes because of its quadratic form. Therefore the Einstein equations can be divided into low frequency part and high frequency part,

$$\bar{R}_{ab} = -[R^{(2)}_{ab}]^{\rm low} + \frac{8\pi G}{c^4}(T_{ab} - \frac{1}{2}g_{ab}T)^{\rm low}, \tag{2.12}$$

$$R^{(1)}_{ab} = -[R^{(2)}_{ab}]^{\rm high} + \frac{8\pi G}{c^4}(T_{ab} - \frac{1}{2}g_{ab}T)^{\rm high}, \tag{2.13}$$

where superscripts low(high) denotes the projection on the long(short) wavelength or on the low(high) frequencies depending on the distinction conditions.

Here, we estimate Eq. (2.12) in order of magnitude. We denote $h = O(|h_{ab}|)$, while we take $\bar{g}_{ab} = O(1)$. We can always set $\bar{g}_{ab} = O(1)$ by suitable rescaling of the coordinates in a limited region. Since $\bar{R}_{ab}$ is formed by the second derivatives of $\bar{g}_{ab}$, the left hand side can be estimated as

$$\bar{R}_{ab} \sim \partial^2 \bar{g}_{ab} \sim 1/L_B^2. \tag{2.14}$$

On the other hand, when the curvature is determined by GWs, the right hand side can be estimated as

$$\text{(left hand side)} \sim -[R^{(2)}_{ab}]^{\rm low} \sim (\partial h)^2 \sim (h/\lambda\!\!\!^{-})^2. \tag{2.15}$$

Thus, we find

$$h \sim \frac{\lambda\!\!\!^{-}}{L_B}, \text{ (GWs dominant)}. \tag{2.16}$$

When the curvature is determined by external matter,

$$\text{(left hand side)} \sim (h/\lambda\!\!\!^{-})^2 + \text{(matter terms)} >> (h/\lambda\!\!\!^{-})^2, \tag{2.17}$$

so we find

$$h << \frac{\lambda}{L_B}, \text{ (matter dominant)}. \tag{2.18}$$

The notion of GWs is well-defined only for small amplitude $h << 1$ because of $\lambda/L_B << 1$ and the above relations.

There is a simple averaging way to perform the projection on the long wavelength modes when there is a clear-cut separation between λ and L_B. The existence of the clear-cut separation means that a scale $\bar{l}$ such that

$$\lambda << \bar{l} << L_B, \tag{2.19}$$

and average over a spatial volume with size $\bar{l}$ can be introduced. Similarly, a time-scale $\bar{t}$ such that

$$1/f << \bar{t} << 1/f_B, \tag{2.20}$$

corresponding to Eq. (2.7) and average over the time $\bar{t}$ can be introduced when h_{ab} have only high frequency perturbation on a quasi-static background. Thus, we denote $\langle\cdot\rangle$ as the spatial average over many reduced wavelength λ and the temporal average over many periods $1/f$ of the GW. These averaging procedure is basically a special case of a general procedure, renormalization group transformations.

First, we focus on the low-frequency part of the Einstein equations, Eq. (2.12). Eq. (2.12) can be written as

$$\bar{R}_{ab} = -\langle R^{(2)}_{ab}\rangle + \frac{8\pi G}{c^4}\langle T_{ab} - \frac{1}{2}g_{ab}T\rangle, \tag{2.21}$$

using the average. We define an effective energy momentum tensor of matter $\bar{T}^{ab}$ as

$$\langle T_{ab} - \frac{1}{2}g_{ab}T\rangle =: \bar{T}^{ab} - \frac{1}{2}\bar{g}_{ab}\bar{T} \tag{2.22}$$

where $\bar{T} := \bar{g}_{ab}\bar{T}^{ab}$. We also define a quantity t_{ab} by

$$t_{ab} := -\frac{c^4}{8\pi G}\langle R^{(2)}_{ab} - \frac{1}{2}\bar{g}_{ab}R^{(2)}\rangle, \tag{2.23}$$

where $R^{(2)} := \bar{g}^{ab} R^{(2)}_{ab}$. t_{ab} are the energy-momentum tensor of the gravitational field. Then, we define the trace as

$$t := \bar{g}^{ab} t_{ab} = \frac{c^4}{8\pi G} \langle R^{(2)} \rangle. \tag{2.24}$$

Finally, we can rewrite Eq. (2.21) using these quantities,

$$\bar{R}_{ab} - \frac{1}{2} \bar{g}_{ab} \bar{R} = \frac{8\pi G}{c^4} (\bar{T}_{ab} + t_{ab}). \tag{2.25}$$

Eq. (2.25) is the coarse-grained form of the Einstein equations, which determine the dynamics of $\bar{g}_{ab}$ in terms of $\bar{T}_{ab}$ and t_{ab}.

Next, we focus on the high-frequency part of the Einstein equations, Eq. (2.13). First, we consider a situation in which the macroscopic external matter dominates the curvature. We limit only to the linear in h and the leading and the next-to-leading order in λ / L_B. In this case, Eq. (2.13) can be re-written as [2]

$$R^{(1)}_{ab} = 0 \Leftrightarrow \bar{g}^{cd} (\bar{D}_c \bar{D}_b h_{ad} + \bar{D}_c \bar{D}_a h_{bd} - \bar{D}_b \bar{D}_a h_{cd} - \bar{D}_c \bar{D}_d h_{ab}) = 0. \tag{2.26}$$

Here, we introduce $h := \bar{g}^{ab} h_{ab}$ and $\bar{h}_{ab} := h_{ab} - \frac{1}{2} \bar{g}_{ab} h$ for simplicity. Furthermore, we impose the Lorentz gauge condition

$$\bar{\nabla}^b \bar{h}_{ab} = 0. \tag{2.27}$$

Eq. (2.26) becomes

$$\bar{\nabla}^c \bar{\nabla}_c \bar{h}_{ab} + 2 \bar{R}_{acbd} \bar{h}^{cd} - \bar{R}_{ac} \bar{h}_b{}^c - \bar{R}_{bc} \bar{h}_a{}^c = 0, \tag{2.28}$$

in this gauge. Outside the matter where $\bar{T}_{ab} = 0$, the terms other than the first term can be ignored compared to the first term by order-of-magnitude

[2] In Eq. (2.13), $R^{(2)}_{ab}$ is smaller than $R^{(1)}_{ab}$ by an order of h and then negligible. The matter term can be estimated as $(T_{ab} - \frac{1}{2} g_{ab} T)^{\text{high}} \sim O(h / L_B^2)$ and is smaller than the $R^{(1)}_{ab}$ by a factor of $O(\lambda^2 / L_B^2)$, because the energy-momentum tensor T_{ab} for macroscopic matter can depend on h through the metric $T_{ab}(g_{ab})$ in general.

estimation, and then we find

$$\bar{\nabla}^c \bar{\nabla}_c \bar{h}_{ab} = 0. \tag{2.29}$$

Eq. (2.27) and Eq. (2.29) are the propagation equations of GWs in the curved background in the short-wavelength approximation, derived from the high-frequency part of the Einstein equations, Eq. (2.13).

The propagation equations can be solved by the eikonal approximation. We set the ansatz like

$$\bar{h}_{ab}(x) = [A_{ab} + \epsilon B_{ab}(x) + \cdots] e^{i\theta(x)/\epsilon}, \tag{2.30}$$

and define $k_a = \partial_a \theta$ and $A_{ab} =: A e_{ab}$ with the scalar amplitude A and the polarization tensor e_{ab} such that $e^{ab} e^*_{ab} = 1$ We substitute the ansatz into Eq. (2.27) and Eq. (2.29). Then, we obtain the eikonal equation

$$\bar{g}_{ab} k^a k^b = 0, \tag{2.31}$$

from Eq. (2.27) and the geodesic equation in the background described by $\bar{g}_{ab}$

$$k^a \bar{\nabla}_a k_b = 0, \tag{2.32}$$

from Eq. (2.29). These equations mean that graviton propagate along the null geodesic of $\bar{g}_{ab}$. We also obtain the condition for the scalar amplitude giving the conservation of the number of photons

$$\bar{\nabla}_a (A^2 k^a) = 0, \tag{2.33}$$

from Eq. (2.29). Furthermore, we get two conditions for the polarization tensor

$$k^b e_{ab} = 0, \tag{2.34}$$

from Eq. (2.27) and

$$k^c \bar{\nabla}_c e_{ab} = 0, \tag{2.35}$$

from .Eq. (2.29). These mean that the polarization tensor is transverse and is parallel-propagated along the null geodesic.

In conclusion, the Einstein equations are divided into the low-frequency part and the high-frequency part in the limit $\lambda << L_B$. The low-frequency part provides the equations describing the effect of GWs and of external matter on the background space-time, while the high frequency part provides the wave propagation equations in curved space, which can be solved by the eikonal approximation of geometric optics.

2.2.2 Flat space-time

Here, we describe the propagation of the GWs in vacuum in the flat space-time background. Given $\bar{g}_{ab} = \eta_{ab}$ or

$$g_{ab} = \eta_{ab} + h_{ab}, \tag{2.36}$$

the propagation equation of Eq. (2.26) in vacuum leads to

$$\Box \bar{h}_{ab} + \eta_{ab}\partial^c\partial^d\bar{h}_{cd} - \partial^c\partial_b\bar{h}_{ac} - \partial^c\partial_a\bar{h}_{bc} = 0. \tag{2.37}$$

However, the linearization Eq. (2.36) is not unique or does not fully specify the coordinate system and a residual gauge symmetry remains. More specifically, when discussing perturbations, we map the coordinates of two manifolds, but if we re-cover the coordinates of one of them, this map should be changed. When a theory has gauge symmetry, it means that the action is invariant to continuous local transformations of the field, called gauge transformations. This means that the theory has non-trivial degrees of freedom (gauge degrees of freedom), and it is difficult to analyze a theory with gauge symmetry. Therefore, we remove the gauge degrees of freedom by fixing the arbitrary functions in the gauge transformation and extract the physical degrees of freedom. We shall consider a transformation as

$$x'^{\mu} = x^{\mu} + \xi^{\mu}(x), \tag{2.38}$$

where the derivatives $|\partial_\mu \xi_\nu|$ have at most the same order $|h_{\mu\nu}|$. Under this transformation, we find [3]

$$h'_{\mu\nu}(x') = h_{\mu\nu}(x) - (\partial_\mu \xi_\nu + \partial_\nu \xi_\mu). \tag{2.39}$$

or

$$\bar{h}'_{\mu\nu}(x') = \bar{h}_{\mu\nu}(x) - (\partial_\mu \xi_\nu + \partial_\nu \xi_\mu - \eta_{\mu\nu}\partial_\rho \xi^\rho). \tag{2.40}$$

The smallness of $h'_{\mu\nu}$ is supported by the smallness of $|\partial_\mu \xi_\nu|$. We can use the Lorentz gauge

$$\partial^b \bar{h}_{ab} = 0, \tag{2.41}$$

which is Eq. (2.27) in the case of the flat backgound. The fact that the Lorentz gauge condition can be imposed is guaranteed from the existence of solutions to the differential equations

$$\begin{aligned}(\partial^\nu \bar{h}_{\mu\nu})' &= \eta^{\nu\beta}(\partial_\beta - (\partial_\beta \xi^\alpha)\partial_\alpha)\bar{h}'_{\mu\nu} \\ &= \partial^\nu \bar{h}_{\mu\nu} - \Box \xi_\mu \\ &= 0\end{aligned} \tag{2.42}$$

because the d'Alembertian operator is invertible. By the Lorentz gauge, the Eq. (2.37) becomes

$$\Box \bar{h}_{ab} = 0. \tag{2.43}$$

The Lorentz gauge Eq. (2.41) is not spoiled by a further gauge transformation Eq. (2.38) with the condition

$$\Box \xi_\mu = 0. \tag{2.44}$$

We utilize this residual gauge degrees of freedom to achieve the radiation gauge

[3] Consider the diffeomorphism ϕ between the real space-time manifold M_p with g_{ab} and the virtual background manifold M_b with η_{ab} to correspond the two manifolds. The metric perturbation is defined by the difference between η_{ab} and the pull-back $(\phi_* g)_{ab}$ as $h_{ab} := (\phi_* g)_{ab} - \eta_{ab}$. There is a freedom of choice for ϕ. Consider a one-parameter transformation group $\psi_\epsilon : M_b \to M_b$ generated by a vector field ξ^a. The new diffeomorphism $(\phi \circ \psi_\epsilon)$ transform the metric perturbation as $h^{(\epsilon)}_{ab} := ((\phi \circ \psi_\epsilon)_* g)_{ab} - \eta_{ab} = (\psi_{\epsilon *}(\phi_* g))_{ab} - \eta_{ab} = (\psi_{\epsilon *} h_{ab}) + (\psi_{\epsilon *}\eta_{ab}) - \eta_{ab} = h_{ab} + (\psi_{\epsilon *}\eta_{ab}) - \eta_{ab} = h_{ab} + \epsilon L_\xi \eta_{ab} = h_{ab} + 2\epsilon \partial_{(a}\xi_{b)}$ where L_ξ denotes the Lie derivative by ξ^a. This shows the mathematical description of the gauge transformation [2, 104].

as [4]

$$\bar{h}' = 0, \tag{2.45}$$

and

$$\bar{h}'_{0i} = 0. \tag{2.46}$$

The fact that the radiation gauge condition can be imposed is guaranteed from the existence of solutions to the differential equations

$$\begin{aligned} \bar{h}' &= \bar{h} + 2\partial_\mu \xi^\mu \\ &= 0, \end{aligned} \tag{2.47}$$

and

$$\begin{aligned} \bar{h}'_{0i} &= \bar{h}_{0i}(x) - (\partial_0 \xi_i + \partial_i \xi_0). \\ &= 0. \end{aligned} \tag{2.48}$$

We derivate these two equations in terms of x_0 (and use Eq. (2.44)) and obtain

$$\partial_0 \bar{h} + 2(-\nabla^2 \xi_0 + \partial_i(\partial_0 \xi^i)) = 0, \tag{2.49}$$

and

$$\partial_0 \bar{h}_{0i}(x) - (-\nabla^2 \xi_i + \partial_i(\partial_0 \xi_0)) = 0. \tag{2.50}$$

From Eq. (2.47), Eq. (2.48), Eq. (2.49), and Eq. (2.50) on the initial surface $t = t_0$, we obtain the initial values of $\xi_0, \xi_1, \xi_2, \xi_3$ and $\partial_0\xi_0, \partial_0\xi_1, \partial_0\xi_2, \partial_0\xi_3$ at $t = t_0$. Solving the Eq. (2.44) with these initial values, we achieve the radiation gauge Eq. (2.45) and Eq. (2.46). As a bonus, Eq. (2.41) yields

$$\partial_0 \bar{h}_{00} = 0 \Rightarrow \bar{h}_{00} = 0. \tag{2.51}$$

In summary, the metric perturbation under the Lorentz gauge and the

[4] For convenience, we omit the prime notation appropriately. To be more precise, we need two primes here because after the gauge transformation to take the Lorentz gauge, we gauge transformed again to take the radiation gauge.

radiation gauge satisfies,

$$h_{0\mu} = 0, \tag{2.52a}$$

$$h = 0, \tag{2.52b}$$

$$\partial^j h_{ij} = 0, \tag{2.52c}$$

where note that $\bar{h}_{\mu\nu} = h_{\mu\nu}$. This gauge condition is called the transverse-traceless gauge. Eq. (2.43) has plane wave solutions

$$h_{ij}^{TT} = H_{ij}(\boldsymbol{k}) e^{ik^\mu x_\mu}. \tag{2.53}$$

where we used $h_{0\mu} = 0$. The condition $\partial^j h_{ij} = 0$ gives $k^\mu = (\omega/c, \boldsymbol{k})$ and $\omega/c = |\boldsymbol{k}|$ and the condition $h = 0$ gives $H = 0$. When we set the x^3 axis to the wave vector direction $\boldsymbol{k}$, the condition $\partial^j h_{ij} = 0$ yields $k^j H_{ij} = H_{i3} = 0$ and then we obtain

$$h_{ij}^{TT} = (h_+ e_{ij}^+ + h_\times e_{ij}^\times) e^{ik^\mu x_\mu}, \tag{2.54}$$

where e_{ij}^+ and $e_{ij}^\times$ are called the polarization tensor defined by

$$e_{ab}^+ = \hat{e}_{x_1} \otimes \hat{e}_{x_1} - \hat{e}_{x_2} \otimes \hat{e}_{x_2}, \tag{2.55}$$

and

$$e_{ab}^\times = \hat{e}_{x_1} \otimes \hat{e}_{x_2} + \hat{e}_{x_2} \otimes \hat{e}_{x_1}, \tag{2.56}$$

where $\hat{e}_{x_1}$ and $\hat{e}_{x_2}$ represent the unit vectors for x_1 and x_2, respectively. We call the physical degrees of freedom corresponding to h_+ and $h_\times$ plus and cross polarization modes, respectively. In GR, GWs can have two tensor modes (plus and cross) as the physical degrees of freedom.

2.2.3 Energy-momentum tensor

t_{ab} in Eq. (2.23) denotes the energy-momentum tensor. Inside the spatial or the temporal average, the derivative ∂_μ can be integrated by parts, neglecting the boundary terms. By integration by parts, the gauge conditions $\partial^\mu h_{\mu\nu}$ and

$h = 0$, and the wave equation $\Box h_{ab}$, we find

$$\langle R^{(2)}_{ab} \rangle = -\frac{1}{4} \langle \partial_a h_{cd} \partial_b h^{cd} \rangle, \tag{2.57}$$

or

$$t_{ab} = \frac{c^4}{32\pi G} \langle \partial_a h_{cd} \partial_b h^{cd} \rangle, \tag{2.58}$$

which is the gauge free expression. Thus, the gauge invariant energy is

$$\begin{aligned} t^{00} &= \frac{c^2}{32\pi G} \langle \dot{h}^{TT}_{ij} \dot{h}^{TT}_{ij} \rangle \\ &= \frac{c^2}{16\pi G} \langle \dot{h}^2_+ + \dot{h}^2_\times \rangle. \end{aligned} \tag{2.59}$$

A GW propagating radially outward at sufficiently large distance r has the general form

$$h^{TT}_{ij}(t, r) = \frac{1}{r} f_{ij}(t - r/c), \tag{2.60}$$

where $t - r/c$ denotes the retarded time. From this general form, we find

$$\frac{\partial}{\partial r} h^{TT}_{ij} = -\partial_0 h^{TT}_{ij} + O(1/r^2), \tag{2.61}$$

or that the derivatives in terms of r and x_0 commute. Note that

$$\partial_a t^{ab} = 0 \Rightarrow \int_V d^3x (\partial_0 t^{00} + \partial_i t^{0i}) = 0, \tag{2.62}$$

so we can define the GW energy inside the volume as

$$E_V := \int_V d^3x t^{00}, \tag{2.63}$$

and consequently rewrite the above equation

$$\begin{aligned} \frac{dE_V}{dt} &= -c \int_V d^3x \partial_i t^{0i} \\ &= -\int_{\partial V} dA n_i t^{0i} \\ &= -\int_{\partial V} dA t^{0r}, \end{aligned} \tag{2.64}$$

where

$$\begin{aligned} t^{0r} &= \frac{c^4}{32\pi G}\langle \partial^0 h_{ij}^{TT} \frac{\partial}{\partial r} h_{ij}^{TT} \rangle \\ &= \frac{c^4}{32\pi G}\langle \partial^0 h_{ij}^{TT} \partial^0 h_{ij}^{TT} \rangle \\ &= t^{00}. \end{aligned} \tag{2.65}$$

or

$$\frac{dE}{dt} = \frac{c^3 r^2}{32\pi G} \int d\Omega \langle \dot{h}_{ij}^{TT} \dot{h}_{ij}^{TT} \rangle. \tag{2.66}$$

This equation gives the change rate of the gravitational field energy. Similarly, considering the change rate $c\partial_0 P_V^k$ where

$$P_V^k := \frac{1}{c} \int_V d^3x t^{0k}, \tag{2.67}$$

is the momentum of the GWs inside a volume V, we find

$$\frac{dP_V^k}{dt} = -\frac{c^3 r^2}{32\pi G} \int d\Omega \langle \dot{h}_{ij}^{TT} \partial^k h_{ij}^{TT} \rangle. \tag{2.68}$$

2.2.4 Generation

Here, we review the generation of the GWs. We start from Eq. (2.43) with the matter under the Lorentz gauge

$$\Box \bar{h}_{ab} = -16\pi T_{ab}. \tag{2.69}$$

The solution can be found by a Green's function with the appropriate boundary conditions

$$\bar{h}_{\mu\nu} = \frac{4G}{c^4} \int d^3x' \frac{1}{|\boldsymbol{x} - \boldsymbol{x}'|} T_{\mu\nu} \left(t - \frac{|\boldsymbol{x} - \boldsymbol{x}'|}{c}, \boldsymbol{x}' \right). \tag{2.70}$$

If we want to derive the TT components, we can act the projecting operator $\Lambda_{ij,kl} := \left(P_m^i P_l^i - \frac{1}{2} P^{ij} P_{ml} \right) \bar{h}^{ml}$ where $P_{ij} := \delta_{ij} - N_i N_j$ (see the expression for

A_{TT}^{ij} in Eq. (3.24)) on the metric perturbation

$$\bar{h}_{ij}^{TT} = \frac{4G}{c^4}\Lambda_{ij,kl}\int d^3x' \frac{1}{|\boldsymbol{x}-\boldsymbol{x}'|}T_{kl}\left(t-\frac{|\boldsymbol{x}-\boldsymbol{x}'|}{c},\boldsymbol{x}'\right). \tag{2.71}$$

Next, we consider the multipole expansion to simplify the stress-energy tensor. Let ω_s be the typical angular frequency of the motion inside the source, d be the typical source size, and $v \sim d\omega_s$ be the typical velocity of the source. The frequency of the radiation ω would be of order ω_s and then we find

$$\lambda := \frac{c}{\omega} \sim \frac{c}{\omega_s} \sim \frac{c}{v}d. \tag{2.72}$$

For a non-relativistic system where $v << c$, the condition

$$\lambda >> d, \tag{2.73}$$

holds. At $r >> d$ note that $|\boldsymbol{x}-\boldsymbol{x}'| = r - \boldsymbol{x}'\cdot\hat{\boldsymbol{x}} + O(d^2/r) \sim r$, and then we find

$$\bar{h}_{\mu\nu} = \frac{1}{r}\frac{4G}{c^4}\Lambda_{ij,kl}\int d^3x' T_{kl}\left(t-\frac{r}{c}+\frac{\boldsymbol{x}'\cdot\hat{\boldsymbol{x}}}{c},\boldsymbol{x}'\right). \tag{2.74}$$

The Fourier transform of T_{kl} is written

$$T_{kl}\left(t-\frac{r}{c}+\frac{\boldsymbol{x}'\cdot\hat{\boldsymbol{x}}}{c},\boldsymbol{x}'\right) = \frac{1}{(2\pi)^4}\int d^4k\tilde{T}_{kl}(\omega,\boldsymbol{k})e^{-i\omega(t-r/c+\boldsymbol{x}'\cdot\hat{\boldsymbol{x}}/c)+i\boldsymbol{k}\cdot\boldsymbol{x}'}. \tag{2.75}$$

and the exponential can be expanded as

$$\begin{aligned} e^{-i\omega(t-r/c+\boldsymbol{x}'\cdot\hat{\boldsymbol{x}}/c)} =& e^{-i\omega(t-r/c)} \\ &\times\left[1-i\frac{\omega}{c}x'^i x^i + \frac{1}{2}\left(-i\frac{\omega}{c}\right)x'^i x^i x'^j x^j + \ldots\right]. \end{aligned} \tag{2.76}$$

After substituting this, we find

$$T_{kl}\left(t-\frac{r}{c}+\frac{\boldsymbol{x}'\cdot\hat{\boldsymbol{x}}}{c},\boldsymbol{x}'\right) \simeq T_{kl}\left(t-\frac{r}{c},\boldsymbol{x}'\right)+\frac{1}{c}x'^i x^i\partial_0 T_{kl}+\frac{1}{2c^2}x'^i x^i x'^j x^j\partial_0^2 T_{kl}+\ldots, \tag{2.77}$$

where the derivatives are evaluated at $(t - \frac{r}{c}, \boldsymbol{x}')$. Finally, we find

$$\begin{aligned}\bar{h}_{\mu\nu} =& \frac{1}{r}\frac{4G}{c^4}\Lambda_{ij,kl} \\ &\times \left[S^{kl} + \frac{1}{c}\hat{x}_m \dot{S}^{kl,m} + \frac{1}{2c^2}\hat{x}_m\hat{x}_n\ddot{S}^{kl,mn}\dots\right]_{t_{\text{ret}}},\end{aligned} \tag{2.78}$$

where

$$S^{ij}(t) := \int d^3x T^{ij}(t, \boldsymbol{x}), \tag{2.79}$$

$$S^{ij,k}(t) := \int d^3x T^{ij}(t, \boldsymbol{x}) x^k, \tag{2.80}$$

$$S^{ij,kl}(t) := \int d^3x T^{ij}(t, \boldsymbol{x}) x^k x^l, \tag{2.81}$$

are the momenta of the stress-energy tensor T^{ij}. By a virtue of the identities from the energy conservation law $T_{ab}{}^{,b} = 0$ in the linearized theory

$$\dot{M} = 0, \tag{2.82a}$$
$$\dot{M}^i = P^i, \tag{2.82b}$$
$$\dot{M}^{ij} = P^{i,j} + P^{j,i}, \tag{2.82c}$$
$$\dot{M}^{ijk} = P^{i,jk} + P^{j,ki} + P^{k,ij}, \tag{2.82d}$$
$$\tag{2.82e}$$

and

$$\dot{P}^i = 0, \tag{2.83a}$$
$$\dot{P}^{i,j} = S^{ij}, \tag{2.83b}$$
$$\dot{P}^{i,jk} = S^{ij,k} + S^{ik,j}, \tag{2.83c}$$
$$\tag{2.83d}$$

we can use the moments of the energy density (M)

$$M := \frac{1}{c^2}\int d^3x T^{00}(t,\boldsymbol{x}), \tag{2.84a}$$

$$M^i := \frac{1}{c^2}\int d^3x T^{00}(t,\boldsymbol{x})x^i, \tag{2.84b}$$

$$M^{ij} := \frac{1}{c^2}\int d^3x T^{00}(t,\boldsymbol{x})x^i x^j, \tag{2.84c}$$

$$M^{ijk} := \frac{1}{c^2}\int d^3x T^{00}(t,\boldsymbol{x})x^i x^j x^k, \tag{2.84d}$$

and linear momentum (P)

$$P^i := \frac{1}{c}\int d^3x T^{0i}(t,\boldsymbol{x}), \tag{2.85a}$$

$$P^{i,j} := \frac{1}{c}\int d^3x T^{0i}(t,\boldsymbol{x})x^j, \tag{2.85b}$$

$$P^{i,jk} := \frac{1}{c}\int d^3x T^{0i}(t,\boldsymbol{x})x^j x^k, \tag{2.85c}$$

to rewrite the moments of the stress tensor as

$$S^{ij} = \frac{1}{2}\ddot{M}^{ij}, \tag{2.86}$$

$$\dot{S}^{ij,k} = \frac{1}{6}\dddot{M}^{ijk} + \frac{1}{3}(\ddot{P}^{i,jk} + \ddot{P}^{j,ik} + \ddot{P}^{k,ij}). \tag{2.87}$$

Chapter 3

Polarization tests

In this chapter, we review the reference frames describing the interaction of GWs with test masses. We also formulate the detector signal of GWs with full polarization modes and provide the antenna pattern functions for the detectors. The specific formulas and the properties of the antenna pattern for the interferometric detectors are provided in Appendix G. We also review the generalized parametrized post-Newtonian waveforms. Finally, we summerize the previous observational tests of the GW polarizations.

3.1 Interaction of GWs with test masses

We consider interaction of GWs with test masses that construct the GW detector. First, we provide the coordinate systems, and then give the motion of test masses.

3.1.1 Coordinate system

We assume the detector far away from the source such that the interaction of GWs with test masses can be described in GR. So, we present the reference frames in the context of GR.

Local inertial frame / Riemann normal coordinate

We construct the local inertial frame in which the metric can be regarded as η_{ab} and the connection $\Gamma^a{}_{bc}$ vanish at an event of the space-time. In other words, the gravity can be eliminated at a space-time point. The local inertial

frame is realized by the Riemann normal coordinate.

The standard existence theorem for ordinary differential equations applied fo the geodesic equations show that given $p \in M$ and $\forall T^a \in T_pM$ where M is the space-time and T_pM is the tangent vector space, there always exists a unique geodesic γ through p with tangent vector T^a. We define the exponential map, from T_pM to M by mapping $T_a \in T_pM$ into the point of M lying at unit affine parameter from p along the geodesic γ. There always exists a sufficiently small neighborhood of the origin of T_pM on which the exponential map is one-to-one. We can introduce the coordinate system x^a by assigning the components of T^a, x^a, with respect to some sets of basis $E_{(a)}$ to the point of M lying at unit affine parameter. The coordinate system is called Riemann normal coordinate. In the Riemann normal coordinate, it can be proved that $g_{ab} = \eta_{ab}$ and $\Gamma^a{}_{bc} = 0$ at p.

Freely falling frame / Fermi normal coordinate

Next, we construct the freely falling frame in which the metric can be regarded as η_{ab} and the connection $\Gamma^a{}_{bc}$ vanish along a geodesic. The freely falling frame can be formulated by the Fermi normal coordinate.

Consider a geodesic γ through $p_0 \in M$ with tangent vector T^a and the proper time t. We carry some orthonormal basis e_μ from p_0 to $p = \gamma(t)$ along the geodesic by Fermi-Walker transport [1]. Then, we also consider a geodesic λ starting from $p = \gamma(t)$ with tangent vector Ω^a orthogonal to T^a at p. As with the case of the construction of the Riemann normal coordinate, we can introduce the Fermi normal coordinate x^a by assigning t and $s\Omega^a$ to a point $q = \lambda(s)$. In the Fermi normal coordinate, it can be proved that $g_{ab} = \eta_{ab}$ and $\Gamma^a{}_{bc} = 0$ along the geodesic γ.

Finally, we construct the proper detector frame. This frame is very intuitive for physical experiments. In a laboratory, one choose an origin and ideally utilize a rigid ruler to define the coordinates. This procedure can be justified by taking the length of the ruler small. If we consider a sufficiently small

[1] The Fermi-Walker transport along a geodesic is identical with the standard parallel transport.

space-time region, the metric can be written as

$$\begin{aligned} ds^2 \simeq & -c^2dt^2(1+R_{0i0j}x^ix^j) \\ & -2cdt\ dx^i\ \left(\frac{2}{3}R_{0jik}x^jx^k+dx^idx^j\right)+dx^i\ dx^j\left(\delta_{ij}-\frac{1}{3}R_{ikjl}x^kx^l\right), \end{aligned} \tag{3.1}$$

by constructing the freely falling frame, that is the Fermi normal coordinates using Taylor expansion and the geodesic deviation equation.

Even in the case of a detector on Earth, in which the detector is not in free fall because it has an acceleration $a^i = -g^i$ with respect to local inertial frame and it rotates with respect to local gyroscopes[2], the metric can reduce to the form Eq. (3.1) by considering assuming that some suspension mechanism compensates the acceleration of gravity and that all other gravitational effects except for GWs such as Newtonian forces produce only slowly varying effects such that the effects are small enough in a high frequency window where the detector is sensitive to GWs. Consequently, we consider the metric form of Eq. (3.1) in this section hereafter.

3.1.2 Motion of test masses

In the Fermi normal coordinate, we use the geodesic deviation equation. We assume that the GW detector moves non-relativistically such that

$$\frac{dx^i}{d\tau} << \frac{dx^0}{d\tau} \Leftrightarrow dt^2 \simeq d\tau^2. \tag{3.2}$$

The geodesic deviation equation

$$\frac{D^2\xi^a}{\partial\tau^2} = -R^a{}_{bcd}\xi^c\frac{dx^b}{d\tau}\frac{dx^d}{d\tau} \tag{3.3}$$

gives

$$\frac{d^2\xi^i}{dt^2} = -c^2R^i{}_{0j0}\xi^j. \tag{3.4}$$

[2]The general form of the metric is given in [1, 105]. The coordinate is called the proper detector frame.

3.2 Gravitational-wave signal

The signal of the GW should be independent of the observer. It takes observer-independent quantity, that is some tensor form. Especially, for most cases, the detector signal become a scalar. In other words, there exists some tensor to project the GW components on a scalar. The tensor is called the detector tensor d^{ab}. We assume that the GW detector has a linear response to GWs and the output is a scalar. Thus, the I-th detector signal must be expressed by the contraction with the detector tensor d^{ab}, which represents the detector's transfer functions.

3.2.1 Polarizations

We shall consider the polarizations of GWs in a generic metric theory of gravity. We assume that the field equations of the alternative theories of gravity can reduce to wave equations in the far-away zone in which the potential fall $O(R^{-1})$ and the propagation speed is equal to the speed of light c. This means that the metric perturbation is assumed to depend on the retarded time $t_{\rm ret}$. Thus, we can decompose the metric perturbation as [3]

$$\bar{h}^{00} = \frac{G}{c^4 R} C(t_{\rm ret}, \boldsymbol{N}), \tag{3.5}$$

$$\bar{h}^{0j} = \frac{G}{c^4 R} D^j(t_{\rm ret}, \boldsymbol{N}), \tag{3.6}$$

$$\bar{h}^{jk} = \frac{G}{c^4 R} A^{jk}(t_{\rm ret}, \boldsymbol{N}), \tag{3.7}$$

and

$$C = C, \tag{3.8a}$$

$$D^j = N^j D + D^j_T, \tag{3.8b}$$

$$A^{jk} = \frac{1}{3}\delta^{jk} A + (N^j N^k - \frac{1}{3}\delta^{jk}) B - N^{(j} A^{k)}_T + A^{jk}_{TT}. \tag{3.8c}$$

[3] G/c^4 is inserted for convenience later.

Please refer to Appendix D for the details of the tensor decomposition. Next, we consider the gauge transformations

$$x^\alpha \to x'^\alpha + \zeta^\alpha(x^\beta). \tag{3.9}$$

The freedom to transform the coordinates must be restricted because we need to keep the general form of h_{ab} in the far-away wave zone. Thereby, the gauge vector ζ must be the following general form,

$$\zeta^0 = \frac{G}{c^4 R}\alpha(t_{\rm ret}, \boldsymbol{N}), \tag{3.10}$$

$$\zeta^j = \frac{G}{c^4 R}\beta^j(t_{\rm ret}, \boldsymbol{N}). \tag{3.11}$$

We can also decompose β^j as $\beta^j = N^j\beta + \beta^j_T$. Under the transformation, the decomposed pieces transform as

$$\bar{h}'^{00} = \frac{G}{c^4 R}C'(t_{\rm ret}, \boldsymbol{N}), \tag{3.12}$$

$$\bar{h}'^{0j} = \frac{G}{c^4 R}D'^j(t_{\rm ret}, \boldsymbol{N}), \tag{3.13}$$

$$\bar{h}'^{jk} = \frac{G}{c^4 R}A'^{jk}(t_{\rm ret}, \boldsymbol{N}), \tag{3.14}$$

where

$$C' = C + \partial_{t_{\rm ret}}(\alpha + \beta), \tag{3.15a}$$
$$D' = D + \partial_{t_{\rm ret}}(\alpha + \beta), \tag{3.15b}$$
$$D'^j_T = D^j_T + \partial_{t_{\rm ret}}\beta^j_T, \tag{3.15c}$$
$$A' = A + \partial_{t_{\rm ret}}(3\alpha - \beta), \tag{3.15d}$$
$$B' = B + 2\partial_{t_{\rm ret}}\beta, \tag{3.15e}$$
$$A'^j_T = A^j_T + \partial_\tau\beta^j_T, \tag{3.15f}$$
$$A'^{jk}_{TT} = A^{jk}_{TT}. \tag{3.15g}$$

Since the components R_{0j0k} are

$$R_{0j0k} = -\frac{1}{2}\left(\partial_{00}\bar{h}^{jk} - \frac{1}{2}\partial_{00}\bar{h}\delta_{jk} + \partial_{jk}\bar{h}^{00} + \frac{1}{2}\partial_{jk}\bar{h} + \partial_{0(j}\bar{h}^{0|k)}\right), \tag{3.16}$$

we obtain the expression for the components

$$c^2 R_{0j0k} = -\frac{G}{2c^4 R}\partial_{t_{\rm ret}t_{\rm ret}} S^{jk}(t_{\rm ret}, \boldsymbol{N}), \tag{3.17}$$

where

$$S^{jk} := (\delta^{jk} - N^j N^k)A_b + N^j N^k A_l + 2N^{(j}A_V^{k)} + A_{TT}^{jk}, \tag{3.18}$$

with

$$A_b = -\frac{1}{6}(A + 2B - 3C), \tag{3.19}$$

$$A_l = \frac{1}{3}(A + 2B + 3C - 6D), \tag{3.20}$$

$$A_V^k = A_T^k - D_T^k. \tag{3.21}$$

Here $t_{\rm ret}$ is the retarded time. Furthermore, we can rewrite S^{jk} in terms of the basis $\{e_X, e_Y, e_Z\}$ for the GW as

$$\begin{aligned} S^{jk} =& h_b(e_X^j e_X^k + e_Y^j e_Y^k) + e_Z^j e_Z^k h_l \\ &+ (e_X^j e_Z^k + e_Z^j e_X^k)h_{Vx} + (e_Y^j e_Z^k + e_Z^j e_Y^k)h_{Vy} \\ &+ (e_X^j e_X^k - e_Y^j e_Y^k)h_+ + (e_X^j e_Y^k + e_Y^j e_X^k)h_\times. \end{aligned} \tag{3.22}$$

with the GW polarizations

$$h_b := A_b, \tag{3.23a}$$

$$h_l := A_l, \tag{3.23b}$$

$$h_{Vx} := e_{X,j}A_V^k, \tag{3.23c}$$

$$h_{Vy} := e_{Y,j}A_V^k, \tag{3.23d}$$

$$h_+ := \frac{1}{2}(e_X^j e_X^k - e_Y^j e_Y^k)A_{TT}^{jk}, \tag{3.23e}$$

$$h_\times := \frac{1}{2}(e_X^j e_Y^k + e_Y^j e_X^k)A_{TT}^{jk}. \tag{3.23f}$$

From Eq. (3.8), we can derive the amplitudes in terms of the trace-reversed

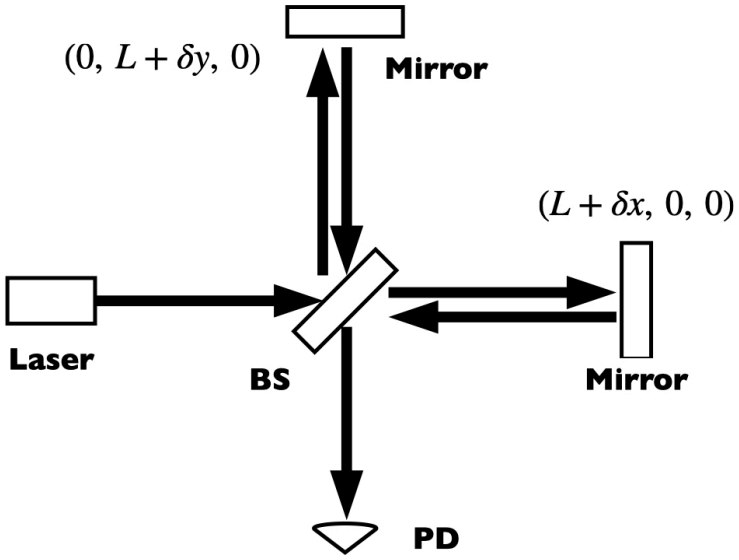

Figure 3.1: The simplest configuration of the interferometric detectors composed of a laser, two mirrors (=free masses), a beam splitter (BS), and a photo diode (PD). The laser light passes through the BS and splits in two directions. Each transmitted light propagates through the arms and reaches the mirror as a free test particle. The reflected lights are combined at the BS and the phase difference between the two light paths is detected by the PD as light intensity.

metric perturbations

$$A_b = \frac{1}{2}(N_j N_k \bar{h}^{jk} - \bar{h}^{00}), \tag{3.24a}$$

$$A_l = N_j N_k \bar{h}^{jk} + \bar{h}^{00} - 2N_j \bar{h}^{0j}, \tag{3.24b}$$

$$A_V^k = P_j^k (N_i \bar{h}^{ij} - \bar{h}^{0j}), \tag{3.24c}$$

$$A_{TT}^{ij} = \left(P_m^i P_l^i - \frac{1}{2} P^{ij} P_{ml} \right) \bar{h}^{ml}, \tag{3.24d}$$

where $P_{ij} := \delta_{ij} - N_i N_j$.

3.2.2 Interferometric detector signal

We restrict attention to the interferometric detector that observes GWs by laser light reading out the differential motion of test masses. Here, we review

the interferometric detector briefly and provide the detector tensor for the interferometric detector in a generic metric theory of gravity. In the case of $\omega_{\rm GW}L/c << 1$ where $\omega_{\rm GW}$ is the angular frequency of the GW and L is the arm length of the interferometric detector, we can describe the motion of the mirrors in the proper detector frame [4] by the geodesic deviation equation Eq. (3.4). The mirror, whose location is expanded in terms of h as $\xi^i_{(1)} = (L + \delta x, 0, 0)$ with $\delta x \sim O(h)$, obeys the equation along the x direction

$$\frac{d^2\delta x}{dt^2} = L\frac{G}{2c^4R}\partial_{t_{\rm ret}t_{\rm ret}}S^{11}, \tag{3.25}$$

and the mirror whose location is expanded in terms of h as $\xi^i_{(2)} = (0, L+\delta y, 0)$ with $\delta y \sim O(h)$, obeys the equation along the y direction

$$\frac{d^2\delta y}{dt^2_{\rm ret}} = L\frac{G}{2c^4R}\partial_{t_{\rm ret}t_{\rm ret}}S^{22}. \tag{3.26}$$

The interferometers measure the phase difference

$$\Delta\Phi = 2\pi\nu\left(\frac{2L_1}{c} - \frac{2L_2}{c}\right), \tag{3.27}$$

where L_1 and L_2 are the positions of the mirrors: $L_1 = \xi^1_{(1)}$ and $L_2 = \xi^2_{(2)}$. Thus, we obtain the expression for the detector signal

$$\Delta\Phi = \frac{4\pi\nu GL}{c^5R}S(t), \tag{3.28}$$

where

$$S(t) = \frac{1}{2}(e^j_1e^k_1 - e^j_2e^k_2)S^{jk}. \tag{3.29}$$

After we define the detector tensor d^{jk}

$$d^{jk} = \frac{1}{2}(e^j_1e^k_1 - e^j_2e^k_2), \tag{3.30}$$

[4] The metric can be effectively regarded as the Fermi normal coordinate considering appropriate compensation system and the frequency range in which the Newtonian forces can be ignored as mentioned in Section 3.1.1.

and the polarization basis

$$e^{+}_{ab} = \hat{e}_X \otimes \hat{e}_X - \hat{e}_Y \otimes \hat{e}_Y, \tag{3.31}$$

$$e^{\times}_{ab} = \hat{e}_X \otimes \hat{e}_Y + \hat{e}_Y \otimes \hat{e}_X, \tag{3.32}$$

$$e^{x}_{ab} = \hat{e}_X \otimes \hat{e}_Z + \hat{e}_Z \otimes \hat{e}_X, \tag{3.33}$$

$$e^{y}_{ab} = \hat{e}_Y \otimes \hat{e}_Z + \hat{e}_Z \otimes \hat{e}_Y, \tag{3.34}$$

$$e^{b}_{ab} = \hat{e}_X \otimes \hat{e}_X + \hat{e}_y \otimes \hat{e}_Y, \tag{3.35}$$

$$e^{l}_{ab} = \sqrt{2}\hat{e}_Z \otimes \hat{e}_Z, \tag{3.36}$$

we can define the antenna pattern functions F^A as

$$F^A := d^{ab} e^A_{ab}, \tag{3.37}$$

where A is the polarization index running over $\{B, L, Vx, Vy, +, \times\}$. [5] The antenna pattern functions can be visualized as shown in Fig. 3.2 for the interferometric detectors. The length in the radial direction denotes the value of the antenna pattern functions in the direction. The specific functions are written in Appendix G. Except for the two scalar modes, the detector response to the polarization modes differently.

Finally, we can write the detector signal as a linear combination of the polarizations with the coefficients of the antenna pattern functions

$$S(t) = \sum_A F^A h_A. \tag{3.38}$$

Hereafter, we denote the detector signal as $h_I(t)$ where I is the detector label. In the same way as in Eq. (3.25) and Eq. (3.26), we can calculate a motion of the test particles arranged on a circle by each polarization mode passing through from the geodesic equation. Fig. 3.3 shows the motion for all polarization modes. The polarization modes of the null GWs can be studied by Newman-Penrose formalism transparently. In Appendix E, the $E(2)$ classification to classify the theories of gravity in terms of the polarization modes is

[5] In some cases, we use the short notation $\{b, l, x, y, +, \times\}$.

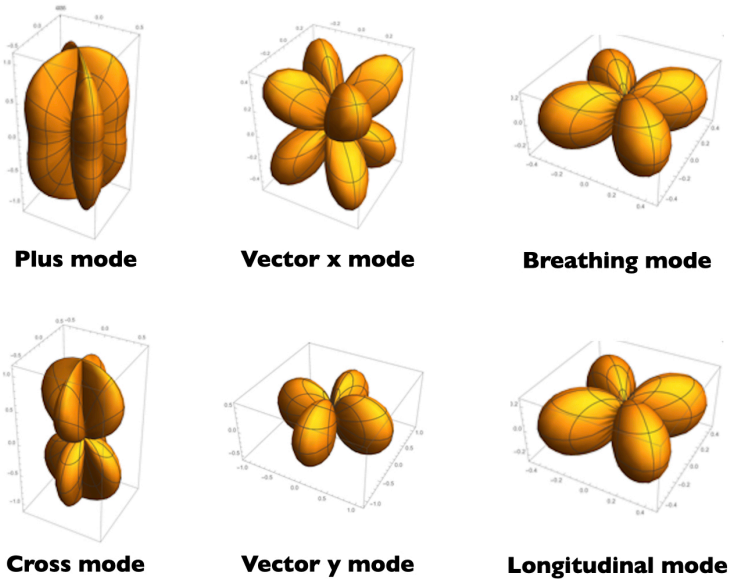

Figure 3.2: The antenna pattern functions of the interferometric detectors. Those of the scalar modes have the same functional form and then they are degenerated.

provided.

3.3 Parametrized waveforms

We shall pay attention to inspiral GWs from CBCs whose component masses are m_1 and m_2. We need to calculate the detector signal for a GW from a CBC in time domain and in frequency domain. We review the generalized parametrized inspiral waveforms with full polarization modes through the deformation of the binding energy and the rate of change of the radiated energy in time. We follow the discussions in [96]. In this section, we use geometric units with $G = c = 1$ to avoid the complexity of the expressions.

We set a source system spanned by a unit vector set of $(\hat{i}, \hat{j}, \hat{k})$ such that the binary motion is on the $i - j$ on the plane and the vector from the source to the detector (observer) is on the $j - k$ plane. In the system, the orbital

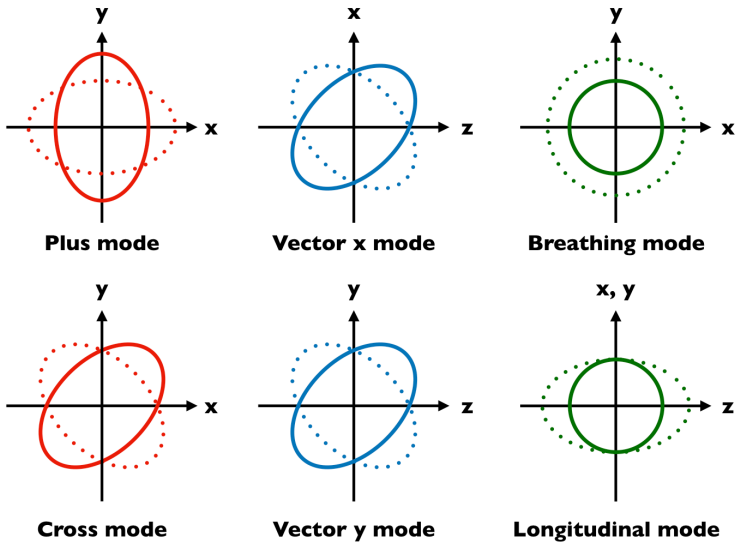

Figure 3.3: Test free particles motion caused by the propagation of the polarization modes. The propagation direction is $+z$.

trajectory $\hat{x}$ and the orbital velocity unit vector $\hat{v}$ are described by

$$\hat{x} = \cos\Phi\hat{i} + \sin\Phi\hat{j}, \tag{3.39}$$

and

$$\hat{v} = -\sin\Phi\hat{i} + \cos\Phi\hat{j}, \tag{3.40}$$

We write the unit vector from the source to the detector (observer) $\hat{N}$ as

$$\hat{N} = \sin\iota\hat{j} + \cos\iota\hat{k}, \tag{3.41}$$

with the inclination angle ι. Then, we choose the GW system $(e_X, e_Y, e_Z := \hat{N})$ as

$$e_Y = -\hat{i}, \tag{3.42}$$

$$e_X = e_Y \times \hat{N} = \cos\iota\hat{j} - \sin\iota\hat{k}. \tag{3.43}$$

3.3.1 Stationary phase approximation

In GW data analysis, we often need to Fourier transform some detector signal to obtain the signal in frequency domain. We usually utilize the stationary phase approximation (SPA) to realize the Fourier transformation. We assume that the signal is composed of a slowly varying amplitude $A(t)$ and a rapidly varying phase $l\Phi(t)$ with $l > 0$

$$h(t) = \frac{1}{2}A(t_{\rm ret})\cos\left(l\Phi(t_{\rm ret})\right) = \frac{1}{2}A(t_{\rm ret})(e^{il\Phi(t_{\rm ret})} + e^{-il\Phi(t_{\rm ret})}). \tag{3.44}$$

The Fourier components become

$$\begin{aligned}\tilde{h}(f) &= \frac{1}{2}\int A(t_{\rm ret})(e^{2\pi ift+il\Phi(t_{\rm ret})} + e^{2\pi ift-il\Phi(t_{\rm ret})})dt. \\ &= \frac{1}{2}\int A(t_{\rm ret})e^{2\pi ifR/c}(e^{2\pi ift_{\rm ret}+il\Phi(t_{\rm ret})} + e^{2\pi ift_{\rm ret}-il\Phi(t_{\rm ret})})dt_{\rm ret} \\ &= \frac{1}{2}\int A(t)e^{2\pi ifR/c}(e^{2\pi ift+il\Phi(t)} + e^{2\pi ift-il\Phi(t)})dt\end{aligned} \tag{3.45}$$

where in the last line we replace and rename the integral variable. Since the first term does not have any stationary point t, at which the derivative of the argument of the exponential function vanishes, the first term oscillates rapidly in time and then the integration can be neglected. The second term has a stationary point t_* satisfying

$$2\pi if - l\dot{\Phi}(t_*) = 0, \tag{3.46}$$

because $\dot{\Phi} = \Omega = 2\pi F > 0$ is the orbital angular frequency [6]. Around the stationary point, the term change slowly in time giving non-zero contributions to the integral from the Riemann-Lebesgue lemma. We expand the argument

[6] We write the angular frequency and the frequency for the orbital motion of the binary system using the capital letters, while we use the small letters for the emitted gravitational wave. The relations are $l\Omega = \omega_{\rm GW}$ or $lF = f_{\rm GW}$.

in the integrand in terms of t around t_* finding

$$\begin{aligned}\tilde{h}(f) &\simeq \frac{1}{2}\int A(t)e^{2\pi i f R/c}e^{2\pi i f t - il\Phi(t)}dt \\ &= \frac{1}{2}e^{2\pi i f R/c}A(t_*)e^{2\pi i f t_* - il\Phi(t_*)}\int dt e^{-i\frac{1}{2}\ddot{\Phi}(t_*)(t-t_*)^2} \\ &= \frac{1}{2}e^{2\pi i f R/c}A(t_*)e^{2\pi i f t_* - il\Phi(t_*)}\sqrt{\frac{2}{l\ddot{\Phi}(t_*)}}\int_\infty^\infty e^{-ix^2} \\ &= \frac{1}{2}A(t_*)\sqrt{\frac{2\pi}{l\ddot{\Phi}(t_*)}}e^{i[2\pi f(t_*+R/c)-l\Phi(t_*)-\pi/4]}.\end{aligned} \tag{3.47}$$

We can simply substitute the stationary point t_* into the argument of the slowly-varying parts to find the Fourier components.

The phase part can be rewritten as

$$\Phi(t_*) = \int^{t_*} 2\pi F dt = \int^{F(t_*)} 2\pi F' dF' \frac{dt}{dF'} = \int^{F(t_*)} 2\pi F' dF' \frac{1}{\dot{F}'}, \tag{3.48}$$

and

$$t_* = \int^{t_*} dt = \int^{F(t_*)} \frac{dt}{dF'} dF' = \int^{F(t_*)} \frac{1}{\dot{F}'} dF', \tag{3.49}$$

where a dot denotes the time derivative. Consequently, we obtain [7]

$$\tilde{h}(f) \simeq \frac{1}{2}A(t_*)\sqrt{\frac{2\pi}{\ddot{\Phi}(t_*)}}e^{i2\pi f R/c}e^{-i\Psi}, \tag{3.50}$$

with

$$\Psi[F(t_*)] := 2\pi\int^{F(t_*)}\left(l\frac{F'}{\dot{F}'} - \frac{f}{\dot{F}'}\right)dF' + \frac{\pi}{4}. \tag{3.51}$$

3.3.2 Parametrized deformation

For SPA, we need to know the time change in frequency $\dot{F}$ in each theory of gravity. To obtain the time change in frequency $\dot{F}$, we use the binary binding energy (= total energy) and the change rate of the binding energy that is

[7] The factor of $e^{i2\pi f R/c}$ represents the Doppler phase. In some cases, it may be omitted for simplicity when discussing the GW waveforms.

the rate of the radiated GW energy. We calculate the rate of change of the binding energy in alternative theories of gravity by equating the derivative of the parametrically deformed binding energy and the parametrically deformed change rate of the binding energy.

By dimensional analysis, the time domain detector signal can be written in a harmonic decomposition as

$$h^{(l)}(t) = Q(\iota, \theta, \phi, \psi)\eta^{2/5}\frac{\mathcal{M}}{D}v^l e^{-il\Phi}, \tag{3.52}$$

where ι is the inclination angle of the binary system, (θ, ϕ) are the sky position angular parameters, and ψ is the polarization angle. $\eta := m_1 m_2/m^2$ is the symmetric mass ratio and $\mathcal{M} := \eta^{3/5}m$ is the chirp mass where $m := m_1 + m_2$ is the binary total mass.

When we Fourier transform this time-domain detector signal by the SPA, we need the binding energy and the change rate of the binding energy. The former is parametrically modified as

$$E = E_{\rm GR}\left[1 + A\left(\frac{m}{r}\right)^p\right], \tag{3.53}$$

where $E_{\rm GR}$ is the binding energy in GR and A and p are the deformation parameters. We assume that A is small. This modification leads modified Kepler's law

$$\Omega^2 = \frac{m}{r^3}\left[1 + \frac{1}{2}Ap\left(\frac{m}{r}\right)^p\right], \tag{3.54}$$

and its inverse

$$r = \left(\frac{m}{\Omega^2}\right)^{1/3}\left[1 + \frac{1}{6}Ap(m\Omega)^{2p/3}\right]. \tag{3.55}$$

The Virial theorem is then modified as

$$v = r\Omega = (m\Omega)^{1/3}\left[1 + \frac{1}{6}Ap(m\Omega)^{2p/3}\right]. \tag{3.56}$$

As a consequence, we obtain the binding energy to leading PN order

$$E = -\frac{1}{2}\eta^{-2/5}(2\pi\mathcal{M}F)^{2/3}\left[1 - \frac{1}{3}A(5p-6)\eta^{-2p/5}(2\pi\mathcal{M}F)^{2p/3}\right]. \tag{3.57}$$

Then, we rewrite the time domain detectors signal

$$h^{(l)}(t) = Q(\iota,\theta,\phi,\psi)\eta^{(2-l)/5}\frac{\mathcal{M}}{d_L}(2\pi\mathcal{M}F)^{l/3}e^{-il\Phi}\left[1+\frac{1}{6}Apl\eta^{-2p/5}(2\pi\mathcal{M}F)^{2p/3}\right]. \tag{3.58}$$

Furthermore, the change rate of the binding energy that is the change rate of the radiate energy is also parametrically modified as

$$\dot{E} = \dot{E}_{\rm GR}\left[1+B\left(\frac{m}{r}\right)^q\right], \tag{3.59}$$

where $\dot{E}_{\rm GR}$ is the energy flux in GR derived below and B and q are the deformation parameters. We can rewrite it using the above modified Kepler's law

$$\dot{E} = -\frac{32}{5}(2\pi\mathcal{M}F)^{10/3}\left[1+B\eta^{-2q/5}(2\pi\mathcal{M}F)^{2q/3}-\frac{1}{3}Ap\eta^{-2p/5}(2\pi\mathcal{M}F)^{2p/3}\right]. \tag{3.60}$$

Finally, by equating the derivative of the binding energy and the rate change of the binding energy, we obtain

$$\begin{aligned}\frac{dF}{dt} =&\frac{48}{5\pi\mathcal{M}^2}(2\pi\mathcal{M}F)^{11/3}\\ &\times\left[1+B\eta^{-2q/5}(2\pi\mathcal{M}F)^{2q/3}+\frac{1}{3}A(5p^2-2p-6)\eta^{-2p/5}(2\pi\mathcal{M}F)^{2p/3}\right],\end{aligned} \tag{3.61}$$

up to leading PN order.

Therefore, employing the SPA, the frequency domain detector signal can be written as

$$\begin{aligned}\tilde{h}^{(l)}(f) =&\sqrt{\frac{5\pi}{48l}}Q\frac{M^2}{d_L}\eta^{(2-l)/5}u_l^{(2l-11)/2}e^{-i\Psi^{(l)}}\\ &\times\left[1-\frac{1}{2}B\eta^{-2q/5}u_l^{2q}+\frac{1}{6}A(lp+6+2p-5p^2)\eta^{-2p/5}u_l^{2p}\right],\end{aligned} \tag{3.62}$$

with

$$\Psi^{(l)} = \Psi^{(l)}_{\rm GR} + \frac{5}{64} A \frac{l(5p^2-2p-5)}{(4-p)(5-2p)} \eta^{-2p/5} u_l^{2p-5} + \frac{15}{64} B \frac{l}{(4-q)(5-2q)} \eta^{-2q/5} u_l^{2q-5}, \tag{3.63}$$

where

$$u_l := \left(\frac{2\pi \mathcal{M} F}{l} \right)^{1/3}. \tag{3.64}$$

The modification to the energy flux introduces corrections to q PN order, while the modification to the binding energy introduces corrections to p PN order in both the amplitude and the phase.

3.3.3 Parametrized post Eiensteinian framework

Based on the detector signals in the specific theories of gravity in Appendix F, we can construct the parametrized inspiral waveforms with full polarization modes as

$$\begin{aligned} \bar{h}_{\rm ppE,0}(f) =& \bar{h}_{\rm GR} e^{i\beta u_2^b} + [\alpha_+ F_+ + \alpha_\times F_\times + \alpha_x F_x + \alpha_y F_y \\ &+ \alpha_b F_b + \alpha_l F_l] \frac{\mathcal{M}^2}{D_L} u_2^a e^{-i\Psi^{(2)}_{\rm GR}} e^{i\beta u_2^b} \\ &+ [\gamma_+ F_+ + \gamma_\times F_\times + \gamma_x F_x + \gamma_y F_y \\ &+ \gamma_b F_b + \gamma_l F_l] \eta^{1/5} \frac{\mathcal{M}^2}{D_L} u_1^c e^{-i\Psi^{(1)}_{\rm GR}} e^{i\delta u_1^d}, \end{aligned} \tag{3.65}$$

Here, we have introduced six independent parameters $(\beta, b, a, c, \delta, d)$ and a number of parameters for each polarizations $(\alpha, \gamma, \Phi_c^{(l)})$ where $\Phi_c^{(l)}$ is the constant phase parameters for the l-th harmonic for modifications of the waveforms. Here, we deal with the parameters as independent, but these parameters are not independent as we see in the above specific theories of gravity. When we consider the relations among the parameters, we can rewrite Eq. (3.65) up

to leading order corrections without preferred frames as

$$\begin{aligned}\bar{h}_{\rm ppE,1}(f) =&\bar{h}_{\rm GR}(1+c\beta u_2^{b+5})e^{2i\beta u_2^b}+[\alpha_x F_x\sin\iota+\alpha_y F_y\sin 2\iota\\&+\alpha_b F_b\sin^2\iota+\alpha_l F_l\sin^2\iota]\frac{\mathcal{M}^2}{D_L}u_2^{-7/2}e^{-i\Psi^{(2)}_{\rm GR}}e^{2i\beta u_2^b}+[\gamma_x F_x+\gamma_y F_y\cos\iota\\&+\gamma_b F_b\sin\iota+\gamma_l F_l\sin\iota]\eta^{1/5}\frac{\mathcal{M}^2}{D_L}u_1^{-9/2}e^{-i\Psi^{(1)}_{\rm GR}}e^{i\beta u_1^b},\end{aligned}\tag{3.66}$$

where $(\beta, b, \alpha, \gamma)$ have been introduced for the modifications. We can also add the effects of the modifications in the propagation of GWs like

$$\begin{aligned}\bar{h}_{\rm ppE,2}(f) =&\bar{h}_{\rm GR}(1+c\beta u_2^{b+5})e^{2i\beta u_2^b}e^{i\kappa u_2^k}+[\alpha_x F_x\sin\iota+\alpha_y F_y\sin 2\iota\\&+\alpha_b F_b\sin^2\iota+\alpha_l F_l\sin^2\iota]\frac{\mathcal{M}^2}{D_L}u_2^{-7/2}e^{-i\Psi^{(2)}_{\rm GR}}e^{2i\beta u_2^b}e^{i\kappa u_2^k}\\&+[\gamma_x F_x+\gamma_y F_y\cos\iota+\gamma_b F_b\sin\iota+\gamma_l F_l\sin\iota]\\&\times\eta^{1/5}\frac{\mathcal{M}^2}{D_L}u_1^{-9/2}e^{-i\Psi^{(1)}_{\rm GR}}e^{i\beta u_1^b}e^{i\kappa u_1^k},\end{aligned}\tag{3.67}$$

where (κ, k) have also been introduced for the propagation modifications.

3.4 Previous tests of polarizations

Here, we review the observational previous tests of the polarization tests of the GWs from CBCs.

3.4.1 PSR B1913+16

PSR B1913+16 or the Hulse-Taylor binary is a binary pulsar, which is composed of a pulsar and another neutron star, discovered in 1974. The change of the orbital period P was constrained as [8],

$$\frac{\Delta\dot{P}}{\dot{P}}=0.003\pm0.002,\tag{3.68}$$

where the dot denotes the derivative in terms of time.

The binary orbital energy $E_{\rm orbit}$ is associated with the radiated GW frequency [1] as

$$E_{\rm orbit} = -\left(\frac{\pi^2 \mathcal{M}^5 f_{\rm GW}^2}{8}\right)^{1/3}, \tag{3.69}$$

at Newtonian order. Then, we find

$$\frac{\Delta \dot{E}_{\rm orbit}}{\dot{E}_{\rm orbit}} = \frac{\Delta \dot{f}}{\dot{f}} = \frac{\Delta \dot{P}}{\dot{P}}, \tag{3.70}$$

Here, we used $f_{\rm GW} = 2f_{\rm orbit}$ and $P = 1/f_{\rm orbit}$ where $f_{\rm orbit}$ is the orbital frequency. On the other hand, $\dot{E}_{\rm orbit} \propto A^2$ implies

$$\frac{\Delta \dot{E}_{\rm orbit}}{\dot{E}_{\rm orbit}} = \frac{\Delta A}{A}. \tag{3.71}$$

Finally, we can estimate a possible deviation of the GW amplitude in GR by

$$A \lesssim 1 \times 10^{-3}. \tag{3.72}$$

3.4.2 Pure polarization test by LVC

LVC has performed model selection of GW170814 (BNS) and GW170817 (BBH) in the framework of the pure polarizations in which the detectors signal is constructed by scalar, vector, or tensor modes purely [16,44]. In GR, the detector signal is expressed as a linear combination of tensor polarization modes with the coefficients of the tensor antenna pattern functions. They express the detector signal in terms of artificial pure scalar or pure vector models by replacing the tensor antenna pattern functions with those of scalar or vector mode.

In a method that involves only replacing the antenna pattern functions, the geometrical patterns for the scalar and vector radiation are assumed to be the same as those for the tensor modes. In other words, the pure scalar polarization model adopts the detector signal as,

$$h_I(t, \hat{\Omega}) = F_I^b(\hat{\Omega}) \frac{1 + \cos^2 \iota}{2} h_{+,\rm GR}(t), \tag{3.73}$$

and the pure vector polarization model adopts the detector signal as,

$$h_I(t,\hat{\Omega}) = F_I^x(\hat{\Omega})\frac{1+\cos^2\iota}{2}h_{+,\mathrm{GR}}(t) + F_I^y(\hat{\Omega})\cos\iota\, h_{\times,\mathrm{GR}}(t), \tag{3.74}$$

where $h_{+,\mathrm{GR}}(t)$ and $h_{\times,\mathrm{GR}}(t)$ are the waveforms of the plus and cross modes of the GW. Note that we take away the inclination dependence to clearly indicate the geometrical radiation patterns. They have conducted model selection in the three polarization models including the above two in addition to standard GR for GW170814 and GW170817 via the Bayesian inference approach[8]. As a results, they found logarithms of the Bayes factors supporting GR: 2.30 (vector vs tensor) and 3.00 (scalar vs tensor) for GW170814 and 20.81 (vector vs tensor) and 23.09 (scalar vs tensor) for GW170817.

3.4.3 Null stream

Null stream is a time series combining the data from a network of detectors that removes certain polarization components and contains only other polarization components. See [96,106] for more information on the null stream. The detector outputs from a network are expressed as

$$d_I(t) = F_I^A h_A(t) + n_I(t), \tag{3.75}$$

in time domain or

$$\tilde{d}_I(f) = F_I^A \tilde{h}_A(f) + \tilde{n}_I(f), \tag{3.76}$$

in frequency domain where A is the polarization index running over $(+,\times,x,y,b,l)$ and I is the detector index running over the detector labels. A tilde denotes the frequency domain. $\tilde{d}_I, F_I^A, \tilde{n}_I$ denotes the noise-weighted detector outputs, antenna pattern functions, noise in frequency domain. The quantities in frequency domain are divided by the PSD $\sqrt{S_I(f)/2}$ for whitening so that the power spectrum of the quantities become flat. The data is whitened by dividing the Fourier coefficients by an estimate of the spectral density of the noise, which ensures that the data in each frequency bin has equal significance by

[8] See Chapter 4 for more details about Bayesian inference.

down weighting frequencies where the noise is loud. The whitened samples are scaled to have unit variance in the time domain. We can rewrite it in the bold matrix notation [9]

$$\tilde{\boldsymbol{d}} = \boldsymbol{F}\tilde{\boldsymbol{h}} + \tilde{\boldsymbol{n}}, \tag{3.77}$$

for simplicity.

Given data of three detectors and the sky location of the GW source, for example, we can construct a null stream consisting of only the non-GR polarization modes as

$$\tilde{h}_{\rm null} = \frac{\epsilon^{IJK} F_J^+ F_K^\times}{|\delta^{JK} F_J^+ F_K^\times|} \tilde{h}_I, \tag{3.78}$$

which can be rewritten as

$$\begin{aligned}\tilde{h}_{\rm null} &= \Delta_{23}\tilde{h}_1 + \Delta_{31}\tilde{h}_2 + \Delta_{12}\tilde{h}_3 \\ &= (\Delta_{23}F_1^x + \Delta_{31}F_2^x + \Delta_{12}F_3^x)\tilde{h}^x + (\Delta_{23}F_1^y + \Delta_{31}F_2^y + \Delta_{12}F_3^y)\tilde{h}^y \\ &+ (\Delta_{23}F_1^s + \Delta_{31}F_2^s + \Delta_{12}F_3^s)\tilde{h}^s + \Delta_{23}\tilde{n}_1 + \Delta_{31}\tilde{n}_2 + \Delta_{12}\tilde{n}_3.\end{aligned} \tag{3.79}$$

In general, from the expressions of the multiple detector signal in Eq. (3.76), F_I^A can be regarded as a projector of $\tilde{h}_I$ into the directions $\{F_I^+, F_I^\times, F_I^x, F_I^y, F_I^b, F_I^l\}$ because the signal terms can be written in

$$\tilde{h}_I = F_I^+\tilde{h}_+ + F_I^\times\tilde{h}_\times + F_I^x\tilde{h}_x + F_I^y\tilde{h}_y + F_I^b\tilde{h}_b + F_I^l\tilde{h}_l, \tag{3.80}$$

where $\tilde{h}_I, F_I^A$ are N-dimensional vectors with the number of detectors N. In other words, the detector signal is in the subspace spanned by the vectors $\{F_I^+, F_I^\times, F_I^x, F_I^y, F_I^b, F_I^l\}$. Note that the breathing and the longitudinal modes must be treated together as only one scalar mode because of the degeneracy between the breathing and the longitudinal mode from the same functional form in F_I^b and F_I^l. Given data of N detectors, we can construct a null stream eliminating $N-1$ polarization modes by constructing appropriate linear combination in general. By removing certain polarization modes, we can find out if the signal contains the polarization modes beyond GR.

Unlike Bayesian inference, while the direction must be given in priori, we

[9] We distinguish the detector outputs d including noise n from the detector signal h. Here, the whitening label "w" is omitted.

do not have to assume a waveform in the null stream approach. In [98], an upper bound

$$|h_x + h_y| < 6.02 \times 10^{-23} \tag{3.81}$$

was put on vector modes in GW170817 in the null stream approach. The authors utilize the fact that the coefficient of the scalar mode in the null stream is significantly small for the GW170817 event but do not assume the waveforms, so the constraint remains comparable to the tensor amplitude in GR. The authors also discuss some null stream topics in polarization tests of GWs [97, 99].

On the other hand, in [100], two data analysis pipelines for polarization tests based on the null energy have been proposed. The null projector is defined by

$$\boldsymbol{P}_{\rm null} := \boldsymbol{I} - \boldsymbol{F}(\boldsymbol{F}^\dagger \boldsymbol{F})^{-1}\boldsymbol{F}^\dagger, \tag{3.82}$$

where

$$\boldsymbol{F} := (\boldsymbol{F}_+, \boldsymbol{F}_\times), \tag{3.83}$$

in the bold notation. Its action on the detector outputs with the true sky position leads to a null stream

$$\begin{aligned} \tilde{\boldsymbol{d}}_{\rm null} &= \boldsymbol{P}_{\rm null}(\hat{\Omega}_{\rm true})\tilde{\boldsymbol{d}}, \\ &= \boldsymbol{P}_{\rm null}(\hat{\Omega}_{\rm true})\tilde{\boldsymbol{n}}. \end{aligned} \tag{3.84}$$

Then, the null energy is defined by

$$\begin{aligned} E_{\rm null} &= \sum_k \tilde{\boldsymbol{d}}^\dagger_{\rm null}\tilde{\boldsymbol{d}}_{\rm null}, \\ &= \sum_k \tilde{\boldsymbol{d}}^\dagger \boldsymbol{P}_{\rm null}\tilde{\boldsymbol{d}}, \\ &= \sum_k \tilde{\boldsymbol{n}}^\dagger \boldsymbol{P}_{\rm null}\tilde{\boldsymbol{n}} + \tilde{\boldsymbol{h}}^\dagger_e \boldsymbol{F}^\dagger_e \boldsymbol{P}_{\rm null}\boldsymbol{F}_{e'}\tilde{\boldsymbol{h}}_{e'} \\ &+ \sum_k 2{\rm Re}(\tilde{\boldsymbol{h}}^\dagger_e \boldsymbol{F}^\dagger_e \boldsymbol{P}_{\rm null}\tilde{\boldsymbol{n}}). \end{aligned} \tag{3.85}$$

where the analysis is performed in the time-frequency domain, a tilde refers to the data matrix resulting from the time-frequency transformation, and $\sum_k$

sums over the discrete time-frequency pixels. Here, "e" is the polarization index for the polarization modes beyond GR. If there do not exist the additional polarization modes, the quantity $E_{\rm null}$ follows a χ^2 distribution with the degrees of freedom of DoF $= N_{\tau f}(N-2)$ where $N_{\tau f}$ is the number of time-frequency pixels. If there exist additional polarization modes, the second and the third terms appear and the null energy follow χ^2 distribution no longer. Thus, we can quantify the deviation from GR in the following two ways.

Null energy method

A p-value to the hypothesis that only tensor polarizations are present is assigned by

$$p = 1 - \int_0^{E_{\rm null}} \chi^2_{\rm DoF}(x)dx. \tag{3.86}$$

A small p-value indicates the deviation from GR.

Sky map method

The probability for obtaining particular data $\tilde{\boldsymbol{d}}$ given the GR hypothesis $\mathcal{H}_{\rm T}$ and a fiducial sky position $\hat{\Omega}$ can be identified with the probability for the associated null energy

$$p(\tilde{\boldsymbol{d}}|\mathcal{H}_{\rm T}, \hat{\Omega}) = \chi^2_{\rm DoF}(E_{\rm null}(\tilde{\boldsymbol{d}}, \hat{\Omega})). \tag{3.87}$$

Through Bayes's theorem

$$p(\hat{\Omega}|\tilde{\boldsymbol{d}}, \mathcal{H}_{\rm T}) \propto p(\tilde{\boldsymbol{d}}|\hat{\Omega}, \mathcal{H}_{\rm T}) p(\hat{\Omega}|\mathcal{H}_{\rm T}), \tag{3.88}$$

when we assume the prior is uniform, we can then check for the consistency between the true sky position $\hat{\Omega}_{\rm true}$ and the sky map $P(\Omega) := p(\hat{\Omega}|\tilde{\boldsymbol{d}}, \mathcal{H}_{\rm T})$ and assign a p-value denoted as q by

$$q = \int_{P(\hat{\Omega}) \leq P(\hat{\Omega}_{\rm true})} P(\hat{\Omega}) d\hat{\Omega}. \tag{3.89}$$

Both methods allow combining information from multiple sources. If GR is correct, these p-values will be uniformly distributed between 0 and 1. If N

samples $\{p_i\}$ follow a uniform distribution between 0 and 1, the statistic

$$S = -2\sum_{i=1}^{N} \log(q_i), \tag{3.90}$$

follows a χ^2 distribution with $2N$ degrees of freedom. Thus, we can assign the combined p-value

$$p_{\text{com}} = \int_S^\infty \chi^2_{2N}(x)dx, \tag{3.91}$$

for multiple sources. In [100], the authors apply the two methods to the binary neutrons star merger signal GW170817 and obtained a p-value of 0.315 by the null energy method and a p-values of 0.790 by the sky map method. In [31], the events from the second Gravitational-wave Transient catalog were analyzed based on the sky map method. The method provides a likelihood function for the hypothesis that the data contain a signal given helicity and sky location. By marginalization over the source sky location, the evidences of different polarization hypotheses and Bayes factors between GR and non-GR hypothesis can be obtained. The authors calculated the Bayes factors for the events from the second Gravitational-wave Transient catalog as shown in [31].

The Bayes factors in [31] are less informative than those of the pure polarization tests by LVC in [16, 44]. This comes from the fact that in the null stream approach, only the power excess is monitored while the Bayesian approach attempts to track the signal based on the waveform templates. The Bayes factors for tensor hypothesis versus scalar hypothesis are larger than those for tensor hypothesis versus vector hypothesis because the geometries of the LIGO-Virgo antenna pattern functions make scalar polarizations easier to separate.

Chapter 4

Data analysis technique

The data analysis technique in GW astronomy is given here. First, we overview the Bayesian inference and then review the parameter estimation including Fisher information matrix. Finally, the we provide an algorithm for obtaining the posterior distributions and the evidence called nested sampling. The basics of probability, signal and noise are provided in Appendix H.

4.1 Bayesian inference

In GW data analysis, we are interested in the detector output including the GW or the noise that depend on the signal model (GW waveform model), parameters θ for the GW source and the noise model in general. We refer to the signal model and the noise model as M together. The system is the all realizations of the detector output. The parameters θ can be regarded a subset (or an event) in which the signal in the detector output can be described by the parameters and the model M can be regarded as a subset (or an event) in which the signal and the noise in the detector output can be described by the model. The obtained detector data is also an elementary event. Thus, the discussions in Section H.1 can be applied. The Bayes theorem is rewritten as

$$\begin{aligned} p(\boldsymbol{\theta}|d,M) &= \frac{p(\boldsymbol{\theta}|M)p(d|\boldsymbol{\theta},M)}{p(d|M)}, \\ &= \frac{p(\boldsymbol{\theta})p(d|\boldsymbol{\theta},M)}{p(d|M)}, \end{aligned} \tag{4.1}$$

where we used the fact that $p(\boldsymbol{\theta}|M) = p(\boldsymbol{\theta} \cap M)/p(M) = p(\boldsymbol{\theta})P(M)/p(M) = p(\boldsymbol{\theta})$. $p(\boldsymbol{\theta}|d,M)$ is the posterior probability distribution for $\boldsymbol{\theta}$ that is the prob-

Table 4.1: Guidelines for interpreting Bayes factors provided in [107].

Bayes factor $B_{\rm XY}$	Evidence against $\mathcal{H}_{\rm Y}$
1 to 3	Not worth more than a bare mention
3 to 20	Positive
20 to 150	Strong
> 150	Very strong

ability distribution function of $\boldsymbol{\theta}$ given the data d and the model or the hypothesis M. $p(\boldsymbol{\theta})$ is the prior probability distribution for the parameters $\boldsymbol{\theta}$, which encodes our knowledge or belief on the source parameters. $p(f|\boldsymbol{\theta}, M)$ is a likelihood function of the data given the parameters $\boldsymbol{\theta}$, which is determined by the properties of the instrumental noise. $Z := p(d|M) = \int d\theta p(d|M, \theta)p(\theta)$ is referred to as evidence, which quantifies how much the hypothesis M is favored by the data d. In the model selection between the hypotheses $\mathcal{H}_{\rm X}$ and $\mathcal{H}_{\rm Y}$, we evaluate the Bayes factor defined by the ratio of two evidences,

$$B_{\rm XY} := \frac{Z_X}{Z_Y} = \frac{p(d|\mathcal{H}_{\rm X})}{p(d|\mathcal{H}_{\rm Y})}. \tag{4.2}$$

The large Bayes factors suggest that $\mathcal{H}_{\rm X}$ is preferred compared to $\mathcal{H}_{\rm Y}$. Several interpretations of the Bayes factors are reported. One of them, widely cited, is provided in [107]. The scaling is shown in Table 4.1.

4.2 Parameter estimation

Suppose that a GW signal has been detected, that is the signal satisfies the predetermined criteria, for example, the value of the signal noise to ratio (SNR), which is defined as the ratio between the expected value of the filtered detector output and the rms value of the filtered detector output when the signal is absent [1]

$$\mathrm{SNR}^2 := \left(\frac{\mathrm{S}}{\mathrm{N}}\right)^2 = 4\int_0^\infty \mathrm{df}\frac{|\tilde{\mathrm{h}}(\mathrm{f})|^2}{\mathrm{S_n(f)}}, \tag{4.3}$$

for some template $h(\boldsymbol{\theta})$ exceeded a threshold. The problem is how to reconstruct the most probable values of the parameters and how to evaluate the errors on the parameters.

The Bayseian approach is suited for the problem. The Gaussian probability distribution for a realization $n_0(t)$ of the noise can be expressed as using the power spectral density as

$$p(n_0) = N \exp\left\{-\frac{1}{2}\int_{-\infty}^{\infty} df \ \frac{|\tilde{n}_0|^2}{(1/2)S_n(f)}\right\} \tag{4.4}$$

because the probability distribution for the value of n at a certain time is given by the Gaussian distribution and the variance becomes the value of the autocorrelation function at 0 by definition. Substituting $s(t) = h(\boldsymbol{\theta})+n(t)$ into the above equation, we obtain the likelihood function for the observed output $s(t)$ given the hypothesis that there exists a GW having the parameters $\boldsymbol{\theta_t}$,

$$p(s|\boldsymbol{\theta_t}) = N \exp\left\{-\frac{1}{2}(s - h(\boldsymbol{\theta_t})|s - h(\boldsymbol{\theta_t}))\right\}, \tag{4.5}$$

where N is the normalization factor. Thus, the posterior distribution becomes

$$p(\boldsymbol{\theta_t}|s) = Np(\boldsymbol{\theta_t}) \exp\left\{(h(\boldsymbol{\theta_t})|s) - \frac{1}{2}(h(\boldsymbol{\theta_t})|h(\boldsymbol{\theta_t}))\right\}, \tag{4.6}$$

through the Bayes theorem where $p(\boldsymbol{\theta_t})$ is the prior distribution and N is the redefined normalization factor by including the constant part of the likelihood.

A rule for assigning the most probable value is called an estimator. Here, we provide famous two estimators: the maximum likelihood estimator and the Bayes estimator.

4.2.1 Maximum likelihood estimator

Suppose that the prior distribution is flat. The posterior distribution becomes equal to the likelihood. The value of $\boldsymbol{\theta_t}$ that maximizes the likelihood defines the maximum likelihood estimator referred to as $\boldsymbol{\theta}_{\rm ML}$. The value of $\boldsymbol{\theta}_{\rm ML}$ is

determined by solving the equations

$$(\partial_i h(\boldsymbol{\theta_t})|s) - (\partial_i h(\boldsymbol{\theta_t})|h(\boldsymbol{\theta_t})), \tag{4.7}$$

which is $\partial p(s|\boldsymbol{\theta_t})/\partial\theta_t^i$ where $\partial_i := \partial/\partial\theta_t^i$. The errors $\delta\theta^i$ can be defined as the width of the posterior distribution as the peak.

4.2.2 Bayes estimator

The Bayes estimator is defined by taking the expectation value with respect to the posterior probability distribution as

$$\theta_B^i := \int d\boldsymbol{\theta}\theta_i p(\boldsymbol{\theta}|s), \tag{4.8}$$

and the errors are defined by taking the expectation value of the deviations from θ_B^i with respect to the posterior probability distribution as

$$\Sigma_B^{jk} = \int d\boldsymbol{\theta}(\theta^j - \theta_B^j)(\theta^k - \theta_B^k)p(\boldsymbol{\theta}|s). \tag{4.9}$$

Even when the prior is not flat, the Bayes estimator is independent on whether we integrate our some parameters from the posterior distribution or not by the definition of the Bayes estimator.

4.2.3 Fisher information

In the limit of the large SNR, all consistent estimators give the same suggestion. The large SNR results in the small errors. For simplicity, we assume that the prior $p(\boldsymbol{\theta})$ is nearly uniform at least around the most probable value estimated by any estimator. Here, we assume that the value is estimated by the maximum likelihood estimator, then we can write $\theta^i = \theta_{ML}^i + \Delta\theta^i$. We can expand the terms in the exponential in the posterior as

$$p(\boldsymbol{\theta}|s) = N \exp\left\{-\frac{1}{2}\Gamma_{ij}\Delta\theta^i\Delta\theta^j\right\} \tag{4.10}$$

where

$$\begin{aligned}\Gamma_{ij} &:= (\partial_i\partial_j h|h-s) + (\partial_i h|\partial_j h) \\ &= -(\partial_i\partial_j h|n) + (\partial_i h|\partial_j h) \\ &\simeq (\partial_i h|\partial_j h).\end{aligned} \tag{4.11}$$

or explicitly

$$\Gamma_{ij} := 4\mathrm{Re}\int_{\mathrm{f_{min}}}^{\mathrm{f_{max}}} df \frac{1}{S_n(f)}\frac{\partial h^*(f)}{\partial\theta^i}\frac{\partial h(f)}{\partial\theta^j}, \tag{4.12}$$

is called the Fisher information matrix.

Fisher information matrix can estimate the model parameter. It represents how precisely the model parameters can be determined by observation, and how strongly the model parameters are correlated [108–110] under several assumptions; strong signal and Gaussian noise [111–113]. The posterior probability distribution becomes the form of the multivariate variable normal distribution. Thus, the root mean square error of a parameter and the correlation coefficients between two model parameters can be read out from the inverse of the Fisher matrix. We can calculate the root mean square error of $\Delta\theta^i$ as

$$(\Delta\theta_i)_{\mathrm{rms}} := \sqrt{\langle\Delta\theta^i\Delta\theta^i\rangle} = \sqrt{(\Gamma^{-1})^{ii}}, \tag{4.13}$$

where $\Delta\theta^i$ is the measurement error of θ^i. The correlation coefficients between θ_i and θ_j are calculated as

$$C(\theta_i,\theta_j) := \frac{\langle\Delta\theta^i\Delta\theta^j\rangle}{\langle(\Delta\theta_i)^2\rangle\langle(\Delta\theta_j)^2\rangle} = \frac{(\Gamma^{-1})^{ij}}{\sqrt{|(\Gamma^{-1})^{ii}(\Gamma^{-1})^{jj}|}}, \tag{4.14}$$

In the thesis, we impose a detection criteria for signal to noise ratio (SNR), SNR > 8, and assume Gaussian noise in the thesis when we treat with Fisher information matrix. In addition, we refer to $(\Delta\lambda_i)_{\mathrm{rms}}$ as $\Delta\lambda_i$ simply, and call it the estimation error of λ_i.

We define the sky localization error of the source as

$$\Delta\Omega_s := 2\pi|\sin\theta_s|\sqrt{\langle(\Delta\theta_s)^2\rangle\langle(\Delta\phi_s)^2\rangle - \langle\Delta\theta_s\Delta\phi_s\rangle^2}. \tag{4.15}$$

where θ_s and ϕ_s stand for the sky location of the source.

4.3 Nested sampling

In the Bayesian approach, we need to calculate the posterior probability distribution and the evidence. The calculations are difficult and have computational cost in general because the calculations involve the integration on multivariate variables and the noise weighted scalar product. Here, we introduce the nested sampling [114–116] that is an algorithm for obtaining the posterior distributions and the evidence. In the method, to find the posterior probability density of the model parameters, we generate thousands of random samples that follow a posterior probability distribution and create a histogram of them.

The purpose is to calculate the posterior probability distribution

$$p(\boldsymbol{\theta}|d, M) = \frac{p(d|\boldsymbol{\theta}, M)p(\boldsymbol{\theta}|M)}{p(d|M)}, \tag{4.16}$$

and the evidence

$$\begin{aligned} p(d|M) &= \int d^N\boldsymbol{\theta} p(d|\boldsymbol{\theta}, M)p(\boldsymbol{\theta}|M) \\ &= \int d^N\boldsymbol{\theta} L(\boldsymbol{\theta})\pi(\boldsymbol{\theta}), \end{aligned} \tag{4.17}$$

where $L(\boldsymbol{\theta}) := p(d|\boldsymbol{\theta}, M)$ is the likelihood and $\pi(\boldsymbol{\theta}) = p(\boldsymbol{\theta}|M)$ is the prior. In the nested sampling, the evidence is rewritten in terms of the prior mass X defined as

$$X(\lambda) = \int\int\cdots\int_{L(\boldsymbol{\theta})>\lambda} \pi(\boldsymbol{\theta})d^N\boldsymbol{\theta}, \tag{4.18}$$

having a range of $X \in [0, 1]$ by definition. Using the prior mass, the evidence can be written by the integral of the single scalar variable

$$Z = \int \tilde{L}(X)dX, \tag{4.19}$$

because the likelihood function can be expressed as

$$\tilde{L}(X(\lambda)) = \lambda, \tag{4.20}$$

and

$$dX = \pi(\boldsymbol{\theta}) d^N \boldsymbol{\theta}. \tag{4.21}$$

Furthermore, the posterior is given by

$$\tilde{P}(X) = \frac{\tilde{L}(X)}{Z}. \tag{4.22}$$

In the nested sampling, the prior mass corresponding to the worst likelihood is estimated statistically to correspond the parameter space to the prior mass. From Eq. (4.21), the density of states of the prior mass is equal to the density of states of the prior in the parameter space. In other words, we can sample points following the prior by sampling in terms of the prior mass uniformly. The probability that the prior masses is less than χ among the M samples is

$$P(\{X_i\} < \chi) = \prod_i^M \int_0^\chi dX_i = \chi^M. \tag{4.23}$$

Then, the probability density that the highest prior mass is χ is given by

$$\begin{aligned} P_X(\chi) &= \frac{\partial P(\{X_i\} < \chi)}{\partial \chi} \\ &= M\chi^{M-1}. \end{aligned} \tag{4.24}$$

When we sample M points from the prior within $0 < X < X^*$, the probability that the prior masses are less than $\chi (< X^*)$ among the M samples within $0 < X < X^*$ can be written by

$$P(\{X_i\} < \chi) = \frac{\prod_i^M \int_0^\chi dX_i}{\prod_i^M \int_0^{X^*} dX_i} = \frac{\chi^M}{X^{*M}}. \tag{4.25}$$

Then, the probability density that the highest prior mass is χ is given by

$$\begin{aligned} P_X(\chi) &= \frac{\partial P(\{X_i\} < \chi)}{\partial \chi} \\ &= M\frac{\chi^{M-1}}{X^{*M}}. \end{aligned} \tag{4.26}$$

or [1]

$$P_{X/X^*}(t) = Mt^{M-1}. \tag{4.27}$$

Thus, we can summarize the Nested Sampling algorithm in terms of pseudo-code with M live points as follows.

1. We sample M points of $\boldsymbol{\theta_1}, \ldots, \boldsymbol{\theta_M}$ from the prior $\pi(\boldsymbol{\theta})$.

2. While not termination condition

(a) We record the live point i with the lowest L_i as L_k.

(b) We assign $X_k = t_k X_{k-1}$ where t_k is given by the distribution $P(t_k) = Mt_k^{M-1}$.

(c) Then, we replace the point i with a sample from $p(\boldsymbol{\theta})$ under $L_i > L_k$.

3. We estimate the evidence and the posterior distributions from $\{L_k, X_k\}$.

Although there is no obvious termination condition about the nested sampling, several practical guidelines are available, for example based on the information [114, 116].

[1] $P_X(x) = \partial_x P(X < x) \Rightarrow \partial_x P(X/X^* < x) = \partial_x P(X < X^* x) = \partial_x (X^* x) \partial_{X^* x} P(X < X^* x) = X^* P_X(X^* x)$.

Chapter 5

Polarization separability with ground-based detectors

In this chapter, we investigate the polarization separability with current ground-based GW detectors such as advanced LIGO (aLIGO), advanced Virgo (AdV), and KAGRA and future ground-based GW detectors such as Einstein telescope (ET) and Cosmic explore (CE). We reveal the separation conditions and the parameter correlation in the mixed polarization models based on the Fisher information matrix. As for the future ground-based detectors, we also provide the prospects of polarization tests using the compact binary distributions. This chapter is based on [117, 118]. For these results, I conducted research ranging from problem formulation and theoretical calculation to analysis and discussion.

5.1 Ground-based detectors

Ground-based laser interferometric GW detectors have been developed all over the world lately. After the first detection of GWs from a BBH in 2015 by aLIGO marked the dawn of the GW astronomy, the observations of GWs by aLIGO and AdV enabled some experimental studies to test GR. Their mirrors as test masses are suspended by pendulum so that the test masses can be regarded as the free masses in the direction of the motion in the frequency region above the resonant frequency of the pendulum. [1] The target frequency is restricted above $5-10$ Hz due to the seismic noise. The current ground-based

[1]The freely falling coordinates can be regarded as the Fermi normal coordinates effectively.

detectors such as aLIGO, Virgo, and KAGRA are categorized as the second generation (2G) ground-based laser interferometric GW detectors. Commonly, the 2G detectors have Dual-Recycled Fabry-Perot Michelson Interferometric configuration. The design sensitivity of the 2G detectors is $\leq$ 100 Mpc in terms of the BNS inspiral range and the arm length is $3 - 4$ km. Fig. 5.1 shows the sensitivity curves of the 2G detectors.

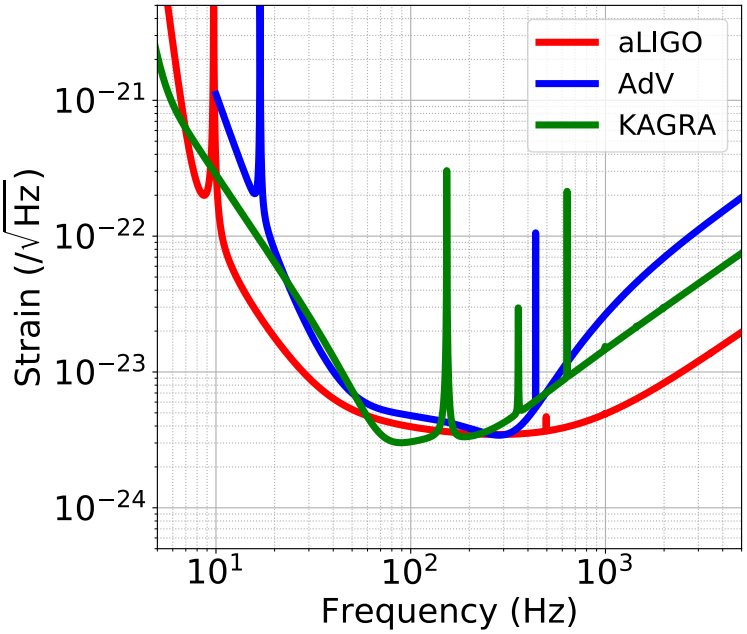

Figure 5.1: Design sensitivity curves for the 2G GW detectors: aLIGO, AdV, and KAGRA.

On the other hand, the next-generation detectors such as ET and CE are under consideration as two leading plans and they are categorized as the third generation (3G) ground-based laser interferometric GW detectors. ET is a proposed European based GW observatory. ET will have three 10km arms in an equilateral triangle and the multiple interferometers will share the arms. There are two sensitivity estimates called ET-B and ET-D. ET-B has a single interferometric detector configuration whose sensitivity range is from 1Hz to 10 kHz. ET-D has the xylophone configuration where each corner has one cryogenic low-frequency interferometer and one room-temperature high-frequency interferometer. The sensitivity around sub- 10 Hz is improved compared to

ET-B. CE is a proposed U.S. based GW detector. CE has an L-shaped configuration in which the arm length is 40 km. The sensitivity estimate suggests that CE is significantly better in the frequency region above 10 Hz than those of ET detectors. Fig. 5.2 shows the sensitivity curves of the 3G detectors.

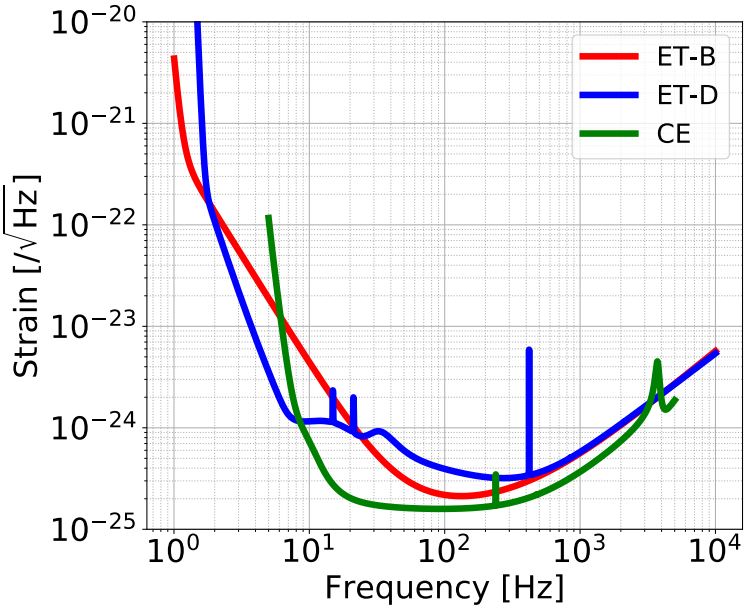

Figure 5.2: Sensitivity curves for the 3G GW detectors: ET and CE. ET has two kinds of sensitivity estimates: ET-B and ET-D.

CBCs are guaranteed sources for all current and future detectors. The notable property is that the 3G detectors are planned to have better sensitivity, in particular in low frequency region around 5 Hz than the current detectors.

5.2 Detector signal

In this section, we start from the detector signal in time domain, and then provide our polarization models consistent with alternative theories of gravity.

5.2.1 Detector signal in time domain

As mentioned in Chapter 3, the detector signal with full polarization content can be written in a linear combination of the polarization components with

antenna pattern functions as the coefficients. When we consider the CBC sources, the I-th GW detector signal Eq. (3.38) can be expressed as

$$h_I(t,\hat{\Omega}) = F_I^A(t,\hat{\Omega})h_A(t), \tag{5.1}$$

writing the dependence on the parameters explicitly, where $\hat{\Omega}$ is the sky location of the source and F_I^A is the I-th detector antenna pattern functions for polarization mode "A", which is defined by

$$F_I^A(t,\hat{\Omega}) := d_I^{ab}(t)e_{ab}^A(\hat{\Omega}). \tag{5.2}$$

Here, the detector tensor of the interferometric detector is defined by

$$d_I^{ab}(t) := \frac{1}{2}(\hat{u}_I^a(t)\otimes\hat{u}_I^b(t) - \hat{v}_I^a(t)\otimes\hat{v}_I^b(t)). \tag{5.3}$$

where $\hat{u}_I, \hat{v}_I$ are unit vectors pointing each direction of the interferometer arms.

In general, the two vectors $\hat{u}_I(t), \hat{v}_I(t)$ are the time dependent vectors because the position and the orientation of the detector change in time because the location and orientation of the detector to the source change with the Earth's rotation and revolution. As a result, the detector tensor and antenna pattern functions also change in time. In the case of the 2G GW detectors such as aLIGO, AdV and KAGRA, we can assume that the antenna pattern functions are constants because the GW duration in the observational band is short enough to ignore the time dependence. On the other hand, as for the 3G GW detectors or the space-based GW detectors such as LISA [119, 120], DECIGO [121] and Tianqin [122], we can not ignore the time dependence because they have great sensitivities even in the lower frequency range below $5-10$ Hz.

5.2.2 Fourier transformation of detector signal

When we estimate the errors of the model parameters, we need to calculate the Fisher information matrix. So, we need the expression of the signal in frequency domain. In Section 3.3, we provide the signal in frequency domain under the assumption that the time dependence of the antenna pattern functions can be ignored. However, it is not true for the 3G detectors that the

time dependence can be negligible because they have great sensitivity at lower frequency. Here, we reconsider the Fourier components including the 3G detectors. We utilize the stationary phase approximation introduced in Section 3.3 again.

For simplicity, let us consider the tensor polarization modes. The inspiral GW detector signal from CBCs in time domain in GR is written as Eq. (F.4),

$$h(t) \simeq \frac{2G^2}{c^4}\frac{m_1 m_2}{r_s(t) D_L}\mathscr{A}(t)\cos\Big(\int^t f_{\rm GW}(t')dt' + \phi_p(t) + \phi_D(t)\Big), \tag{5.4}$$

where the polarization amplitude $\mathscr{A}(t)$ and the polarization phase $\phi_p(t)$ are defined by

$$\mathscr{A}(t) := \sqrt{(1+\cos^2\iota)^2 F^+(t)^2 + 4\cos^2\iota F^\times(t)^2}, \tag{5.5}$$

and

$$\phi_p(t) := \arctan\left(\frac{2\cos\iota F^\times(t)}{(1+\cos^2\iota)F^+(t)}\right), \tag{5.6}$$

respectively. Here, the physical quantities are defined in the same way as in Eq. (F.4).

The SPA leads to the Fourier components $h(f)$ of the measured detector signal $h(t)$. Note that $\mathscr{A}(t), \phi_p$, ϕ_D, and $(2m_1m_2)/(r_s(t)D_L)$ vary slowly in time compared to the phase evolution $\int f_{\rm GW}$ as far as we consider the quasi-circular motion . We write Eq. (F.4) as

$$\begin{aligned} h(t) \simeq & \frac{G^2}{c^4}\frac{m_1 m_2}{r_s(t) D_L}\mathscr{A}(t) e^{i(\phi_p(t)+\phi_D(t))} e^{i(\int^t f_{\rm gw}(t')dt')} \\ & + \frac{G^2}{c^4}\frac{m_1 m_2}{r_s(t) D_L}\mathscr{A}(t) e^{-i(\phi_p(t)+\phi_D(t))} e^{-i(\int^t f_{\rm gw}(t')dt')}. \end{aligned} \tag{5.7}$$

Here, when we regard the slowly varying parts $(m_1m_2)/(r_s(t)D_L)\mathscr{A}(t)e^{i(\phi_p(t)+\phi_D(t))}$ and $(m_1m_2)/(r_s(t)D_L)\mathscr{A}(t)e^{-i(\phi_p(t)+\phi_D(t))}$ as something like A in Eq. (3.44), we can apply the discussions in the stationary phase approximation provided in Section 3.3 even in this case and ignore the Fourier components corresponding to the first term.

$t(f)$ is the stationary point obtained from Eq. (3.46)

$$t(f) := t_* = t_c - \frac{5}{256}\left(\frac{G\mathcal{M}}{c^3}\right)^{-5/3}(\pi f)^{-8/3}, \tag{5.8}$$

so that

$$f = f_{\rm GW}(t(f)). \tag{5.9}$$

$t(f)$ maps the GW frequency to the time before the coalescence. Fig. 5.3 shows $t(f)$ for $1.4M_\odot - 1.4M_\odot$ binary system in blue, $10M_\odot - 10M_\odot$ binary system in red, and $30M_\odot - 30M_\odot$ binary system in green. Furthermore, the amplitude term in Eq. (3.47) becomes

$$\frac{1}{2}A(t_*)\sqrt{\frac{2\pi}{\ddot{\Phi}(t_*)}} = \frac{G^2}{c^4}\frac{m_1 m_2}{r_s(t(f))D_L}\mathscr{A}(t(f))e^{-i(\phi_p(t(f))+\phi_D(t(f)))}\sqrt{\frac{2\pi}{\ddot{\Phi}(t_*)}}, \tag{5.10}$$

where we used the fact that

$$r_s = \left(\frac{\pi^2 Gm}{f_{\rm GW}^2}\right)^{1/3} = \left(\frac{\pi^2 Gm}{f^2}\right)^{1/3}, \tag{5.11}$$

from Kepler's law where $m = m_1 + m_2$ is the binary total mass and $2\omega_s = \omega_{\rm GW}$, and then

$$\ddot{\Phi}(t_*) = \frac{15}{32}\left(\frac{5G\mathcal{M}}{c^3}\right)^{-5/8}\left(\frac{5}{256}\left(\frac{G\mathcal{M}}{c^3}\right)^{-5/3}(\pi f)^{-8/3}\right)^{-11/8}. \tag{5.12}$$

Finally, we find the Fourier components [1, 123–126],

$$h_I(f) = \mathcal{A}f^{-7/6}e^{i\Psi(f)}\left\{\frac{5}{4}\mathscr{A}(t(f))\right\}e^{-i(\phi_p(t(f))+\phi_D(t(f)))}. \tag{5.13}$$

Defining the geometrical factor for the tensor modes as

$$\begin{aligned}\mathcal{G}_{T,I} := \frac{5}{4}\{&(1+\cos^2\iota)F_{+,I}(t)\\ &+2i\cos\iota F_{\times,I}(t)\}e^{i\phi_{D,I}(\theta_s,\phi_s,\theta_e,\phi_e)},\end{aligned} \tag{5.14}$$

we find

$$h_I(f) = \mathcal{A} f^{-7/6} e^{i\Psi(f)} \mathcal{G}_{T,I}(t(f)). \tag{5.15}$$

The amplitude $\mathcal{A}$ up to 3 post-Newtonian order (PN order) and the phase $\Psi(f)$ up to 3.5 PN order are explicitly written as

$$\mathcal{A} f^{-7/6} = \frac{1}{\sqrt{30}\pi^{2/3} d_L} \left(\frac{G\mathcal{M}}{c^3}\right)^{5/6} f^{-7/6} \sum_{i=0}^{6} \left(\pi \frac{G\mathcal{M}}{c^3} f\right)^{i/3}, \tag{5.16}$$

and

$$\Psi(f) = 2\pi f t_c - \phi_c - \frac{\pi}{4} + \frac{3}{128} \left(\pi \frac{G\mathcal{M}}{c^3} f\right)^{-5/3} \sum_{i=0}^{7} \phi_i \left(\pi \frac{G\mathcal{M}}{c^3} f\right)^{i/3}, \tag{5.17}$$

respectively, compiled in [127]. However, when we evaluate the Fourier components using $t(f)$, for example, for the 3G detectors, we use the amplitude up to Newtonian order because the expression of $t(f)$ is up to Newtonian order. However, since the change in Eq. (F.16) for the 2G detector in the frequency band is small, we can regard the factors depending on the $t(f)$ as constants.

If we want to express each Fourier components separately, we find

$$h_+(f) = \mathcal{A} f^{-7/6} e^{i\Psi(f)} \frac{5}{4} (1 + \cos^2 \iota) F_{+,I}(t(f)) \tag{5.18}$$

$$h_\times(f) = \mathcal{A} f^{-7/6} e^{i[\Psi(f)+\pi/2]} \frac{5}{2} \cos\iota F_{\times,I}(t(f)) \tag{5.19}$$

in the same way as above from

$$h_+(t) = \frac{2G^2}{c^4} \frac{2m_1 m_2}{r_s(t) D_L} (1 + \cos^2 \iota) F^+(t) \cos\Big(\int^t f_{\rm gw}(t')dt' + \phi_p(t) + \phi_D(t)\Big), \tag{5.20}$$

and

$$h_\times(t) = \frac{2G^2}{c^4} \frac{2m_1 m_2}{r_s(t) D_L} 2\cos\iota F^\times(t) \cos\Big(\int^t f_{\rm gw}(t')dt' + \pi/2 + \phi_p(t) + \phi_D(t)\Big). \tag{5.21}$$

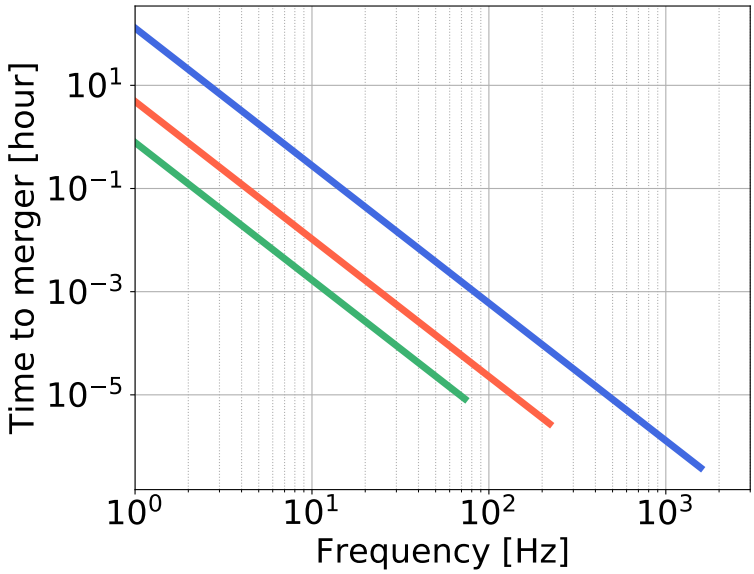

Figure 5.3: Time to merger versus frequency for $1.4M_{\odot} - 1.4M_{\odot}$ BNS (blue), $10M_{\odot} - 10M_{\odot}$ BBH (red), and $30M_{\odot} - 30M_{\odot}$ BBH (green).

5.3 Polarization models

In this section, we provide our polarization models. We study the polarization separability calculating the estimation errors in the mixed polarization models.

From the derivations of the parametrized waveforms in Section 3.3, we can define the geometrical factors for the quadrupole vector modes (V_x, V_y) and the quadrupole scalar mode (S_2) including the geometrical patterns of the radiation or the inclination dependence, which is determined only by the geometry of the system and then is independent of a specific theory of gravity, as follows.

$$\mathcal{G}_{V_x,I} := \sqrt{\frac{525}{56}} \sin 2\iota F_{V_x,I}(\boldsymbol{\theta_s}, \boldsymbol{\theta_e}) e^{i\phi_{D,I}(\theta_s,\phi_s,\theta_e,\phi_e)}, \tag{5.22}$$

$$\mathcal{G}_{V_y,I} := \sqrt{\frac{15}{2}} \sin \iota F_{V_y,I}(\boldsymbol{\theta_s}, \boldsymbol{\theta_e}) e^{i\phi_{D,I}(\theta_s,\phi_s,\theta_e,\phi_e)}, \tag{5.23}$$

$$\mathcal{G}_{S_2,I} := \sqrt{\frac{225}{8}} \sin^2 \iota F_{b,I}(\boldsymbol{\theta_s}, \boldsymbol{\theta_e}) e^{i\phi_{D,I}(\theta_s,\phi_s,\theta_e,\phi_e)}. \tag{5.24}$$

The scalar dipole radiation may exist in some modified gravity theories as shown in Section 3.3. From the general dependence on the inclination angle for the scalar dipole mode, we can define the geometrical factor for the scalar dipole mode as

$$\mathcal{G}_{S_1,I} := \sqrt{\frac{45}{2}} \sin\iota F_{b,I}(\boldsymbol{\theta_s}, \boldsymbol{\theta_e}) e^{i\phi_{D,I}(\theta_s,\phi_s,\theta_e,\phi_e)}. \tag{5.25}$$

The overall factors of these geometrical factors are inserted for normalization with respect to the sky location parameters and the inclination angle.

Next, we provide our polarization models. We set the mixed polarization model including GR. The polarization models except for GR include some non-tensorial polarization modes in addition to tensor modes. We can Fourier transform the detector signal in each polarization model by substituting $t(f)$ into the slowly varying parts such as the geometrical factors even for the non-tensorial polarization modes as we derived Eq. (F.13). The actual waveforms should depend on the parameters peculiar to the theory [96]. Nevertheless, it is assumed that non-tensorial polarization follow the same phase evolution as that of the tensor polarization in our models. This means that we consider pessimistic cases from the viewpoint of polarization separation as far as we assume a known phase evolution and do not introduce any parameters specific to the theory, because it should be more difficult to separate the polarization modes whose waveforms are same. Since a radiation process in merging and ringdown phase is complex even in GR, it is hard to associate the polarization contents in inspiral phase to those in merger and ringdown phases in general. Here, we concentrate only on an inspiral phase keeping results robust and conservative. Furthermore, for simplicity, we do not consider the waveform corrections by the additional non-tensorial radiation, which are taken into account in the latter chapter Chapter 7, because all modes are corrected in the same way and it would not affect the fundamental separation condition while the appearance of degeneracy may change. We enumerate our polarization models below.

Model T: GR model

This is a GR model. There are not any additional polarization parameters.

The signal of the I-th detector in the frequency domain is written as

$$h_I = \mathcal{G}_{T,I}(t(f))h_{\rm GR}. \tag{5.26}$$

Model TS1: scalar-tensor dipole model

This model includes a dipole scalar mode in addition to the tensor modes. The additional scalar mode is characterized by an additional amplitude parameter A_{S_1}. Here, we assume the same frequency evolution for the additional dipole mode as that for the tensor mode because we are interested in the influence of the geometrical radiation pattern here. The waveform for the dipole radiation is theory dependent. We need more improved model when we search for the dipole radiation with real data. The signal of the I-th detector in the frequency domain is written as

$$h_I = \{\mathcal{G}_{T,I}(t(f)) + A_{S_1}\mathcal{G}_{S_1,I}(t(f))\}h_{\rm GR}. \tag{5.27}$$

Model TS2: scalar-tensor quadrupole model

This model includes a quadrupole scalar mode in addition to the tensor modes. The additional scalar mode is characterized by an additional amplitude parameter A_{S_2}. The signal of the I-th detector in the frequency domain is written as

$$h_I = \{\mathcal{G}_{T,I}(t(f)) + A_{S_2}\mathcal{G}_{S_2,I}(t(f))\}h_{\rm GR}. \tag{5.28}$$

Model TVxS2: quadrupole scalar-vector x - tensor model

This model includes a quadrupole scalar mode and a vector x mode in addition to the tensor modes. The additional scalar and vector mode are characterized by amplitude parameters (A_{S_2}, A_{V_x}), respectively. The signal of the I-th detector in the frequency domain is written as

$$h_I = \{\mathcal{G}_{T,I}(t(f)) + A_{S_2}\mathcal{G}_{S_2,I}(t(f)) + A_{V_x}\mathcal{G}_{V_x,I}(t(f))\}h_{\rm GR}. \tag{5.29}$$

Model TVyS1: dipole scalar and quadrupole vector y-tensor model

This model includes a dipole scalar mode and a quadrupole vector y mode in addition to the tensor modes. The additional scalar and vector mode are characterized by amplitude parameters (A_{S_1}, A_{V_y}), respectively. The reason

why we choose this polarization combination is to consider a pessimistic case in polarization separation for the same geometrical patterns. The signal of the I-th detector in the frequency domain is written as

$$h_I = \{\mathcal{G}_{T,I}(t(f)) + A_{S_1}\mathcal{G}_{S_1,I}(t(f)) + A_{V_y}\mathcal{G}_{V_y,I}(t(f))\}h_{\rm GR}. \tag{5.30}$$

Model TV: quadrupole vector-tensor model

This model includes a quadrupole vector x and a vector y mode in addition to the tensor modes. The additional vector modes are characterized by amplitude parameters (A_{V_x}, A_{V_y}). The signal of the I-th detector in the frequency domain is written as

$$h_I = \{\mathcal{G}_{T,I}(t(f)) + A_{V_x}\mathcal{G}_{V_x,I}(t(f)) + A_{V_y}\mathcal{G}_{V_y,I}(t(f))\}h_{\rm GR}. \tag{5.31}$$

5.4 Separability with the 2G detectors

In this section, we show the polarization separability with the 2G detectors. First, we summarize the analytical settings and then we provide the results of the parameter estimation. The analysis is based on the Fisher information matrix. We evaluate the polarization separability by estimating the parameter estimation errors of the additional polarization amplitude parameters and compare them with their fiducial values.

5.4.1 Analytical settings

We use our six polarization models from Model T to Model TV in the previous section as the signal model. Since we can ignore time variation for the 2G detectors, we adopt the inspiral waveform Eq. (F.13) up to 3 PN order in GW amplitude and 3.5 PN order in GW phase. The frequency lower end of integration $f_{\rm min}$ is set to 30 Hz and the frequency upper end $f_{\rm max}$ is set to the frequency $f_{\rm ISCO}$ that is twice the innermost stable circular orbit frequency defined by

$$f_{\rm ISCO} = (6^{3/2}\pi m)^{-1} \simeq 0.0217 m^{-1}. \tag{5.32}$$

11 model parameters in GR

$$(\log \mathcal{M}, \log \eta, t_c, \phi_c, \log d_L, \chi_s, \chi_a, \theta_s, \phi_s, \cos\iota, \psi_p), \tag{5.33}$$

are considered and additional polarization amplitude parameters in each model. It is assumed that the fiducial values of the additional polarization amplitude parameters are equal to unity unless otherwise noted. Here $\log\eta, \chi_s$, and χ_a are the logarithm of the mass ratio, the symmetric spin, and the antisymmetric spin, respectively. The fiducial values of $t_c, \phi_c, \chi_s, \chi_a$ are set to be zero in all models. The priors are imposed on the parameters having domain of definition; $\log\eta$, ϕ_c, angular parameters $(\theta_s, \phi_s, \cos\iota, \psi_p)$, and the spin parameters of the compact binary star (χ_s, χ_a).

We estimate the model parameters of BBHs with $10M_\odot$ equal masses at $z = 0.05$ and of BNSs with $1.4M_\odot$ equal masses at $z = 0.01$ under each polarization model. The detection criterion is that the network total SNR > 8 and the angular parameters $(\cos\theta_s, \phi_s, \cos\iota, \psi_p)$ are uniformly random distributed because we want to evaluate the general polarization separability by integrating out the angular parameters. The number of sources is 500 in each case.

We consider two global GW detector networks. The first is formed by the two aLIGOs at Hanford and Livingston and AdV(HLV), and the second is formed by HLV with KAGRA(HLVK). It is assumed that aLIGOs and KAGRA have the design sensitivity [128]. It is also assumed that AdV have its optimized sensitivity to BNS [128]. Their sensitivity curves are shown in Fig. 5.1 and Fig. 5.2.

We estimate the model parameters of 500 BBHs or 500 BNSs by Fisher information matrix with HLV or HLVK in each polarization model. When the polarization modes would be able to be separated, the error of the additional polarization amplitude parameter decreases linearly with the detector sensitivity because the degeneracy among parameters is broken. We utilize this scaling law to discuss the polarization separability. On the other hand, we can find the scaling law when the errors are less than their fiducial values as described below. Thus, we can see that the polarizations would be separable when the errors of the additional polarization amplitude parameters are less

than their fiducial values simply.

5.4.2 Results

The parameter estimation results are shown in Table 5.1 and Table 5.2 for the case of BBH and in Table 5.3 and Table 5.4 for the case of BNS. We show the median values of the estimated errors for the luminosity distance, the sky localization, and the additional polarization amplitude in Table 5.1 and Table 5.3. The median values of the correlation coefficients larger than 10% for the additional polarization amplitude are also shown in Table 5.2 and Table 5.4. It is found that the amplitudes of the non-tensorial polarization modes strongly correlate with $\ln d_L$ and $\cos\iota$ in general.

Fig. 5.4 shows the histograms of the estimated errors for the luminosity distance, the sky localization, the inclination angle, and the polarization angle in GR (Model T). We can see that the estimated errors are reduced by participation of KAGRA as the fourth detector. The participation of KAGRA reduces the amplitude parameter errors including $\cos\iota$ and ψ_p. The luminosity distance $\ln d_L$ error is reduced by a factor of about 2 and the sky localization error Ω_s is also reduced by a factor of about 3.

Fig. 5.5 shows the estimation error histograms for the luminosity distance, the sky localization, the inclination angle, the polarization angle, and the additional polarization amplitude in the model TS1. Since the estimation errors of the amplitude parameters are reduced by the participation of KAGRA as the fourth detector compared to the model T, the four-detector network can break a degeneracy among amplitude parameters. A_s for BNS would be identified even with three detectors, while the additional scalar mode for BBH would be not separable. The error for BBH is much reduced by KAGRA as the fourth detector. The reason is that the signal duration of BBH is shorter than that of BNS in the observational band. The shortness of the signal would cause the worse chirp mass error, which is estimated mainly from the GW phase. In our analysis, the median value is $\Delta\ln\mathcal{M} = 0.0019$ for BBH, while that is $\Delta\ln\mathcal{M} = 0.00015$ (median) for BNS with HLV. Since the chirp mass also appears in the GW amplitude, the worse estimation error causes the worse estimation of the other amplitude parameters. With HLVK, the

Table 5.1: Median values of parameter estimation errors in the case of BBH. Component masse of BBH are $10M_\odot - 10M_\odot$. The polarization modes would be separable when the errors of the additional polarization amplitudes are less than its fiducial value, which is unity here. We define the improvement factor as the ratio of the error with HLV to the error with HLVK.

	Parameter	BBH(HLV)	BBH(HLVK)	Improvement factor
ModelT	SNR	33.3	40.2	
	$\Delta \ln d_L$	0.269	0.137	1.96
	$\Delta\Omega_s[\mathrm{deg}^2]$	5.91	1.77	3.34
ModelTS1	$\Delta \ln d_L$	0.678	0.179	3.79
	$\Delta\Omega_s[\mathrm{deg}^2]$	4.74	0.912	5.20
	ΔA_{S1}	1.16	0.284	4.08
ModelTS2	$\Delta \ln d_L$	0.676	0.182	3.71
	$\Delta\Omega_s[\mathrm{deg}^2]$	4.74	0.913	5.09
	ΔA_{S2}	1.51	0.385	3.92
ModelTVxS2	$\Delta \ln d_L$	1.58	0.258	6.12
	$\Delta\Omega_s[\mathrm{deg}^2]$	6.13	0.885	6.92
	ΔA_{S2}	4.15	0.486	8.54
	ΔA_{V_x}	2.23	0.399	5.59
ModelTVyS1	$\Delta \ln d_L$	1.69	0.253	6.68
	$\Delta\Omega_s[\mathrm{deg}^2]$	6.76	0.879	7.69
	ΔA_{S1}	3.72	0.383	9.71
	ΔA_{V_y}	3.12	0.389	8.02
ModelTV	$\Delta \ln d_L$	1.98	0.310	6.39
	$\Delta\Omega_s[\mathrm{deg}^2]$	5.68	0.795	7.14
	ΔA_{V_x}	2.55	0.420	6.07
	ΔA_{V_y}	3.91	0.513	7.62

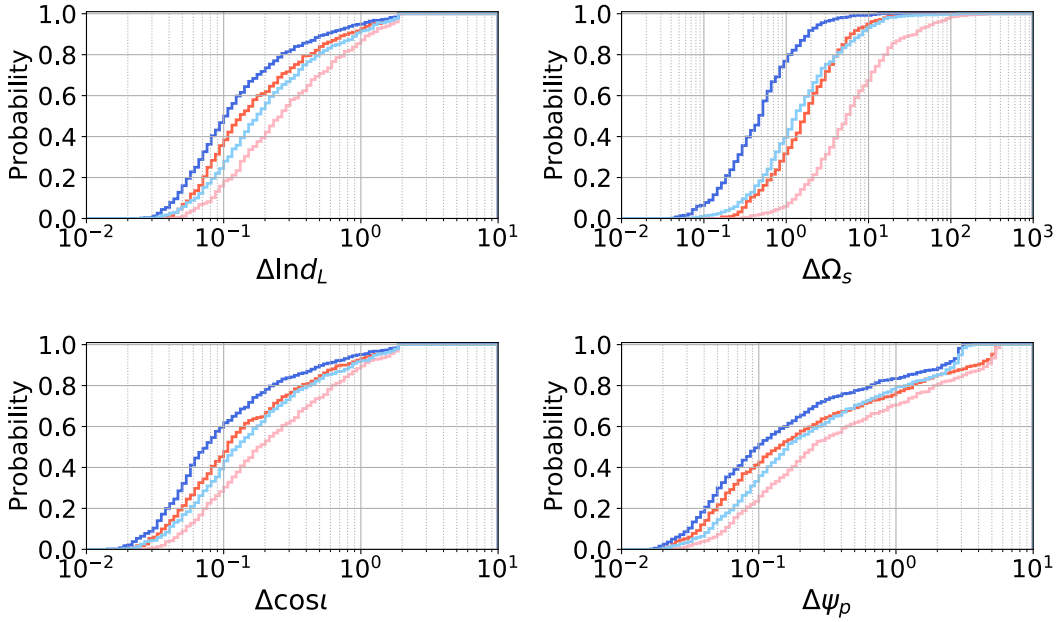

Figure 5.4: Estimation errors in the model T. The results of $10M_\odot - 10M_\odot$ with HLV are shown in light red, $10M_\odot - 10M_\odot$ with HLVK in red, $1.4M_\odot - 1.4M_\odot$ with HLV in light blue, and $1.4M_\odot - 1.4M_\odot$ with HLVK in blue. The rapid change of $\Delta\psi_p$ at around 3 is caused by the fact that we impose the priors on the parameters having domain of definition; angular parameters and spin parameters.

Table 5.2: Medians of the correlation coefficients in the case of BBH. Component masse of BBH are $10M_\odot - 10M_\odot$. The correlation coefficients larger than 10% are shown in the table.

	Parameter	BBH(HLV)	BBH(HLVK)
ModelT	SNR	33.3	40.2
ModelTS1	$C(A_{S1}, \log d_L)$	0.998	0.989
	$C(A_{S1}, \cos\iota)$	-0.553	-0.500
ModelTS2	$C(A_{S2}, \log d_L)$	0.997	0.989
	$C(A_{S2}, \cos\iota)$	-0.609	-0.564
ModelTVxS2	$C(A_{V_x}, \log d_L)$	0.945	0.690
	$C(A_{V_x}, \cos\iota)$	0.412	0.360
	$C(A_{V_x}, A_{S2})$	0.919	0.576
ModelTVyS1	$C(A_{V_y}, \log d_L)$	0.996	0.990
	$C(A_{V_y}, \cos\iota)$	-0.660	-0.322
	$C(A_{V_y}, A_{S1})$	0.996	0.983
ModelTV	$C(A_{V_y}, \log d_L)$	0.999	0.993
	$C(A_{V_y}, \cos\iota)$	-0.846	-0.335
	$C(A_{V_x}, A_{V_y})$	0.987	0.814

median value is $\Delta \ln \mathcal{M} = 0.0017$ for BBH, while the median value is $\Delta \ln \mathcal{M} = 0.00014$ for BNS. $\Delta \ln \mathcal{M}$ for BBH is improved by 11%, while $\Delta \ln \mathcal{M}$ for BNS is improved by 7%. This result suggests that a four-detector network is needed for separation of the additional scalar mode for BBH, although in principle a three-detector network is able to distinguish three polarization modes. Even in the model TS2, the errors and correlations behave the same way as in the model TS1.

Fig. 5.6 shows the results in other polarization models. Table 5.1 and Table 5.3 also shows that the errors of the additional polarization amplitude parameters with HLV in the model TVxS2, TVyS1, and TV, are larger than unity in both cases of BBH and BNS. Four GW detectors are always needed for separation. The KAGRA as the fourth detector reduced the estimation errors of the additional polarization modes than in the model TS1 and the model TS2. The estimation errors are more than 5 times reduced in both cases of BBH and BNS.

Table 5.3: Median values of parameter estimation errors in the case of BBH. Component masse of BNS are $1.4M_\odot - 1.4M_\odot$. The polarization modes would be separable when the errors of the additional polarization amplitudes are less than its fiducial value, which is unity here. We define the improvement factor as the ratio of the error with HLV to the error with HLVK.

	Parameter	BNS(HLV)	BNS(HLVK)	Improvement factor
ModelT	SNR	36.4	44.3	
	$\Delta \ln d_L$	0.183	0.107	1.71
	$\Delta\Omega_s[\mathrm{deg}^2]$	1.39	0.517	2.69
ModelTS1	$\Delta \ln d_L$	0.359	0.134	2.68
	$\Delta\Omega_s[\mathrm{deg}^2]$	0.919	0.250	3.68
	ΔA_{S1}	0.606	0.197	3.08
ModelTS2	$\Delta \ln d_L$	0.358	0.134	2.67
	$\Delta\Omega_s[\mathrm{deg}^2]$	0.862	0.246	3.50
	ΔA_{S2}	0.765	0.256	2.99
ModelTVxS2	$\Delta \ln d_L$	1.05	0.190	5.53
	$\Delta\Omega_s[\mathrm{deg}^2]$	0.783	0.179	4.37
	ΔA_{S2}	2.48	0.340	7.29
	ΔA_{V_x}	1.24	0.228	5.44
ModelTVyS1	$\Delta \ln d_L$	1.05	0.183	5.74
	$\Delta\Omega_s[\mathrm{deg}^2]$	0.831	0.187	4.44
	ΔA_{S1}	1.81	0.273	6.63
	ΔA_{V_y}	1.75	0.270	6.48
ModelTV	$\Delta \ln d_L$	1.22	0.193	6.32
	$\Delta\Omega_s[\mathrm{deg}^2]$	0.813	0.187	4.35
	ΔA_{V_x}	1.37	0.241	5.68
	ΔA_{V_y}	2.12	0.298	7.11

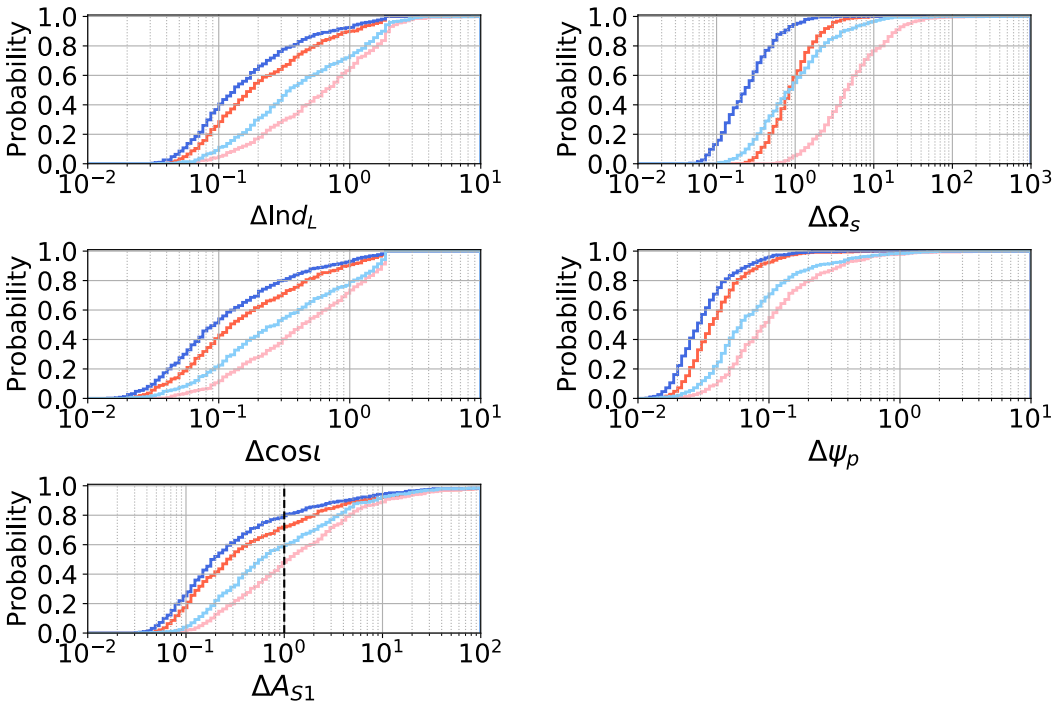

Figure 5.5: Estimation errors in the model TS1. The results of $10M_\odot - 10M_\odot$ with HLV are shown in light red, $10M_\odot - 10M_\odot$ with HLVK in red, $1.4M_\odot - 1.4M_\odot$ with HLV in light blue, and $1.4M_\odot - 1.4M_\odot$ with HLVK in blue.

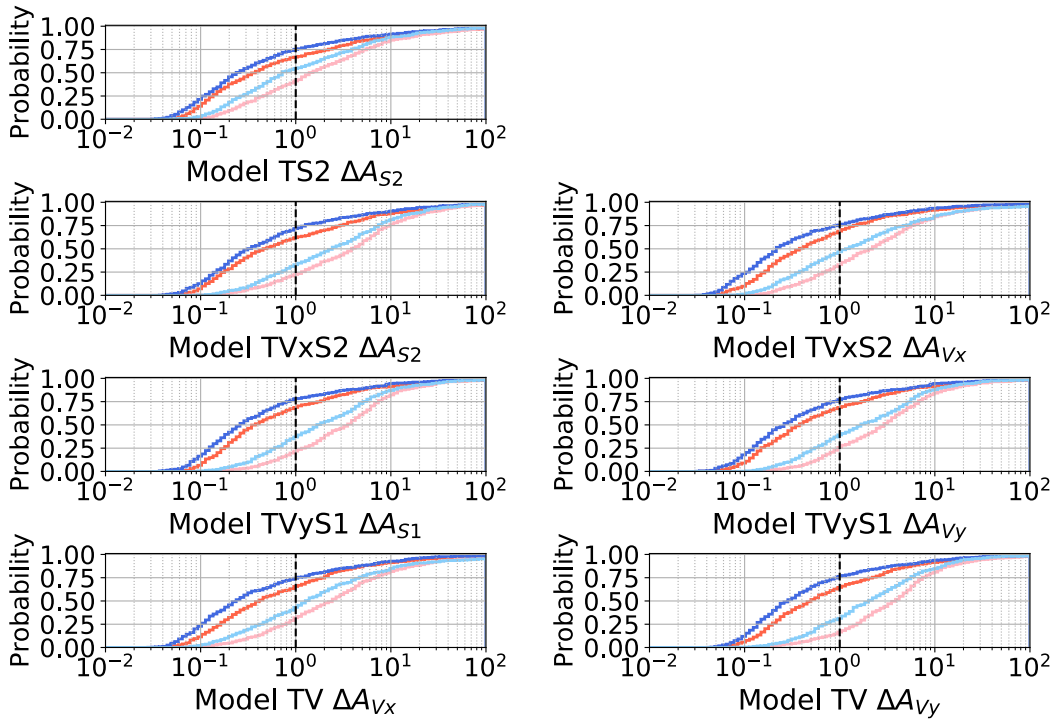

Figure 5.6: Estimation errors of the additional polarization amplitudes in all models.The results of $10M_{\odot} - 10M_{\odot}$ with HLV are shown in light red, $10M_{\odot} - 10M_{\odot}$ with HLVK in red, $1.4M_{\odot} - 1.4M_{\odot}$ with HLV in light blue, and $1.4M_{\odot} - 1.4M_{\odot}$ with HLVK in blue.

Table 5.4: Medians of the correlation coefficients in the case of BNS. Component masse of BNS are $1.4M_\odot - 1.4M_\odot$. The correlation coefficients larger than 10% are shown in the table.

	Parameter	BNS(HLV)	BNS(HLVK)
ModelT	SNR	36.4	44.3
ModelTS1	$C(A_{S1}, \log d_L)$	0.996	0.984
	$C(A_{S1}, \cos\iota)$	-0.231	-0.159
ModelTS2	$C(A_{S2}, \log d_L)$	0.996	0.984
	$C(A_{S2}, \cos\iota)$	-0.246	-0.189
ModelTVxS2	$C(A_{V_x}, \log d_L)$	0.901	0.633
	$C(A_{V_x}, \cos\iota)$	-0.189	-0.072
	$C(A_{V_x}, A_{S2})$	0.828	0.557
ModelTVyS1	$C(A_{V_y}, \log d_L)$	0.997	0.986
	$C(A_{V_y}, \cos\iota)$	-0.446	-0.010
	$C(A_{V_y}, A_{S1})$	0.996	0.982
ModelTV	$C(A_{V_y}, \log d_L)$	0.998	0.991
	$C(A_{V_y}, \cos\iota)$	-0.307	-0.207
	$C(A_{V_x}, A_{V_y})$	0.948	0.624

5.4.3 Discussion

We changed the detector sensitivities by a factor of 10 to verify the scaling law for separation. In the model TS1 and TS2 the estimation errors of the additional polarization amplitude parameters with HLV decreased scaling to the sensitivity, but those in the model TVsS2, TVyS1, and TV did not decrease with HLV due to the mode degeneracy. This fact indicates that the polarization degrees of freedom are characterized by the overall amplitude parameters. The same number of detectors as the polarization modes are basically required for the GWs from the CBCs in principle.

It is assumed that the coalescence time and the phase at the coalescence time for the non-tensorial mode are the same as those of the tensor mode in the above analysis. Consideration of the parameters may affect the parameter estimation results. We check the influence of the coalescence time and the phase at coalescence in two ways. One is changing their fiducial values and another is introducing additional parameters to the non-tensorial modes.

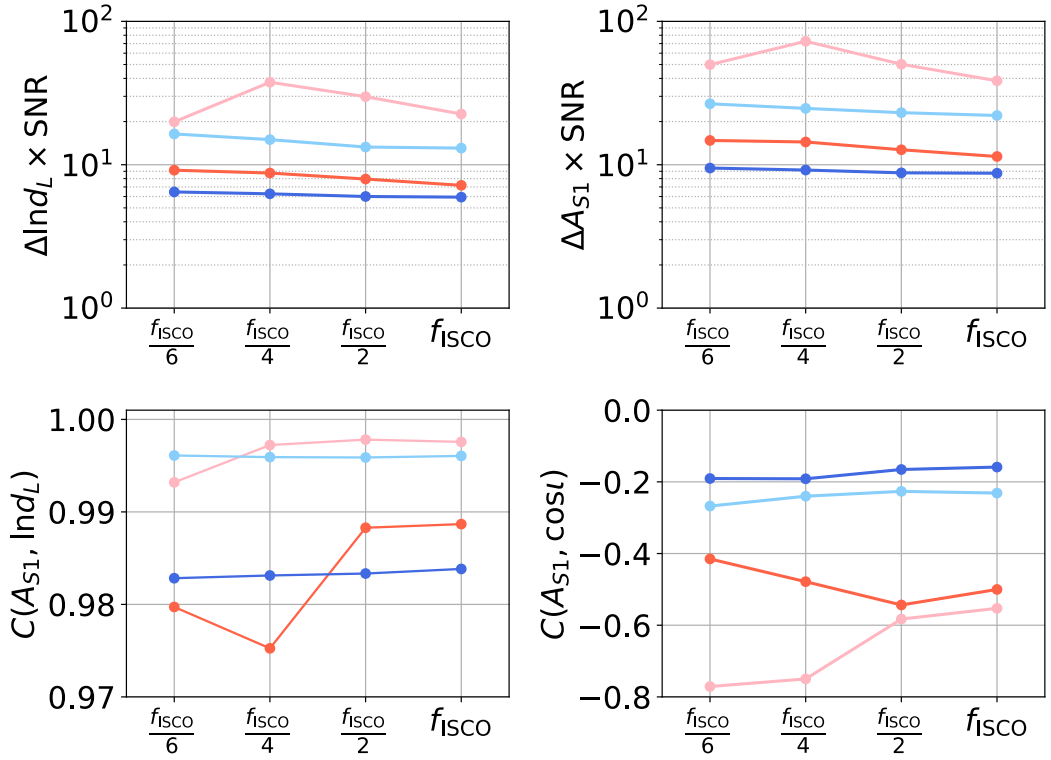

Figure 5.7: The estimation errors multiplied by SNR and the correlation coefficients in the model TS1 vs the upper frequency end. The results of $10M_\odot - 10M_\odot$ with HLV are shown in light red, $10M_\odot - 10M_\odot$ with HLVK in red, $1.4M_\odot - 1.4M_\odot$ with HLV in light blue, and $1.4M_\odot - 1.4M_\odot$ with HLVK in blue.

Consequently, it was found that the results hardly changed in both.

We change the f_{max} to $f_{\mathrm{ISCO}}/2, f_{\mathrm{ISCO}}/4, f_{\mathrm{ISCO}}/6$ in the model TS1 to investigate the dependence of the errors on the upper end frequency. Fig. 5.7 shows the results, and plots the errors multiplied by SNR and the parameter correlation coefficients. There is a tendency for the errors scale to SNR because the errors multiplied by SNR are flat. In other words, the amplitude error as well as SNR is scaled by the change of f_{max}. The exceptions such as the correlations at $f_{\mathrm{ISCO}}/6 \simeq 35$ Hz, $f_{\mathrm{ISCO}}/4 \simeq 52$ Hz for BBH, would happen because of the shortness of the integration range noting that $f_{\mathrm{min}} = 30$ Hz.

Table 5.2 and Table 5.4 show that the additional polarization amplitude parameters highly correlate with the inclination angle in general. Fig. 5.8

shows the scatter plots for the errors of the additional polarization amplitudes vs the error of the inclination angle for BNS in the model TVxS2. The errors of the additional polarization amplitudes for different polarization modes differently depend on the errors of the inclination angle. Fig. 5.9 is the same scatter plot of ΔA_{V_x} vs $\Delta \cos\iota$ for BNS but in the model TV.

It is shown in Fig. 5.8 and Fig. 5.9 that even in different polarization models the errors for the same polarization mode depend on the errors of the inclination angle in the same way. We also check that ΔA_{V_y} in both the model TVyS1 and TV show the same trend, and $\Delta A_{S_1}, \Delta A_{S_2}$ also show the same trend in the different models.

Fig. 5.10 is the scatter plots for the errors of the additional polarization amplitude A_{S_2} vs the errors of the inclination angle in the model TS2 for BBH and BNS. The distributions have the same appearance between for BBH and BNS.

In the above analysis, the unity fiducial values of all the additional amplitude parameters are assumed because we first need to reveal the principle conditions for separation and to catch the parameter correlations. Here, we change the fiducial values to $1/1000, 1/100, 1/10$ to investigate the influence of the fiducial values in the parameter estimation. Fig. 5.11 shows the dependence of the errors on the fiducial values and correlation coefficients in the model TS1. The errors of the luminosity distance and the sky localization change very little. It suggests that the errors are mainly identified by the tensor modes. The error of A_{S_1} is not changed significantly below $1/10$. It implies that we can estimate the detection limit of the amplitude A_{S_1} as roughly 1/SNR. As for the correlation coefficients, $C(A_{S_1}, \ln d_L)$ and $C(A_{S_1}, \cos\iota)$ become smaller as the fiducial values get smaller. This results also imply the difficulty to detect the additional modes below the detection limit. The main purpose of our analysis is to reveal the fundamental separation condition of the mixed polarization modes. In other words, we are interested in whether there are sufficient detectors, and the polarization modes are in principle separable. The fundamental condition should be supported by the fact that the errors of the additional polarization amplitudes are reduced by the artificial improvement of the detector sensitivity. We verified that we could see the SNR scaling typically when the error of the additional amplitude parameter

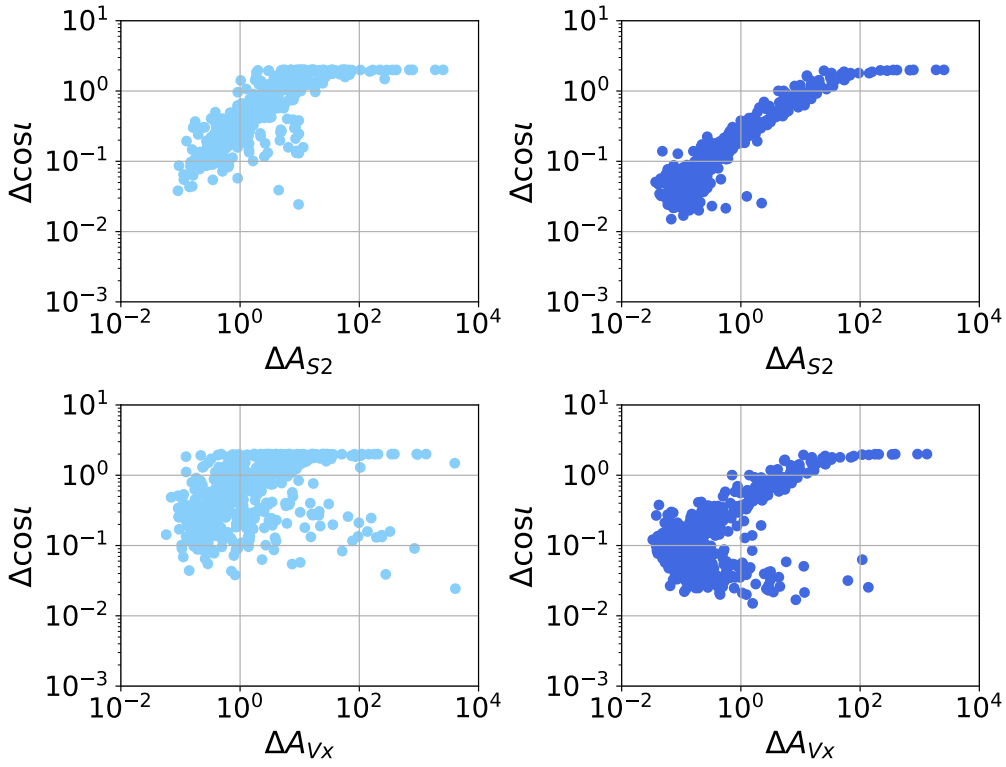

Figure 5.8: Scatter plots for the estimated error of the additional polarization amplitudes and of the inclination angle are shown for BNS in the model TVxS2. The results of $1.4M_\odot - 1.4M_\odot$ with HLV in light blue, and $1.4M_\odot - 1.4M_\odot$ with HLVK in blue.

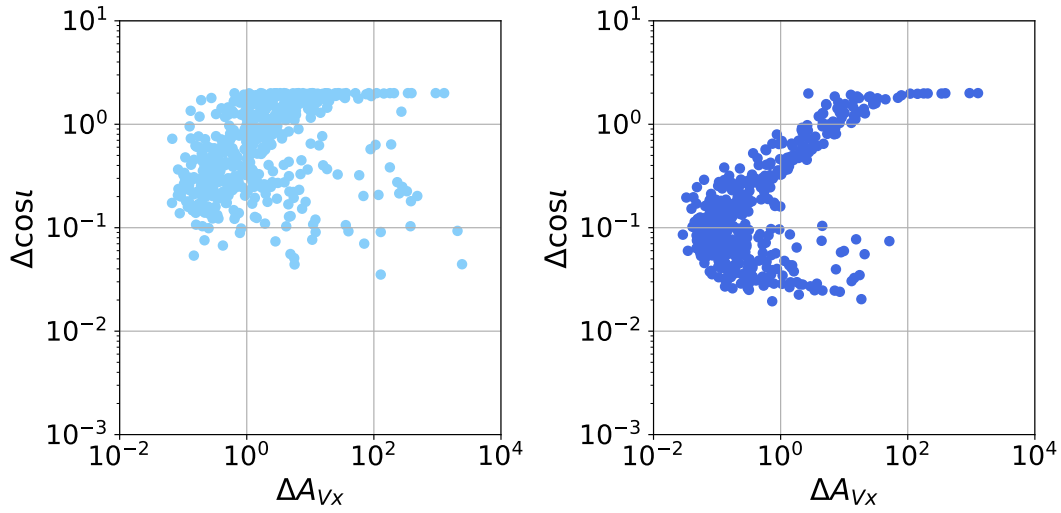

Figure 5.9: Scatter plots for the estimated error of the additional polarization amplitudes and of the inclination angle are shown for BNS in the model TV. The results of $1.4M_\odot - 1.4M_\odot$ with HLV are shown in light blue, and $1.4M_\odot - 1.4M_\odot$ with HLVK in blue.

is less than the fiducial value. Here, we are considering a situation where the modes should be separable given the SNR. If the error is not less than the fiducial value, we can say that the reason for this is the insufficient number of detectors. Therefore, we adopt the large-small relationship in comparison with the fiducial value as the separation criteria for convenience. If the separability is given by the detector noise level, ΔA should not change when the fiducial value of A is changed. The ΔA gives the detection limit. When $A_{S_1} = 1$ in Fig. 5.11, the error is more than the detection limit and the correlations $C(A_{S_1}, \ln d_L)$ and $C(A_{S_1}, \cos\iota)$ take values close to 1, though we claim that the polarizations would be separable in some cases, for example, in the case of BNS-HLV. In such a situation, we can think that the error would be limited by the partial degeneracy of the amplitude parameters from the values of $C(A_{S_1}, \ln d_L)$ and $C(A_{S_1}, \cos\iota)$ close to 1. It was found that the polarizations could be separable even when the correlation is very close to 1. However, it is also true that there is still a strong degeneracy from the correlation close to 1. Breaking this degeneracy would lead to an improvement of accuracy; this would be a subject for further study in the future.

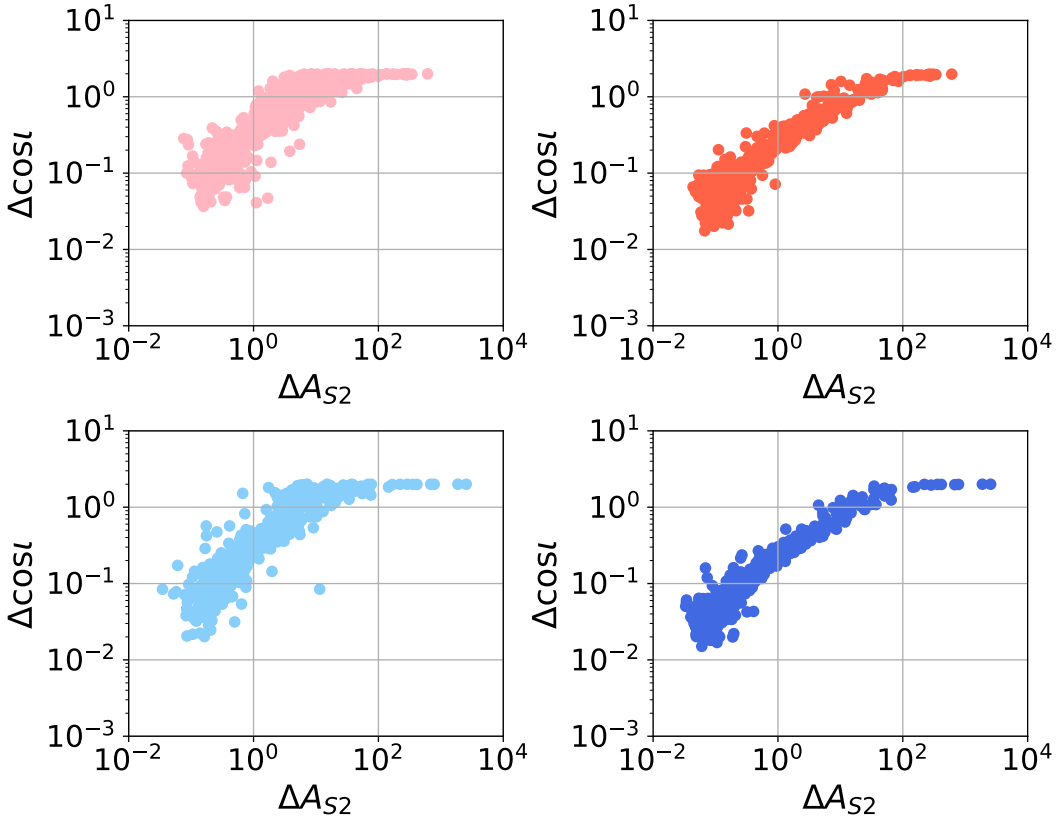

Figure 5.10: Scatter plots for the estimated error of the additional polarization amplitudes and of the inclination angle are shown in the model TS2. The results of $10M_\odot - 10M_\odot$ with HLV are shown in light red, $10M_\odot - 10M_\odot$ with HLVK in red, $1.4M_\odot - 1.4M_\odot$ with HLV in light blue, and $1.4M_\odot - 1.4M_\odot$ with HLVK in blue.

In the model TS2, TVxS2, TVyS1, and TV, we also checked the above fiducial value dependence. The behavior was same as with the case of the model TS1. Under the detection limit that is roughly estimated by 1/SNR, the errors of the additional polarization amplitude parameters are changed very little. We find the same conclusion of separation difficulty under the detection limit as in the model TS1.

5.4.4 Conclusion

We investigated the parameter estimation of the model parameters for the GWs from CBCs with the two global GW detector networks such as aLIGO-AdV and aLIGO-AdV-KAGRA in the mixed polarization models where the polarization degrees of freedom of GWs are characterized by overall additional polarization amplitudes. We revealed a principle condition for separation that at least the same number of detectors as the polarizations is necessary to separate the polarization modes from the observed detector signal as expected. However, even if we have enough detectors, separation could be difficult in some cases due to the mode degeneracy. In conclusion, there exists two polarization separation conditions; (i) the number of detectors should be equal to or more than the number of polarization modes under consideration and (ii) enough SNR and long enough signal duration. The entry of a fourth detector into the network of GW detectors makes it possible to distinguish the polarization mode from the CBC, even when there are two additional non-tensorial modes in addition to the tensor modes. Even in presence of one extra non-tensorial polarizations, the polarization separation is improved by the fourth detector breaking the amplitude parameter degeneracy. The expansion of the global detector network is intrinsically important for testing the theory of gravity that includes more polarization modes.

5.5 Separability with the 3G detectors

In this section, we show the polarization separability with the 3G detectors as with the case of the 2G detectors in the previous section. First, we give the analytical settings and then we show the results of the parameter estimation.

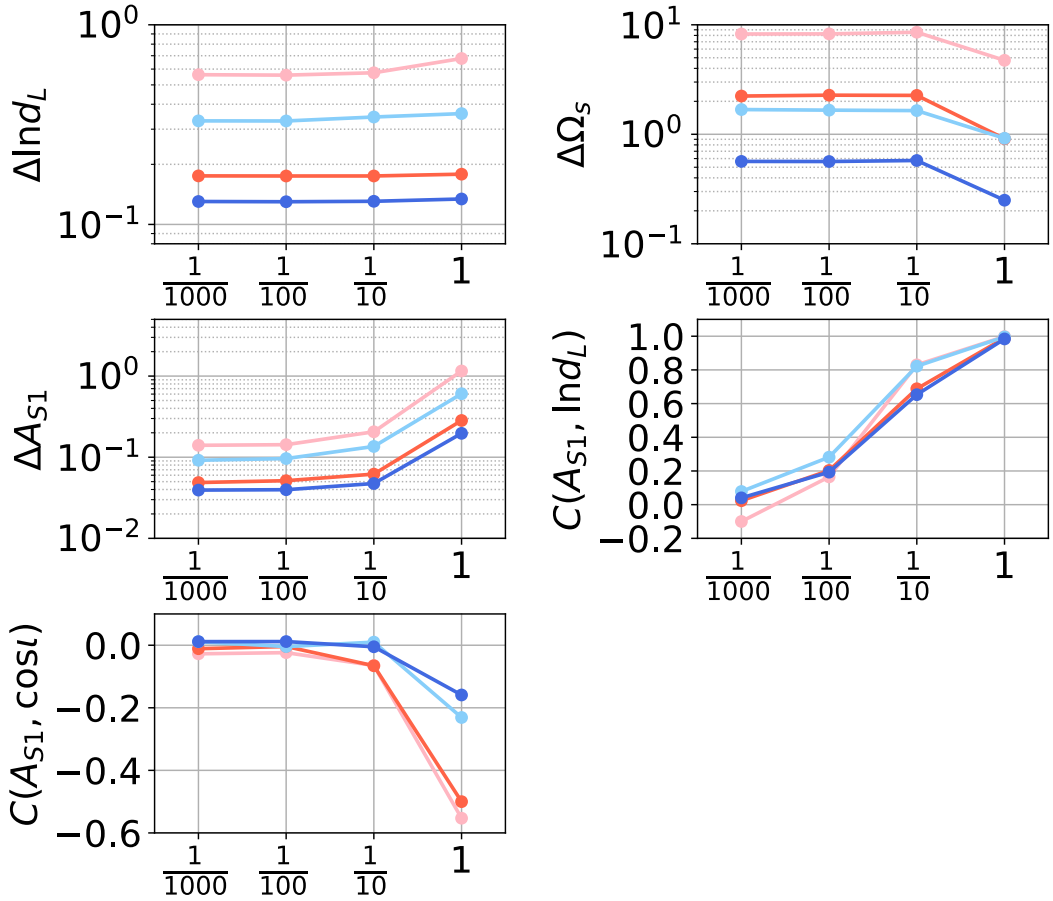

Figure 5.11: Plots for the estimation errors and the correlation coefficients and the fiducial values of the amplitude parameter A_{S_1} are shown in the model TS1. The results of $10M_\odot - 10M_\odot$ with HLV are shown in light red, $10M_\odot - 10M_\odot$ with HLVK in red, $1.4M_\odot - 1.4M_\odot$ with HLV in light blue, and $1.4M_\odot - 1.4M_\odot$ with HLVK in blue.

The analysis is based on the Fisher information matrix again. We evaluate the polarization separability by the estimated errors of the additional polarization amplitudes and compare them with their fiducial values. In particular, we show how the detector sensitivity at low frequency help with the polarization test of the GW from CBC.

5.5.1 Analytical settings

Here, we consider only the Model TS1 including one additional dipole scalar polarization mode to reveal the principle conditions and investigate the polarization separation properties specific to the 3G detectors that have the time-dependent antenna pattern functions. In Section 5.4, we showed that the choice of polarization models does not lead to a qualitative difference in the principle separation conditions as long as we consider enough detectors corresponding to the polarizations modes under consideration and integrate out the angular parameters by taking the median values.

The inspiral waveform Eq. (F.13) up to Newtonian order in GW amplitude and 3.5 PN order in GW phase is used because we want to keep consistency between the amplitude of the waveform and Eq. (F.16) as mentioned around Eq. (F.13). The frequency lower end $f_{\rm min}$ is set to 1 Hz and the frequency upper end $f_{\rm max}$ is set to the frequency $f_{\rm ISCO}$ that is twice the innermost stable circular orbit frequency Eq. (5.32) again. The considered parameters are Eq. (5.33) in GR and A_{S_1} in the model TS1. The settings of the fiducial values are same as Section 5.4. The fiducial values of $t_c, \phi_c, \chi_s, \chi_a$ is set to zero because we showed in Section 5.4 that the consideration of the coalescence time and the phase at the coalescence time do not affect the parameter estimation results. For a proof-of-principle study, in order to study the principle separation conditions, the unity fiducial values of the additional polarization amplitude parameters are assumed again unless otherwise noted. The prior settings for the parameters having domain of definition are same as in Section 5.4.

It is assumed that the 3G detectors have their design sensitivity in Fig. 5.2 and the Livingston site of aLIGO or Virgo site are assumed as in [129]. We deal with ET detectors as three independent interferometric detectors rotated each other by 120 deg. The polarization separability is defined by when the

Table 5.5: Median values of the estimation errors for $1.4M_\odot - 1.4M_\odot$ BNS at $z = 0.1$ with a single 3G GW detector in the model TS1. Three polarization modes that consist of a scalar mode and two tensor modes would be separable with either a ET-D detector and an ideal detector.

	Parameter	BNS(ET-B)	BNS(ET-D)	BNS(CE)	BNS(Ideal)
ModelTS1	SNR	57.8	50.7	105	170
	$\Delta \ln d_L$	0.979	0.355	6.67	0.197
	$\Delta\Omega_s[\mathrm{deg}^2]$	490	55.6	72105	7.56
	ΔA_{S1}	1.30	0.459	12.9	0.322

additional amplitude errors are less than their fiducial values again, which is supported by the scaling law.

5.5.2 Binary neutron stars

First, we conduct parameter estimation for BNS with equal mass $1.4M_\odot$ at z=0.1with a single 3G GW detector such as ET-B, ET-D, CE and an ideal detector in the model TS1. The ideal detector is a virtual detector having a constant sensitivity at lower frequency in terms of power spectral density 10^{-49} 1/Hz below 400 Hz and the same sensitivity as that of ET-D above. The reason why we also consider the ideal detector is to reveal the benefit of better sensitivity in the frequency region for the polarization test of GWs from CBCs. It is assumed that the ideal detector has same configuration as that of ET detector. 500 sources whose angular parameters $(\cos\theta_s, \phi_s, \cos\iota, \psi_p)$ are uniformly random are estimated by the Fisher information matrix.

The results for BNS with a single 3G detector are shown in Table 5.5. We show the median values of the estimation errors of the luminosity distance, the sky localization, and the additional polarization amplitude parameter. Since the errors ΔA_{S1} are less than unity with an ET-D and an ideal detector, three polarization modes that consist of a scalar mode and two tensor modes would be separable with either an ET-D or an ideal detector. On the other hand, the polarization modes would not be separable with either an ET-B or a CE. Since the polarization modes would be separable with an ET-D but not with an ET-B in spite of their same configuration, the better sensitivity at low

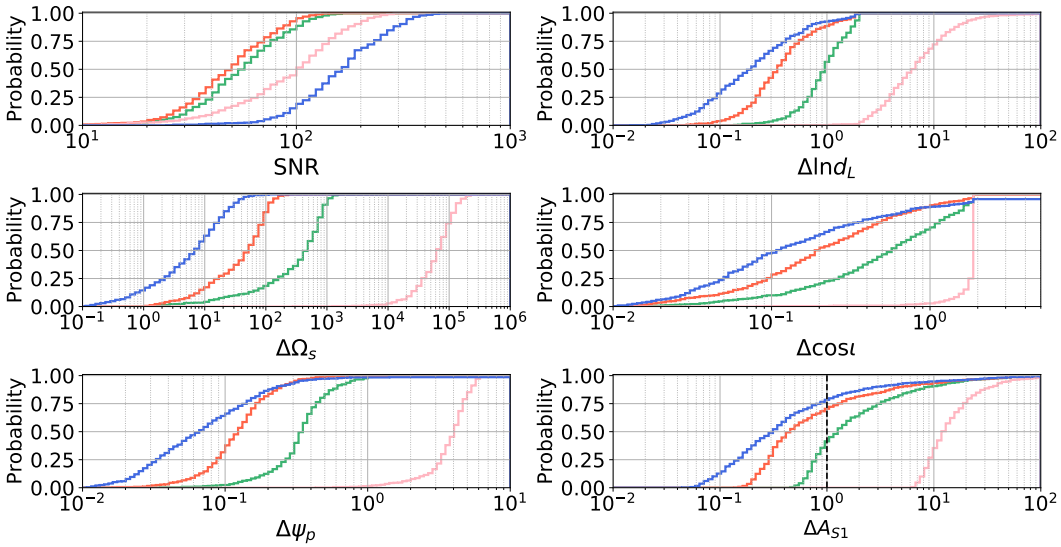

Figure 5.12: Histograms for the estimation errors for $1.4M_\odot - 1.4M_\odot$ BNS at $z = 0.1$ with a single 3G detector in the model TS1 . The results with ET-B are shown in green, with ET-D in red, CE in light red, and with ideal detector in blue.

frequency is helpful to separate the polarization modes. According to [126,130], the sensitivity around sub-5 Hz is important to localize the sky position of the GW source. The sensitivities of an ET-D and an ideal detector are better than those of an ET-B and a CE in the sub-5Hz low-frequency region. Thus, we can recognize that the time-varying antenna pattern functions help us for better separation of the polarization modes of GWs from CBCs. In the configuration of the ET detector, three colocated but not co-aligned interferometers may contribute to the polarization resolution. The estimation error for an ET-D having only one interferometer is $\Delta A_{S1} = 2.11$ compared to $\Delta A_{S1} = 0.459$ with three interferometric configuration. It is true that the configuration having three interferometers contributes to the polarization separability as well as the better sensitivity at low frequencies.

Fig. 5.12 shows the histograms for the luminosity distance, the sky localization, the inclination angle, the polarization angle, and the additional polarization amplitude for all 500 sources in the model TS1. It is also shown that the Earth's rotational effect can break the degeneracies among amplitude

Table 5.6: Median values of the estimation errors for $1.4M_\odot - 1.4M_\odot$ BNS at $z = 0.1$ when improving the sensitivity by a factor of 10. The error of the additional polarization amplitude parameter is improved by $10^{0.998}$ with an ET-D and by $10^{0.185}$ with a CE.

	Parameter	BNS(ET-D×10)	BNS(CE×10)
ModelTS1	SNR	507	1047
	$\Delta \ln d_L$	0.0357	3.73
	$\Delta\Omega_s[\mathrm{deg}^2]$	0.558	12727
	ΔA_{S1}	0.0461	8.43

parameters. The errors of the additional polarization amplitude parameter for some BNSs are less than unity even with an ET-B depending on the angular parameters of the source. This also indicates that the time dependence of the antenna pattern functions can help breaking the degeneracy among amplitude parameters partially. A single ET-like 3G detector is available for testing an additional polarization mode in addition to two tensor modes from the observations of BNS.

The polarization separability should be backed up by the scaling of the error of the additional polarization amplitude to the SNR. We checked the scaling by artificially improving the detector sensitivity of an ET-D and a CE by a factor of 10. Table 5.6 shows the results. It shows that the error of the additional polarization amplitude is improved by $10^{0.998}$ with an ET-D scaling to SNR, while the error with a CE is improved by only $10^{0.185}$. This indicates that we can find the scaling by SNR happens and then we can claim the polarizations would be separable when the errors are less than their fiducial values. For a single ET-like detector, the virtual detector network including a set of detectors along its trajectory could break the degeneracies among the amplitude parameters, while the low-frequency sensitivity of a single CE-like detector does not allow us to take advantage of the effects of Earth's rotation. We can characterize how the degeneracies are broken by the index of the improvement as 0.998 for ET-D and 0.185 for CE.

We also change the lower cutoff frequency f_{min} with an ET-D to explore the essential frequency region. Fig. 5.13 shows the results. The frequencies of

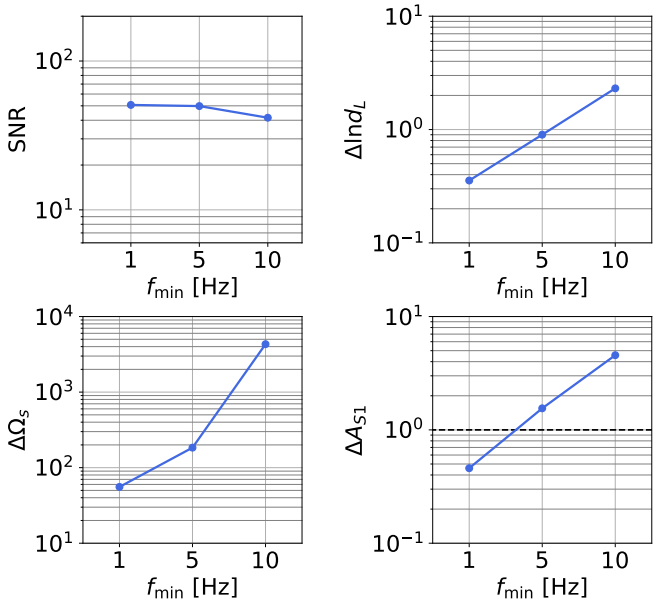

Figure 5.13: Median values of the estimation errors for $1.4M_\odot - 1.4M_\odot$ BNS at $z = 0.1$ when changing the lower cutoff frequency $f_{\rm min}$ with an ET-D. The range below 5 Hz is essential for the polarization test of GWs from CBCs.

1 Hz, 5 Hz, and 10 Hz correspond to the time to merger 5.38 days, 1.77 hours, and 0.28 hours, respectively, for $1.4M_\odot - 1.4M_\odot$ BNS as we can see in Fig. 5.3. Note that $f_{\rm max}$ is equal to 1428 Hz from the definition of the upper cutoff frequency Eq. (5.32). The polarization modes would be inseparable with $f_{\rm min} = 5$ Hz even with an ET-D. This means that the sub-5 Hz region, especially the range below 5 Hz is crucial for the polarization test using the BNS. The 3G detectors are designed so that the sensitivity at low frequencies is limited by the Newtonian noise that is a noise caused by the fluctuations of the surrounding gravitational potential [131, 132]. Hence, it is necessarily to gain better understanding about the Newtonian noise for future tests of the polarizations with 3G detectors because the Newtonian noise is poorly understood yet.

Next, we investigate how the setting of the fiducial values affect the results by changing the fiducial values to $1/1000, 1/100$, and $1/10$. Fig. 5.14 shows the dependence of the errors of the additional polarization amplitudes on the fiducial values with an ET-D in the model TS1. ΔA_{S_1} is hardly changed

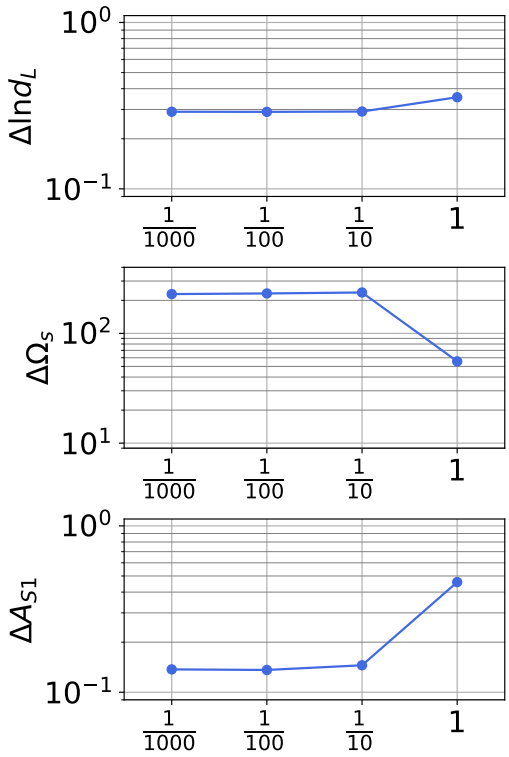

Figure 5.14: Median values of the parameter estimation errors for $1.4M_\odot - 1.4M_\odot$ BNS at $z = 0.1$ when changing the fiducial value of A_{S1} with an ET-D. The error of A_{S1} is hardly changed if the fiducial values are less than 1/10. The detection limit is given by the converged value.

below 1/10. The dependence is consistent with the 2G detector networks in Fig. 5.11. However, the detection limit is not given by 1/SNR in this case. It would come from the fact that an effective detector network is formed by a single 3G detector at each time, while the 2G detectors form a real multi-detector network at the same time.

Finally, we also consider three types of detector networks (ET-D - ET-D, ET-D - CE, CE-CE). Each two detectors are located at the Livingston site of aLIGO and Virgo site. Table 5.7 shows the results, taking the fiducial values of the additional polarization amplitude parameters unity again. The ET-D - ET-D can separate the polarizations more precisely. The polarization modes would also be separable with ET-D - CE. The polarization modes would

Table 5.7: Median values of the estimation errors for $1.4M_\odot - 1.4M_\odot$ BNS at $z = 0.1$ with three types of detector networks (ET-D - ET-D, ET-D - CE, CE-CE). Two 3G detectors could distinguish three polarization modes.

	Parameter	BNS(ET-D - ET-D)	BNS(ET-D - CE)	BNS(CE-CE)
ModelTS1	SNR	75.2	120	151
	$\Delta \ln d_L$	0.0520	0.124	0.569
	$\Delta\Omega_s[\mathrm{deg}^2]$	0.346	0.643	3.51
	ΔA_{S1}	0.0797	0.178	0.913

be separable even with two CE-like detectors to some extent. However, its separability is limited because CE detectors do not take advantage of the Earth's rotational effect fully and they have one-interferometric configuration, though a CE detector can achieve high SNR thanks to its significantly better sensitivity above 10 Hz.

5.5.3 Binary black hole

Here, we consider polarization tests with BBHs. We conduct parameter estimation for BBHs with equal mass $10M_\odot$ at z=0.5 with a single 3G GW detector such as ET-B, ET-D, CE and an ideal detector in the model TS1. 500 sources whose angular parameters are uniformly random are estimated by the Fisher information matrix as with the case of BNSs. Table 5.8 shows the results for BBH with a single 3G detector. The median values of the estimation errors are shown. However, the upper cutoff frequency for $10M_\odot - 10M_\odot$ BBHs at z=0.5 is 147 Hz by the definition of Eq. (5.32). The duration of the signal is shorter than that of BNS. Hence, it is difficult to localize the source with a single detector. It results in the worse estimation of the additional polarization amplitude and the polarizations would be inseparable.

Table 5.9 shows the results of the parameter estimation for BBHs with two-detector networks (ET-D - ET-D, ET-D - CE, CE-CE). Three polarization modes would be separable with a two-detector network including an ET-D. It suggests that the 3G detector networks can also utilize the Earth's rotation effect in polarization tests even for BBHs.

Table 5.8: Median values of the estimation errors for $10M_{\odot} - 10M_{\odot}$ BBH at $z = 0.5$ with a single 3G GW detector. it is more difficult for a single 3G detector to determine the sky location and the amplitude parameters due to the shortness of the signal duration.

	Parameter	BBH(ET-B)	BBH(ET-D)	BBH(CE)	BBH(Ideal)
	SNR	57.9	51.6	111	181
ModelTS1	$\Delta \ln d_L$	4.204	3.390	20.45	2.181
	$\Delta\Omega_s[\mathrm{deg}^2]$	26437	15618	219581	3133
	ΔA_{S1}	7.52	6.36	41.7	4.34

Table 5.9: Median values of the estimation errors for $10M_{\odot} - 10M_{\odot}$ BBH at $z = 0.5$ with two-detectors (ET-D - ET-D, ET-D - CE, CE-CE). The two 3G detector networks including an ET-D could distinguish three polarization modes.

	Parameter	BBH(ET-D - ET-D)	BBH(ET-D - CE)	BBH(CE-CE)
ModelTS1	SNR	77.4	126	161
	$\Delta \ln d_L$	0.062	0.045	3.12
	$\Delta\Omega_s[\mathrm{deg}^2]$	0.819	2.79	122
	ΔA_{S1}	0.089	0.521	6.45

5.5.4 Multiple sources

At the last of this section, we show the prospects for polarization tests by future observations of CBCs with the 3G ground-based detectors by considering the redshift distribution of the binary system in our universe.

Binary coalesence rate and detection rate

Let $R_c(z)$ the redshift rate density in the detector frame. It is defined as the number of coalescences per detector time per redshift,

$$R_c(z) := \frac{dN_c(t_d, z)}{dt_d dz}, \tag{5.34}$$

where N_c is the number of CBCs and t_d is the detector-frame time. We shall consider binary systems coalescing at a lookback time t_c [2] and write $z_c = z(t_c)$. The redshift rate density can be rewritten in terms of the volumetric coalescence rate in the source frame [133] as

$$\begin{aligned} R_c(z_c) &= \left.\frac{dN_c(t_d, z)}{dt_d dz}\right|_{z=z_c} \\ &= \left.\frac{dN_c}{dt_s dV_c}\right|_{z=z_c} \left.\frac{dt_s}{dt_d}\right|_{z=z_c} \left.\frac{dV_c}{dz}\right|_{z=z_c} \\ &= \frac{1}{1+z_c} \left.\frac{dV_c}{dz}\right|_{z=z_c} \left.\frac{dN_c}{dt_s dV_c}\right|_{z=z_c} \\ &=: \frac{1}{1+z_c} \left.\frac{dV_c}{dz}\right|_{z=z_c} \mathcal{R}_c(z_c), \end{aligned} \tag{5.35}$$

where t_s is the source-frame time [3] and $V_c(z)$ is the comoving volume. Here $\mathcal{R}_m$ denotes the volumetric merger rate in the source frame that is the number

[2] Note that the lookback time is the difference between the age of the universe now and the age at redshift z.

[3] Note that $(1+z)dt_s = dt_d$ derived by considering the arrival time difference Δt_d of signals emitted at t_s and $t_s + \Delta t_s$.

of the coalescences per source-frame time per comoving volume [4]

$$\mathcal{R}_c(z) := \frac{dN_c(t_s, V_c(z))}{dt_s dV_c}. \tag{5.36}$$

The volumetric merger rate should be related to the formation rate of the binary system and the distribution for the delay time between the formation and the coalescence of the binary system

$$\mathcal{R}_c(t_c) = \int_{t_c}^{\infty} dt_f \mathcal{R}_f(t_f) p(t_c|t_f; \lambda_f), \tag{5.37}$$

where $\mathcal{R}_f$ is referred to as the binary formation rate and the delay time distribution $p(t_m|t_f; \lambda_f)$ is referred to as the probability density that binary systems formed at lookback time t_f coalesce at lookback time t_c. The delay time distribution should depend on some other parameters λ_f, for example some time scale parameters, some parameters of the binary system and so on. The above equation also can be written in terms of redshift,

$$\begin{aligned} \mathcal{R}_c(t_c(z_c)) &= \int_{z_c}^{\infty} dz_f \frac{dt_f}{dz_f} \mathcal{R}_f(t_f(z_f)) p(t_c(z_c)|t_f(z_f); \lambda_f), \\ &= \int_{z_c}^{\infty} dz_f \frac{dt_f}{dz_f} \mathcal{R}_f(t_f(z_f)) p(t_c(z_c)|t_f(z_f); \lambda_f), \end{aligned} \tag{5.38}$$

where $z_f := z(t_f)$ is the redshift corresponding to a lookback time t_f.

We assume that the volumetric binary formation rate $\mathcal{R}_f(z_f)$, which is the number of the binaries formed at z_f per source-frame time and per comoving volume, is proportional to the star formation rate density described by Madau plot $\psi(z)$ [134] for simplicity, though the volumetric formation rate or the delay time distribution should depend on some properties of the binary systems. Furthermore, we assume the delay-time distribution is uniform in the logarithm of the time delay between the formation and the coalescence,

[4] Mathematically, the definition of the coalescence rate or the star formation rate infer that N may depend on t_d or t_s. However, the dependence of t_d in the redshift rate density and the dependence of t_s in the volumetric coalescence rate are assumed to be naturally dropped because we can assume that the human timescale is short enough.

$$p(t_m|t_f) = p(\log(t_m - t_f)) \propto \begin{cases} 1 & (10\ \mathrm{Myr} < t_f - t_m < 10\ \mathrm{Gyr}) \\ 0 & (10\ \mathrm{Myr} > t_f - t_m \vee t_f - t_m > 10\ \mathrm{Gyr}). \end{cases} \tag{5.39}$$

as population synthesis suggests [135].

Future prospects with the 3G detectors

We produce the source catalog following the binary coalescence rate distribution. Our procedure to produce the catalog is as follows. First, we calculate the volumetric merger rate in the source frame $\mathcal{R}_c(z_c)$ using Eq. (5.38). We then calculate the redshift rate density in the detector frame $R_c(z)$ from Eq. (5.35). As a result, we obtain the binary coalescence rate at redshift z with redshift-bin $\Delta z = 0.1$ by integrating Eq. (5.34). We produce each 5000 sources of $1.4M_\odot - 1.4M_\odot$ BNS and $10M_\odot - 10M_\odot$ BBH following the produced redshift merger distribution. We estimate their model parameters in the model TS1 and obtained the median values of the errors of the additional polarization amplitude parameters within the redshift bin. We denote the median values as $\Delta A_{S1}(z)$. Here, we set the fiducial values of the additional polarization amplitude parameters to be small enough $A_{S1} = 1/1000$ such that the estimation errors give the detection limit. So, the obtained values are the general values independent of their fiducial value settings. It is expected that the errors would be improved statistically from future observations of multiple CBCs. The fisher information matrix appears in the posterior having the form of the multivariate variable normal distribution. We can assume that the errors improve inversely proportional to square root of the expected number of detections N_z at the redshift z,

$$\Delta A_{s,S1}(z) = \frac{\Delta A_{S1}(z)}{\sqrt{N_z}}. \tag{5.40}$$

We calculate the expected number of detections N_z in a redshift bin from $z - \Delta z$ to z as the product of the number of coalesces $N_{c,z}$ in the same redshift

Table 5.10: Parameter estimation results for $1.4M_\odot - 1.4M_\odot$ BNS with an ET-D in a redshift bin from $z - \Delta z$ to z ($\Delta z = 0.1$). Assuming the binary coalescence rate for BNS as 320 $\mathrm{Gpc}^{-3}\mathrm{yr}^{-1}$, observation period 8.68 yr is chosen so that a single BNS is observed within the distance of $z = 0.01$ during the period.

	z=0.1	z=0.2	z=0.3	z=0.4	z=0.5	z=0.6	z=0.7	z=0.8	z=0.9	z=1.0
Detection Probability p_d	1	0.97	0.92	0.85	0.77	0.58	0.48	0.38	0.31	0.28
Merger rate $N_{m,z}$	120	525	1197	2088	3176	4422	5779	7198	8627	10013
Detection rate N_z	120	508	1102	1769	2460	2574	2795	2762	2709	2788
$\Delta A_{S1}/\sqrt{N_z}$ [$\times 10^{-2}$]	1.22	1.16	1.14	1.18	1.23	1.49	1.63	1.95	2.11	2.43

bin calculated above and detection probability at each redshift $p_d(z)$,

$$N_z = N_{c,z} p_d(z). \tag{5.41}$$

The detection probability $p_d(z)$ is the ratio of the number of detections to the total number of binary coalesces at z. We evaluated the detection probability by calculating SNR in a criterion network SNR > 8. Table 5.10 summarizes these procedures for BNS.

Here, when we calculate the binary coalescence rate of BNSs, the overall factor1540 of the star formation rate density is chosen such that a BNS coalesces within $z = 0.01$ during the observation. This corresponds to the observation period of 8.68 yr when we assume the BNS coalescence rate 320 $\mathrm{Gpc}^{-3}\mathrm{yr}^{-1}$ [17]. For BBH, the overall factor of the star formation rate density is determined by an assumption that the binary merger rate for BBH is 23.9 $\mathrm{Gpc}^{-3}\mathrm{yr}^{-1}$ [136]. Fig. 5.15 shows our binary coalescence distribution.

We find the error of the additional polarization amplitude parameter expected from future independent observations of CBCs from [5]

$$\frac{1}{\Delta A^2_{F,S1}} = \sum_z \frac{1}{\Delta A_{s,S1}(z)^2}, \tag{5.42}$$

[5]Note that $p(\boldsymbol{\theta}|\{s_I\}) = N \exp\left\{-\frac{1}{2}\{\sum_I \Gamma_{ij,I}\}\Delta\theta^i\Delta\theta^j\right\} \Rightarrow \{\sum_I \Gamma_I\}^{-1} \simeq \{\sum_I \mathrm{diag}\{1/(\Delta\theta_{1,I})^2, \ldots, 1/(\Delta\theta_{n,I})^2\}\}^{-1} \Rightarrow (\{\sum_I \Gamma_I\}^{-1})^{ii} = 1/(\Delta\theta_i)^2 \simeq (\sum_I 1/(\Delta\theta^2_{i,I}))^{-1}$, when we assume that the degeneracies are broken and we can regard the Fisher information matrix as a diagonal matrix.

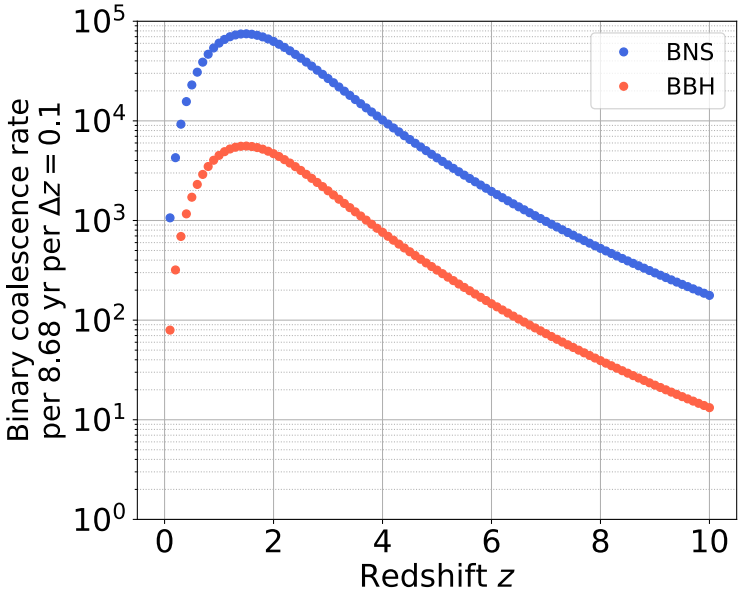

Figure 5.15: CBC rate distribution from Madau plot as a binary formation rate with the delay-time distribution of flat-in-log. The overall factors are determined by the BNS coalescence rate 320 $\mathrm{Gpc}^{-3}\mathrm{yr}^{-1}$ [17] and the BBH coalescence rate 23.9 $\mathrm{Gpc}^{-3}\mathrm{yr}^{-1}$ [136].

as long as ignoring properties of BHs or NSs and the dependence of the additional polarization amplitude on the source properties.

The expected error from future observations of $1.4M_\odot - 1.4M_\odot$ BNS with an ET-D is estimated as

$$\Delta A_{F,S1,ET-D} = 1.62 \times 10^{-3} \times \left(\frac{T_{\rm obs}}{8.68\ {\rm yr}}\right)^{-1/2}. \tag{5.43}$$

On the other hand, the expected error from future observations of $10M_\odot - 10M_\odot$ BBH with ET-D - CE is estimated as

$$\Delta A_{F,S1,ET-D-CE} = 3.15 \times 10^{-4} \times \left(\frac{T_{\rm obs}}{8.68\ {\rm yr}}\right)^{-1/2}, \tag{5.44}$$

and that with ET-D - ET-D is estimated as

$$\Delta A_{F,S1,ET-D-ET-D} = 1.31 \times 10^{-4} \times \left(\frac{T_{\rm obs}}{8.68\ {\rm yr}}\right)^{-1/2}. \tag{5.45}$$

5.5.5 Discussions

Dependence of polarization model

In the analysis, we only deal with the model TS1 consisting of three polarizations to clarify the situation and focus on the basic conditions of polarization separation specific to the 3G detectors. Types of polarizations or geometrical patterns of the radiation cause only the difference of the angular dependence in the signal. The fundamental conditions of polarization separation lead by the median values are not affected by the different angular dependences much as with the case of the 2G detectors in Section 5.4. On the other hand, if we consider more polarization modes and we do not consider more detectors, polarization separation should be harder because of the parameter correlations. However, it is easily expected that the polarizations could be separated with a detector network consisting of more detectors. Even if we consider the other model having different or more polarizations, the polarization modes should be separable with the appropriately enough GW detectors. The number of detectors would be less than the number of the polarization modes thanks to the Earth motion to the GW source. As a result, the above discussion in the

model TS1 can be applied to the other models as well.

Nearby source vs multiple sources

We can expect the statistically improvement of the errors from multiple sources. However, if the sources include very nearby events, the events may dominantly contribute to the statistical error. In order to clarify this, we also conducted parameter estimation for the sources of BNS at $z = 0.01$ whose angular parameters are uniformly random to compare the median value of the estimation error of the additional polarization amplitude with above expected statistical values. We found the median value of the error as

$$\Delta A_{S1} = 1.40 \times 10^{-2}. \tag{5.46}$$

This calculation suggests that we can utilize a near event at $z \simeq 0.01$ for testing GW polarizations with a precision of $\Delta A_{S1} \simeq 1.40 \times 10^{-2}$, while we can use the multiple sources for which the precisions of 1.62×10^{-3} or 4.63×10^{-4} are expected within the period when such a near BNS coalescence event would be observed at least once. The error gets worse as $\Delta A_{S1} \sim 1/\mathrm{SNR} \propto d_L$, while the expected error can be estimated like $\Delta A_{S1} \sim 1/\mathrm{SNR}/\sqrt{N} \propto d_L/\sqrt{d_L^2} \sim$ constant for multiple events in a redshift bin. Hence, combining multiple sources would reduce total expected estimation error ΔA_{S1} by the square root of the number of the bin. The future more direct and robust constrains on the additional polarization amplitude with the 3G detectors are expected to reach comparable level to the current constraint given from PSR B1913+16 Eq. (3.72). Note that the constraint from PSR B1913+16 has been achieved in a weak gravity field much before a CBC.

The additional amplitude should depend on the system properties. In addition, we assume that the error for multiple sources in a redshift bin is statistically improved. It is necessarily to develop a specific method to combine the information from observations of CBCs statistically in the future. A stacking method [137] could be a candidate method to enhance the small non-tensorial modes. A method without the limitation that the deviation from GR can be reduced to the same form for all multiple events is required.

Source distrobution

We did not take into account some parameter distributions of BHs or NSs such as mass, mass ratio and so on for simplicity.

A CE-like detector would be able to observe BBHs at high redshifts depending on the binary masses [138]. A CE can detect more $10M_\odot - 10M_\odot$ BBHs at higher redshifts than an ET-D. However, since an ET-D has a better polarization separability than a CE from their low frequency sensitivity and configuration, the estimated error with ET-D - ET-D network in Eq. (5.45) is less than that with ET-D - CE network Eq. (5.44) for multiple $10M_\odot - 10M_\odot$ BBH sources.

We also calculated the errors in the same way for $30M_\odot - 30M_\odot$ BBHs and verified that we obtained almost the same values. For instance, the median values of the errors at each redshift are $\Delta A_{S1}(z = 0.5) = 5.18 \times 10^{-2}$ and $\Delta A_{S1}(z = 5) = 6.89 \times 10^{-1}$ with ET-D - CE for $30M_\odot - 30M_\odot$ BBHs. For the sake of comparison, those for $10M_\odot - 10M_\odot$ BBH are $\Delta A_{S1}(z = 0.5) = 5.82 \times 10^{-2}$ and $\Delta A_{S1}(z = 5) = 4.18 \times 10^{-1}$. Though an ET-D can detect more $30M_\odot - 30M_\odot$ BBH, there are not many BBH at higher redshift in our redshift distribution. As a result, the mass of BBH around $10M_\odot$ would not affect the expected error much though the amplitude of the scalar mode and the redshift binary distribution may depend on the parameters such as mass.

We also did not consider the other formation channels than isolated field binaries. BBHs formed in globular clusters may have a contribution to the formation rate of the compact binary stars [139–142]. However, it is known that the redshift dependence on the formation rate of BBHs formed in globular clusters would follow similar that of the star formation rate. In this sense, we could say that our analysis would also take into account the contributions from globular clusters. Furthermore, the compact binary stars from population III stars could be considered [143, 144]. While it is unlikely that Population III star will become a BNS, they could produce BBH at high redshift $z > 6$. When we consider a specific formation channel that have different redshift distribution, the precision may be improved with the increase of the events depending on the polarization resolution as such high redshift. In particular, the contributions from population III stars to the numbers of BBHs would be

important for the 3G detectors such as ET-D and CE that are GW detectors with large inspiral range.

Detector development

As mentioned above, the low frequency sensitivity below 5 Hz is crucial in the test. Hence, the challenge is to achieve sensitivity in the low-frequency region. The dominant noise in the lower frequency region below 30 Hz is local gravitational field fluctuations due to the masses moving around the test masses of a detector, which is called Newtonian noise [131, 132]. It has been reported that seismic Newtonian noise [145] and atmospheric Newtonian noise [146] will become dominant in the future ground-based GW detector. So far, as for seismic Newtonian noise, some cancellation schemes utilizing an array of seismometers or tiltmeters [147–149] and passive suppression method [150] have been proposed. On the other hand, local gravitational noise suppression installing detectors underground has also been proposed for atmospheric Newtonian noise [146].

5.5.6 Conclusion

We studied polarization separability and the benefit of the motion of the Earth to the source in the polarization test of GWs from CBCs by the 3G detectors such as ET and CE. Our analysis was based on a parameter estimation using the Fisher information matrix. The mixed polarization models reflecting the geometrical patterns of the radiation consistent with alternative theories of gravity were considered. Table 5.11 shows summary of the results.

As for BNS, even a single ET-D could separate the three polarizations because it can take advantage of the Earth's rotational motion thanks to the better lower-frequency sensitivity below 5 Hz and it adopts three not co-aligned interferometric configuration.

An effective GW detector network along the trajectory of a detector is formed by the time dependent antenna pattern functions. Three polarizations would be probed with a single 3G detector by the effective detector network. However, for a single CE detector, the polarization modes could not be separated because the sensitivity in the low frequency region is not better than

Table 5.11: Summary of the polarization separability of GWs from CBCs with 3G detectors for $1.4M_\odot - 1.4M_\odot$ BNS at $z = 0.1$ or $10M_\odot - 10M_\odot$ BBH at $z = 0.5$ in the model TS1. The median values of the errors for A_{S1} are shown when $A_S = 1$.

	ET-B	ET-D	CE	ET-D - ET-D	ET-D - CE	CE - CE
BNS	inseparable	separable	inseparable	separable	separable	separable
ΔA_{S1}		0.459		0.0797	0.178	0.913
BBH	inseparable	inseparable	inseparable	separable	separable	inseparable
ΔA_{S1}				0.089	0.521	

an ET-D and it has standard one-interferometric configuration. As for BBH, it would be difficult for a single 3G detector to separate three polarizations because of the short signal duration. However, the time-varying effect in the antenna patterns could be partially utilized. Thefore, three polarizations from BBH with around $10M_\odot$ would be separable with two 3G detectors including an ET-D.

Finally, we investigated future statistical prospects considering the CBC redshift distributions. A single golden event (= a nearby BNS coalescence at $z \simeq 0.01$) could be utilized for the polarization test with precisions of 1.40×10^{-2}. On the other hand, the observations of binary systems are available for the polarization test with precisions of 1.62×10^{-3} for BNSs and 4.63×10^{-4} for BBHs within the period in which such golden event would be observed at least once. These precisions are comparable to the current constraints on the deviation from the GR amplitude from the observations of PSR B1913+16. Note that the current constraint has been given much before coalescence, where the gravitational field is weak compared to the inspiral phase before merger.

Chapter 6

Pure polarization search

As we reviewed in Section 3.4, the LVC has conducted polarization tests by analyzing several CBC events in their observing run O1 and O2 in the pure polarization frameworks. In their Bayesian approach, three detector signal models consist of only the scalar, vector, or tensor are prepared. They investigated what types of polarization modes match with the observed signal by evaluating the Bayes factor between scalar or vector model and tensor model that is standard GR. When constructing pure polarization models, they change the antenna pattern functions for the tensor modes to those of the scalar or vector modes but not taking into account the geometrical radiation patterns peculiar to the non-tensorial modes. The inclination dependence may affect the parameter estimations and the Bayes factors. Furthermore, we may be able to take advantage of the dependency difference among the polarization modes when the binary parameters are limited by information from phenomena independent of GW, such as electromagnetic counterpart objects. For example, the location of GW170817 was constrained by the optical and near-infrared electromagnetic counterpart and the inclination angle was also constrained by the associated gamma ray burst. If there are not any limitations for the priors, the analysis tries to reproduce the signal as the parameters (such as the sky position and the orientation of the binary system) freely compensate each other. Thereby, since the range of parameters can be limited in advance utilizing such information, it may be possible to obtain better Bayes factors or observational constraints. In this section, we examine the impact of the geometrical patterns of the radiation in metric theories of gravity on Bayesian inference. We reanalyze GW170814 and GW170817 and test the polarization modes purely with the waveforms consistent with the metric theories of

gravity. As shown in Chapter 5, sufficient number of detectors is required for separation. We target GW170814 and GW170817 because they were first observed by the three GW detectors. For GW170817, we utilize the information about the electromagnetic counterpart and limit the range of the prior of the location and orientation parameters in the polarization modes reflected by the inclination angle difference for more realistic and robust tests.

This chapter is organized as follows. In the first section, we provide the pure polarization models in our analysis and the analytical setups. Next, we give the injection test to verify the bias. Then, we show our results of the pure polarization tests with real data. Finally, we devote the last section to the discussions and conclusions. This chapter is based on [151]. For these results, I conducted research ranging from problem formulation and theoretical calculation to analysis and discussion again.

6.1 Analysis

We conduct pure polarization test using the real detector signal of GW170814 and GW170817 under one of the three hypotheses: pure scalar hypothesis $\mathcal{H}_{\rm S}$, pure vector hypothesis $\mathcal{H}_{\rm V}$ and pure tensor hypothesis $\mathcal{H}_{\rm T}$, in which the detector signal is written as

$$\mathcal{H}_{\rm S}\colon\ h_I(t,\hat{\Omega}) = F_I^b(\hat{\Omega})h_b(t), \tag{6.1}$$

$$\mathcal{H}_{\rm V}\colon\ h_I(t,\hat{\Omega}) = F_I^x(\hat{\Omega})h_x(t) + F_I^y(\hat{\Omega})h_y(t), \tag{6.2}$$

$$\mathcal{H}_{\rm T}\colon\ h_I(t,\hat{\Omega}) = F_I^+(\hat{\Omega})\frac{1+\cos^2\iota}{2}h_{+,\rm GR}(t) + F_I^\times(\hat{\Omega})\cos\iota\, h_{\times,\rm GR}(t), \tag{6.3}$$

where the phase evolution of the non-tensorial polarization modes is assumed to be those of the tensor modes,

$$h_b(t) = \sin^2\iota\, h_{+,\rm GR}, \tag{6.4}$$

$$h_x(t) = \sin 2\iota\, h_{+,\rm GR}(t), \tag{6.5}$$

$$h_y(t) = \sin\iota\, h_{\times,\rm GR}(t). \tag{6.6}$$

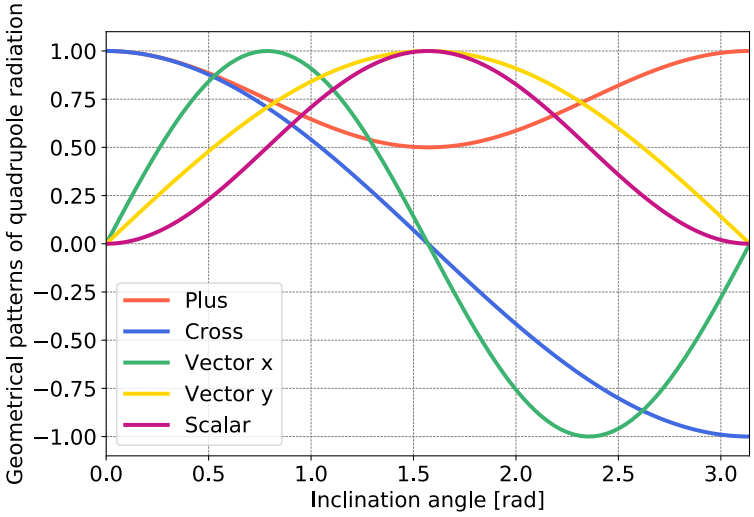

Figure 6.1: Geometrical patterns of the GW quadrupole radiation for the tensorial and non-tensorial polarization modes.

In $\mathcal{H}_{\rm S}$, we can consider only the breathing mode because of the inseparability from the degeneracy of the antenna pattern functions between the breathing and the longitudinal mode.

Fig. 6.1 shows the geometrical patterns of the quadrupole radiation.

We conduct Bayesian inference to estimate source parameters $\boldsymbol{\theta}$ under one of three hypotheses. In the analysis, the total parameters are

$$\boldsymbol{\theta} = (\alpha, \delta, \iota, \psi, d_L, t_{\rm c}, \phi_{\rm c}, m_1, m_2, \chi_1, \chi_2, \Lambda_1, \Lambda_2). \tag{6.7}$$

where α and δ are the right ascension and declination of the binary, ι is the inclination angle, ψ is the polarization angle, and d_L is the luminosity distance. $t_{\rm c}$ and $\phi_{\rm c}$ is the time and phase at coalescence, respectively. m_1 and m_2 are detector-frame component masses. χ_1 and χ_2 are dimensionless spin parameters. Λ_1 and Λ_2 are tidal deformability parameters.

In the Bayesian approach, the posterior probability distribution is calculated through the Bayes' theorem as described in Chapter 4. For the sake of clarity, we rewrite the basic expressions under the setting here. The Bayes'

theorem can be written as

$$p(\boldsymbol{\theta}|\{d_I\}_{I=1}^N, \mathcal{H}_{\rm X}) = \frac{p(\boldsymbol{\theta})p(\{d_I\}_{I=1}^N|\boldsymbol{\theta}, \mathcal{H}_{\rm X})}{p(\{d_I\}_{I=1}^N|\mathcal{H}_{\rm X})}, \tag{6.8}$$

where X denotes S, V or T. $p(\boldsymbol{\theta})$ is a prior probability distribution. We apply the standard prior used by the LVC [24]. The prior on (α, δ) is isotropic. The prior on (ι, ψ) is determined such that the orbital angular momentum is isotropically distributed. The prior on d_L is proportional to d_L^2, which is based on the assumption that the binary systems are uniformly distributed in comoving volume. The priors on $t_{\rm c}$, $\phi_{\rm c}$, m_1 and m_2 are uniform. The prior on χ_1 and χ_2 is aligned-z prior, with the range of $-0.99 < \chi_1, \chi_2 < 0.99$. The priors on Λ_1 and Λ_2 are $\delta(\Lambda_1, \Lambda_2)$ for GW170814 based on the assumption that it is a BBH event and uniform over $\Lambda_1, \Lambda_2 < 5000$ for GW170817.

We adopt the standard Gaussian noise likelihood Eq. (4.5) for a likelihood function $p(\{d_I\}_{I=1}^N|\boldsymbol{\theta}, \mathcal{H}_{\rm X})$. The lower cutoff frequency for the likelihood calculations is 20 Hz for GW170814 and 23 Hz for GW170817, which are also used by the LVC [24, 152].

$p(\{d_I\}_{I=1}^N|\mathcal{H}_{\rm X})$ denotes the evidence, which is an indicator showing how much the hypothesis $\mathcal{H}_{\rm X}$ is preferred from the observed data. In the model selection between the hypotheses $\mathcal{H}_{\rm X}$ and $\mathcal{H}_{\rm Y}$, we evaluate the Bayes factor defined by the ratio of two evidences,

$$B_{\rm XY} := \frac{p(\{d_I\}_{I=1}^N|\mathcal{H}_{\rm X})}{p(\{d_I\}_{I=1}^N|\mathcal{H}_{\rm Y})}. \tag{6.9}$$

We generate thousands of random samples following the posterior distribution and make their histograms, in order to obtain the probability density distributions of the model parameters. In our definition, the large Bayes factors $B_{\rm TS}$ and $B_{\rm TV}$ suggest that GR is preferred in comparison with the pure scalar and vector models.

We utilize the Bilby software [153, 154] and the cpnest sampler [155], which is one of the implementations of the nested sampling technique [114], for the calculations of the posterior distribution and the evidence. We apply IMRPhenomD [127] for GW170814 and IMRPhenomD_NRTidal [156] for GW170817 as the waveforms in GR. As mentioned in Chapter 5, the waveforms of the

polarization modes in the merger and ringdown phase beyond GR are not well known because it is difficult to derive them even in GR due to the complexity and non-linearity of the field equations. In the merger and the ringdown phase that is strong gravity regime, the waveforms of the non-tensorial polarizations may be heavily deformed. However, we include the merger and ringdown phase here for comparison with the LVC results.

The generation of templates is computationally costly for a BNS. To make the analysis speed up, we utilize the technique of the focused reduced order quadrature [157], in which the reduced order quadrature basis vectors [158,159] of templates are constructed within a narrow range of the chirp mass.

6.2 Injection test for bias from inclination dependence

Here, we investigate the bias from the inclination dependence of the geometrical factors on the Bayesian parameter estimation by injection tests.

In the framework of the pure vector theory, we inject a signal with the true vector radiation pattern and but analyze the injected signal by a signal model with the vector antenna pattern functions, but with the tensor radiation pattern. This situation corresponds to the previous analysis by the LVC. The difference between the injected signal and the search model is only the inclination angle dependence of the radiation.

The injected parameters are set to be similar parameters to GW170814: the component masses in the source-frame, $m_1 = 30.5\ M_\odot$ and $m_2 = 25.3\ M_\odot$, the luminosity distance $d_L = 540$ Mpc, the inclination angle $\iota = 75$ deg $= 1.31$ rad, the right ascension $\alpha = 0.83$ rad, and the declination $\delta = -0.78$ rad. Fig. 6.2 shows the results of the Bayesian inference with $\iota = 75$ deg. It shows that the analysis could cause some biases without appropriate geometrical dependence. In this case, a larger amount of vector modes is radiated as shown in Fig. 6.1. However, since the search template has the tensor inclination dependence, the parameters try to compensate such large amplitude. Consequently, the luminosity distance is estimated to be smaller than the true value. The chirp mass in the source frame is also estimated toward a larger value than the true

value.

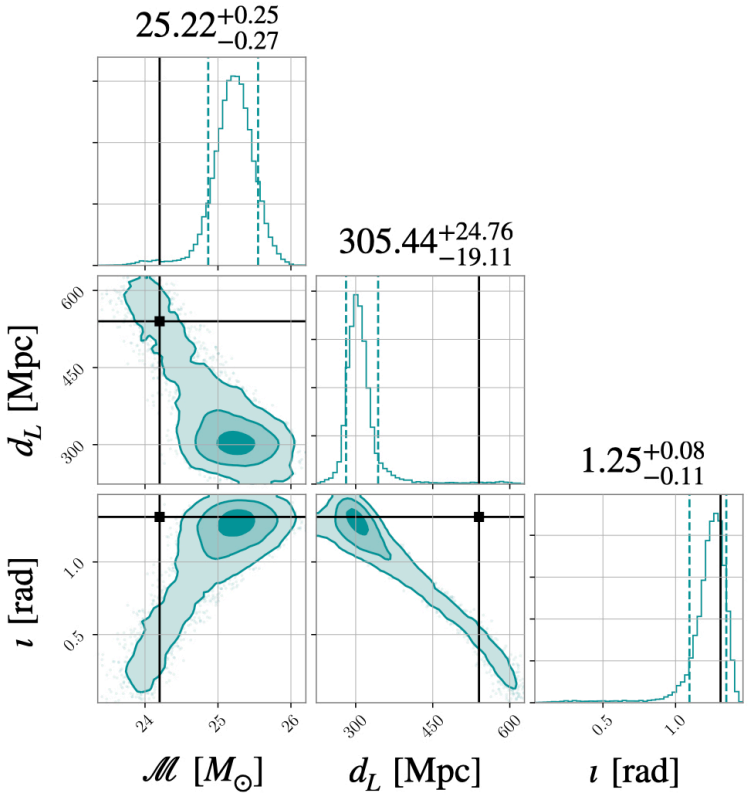

Figure 6.2: The posterior probability distributions for the chirp mass in the source frame, the luminosity distance, and the inclination angle are shown with a signal injection in the pure vector theory. We inject a BBH signal with $\iota = 75$ deg $= 1.31$ rad with the geometrical patterns of the vector quadrupole radiation but analyze the injected signal with the geometrical patterns of the tensor quadrupole radiation. The black lines show the injected true values. The vertical dotted lines show the 90% confidence intervals.

6.3 Real data analysis

Here, we analyze the real data of GW170814 and GW170817 in the pure polarization framework. We use the data of GW170814 with the duration 4 seconds and sampling frequency 4096 Hz and the data of GW170817 with the removal of glitch, the duration 128 seconds, the sampling frequency 4096 Hz

from Gravitational Wave Open Science Center [160]. In the real data analysis of Chapter 6 and Chapter 7, we consider only the statistical error because we expect the systematic biases to be significantly smaller than the statistical error as in [16]. 5% in amplitude 3° in phase calibration errors were reported over the frequency range $20 - 1024$ Hz in O1 and O2 [161]. The statistical error in amplitude can be estimated by 1/SNR. It is true for the current detectors that the systematical error is sufficiently smaller than the statistical error and we can expect that the affect of the calibration error on the parameter estimation of the binary parameters can be small. Bayesian analysis including the effect of the calibration uncertainties on the received signal, which will be needed in the future, is the future work.

6.3.1 GW170814

We perform the model selection of GW170814 under $\mathcal{H}_{\rm S}$, $\mathcal{H}_{\rm V}$, and $\mathcal{H}_{\rm T}$. Figs. 6.3 and 6.4 shows the results. Fig. 6.3 shows the posterior distributions for the chirp mass in the source frame, the luminosity distance, and the inclination angle and Fig. 6.4 shows the posterior distributions for the right ascension (RA) and the declination (DEC). The results under $\mathcal{H}_{\rm T}$ (GR) are shown in red, $\mathcal{H}_{\rm V}$ in blue, and $\mathcal{H}_{\rm S}$ in green.

Fig. 6.3 shows that the inclination angles under each polarization hypotheses are estimated to different values reflecting the geometrical patterns of the quadrupole radiation. The luminosity distance under $\mathcal{H}_{\rm V}$ is estimated to slightly larger value than under $\mathcal{H}_{\rm T}$ and $\mathcal{H}_{\rm S}$ because the luminosity distance and the inclination angle are correlated each other strongly as we saw in Chapter 5 and they try to compensate each other. The slightly larger luminosity distance leads the smaller chirp mass in the source frame. The RA and DEC also compensate the change in the values of other parameters through the antenna pattern functions.

As a result, we obtain the logarightms of the Bayes factors $\ln B_{TS} = 3.636$ and $\ln B_{TV} = 2.775$, which support the pure tensor hypothesis that is GR.

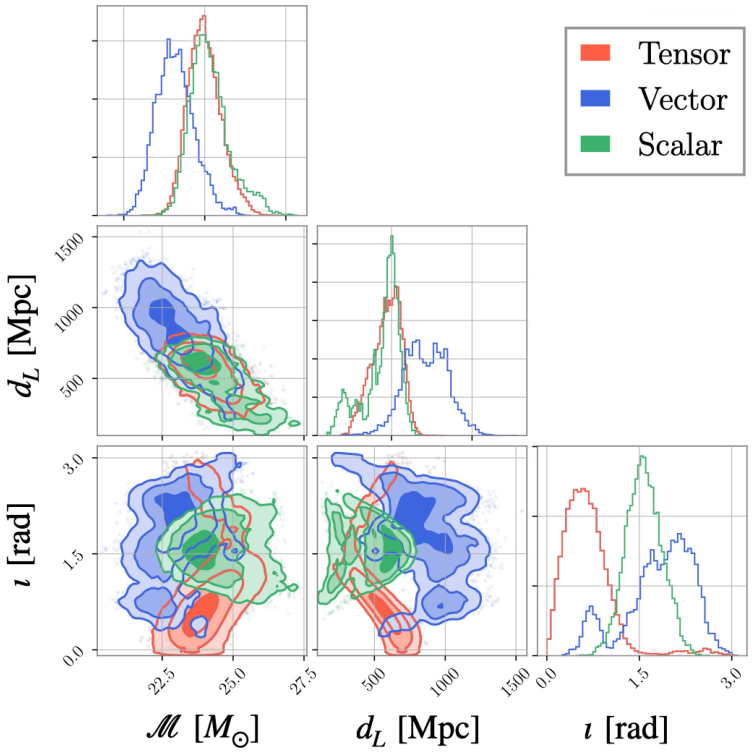

Figure 6.3: The posterior probability distributions of GW170814 for the chirp mass in the source frame, the luminosity distance, and the inclination angle under the three pure polarization hypotheses with the radiation patterns in the metric theories of gravity. The results under $\mathcal{H}_{\rm T}$ (GR) are shown in red, $\mathcal{H}_{\rm V}$ in blue, and $\mathcal{H}_{\rm S}$ in green.

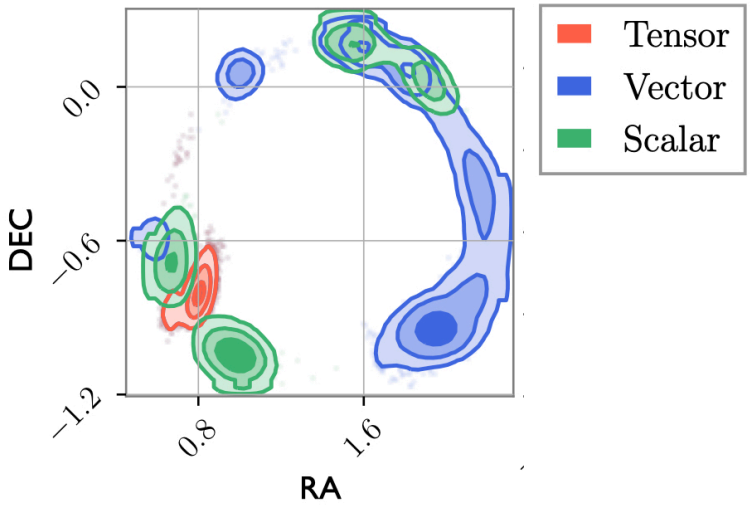

Figure 6.4: The posterior probability distributions of GW170814 for the RA and the DEC under the three pure polarization hypotheses with the radiation patterns in the metric theories of gravity. The results under $\mathcal{H}_{\rm T}$ (GR) are shown in red, $\mathcal{H}_{\rm V}$ in blue, and $\mathcal{H}_{\rm S}$ in green.

6.3.2 GW170817

The electromagnetic counterparts of GW170817 were reported. An optical [162] and near-infrared [163] electromagnetic counterpart was localized to the galaxy NGC 4993 half a day after the GW170817 event [164]. From the localization, we can impose the location prior on the luminosity distance, the right ascension, and the declination in our polarization analysis. We utilize this information about the location and orientation of the binary system. We set the Gaussian prior of the luminosity distance with the mean of 42.9 Mpc and the standard deviation of 3.2 Mpc. We also fix the right ascension and the declination as RA = 13h09m48s.085 and DEC = $-23°22'53''.343$ [164]. In the previous test by the LVC for GW170817, the sky location of GW170817 is constrained to NGC 4993.

The Fermi Gamma-ray Burst Monitor [165], and the Anti-Coincidence Shield for the Spectrometer for the International Gamma-Ray Astrophysics Laboratory [166] also observe the gamma-ray burst, GRB 170817A independently. GRB 170817A was confirmed with high statistical significance in

relation to GW170817 [164]. The estimation of the jet by hydrodynamics simulations gives the constraint on the orientation of the binary system as $0.25 \text{ rad} < \theta_{\rm obs}(d_L/41 \text{ Mpc}) < 0.45 \text{ rad}$ [167, 168] where $\theta_{\rm obs}$ is the viewing angle. It can be identified with the inclination angle, $\theta_{\rm obs} = \iota$ or $\theta_{\rm obs} = \pi - \iota$, from the assumption that the jet is orthogonal to the orbital plane of the binary system. We adopt the relation $\theta_{\rm obs} = \pi - \iota$ from the estimation of the inclination angle for GW170817. We set the prior on the inclination angle in the range of $2.68\,\text{rad} < \iota < 2.92\,\text{rad}$ optionally. This range can be estimated from the range of our prior on the luminosity distance. We call this prior the jet prior hereafter.

In the following, we perform the model selection of GW170817 under $\mathcal{H}_{\rm S}$, $\mathcal{H}_{\rm V}$, and $\mathcal{H}_{\rm T}$ just like in the above analysis of GW170814. However, we impose the priors on the luminosity distance, the right ascension, and the declination from the host galaxy, NGC4993 for all analysis and impose the priors of the inclination angle from the gamma ray burst, GRB170817A optionally.

Without jet prior

Fig. 6.5 shows the posterior probability distributions for the chirp mass in the source frame, the luminosity distance, and the inclination angle, under the pure polarization hypotheses. Again, the results under $\mathcal{H}_{\rm T}$ (GR) are shown in red, for $\mathcal{H}_{\rm V}$ in blue, and for $\mathcal{H}_{\rm S}$ in green.

The amplitude parameters in the pure vector polarizations are determined better than GR. The difference is caused by the degeneracy between the polarization angle and the phase at the coalescence time in GR when the binary system is nearly face-on. Even under $\mathcal{H}_{\rm V}$, there is the degeneracy between the polarization angle and the phase at the coalescence time when the nearly face-on. However, the radiation pattern specific to the non-tensorial polarizations infer that the binary system is estimated to nearly edge-on binary under $\mathcal{H}_{\rm V}$. Then, the degeneracy is broken and the amplitude parameters are well determined. Under $\mathcal{H}_{\rm S}$, the signal does not depend on the polarization angle to begin with due to its rotational symmetry around the propagation direction.

In Fig. 6.5, the luminosity distance under $\mathcal{H}_{\rm S}$ is estimated to be significantly small from the difference of the antenna pattern functions. The antenna

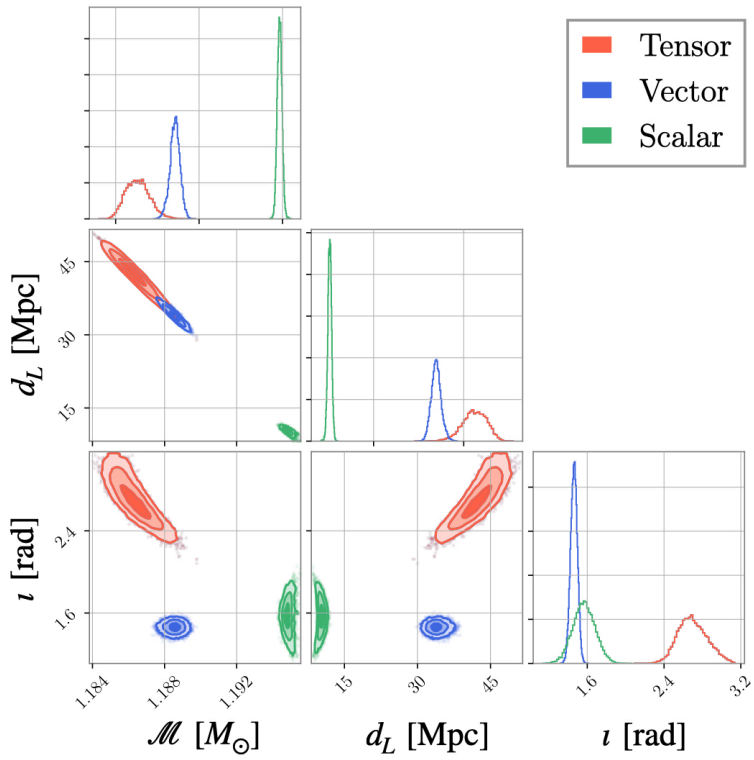

Figure 6.5: The posterior probability distributions of GW170817 for the chirp mass in the source frame, the luminosity distance, and the inclination angle under the three pure polarization hypotheses with the radiation patterns in the metric theories of gravity. The results under $\mathcal{H}_{\rm T}$ (GR) are shown in red, $\mathcal{H}_{\rm V}$ in blue, and $\mathcal{H}_{\rm S}$ in green. The priors on the luminosity distance, the RA, and the DEC from NGC4993 are imposed but not imposing the jet prior.

pattern function for the scalar mode is 2-6 times smaller than those of the tensor and vector modes at the fixed sky location. Consequently, the luminosity distance needs to be small to compensate the small values of the antenna pattern function.

As a result, we obtain the logarightms of the Bayes factors $\ln B_{TS} = 43.953$ and $\ln B_{TV} = 21.417$, which more strongly supports the pure tensor hypothesis that is GR. In particular, when we compare GR with the scalar hypothesis, GR is strongly preferred. It is assumed that this is because there is only one polarization component and there are few degrees of freedom to compensate among the parameters under $\mathcal{H}_{\rm S}$.

With jet prior

Fig. 6.6 shows the posterior probability distributions for the chirp mass in the source frame, the luminosity distance, and the inclination angle, under the pure polarization hypotheses considering the jet prior. Again the results for $\mathcal{H}_{\rm T}$ (GR) are shown in red, for $\mathcal{H}_{\rm V}$ in blue, and for $\mathcal{H}_{\rm S}$ in green.

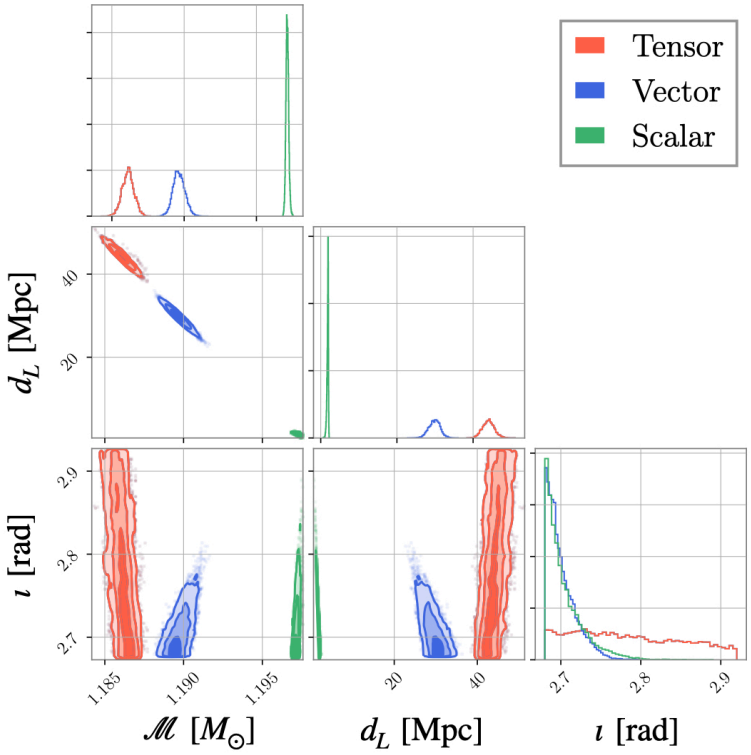

Figure 6.6: The posterior probability distributions of GW170814 for the chirp mass in the source frame, the luminosity distance, and the inclination angle under the three pure polarization hypotheses with the radiation patterns in the metric theories of gravity and the jet prior. The priors on the luminosity distance, the RA, and the DEC from NGC4993 are imposed and the jet prior is also imposed.

The inclination angle is estimated around the lower bound under $\mathcal{H}_{\rm S}$ and $\mathcal{H}_{\rm T}$ because of the jet prior. We find the similar trend in Fig. 6.6 to in Fig. 6.5 though the estimated luminosity distance slightly changes from the estimated values of the inclination angle.

As a result, we find the logarightms of the Bayes factors $\ln B_{TS} = 60.271$ and $\ln B_{TV} = 51.043$, which strongly support the pure tensor hypothesis that is GR.

In general, the posterior distributions of the inclination angle under the pure polarization hypotheses are different each other from the difference of the geometrical patterns of the radiation. However, we can impose the additional priors on the location and the orientation utilizing the information about a host galaxy and a jet for an event with the electromagnetic counterpart. The fact that we observed the associated jet from the binary neutron stars indicates that the binary system is a nearly face-on binary. However, as Fig. 6.1 shows, the non-tensorial polarization modes are not radiated from such a nearly face-on binary much. Therefore, binary neutron star events with jets are strong tool to distinguish the pure polarization theories. In consequence, we can obtain the stronger constraints on the beyond-GR polarization components.

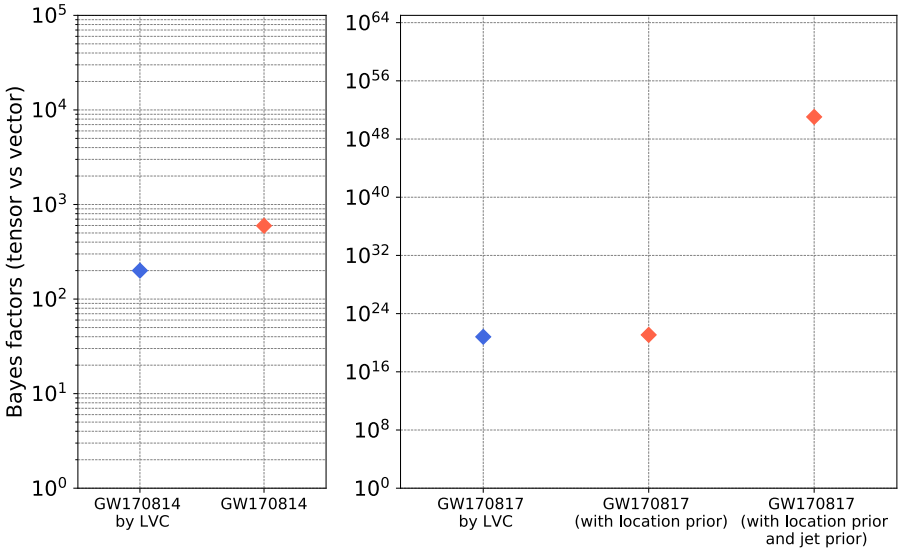

Figure 6.7: The Bayes factors between the pure tensor and the pure vector polarization hypothesis. The results by LVC for GW170814 [16] and for GW170817 [44] are referred in blue.

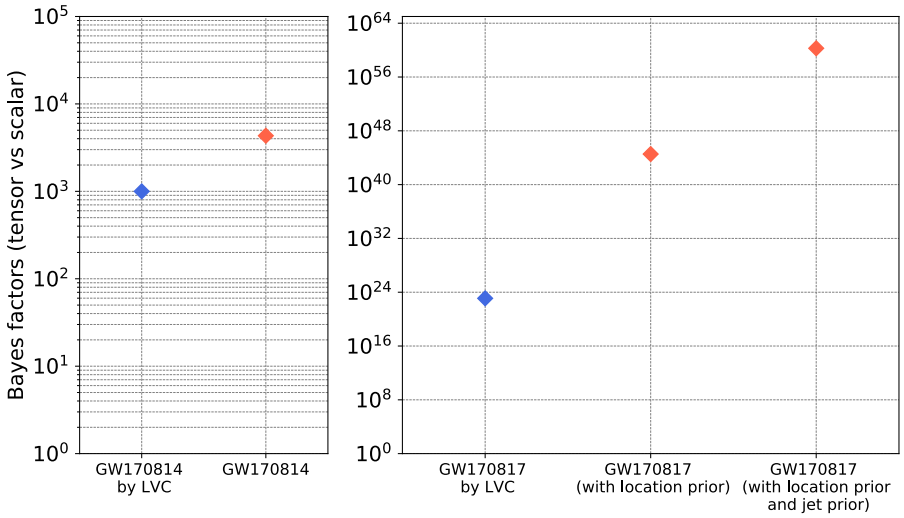

Figure 6.8: The Bayes factors between the pure tensor and the pure scalar polarization hypothesis. The results by LVC for GW170814 [16] and for GW170817 [44] are referred in blue.

6.4 Discussions and conclusion

We investigated the effect of the geometrical patterns of the non-tensorial radiations in the pure polarization tests. We showed that the estimated values of the amplitude parameters are potentially biased when adopting the radiation patterns for the tensor polarization modes in GR. Furthermore, we tested the polarizations of GW170814 and GW170817 under the three pure polarization hypotheses with the non-tensorial radiation patterns in which only scalar, vector or tensor polarization modes are allowed.

Figures 6.7 and 6.8 show the summary of the obtained Bayes factors for GW170814 and GW170817 of the scalar or vector hypotheses against the tensor hypothesis. For GW170814, we found the logarithms of the Bayes factors of 2.775 and 3.636 between the pure tensor polarization, and the pure vector or scalar polarizations, respectively. The values of the Bayes factors are consistent with the previous results by the LVC, though the estimated parameters are biased. For GW170817, we took advantage of the information about the location and the orientation of the binary system from the electromagnetic counterparts. For GW170817 accompanied by the optical, infrared, and

gamma ray burst electromagnetic counterparts, we found the logarithms of the Bayes factors of 21.417 and 43.953 between the pure tensor polarization, and pure vector or scalar polarization with the location prior, respectively. They are improved to 51.043 and 60.271, respectively, additionally imposing the jet prior. These Bayes factors are significantly improved in comparison with the previous results by the LVC. Note that the non-tensorial radiation mechanism may differ for the sources such as the BBHs and the BNSs. Therefore, it is difficult to simply compare the results of the BBH and the BNS.

On the other hand, almost all metric theories of gravity predict the mixed polarization modes composed of the non-tensorial modes in addition to tensor modes. A nearly face-on binary with the observation of the jet is important in terms of bringing information about the location and orientation of a binary in advance. Due to the difference in the radiation patterns between tensor modes and non-tensor modes, BNS events with electromagnetic counterparts will continue to be utilized for strong pure polarization tests. However, the amplitudes of the radiated non-tensorial modes from such a nearly face-on binary system are expected to be relatively small from the inclination dependence. In other words, an edge-on binary could be crucial in search for the mixed polarizations. We will describe the first direct mixed polarization search in the next chapter.

Chapter 7

Scalar-tensor mixed polarization search

In this chapter, we search for a mixed polarizations of GW170814 and GW170817.

The polarization tests of the GWs from CBCs based on the Bayesian inference have been conducted in the frameworks of the pure polarization modes by the LVC so far. In other words, the Bayesian model selections between GR and the artificial gravity theory allowing only scalar or vector polarization modes have been performed as discussed in the previous chapter.

However, almost all realistic alternative theories of gravity predict tensor modes along with vector and/or scalar polarization states as we introduced in Chapter 3. The detector signal would be composed of a mixture of tensor and non-tensorial polarization modes. Here, we search for the mixed scalar-tensor polarizations and evaluate the additional polarization amplitude for the scalar mode for GW170814 and GW170817. This is the first direct search for the mixture of the polarization modes of the GWs from CBCs based on the Bayesian approach. We target GW170814 and GW170817 because they were first observed by the GW detector network of three detectors. As we revealed in Chapter 5, it is expected that the event observed by three detectors can be utilized to test the theory allowing three polarization modes.

This chapter is organized as follows. In the first section, we show the scalar-tensor polarization model used in the analysis and the analytical setups. Then, we provide our results of the scalar-tensor polarization search. Finally, we present the discussions and conclusions. For these results, I conducted research ranging from problem formulation and theoretical calculation to analysis and discussion again.

7.1 Analysis

We analyze the data of GW170814 and GW170817 in a scalar-tensor polarization framework. As with the case of the pure scalar model in Chapter 6 we only consider the breathing mode because the two scalar polarizations are completely degenerated. Thus, we analyze the data under the scalar-tensor hypothesis $\mathcal{H}_{\rm ST}$ in which the detector signal is consist of two tensor modes and one scalar mode as

$$\begin{aligned}\mathcal{H}_{\rm ST}\colon\ h_I(t,\hat{\Omega}) =& F_I^{+}(\hat{\Omega})\frac{1+\cos^2\iota}{2}(1+\delta A)h_{+,\rm GR}(t)e^{i\delta\Psi}\\ &+ F_I^{\times}(\hat{\Omega})\cos\iota(1+\delta A)h_{\times,\rm GR}(t)e^{i\delta\Psi}\\ &+ F_I^{s=b}(\hat{\Omega})A_S\sin^2\iota h_{+,\rm GR}(t)e^{i\delta\Psi},\end{aligned} \tag{7.1}$$

where the dependence of the antenna pattern functions and the inclination angle dependence are independent of a specific theory of gravity again. Here, $h_{+,\rm GR}(t)$ and $h_{\times,\rm GR}(t)$ are the GW waveforms of CBCs for plus and cross modes in GR whose inclination dependence is dropped for convenience. A_S denotes the additional polarization amplitude parameter for the scalar mode. δA and $\delta\Psi$ are the amplitude and the phase corrections from the additional scalar radiation. When we consider additional scalar radiation $A_S\sin^2\iota h_{+,\rm GR}(t)$ in addition to two tensor modes in GR, the change rate of the binding energy is modified as

$$\begin{aligned}\dot{E} &= \frac{r^2}{32\pi}\int d\Omega\langle\dot{h}_{ij}\dot{h}^{ij}\rangle\\ &= \dot{E}^{(\rm GR)} + \frac{r^2}{16\pi}\int d\Omega[\sin^4\iota\dot{h}_{+}^2]\\ &= \dot{E}^{(\rm GR)} + \frac{2}{15}A_S^2 r^2\dot{h}_{+}^2,\end{aligned} \tag{7.2}$$

where $\dot{E}^{(\rm GR)}$ is the change rate of the binding energy in GR

$$\begin{aligned}\dot{E}^{(\rm GR)} &= \frac{r^2}{16\pi}\int d\Omega\left[\frac{1+\cos^2\iota}{4}\dot{h}_{+}^2+\cos^2\iota\dot{h}_{\times}^2\right]\\ &= \frac{1}{5}r^2\dot{h}_{+}^2.\end{aligned} \tag{7.3}$$

Thus, the above binding energy change rate can be rewritten as

$$\dot{E} = \dot{E}^{(\mathrm{GR})} \left[1 + B \left(\frac{m}{r}\right)^q\right], \tag{7.4}$$

with $q = 0$ and $B = (2/3)A_S^2$. Comparing this with Eq. (3.59), we find the amplitude correction δA and the phase correction $\delta\Psi$ as

$$\delta A = -\frac{1}{3}A_S^2, \tag{7.5}$$

and

$$\delta\Psi = \frac{1}{64}A_S^2(\pi\mathcal{M}f)^{-5/3}. \tag{7.6}$$

Finally, we obtain the expressions in Eq. (7.1) up to leading order in terms of A_S.

Here, we focus on only inspiral phase, while the large corrections might be expected in the merger and ringdown phase, which are stronger gravity regime because the waveforms in the merger and ringdown phase are still unknown. It is difficult to calculate the waveforms in the merger and ringdown phase even in GR. For these reasons, we employ the inspiral waveforms in GR to keep the results robust and model-independent.

We conduct search for the mixed scalar-tensor polarization modes using the real detector signal of GW170814 and GW170817 under the scalar-tensor hypothesis $\mathcal{H}_{\mathrm{ST}}$ whose signal is expressed as Eq. (7.1). In the analysis, the total parameters are

$$\boldsymbol{\theta} = (\alpha, \delta, \iota, \psi, d_L, t_{\mathrm{c}}, \phi_{\mathrm{c}}, m_1, m_2, \chi_1, \chi_2, \Lambda_1, \Lambda_2). \tag{7.7}$$

where each parameter represents the same physical quantity as in Chapter 6.

Here, the Bayes ' theorem can be written as

$$p(\boldsymbol{\theta}|\{d_I\}_{I=1}^N, \mathcal{H}_{\mathrm{ST}}) = \frac{p(\boldsymbol{\theta})p(\{d_I\}_{I=1}^N|\boldsymbol{\theta}, \mathcal{H}_{\mathrm{ST}})}{p(\{d_I\}_{I=1}^N|\mathcal{H}_{\mathrm{ST}})}. \tag{7.8}$$

$p(\boldsymbol{\theta})$ represents the prior probability distribution.

Furthermore, as in Chapter 6, we also adopt the standard priors used by the LVC [24] and we apply the standard Gaussian noise likelihood [24] again. The

lower frequency cutoff for the likelihood calculations is 20 Hz for GW170814 and 23 Hz for GW170817 [24, 152] again. We utilize the Bilby software and the cpnest sampler for the Bayesian inference here again.

As a template for the inspiral waveforms, we apply TaylorF2 [169] for GW170814 and TaylorF2_NRTidal [156] for GW170817. For GW170817, we utilize the focused reduced order quadrature technique for quick calculations again.

7.2 Real data analysis

Here, we analyze the real data of GW170814 and GW170817 in the scalar-tensor polarization model. The data used in the analysis is same as in Chapter 6. From Gravitational Wave Open Science Center [160], the data of GW170814 has the 4 seconds duration and the sampling frequency 4096 Hz and the data of GW170817 with the removal of glitch has the 128 seconds duration and the sampling frequency 4096 Hz.

7.2.1 GW170814

We perform the Bayesian inference for GW170814 under $\mathcal{H}_{\rm ST}$. The posterior probability distribution under $\mathcal{H}_{\rm ST}$ for the chirp mass in the source frame, the luminosity distance, and the inclination angle are shown in Fig. 7.1. We also perform the Bayesian inference for GW170814 under GR where we use the TaylorF2 template for comparison. The posterior probability distributions under GR are shown in Fig. 7.2. The posterior probability distribution of the right ascension and the declination are shown in Fig. 7.3 under $\mathcal{H}_{\rm ST}$ in blue. The results in GR are also shown in red for comparison. The vertical dashed lines show the 90% confidence intervals. These estimated amplitude parameters are mostly the same between GR and the scalar-tensor model.

The estimated additional scalar polarization amplitude for GW170814 under $\mathcal{H}_{\rm ST}$ is shown in Fig. 7.1. We obtain the additional scalar amplitude as $-0.08^{+0.59}_{-0.57}$. The phase for the scalar mode and the other phase parameters such as ψ and ϕ are correlated each other strongly. Hence, it is difficult to determine the phase of the scalar mode and the distribution of the additional

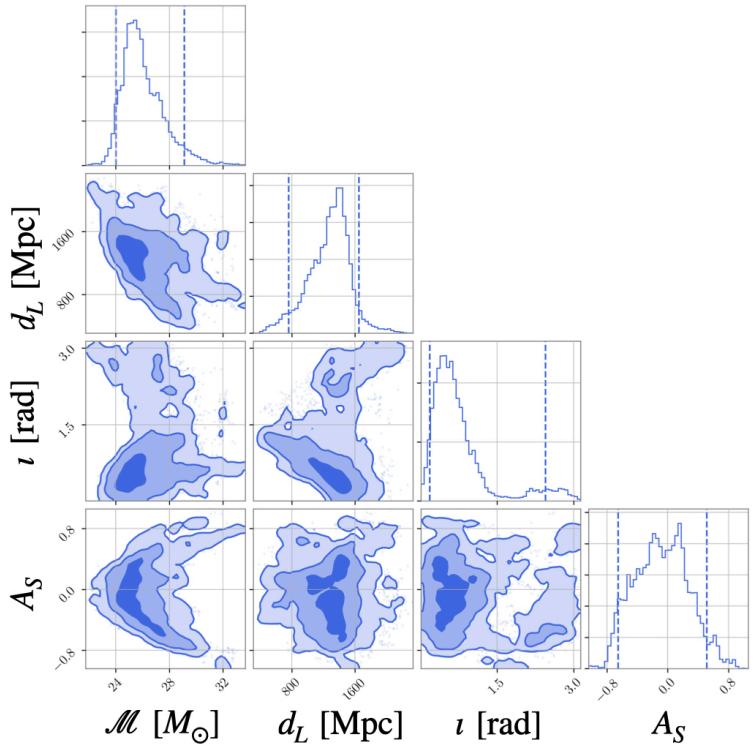

Figure 7.1: The posterior probability distributions of the chirp mass in the source frame, the luminosity distance, and the inclination angle for GW170814 under the scalar-tensor hypothesis $\mathcal{H}_{\rm ST}$.

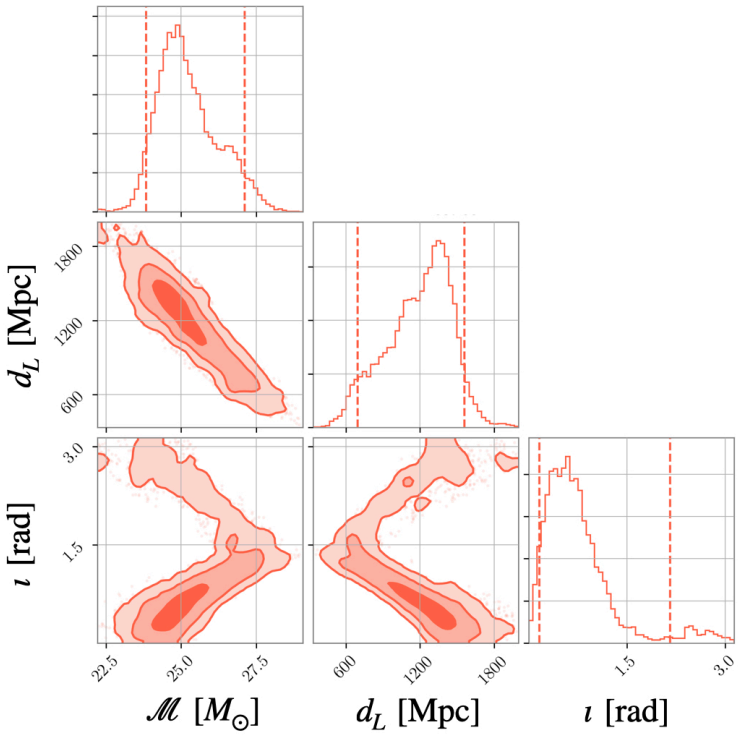

Figure 7.2: The posterior probability distributions of the chirp mass in the source frame, the luminosity distance, and the inclination angle for GW170814 under GR.

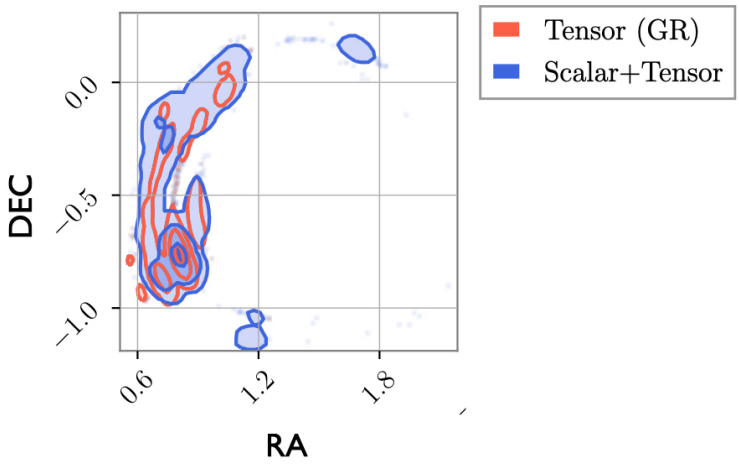

Figure 7.3: The posterior probability distributions of the right ascension and the declination for GW170814. The results under the scalar-tensor hypothesis $\mathcal{H}_{\rm ST}$ are shown in blue and those under GR in red.

scalar amplitude become symmetry in general. However, the symmetry can be broken when the SNR is low. The constraint on the scalar polarization amplitude except for the dependence of the luminosity distance and the inclination angle can be translated into the constraint on the amplitude ratio between the tensor modes and the scalar mode defined by

$$R_{ST} := \frac{A_{\rm S} \sin^2 \iota}{\sqrt{(1+\cos^2 \iota)^2/4 + \cos^2 \iota}}. \tag{7.9}$$

For GW170814, we find the constraint on R_{ST} as

$$R_{ST} = -0.02^{+0.16}_{-0.15}. \tag{7.10}$$

The results are consistent with GR inferring the zero-consistent small additional amplitude. This is thought to be because if more scalar waves are radiated, the tensor mode is greatly deformed and the observed signal cannot be explained. Concomitantly, the amplitude parameters and the location parameters are hardly changed.

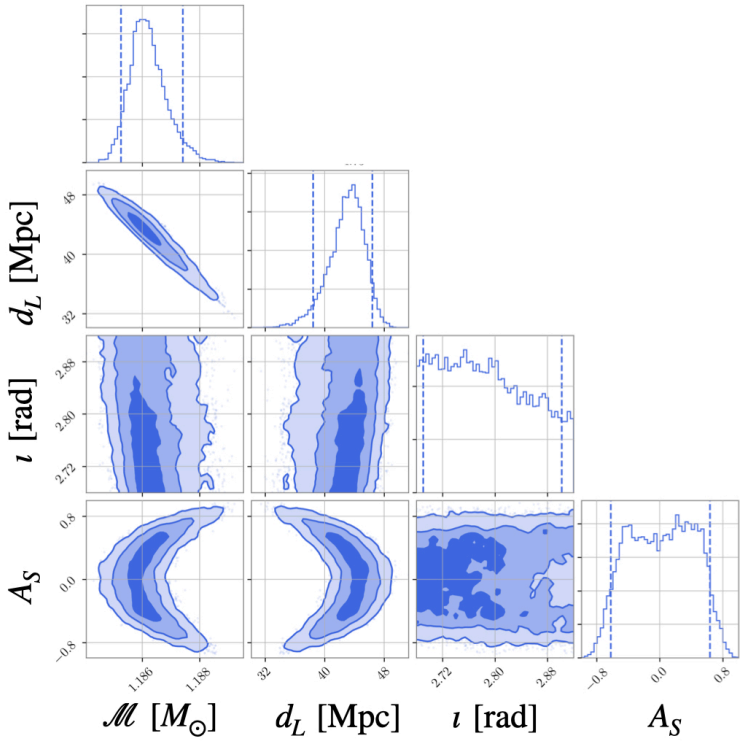

Figure 7.4: The posterior probability distributions of the chirp mass in the source frame, the luminosity distance, and the inclination angle for GW170817 under the scalar-tensor hypothesis $\mathcal{H}_{\rm ST}$.

7.2.2 GW170817

In the analysis of GW170817, we utilize the location prior and the jet prior from electromagnetic observations used in the pure polarization tests above again. The sky location is fixed to RA = 13h09m48s.085 and DEC = $-23°22'53''.343$, and the prior for the luminosity distance is the Gaussian distribution with the mean 42.9 Mpc and the standard deviation 3.2 Mpc. In addition, this location prior, the orientation is limited by the jet prior in the range of $2.68\,\mathrm{rad} < \iota < 2.92\,\mathrm{rad}$.

We perform the Bayesian inference for GW170814 under $\mathcal{H}_{\rm ST}$ with the location prior and the jet prior. The posterior probability distribution under $\mathcal{H}_{\rm ST}$ for the chirp mass in the source frame, the luminosity distance, and the inclination angle are shown in Fig. 7.4. We also perform the Bayesian inference

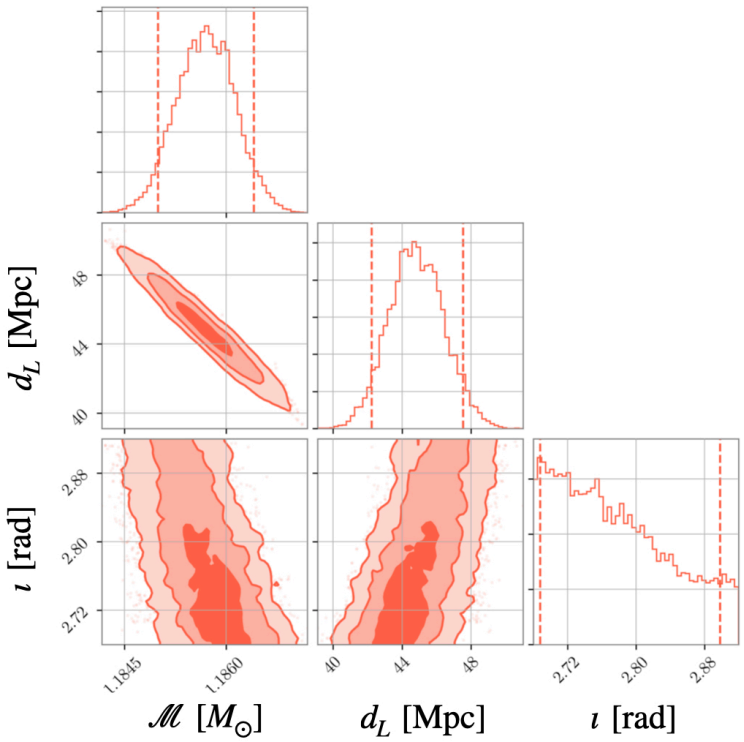

Figure 7.5: The posterior probability distributions of the chirp mass in the source frame, the luminosity distance, and the inclination angle for GW170817 under GR.

for GW170817 under GR where we use the TaylorF2 template for comparison again. The posterior probability distributions under GR are shown in Fig. 7.5. It shows that the estimated values of the amplitude parameters under $\mathcal{H}_{\rm ST}$ are nearly equal to those under GR. In Fig. 7.4, the correlation between the additional amplitude and the chirp mass or the luminosity distance is clearly apparent. The chirp mass and the luminosity distance compensate for the decrease in the tensor modes associated with the scalar radiation.

The estimated additional scalar polarization amplitude for GW170817 under $\mathcal{H}_{\rm ST}$ is shown in Fig. 7.4 . We obtain the additional scalar amplitude as $0.04^{+0.60}_{-0.66}$. The above constraint on the scalar polarization amplitude except for the dependence of the luminosity distance and the inclination angle also can be translated into the constraint on the amplitude ratio between the tensor modes and the scalar mode as

$$R_{ST} = 0.004^{+0.057}_{-0.062}. \tag{7.11}$$

The results are also consistent with GR inferring the zero-consistent small additional amplitude. In this case, it is also thought that the reaction to the tensor waveform due to scalar radiation is at work.

7.3 Discussions

So far, the CBC polarization tests have been reported mainly involving model selection between GR and the pure non-tensorial theories. In [98], in addition to two tensor modes, the vector polarization modes have been constrained for GW170817 using null stream in terms of the amplitude $< 6 \times 10^{-23}$. The method in [31] can be applied to the mixed polarization search, but what is currently reported is limited to simple comparisons between GR and the pure non-tensorial theories. In [100], the mixed analysis was done in a broad sense based on the assumption of the existence of tensor modes, but no waveform is assumed and only p-values are reported. Finally, note that we cannot compare the results between BBH and BNS because the radiation physical mechanism may be different.

As shown in Chapter 5, the detection limit for the additional amplitude

is determined by the SNR. Thus, it is expected that the event with the large SNR can be utilized for more precise tests. In addition, when the fourth and fifth detector such as KAGRA and LIGO India participates in the GW detector network, four and five polarization modes can be probed. Therefore, the expansion of the detector network will make it possible to test the GWs under a vector-tensor framework or a scalar-vector-tensor framework in the future. Such expanded frameworks can be straightforwardly formulated by expanding the formalism in this thesis. As mentioned in Chapter 5, combining multiple results by some method of superimposing GW signals could also statistically improve the test sensitivity or the constraints.

7.4 Conclusion

We searched for the mixed scalar-tensor polarizations using the data of GW170814 and GW170817. We find the observational constraints on the polarization amplitudes of the additional scalar mode except for the dependence of the distance and the inclination angle as $-0.08^{+0.59}_{-0.57}$ for GW170814 and $0.04^{+0.60}_{-0.66}$ for GW170817 by the Bayesian inference. These constraints can be written by the ratio of the scalar mode amplitude to the tensor mode amplitude, $R_{ST} = -0.02^{+0.16}_{-0.15}$ for GW170814 and $R_{ST} = 0.004^{+0.057}_{-0.062}$ for GW170817. These results are consistent with GR. This is the first direct search for the scalar-tensor polarizations.

Chapter 8

Conclusion

8.1 Summary

First, we studied the polarization separability with the current and future ground-based detector networks systematically in Chapter 5. We adopted the five mixed polarization models including the non-tensorial modes in addition to the two standard tensor modes in general relativity (GR). The gravitational wave (GW) radiation patterns, which describe how GWs are emitted with respect to the orbital inclination angle, are determined by the geometry of the system. We constructed the mixed polarization models from a compact binary coalescence (CBC) system with the waveform elements that do not depend on the theories of gravity, such as the GW radiation patterns derived from the quadrupole formula. Using the constructed waveform models, we estimated the Fisher information matrix and analyzed the polarization separability of the current and the future ground-based GW telescopes by estimating their sensitivity to the amplitudes of the non-tensorial modes. We showed the conditions for the polarization tests of the strong gravity field including the fact that in principle, the polarization mode separation of a CBC with the current ground-based GW detectors requires the same number of the detectors as the polarization modes. On the other hand, the polarization test of a CBC with the next-generation ground-based GW detectors such as Einstein telescope and Cosmic explorer does not necessarily require the same number of the detectors as the polarization modes because they can take advantage of the Earth's rotation due to their great low-frequency sensitivity. We also showed that new tests in strong gravity field would be possible with a precision comparable to the limit on scalar mode amplitudes under weak gravity field from

pulsar PSR B1913+16, from the binary distribution generated by the star formation and the compact binary coalescence rates revealed by the LIGO-Virgo collaboration.

Second, we reanalyzed the GW170814 (binary blackhole merger) and GW170817 (binary neutron star merger) in the pure polarization frameworks in which only tensor, vector, or scalar polarization modes are allowed including the non-tensorial radiation patterns in Chapter 6. In addition, we took advantage of the location and orientation information of GW170817 from the optical and near-infrared electromagnetic counterpart and the associated gamma-ray burst jet. For GW170814, we found the logarithms of the Bayes factors of 2.775 and 3.636 between the pure tensor polarization, and the pure vector or scalar polarizations, respectively. For GW170817, we found the logarithms of the Bayes factors of 21.417 and 43.953 between the pure tensor polarization, and pure vector or scalar polarization with the location prior, respectively. Furthermore, with the location prior and the jet prior, they are improved to 51.043 and 60.271.

Finally, we searched for the scalar-tensor mixed polarizations for GW170814 and GW170817 based on the Bayesian approach. We estimated the amplitude for the additional scalar polarization mode in addition to the tensor modes. We consider the amplitude and phase deformation of the waveforms accompanied by the modification of the change rate of the binding energy from the extra quadrupole scalar radiation. We found the constraints $-0.08^{+0.59}_{-0.57}$ for GW170814 and $0.04^{+0.60}_{-0.66}$ for GW170817 in terms of the amplitudes of the additional scalar mode except for the dependence of the distance and the inclination angle (see the definition in Eq. (7.1)). This constraint can be rephrased to the ratio of the scalar mode amplitude to the tensor mode amplitude, $R_{ST} = -0.02^{+0.16}_{-0.15}$ for GW170814 and $R_{ST} = 0.004^{+0.057}_{-0.062}$ for GW170817.

8.2 Future prospects

It is promised that more CBCs will be observed by the current and the future ground-based interferometric detectors with the expansion of the global detector network [170]. As we showed, the types and the number of testable polarization modes are determined by the number of the detectors. In other

words, the expansion of the detector network is qualitatively crucial in the polarization tests of the CBCs. In the near future, CBC observations with four LIGO-Virgo-KAGRA detectors will enable tests of the vector-tensor modes. Furthermore, if LIGO-India [171] add to the detector network, the most common test in the scalar-vector-tensor framework will be possible. In the longer term, CBC observations of heavier masses with the space-based GW telescope such as LISA [119, 120], DECIGO [121], Tianqin [122], and Taiji [172] will enable us to test the theories of gravity in a wide range of masses from 10^0 to 10^7 solar masses. For the space-based GW telescope, the short-wavelength approximation may be broken depending on the sources. In such situations, non-trivial transfer function would make it possible to distinguish two scalar modes, the breathing and the longitudinal mode [102].

From a theoretical point of view, enhancing the waveform model is one of the themes. The currently known generalized ppE waveform model was built on a kind of scalar tensor model and two bimetric theories and have a limited range of application. Recently, the extension to the Einstein-æther theory has been reported [173]. It is expected that more general ppE waveform model will be constructed including vector-tensor theory, scalar-vector-tensor theory and so on. The construction of a phenomenological waveform model that takes into account the independence between parameters will allow for model independent tests involving more alternative theories of gravity. On the other hand, signal stacking is also a key because a lot of CBCs are promising to be detected in the future as well in order to improve the test sensitivity. As we noted in Chapter 5, to estimate the statistical improvement of the constraints on the additional polarization parameters, we assumed that the additional amplitude does not depend on the source parameters and the statistical improvement of the error in a redshift bin. It is required to develop a specific method to combine the information from multiple CBC sources statistically. A method for shaping and overlapping the constructed null streams according to the waveform model is currently under development. Furthermore, formulation of unknown phenomena such as helicity transformation of GWs due to gravitational nonlinear effects is one possible direction. Phenomena that do not involve waveform deformation can be explored only by polarization tests, which is valuable as an observational attempt.

8.3 Conclusion

The mixed polarization modes of GWs predicted in realistic alternative theories of gravity were explored for strong and dynamical system of CBCs. First, we found the fundamental separation conditions of the polarization modes in the mixed polarization models and investigated the correlations among parameters. For the first time, the previously implicitly believed relationship between the detector and the mode was systematically clarified, and the details of the situation necessary for tests were captured. This becomes the basis for the analysis settings in the analysis using real data. In fact, we selected events that fit these conditions required for the polarization tests and performed the polarization mode search such as the pure polarization tests and the scalar-tensor searches. In these searches, we include the factors independent of the specific theory of gravity such as the antenna pattern functions and the dependence of the inclination angle. Viewed differently, since the dependences of the inclination angle are different among the polarization modes, given the conditions of analysis beforehand, strong limitations may be obtained. For the binary neutron star event, we utilize the location and the orientation of the source from the electromagnetic counterparts and impose the additional priors. In the pure polarization tests of GW170817, we obtained the strongest constraint between GR and the pure vector or scalar theories. In the scalar-tensor search, we consider the waveform corrections from the additional non-tensorial mode radiation. For the first time, we obtained the constraint on the additional scalar polarization mode in the strong gravity field where the gravitational potential $\sim 10^{-1}$. Using the methods in this thesis, further high-precision tests will be possible for the promising CBC sources in future observations.

Appendix A

Variation

definition A.1 (Action)
Let $\mathscr{M}$ be a differentiable manifold and Ψ be some tensor fields on $\mathscr{M}$. Ψ are simply called the fields. Consider the function of Ψ, $S[\Psi]$. This S is a map from the set of the fields on $\mathscr{M}$ to the set of real numbers and called the action.

Ψ actually represents some fields ${\Psi_{(i)}}^{a\cdots b}{}_{c\cdots d}(i = 1, 2, \cdots, n)$. I left out the indices i that indicate the number of fields and the abstract indices for the tensors. The tensor of the tensor fields ${\Psi_{(i)}}^{a\cdots b}{}_{c\cdots d}(i = 1, 2, \cdots, n)$ at $x \in \mathscr{M}$ is written by $\Psi_{(i)}|_x{}^{a\cdots b}{}_{c\cdots d}(i = 1, 2, \cdots, n)$. Similarly I denote the tensor of the tensor fields Ψ at $x \in \mathscr{M}$ by $\Psi|_x$.

definition A.2 (Variation)
Let $\mathscr{D} \subset \mathscr{M}$ be a submanifold of $\mathscr{M}$ and $\Psi|_x(u)$, $u \in (-\epsilon, \epsilon)$, $x \in \mathscr{M}$ be the tensors of one-parameter family of the tensor fields $\Psi(u)$, $u \in (-\epsilon, \epsilon)$ at $x \in \mathscr{M}$ such that

$$(1)\ \Psi|_x(0) = \Psi \text{ in } \mathscr{M}, \tag{A.1}$$

$$(2)\ \Psi|_x(u) = \Psi \text{ in } \mathscr{M} - \mathfrak{D}. \tag{A.2}$$

Then I define the variation of the fields as follows,

$$\delta\Psi := \left.\frac{d\Psi(u)}{du}\right|_{u=0}. \tag{A.3}$$

In this note, I suppose the existence of the derivatives $dS/du|_{u=0}$ for all one-parameter family $\Psi(u)$.

definition A.3 (Functional derivative)
I assume the existence of the smooth tensor fields χ which is dual to ψ such

that

$$\left.\frac{dS}{du}\right|_{u=0} = \int_{\mathfrak{D}} \chi \delta\Psi, \tag{A.4}$$

for any one-parameter family. [1] Then we say that S is functionally differentiable at $\Psi(0)$. We call χ the functional derivative of S and denote it as

$$\left.\frac{\delta S}{\delta \Psi}\right|_{\Psi_0} := \chi.^{[2]} \tag{A.5}$$

definition A.4 (Lagrangian)
Consider a functional form of S

$$S[\Psi] = \int_{\mathfrak{D}} L[\Psi] \tag{A.6}$$

where L is a local function of ψ and a finite number of its derivatives,

$$L|_x = L(\Psi(x), \nabla\Psi(x), \cdots, \nabla^k\Psi(x)). \tag{A.7}$$

L is called by Lagrangian density.

definition A.5 (Variational principle)
Let S be functionally differentiable. We require that the fields Ψ maximize S,

$$\left.\frac{dS}{du}\right|_{u=0} = 0. \tag{A.8}$$

This principle is called by variational principle. Hence, the following equation is hold by the definition of the functional derivative and the following fundamental lemma of variational calculus.

$$\left.\frac{\delta S}{\delta \Psi}\right|_{\Psi_0} = 0. \tag{A.9}$$

[1] If the type of tensor field of Ψ is (k, l), that of χ is (l, k). Here contraction of all indices in the integral is understood.

[2] More generally, if there exists a tensor distribution χ such that $dS/du|_{u=0} = \chi[\delta\Psi]$, we say that S is functionally differentiable and call χ the functional derivative of S at $\Psi(0)$. Here the tensor distribution is a distribution whose type is tensor, so called generalized function. The bracket on the right hand side denotes the scalar product (distribution) which is defined by $\chi[\delta\Psi] =< \chi, \delta\Psi >= \int_{\mathfrak{D}} \chi\delta\Psi$.

This gives us the fundamental equations for the fields.

lemma A.1 (Fundamental lemma of variational calculus)
Let $\mathscr{D} \subset \mathscr{M}$ be a submanifold of $\mathscr{M}$ and $\Psi|_x(u)$, $u \in (-\epsilon, \epsilon)$, $x \in \mathscr{M}$ be any one-parameter family satisfying a proper boundary conditions. The following is held.

$$\left.\frac{dS}{du}\right|_{u=0} = \int_{\mathfrak{D}} \chi \delta\Psi = 0 \Rightarrow \chi = 0. \tag{A.10}$$

This statement is called by fundamental lemma of variational calculus.

Appendix B

General Relativity

definition B.1 (Space-time)
Space-time is the set of events. In general relativity, the mathematical model of space-time is $(\mathscr{M}, g)$ where $\mathscr{M}$ is a connected four-dimensional Hausdorff C^∞ manifold and g is a Lorentz metric [1]on $\mathscr{M}$.

First, I derive the fundamental equations for fields by variational method. Hereafter I refer to the fields Ψ as ${\Psi_{(i)}}^{a\cdots b}{}_{c\cdots d},\ (i = 1, 2, \cdots, n)$ without omitting the indices. I assume the form of the action is Lagrangian form and the Lagrangian depends on the fields and their first covariant derivatives.

Consider the variation of the fields ${\Psi_{(i)}}^{a\cdots b}{}_{c\cdots d},\ (i = 1, 2, \cdots, n)$. Then

$$\left.\frac{dS}{du}\right|_{u=0} = \sum_i \int_{\mathfrak{D}} \left(\frac{\partial L}{\partial {\Psi_{(i)}}^{a\cdots b}{}_{c\cdots d}} \delta {\Psi_{(i)}}^{a\cdots b}{}_{c\cdots d} - \frac{\partial L}{\partial {\Psi_{(i)}}^{a\cdots b}{}_{c\cdots d;e}} \delta({\Psi_{(i)}}^{a\cdots b}{}_{c\cdots d;e}) \right). \tag{B.1}$$

Since$\delta({\Psi_{(i)}}^{a\cdots b}{}_{c\cdots d;e}) = (\delta {\Psi_{(i)}}^{a\cdots b}{}_{c\cdots d})_{;e}$, the second term can be written as

$$\sum_i \int_{\mathfrak{D}} \left[\left(\frac{\partial L}{\partial {\Psi_{(i)}}^{a\cdots b}{}_{c\cdots d;e}} \delta {\Psi_{(i)}}^{a\cdots b}{}_{c\cdots d} \right)_{;e} - \left(\frac{\partial L}{\partial {\Psi_{(i)}}^{a\cdots b}{}_{c\cdots d;e}} \right)_{;e} \delta {\Psi_{(i)}}^{a\cdots b}{}_{c\cdots d} \right]. \tag{B.2}$$

According to Stokes' theorem, the first term can be written as

$$\int_{\mathfrak{D}} Q^a{}_{;a} = \int_{\partial\mathfrak{D}} Q^a d\sigma_a, \tag{B.3}$$

[1]Its signature is +2

where

$$Q^e := \sum_i \frac{\partial L}{\partial \Psi_{(i)}{}^{a\cdots b}{}_{c\cdots d;e}} \delta\Psi_{(i)}{}^{a\cdots b}{}_{c\cdots d}. \tag{B.4}$$

This integral have to vanish because $\delta\Psi_{(i)}{}^{a\cdots b}{}_{c\cdots d} = 0$ is held at the boundary $\partial\mathfrak{D}$ from the second condition of variation Eq. (A.2). Finally we get the following expression,

$$\left.\frac{dS}{du}\right|_{u=0} = \sum_i \int_{\mathfrak{D}} \left(\frac{\partial L}{\partial \Psi_{(i)}{}^{a\cdots b}{}_{c\cdots d}} - \left(\frac{\partial L}{\partial \Psi_{(i)}{}^{a\cdots b}{}_{c\cdots d;e}} \right)_{;e} \right) \delta\Psi_{(i)}{}^{a\cdots b}{}_{c\cdots d} = 0. \tag{B.5}$$

Thus, we can get the following Euler-Lagrange equations from fundamental lemma of variational calculus Eq. (A.10),

$$\chi = \frac{\partial L}{\partial \Psi_{(i)}{}^{a\cdots b}{}_{c\cdots d}} - \left(\frac{\partial L}{\partial \Psi_{(i)}{}^{a\cdots b}{}_{c\cdots d;e}} \right)_{;e} = 0. \tag{B.6}$$

Then we get the energy-momentum tensor from the Lagrangian by considering a variation with respect to the metric. Suppose a variation of the metric $g_{ab}(u, x)$ does not change the fields $\Psi_{(i)}{}^{a\cdots b}{}_{c\cdots d}$. Then,

$$\left.\frac{dS}{du}\right|_{u=0} = \int_{\mathfrak{D}} \left(\sum_i \frac{\partial L}{\partial \Psi_{(i)}{}^{a\cdots b}{}_{c\cdots d;e}} \delta(\Psi_{(i)}{}^{a\cdots b}{}_{c\cdots d;e}) + \frac{\partial L}{\partial g_{ab}} \delta g_{ab} \right) + \int_{\mathfrak{D}} L \frac{\partial \boldsymbol{\epsilon}}{\partial g_{ab}} \delta g_{ab}. \tag{B.7}$$

The last term comes from the fact that the integral is defined by $\int f = \int f\boldsymbol{\epsilon}$. Since $\boldsymbol{\epsilon} = (4!)^{-1}\boldsymbol{\eta}$, $\eta_{abcd} = (-g)^{1/2} 4! \delta_{[a}{}^1 \delta_b{}^2 \delta_c{}^3 \delta_{d]}{}^4$ and $g := \det(g_{ab})$,

$$\frac{\partial \eta_{abcd}}{\partial g_{ef}} = -\frac{1}{2}(-g)^{-1/2} \frac{\partial g}{\partial g_{ef}} 4! \delta_{[a}{}^1 \delta_b{}^2 \delta_c{}^3 \delta_{d]}{}^4. \tag{B.8}$$

Thus, we obtain

$$\frac{\partial \boldsymbol{\epsilon}}{\partial g_{ab}} = \frac{1}{2} g^{ab} \boldsymbol{\epsilon}. \tag{B.9}$$

Here I use the the fact that the cofactor of the matrix can be expressed as a product of the component of the inverse matrix and the determinant od the matrix, that is the relation $\partial g / \partial g_{ef} = g^{ef} g$ to evaluate $\partial g / \partial g_{ef}$. The first term arises because $\delta(\Psi_{(i)}{}^{a\cdots b}{}_{c\cdots d;e})$ does not necessarily become zero unlike

$\delta\Psi_{(i)}{}^{a\cdots b}{}_{c\cdots d}$ due to a variation of the components of the connection $\Gamma^a{}_{bc}$ induced by a variation of the metric. $\partial\Gamma^a{}_{bc}/\partial u = \delta\Gamma^a{}_{bc}$ should be a tensor because the difference between two connections should be a tensor. This can be calculated as follows,

$$\delta\Gamma^a{}_{bc} = \frac{1}{2}g^{ad}\{(\delta g_{db})_{;c} + (\delta g_{dc})_{;b} - (\delta g_{bc})_{;d}\}. \tag{B.10}$$

One can verify this equation by checking that this equation is held in normal coordinates at p where the components $\Gamma^a{}_{bc}$ and the coordinate derivatives of the components g_{ab} vanish because this equation is a tensor equation. For Riemann normal coordinate,

$$(l.h.s) = \frac{1}{2}g^{ad}\left(\frac{\partial\delta g_{cd}}{\partial x^b} + \frac{\partial\delta g_{bd}}{\partial x^c} - \frac{\partial\delta g_{bc}}{\partial x^d}\right), \tag{B.11}$$

and, since the components $\Gamma^a{}_{bc}$ at p induced by the covariant derivatives vanish,

$$(r.h.s) = \frac{1}{2}g^{ad}\{(\delta g_{db})_{;c} + (\delta g_{dc})_{;b} - (\delta g_{bc})_{;d}\} = (l.h.s.). \tag{B.12}$$

If the tensor equation is held in a specified coordinate, it is held in any coordinates. This method is often used to derive equations in relativity. However, one should be careful to calculations including the variation and the covariant derivative. Note that $\delta(A+B) = \delta A + \delta B$, $\delta(AB) = (\delta A)B + A(\delta B)$ and $\delta(\partial A) = \partial(\delta A)$. Especially, the variation operator does not commute the covariant derivative for any tensors g (here its type is $(0,2)$ as an example),

$$\nabla_a(\delta g_{bc}) = \delta(\nabla_a g_{bc}) + g_{dc}\,\delta\Gamma^d_{ba} + g_{bd}\,\delta\Gamma^d_{ac}, \tag{B.13}$$

when one consider the variation of the metric because a change of the connection is induced. This can be easily derived by the above three equations. On the other hand, the variation operator does commute the covariant derivative when you consider the variation of the fields except for the metric as I mentioned above. Eq. (B.9) can be also derived by this equation straightforward. One also should be careful to that since the metricity condition holds only for the unperturbed metric g_{ab}, $\nabla(g(0)) = 0$ does not mean that $\nabla(g(\Delta u)) = 0$. Using to leave only terms multiplied by δg_{ab}, The first term in Eq. (B.7) can be expressed by the terms involving only $\delta\Gamma$ by using the similar relation as Eq.

(B.13). Then, using Eq. (B.9) and the integration by parts, it finally can be expressed by the only terms involving only δg. Thus, the energy-momentum tensor T^{ab} can be defined as follows,

$$\left.\frac{dS}{du}\right|_{u=0} = \frac{1}{2}\int_{\mathfrak{D}} (T^{ab}\delta g_{ab}). \tag{B.14}$$

The energy-momentum tensor satisfies the conservation equations. Let ϕ be a diffeomorphism which is is the identity except in the interior of $\mathscr{D}$. Then,

$$S = \int_{\mathfrak{D}} L = \frac{1}{4!}\int_{\mathfrak{D}} L\boldsymbol{\eta} = \frac{1}{4!}\int_{\phi(\mathfrak{D})} L\boldsymbol{\eta} = \frac{1}{4!}\int_{\mathfrak{D}} \phi^*(L\boldsymbol{\eta}). \tag{B.15}$$

Here I used the condition that ϕ is the identity except in the interior of $\mathscr{D}$ for the third equality, and the invariance of integrals under a differential map for the forth equality. Thus,

$$\frac{1}{4!}\int_{\mathfrak{D}} (L\boldsymbol{\eta} - \phi^*(L\boldsymbol{\eta})) = 0. \tag{B.16}$$

If ϕ is generated by a vector field $\boldsymbol{X}$ which is non-zero only in the interior of $\mathfrak{D}$,

$$\frac{1}{4!}\int_{\mathfrak{D}} L_{\boldsymbol{X}}(L\boldsymbol{\eta}) = 0, \tag{B.17}$$

by the definition of the Lie derivatives. On the other hand,

$$\begin{aligned}(l.h.s.) &= \sum_i \int_{\mathfrak{D}} \left(\frac{\partial L}{\partial \Psi_{(i)}{}^{a\cdots b}{}_{c\cdots d}} - \left(\frac{\partial L}{\partial \Psi_{(i)}{}^{a\cdots b}{}_{c\cdots d;e}} \right)_{;e} \right) L_{\boldsymbol{X}} \Psi_{(i)}{}^{a\cdots b}{}_{c\cdots d} \\ &\quad + \frac{1}{2}\int_{\mathfrak{D}} T^{ab} L_{\boldsymbol{X}} g_{ab} \\ &= \frac{1}{2}\int_{\mathfrak{D}} T^{ab} L_{\boldsymbol{X}} g_{ab} \\ &= \int_{\mathfrak{D}} ((T^{ab}X_a)_{;b} - T^{ab}{}_{;b}X_a).\end{aligned} \tag{B.18}$$

I used the field equation for the second equality and the relation $L_{\boldsymbol{X}} g_{ab} = 2X_{(a;b)}$ for the third equality. The first term can be an integral over $\partial\mathfrak{D}$ by

Stokes' theorem. It can vanish because $\boldsymbol{X}$ vanishes there. Thus,

$$\int_{\mathfrak{D}} T^{ab}{}_{;b} X_a = 0, \tag{B.19}$$

is satisfied for all vector fields $\boldsymbol{X}$. Hence, the conservation law of the energy-momentum tensor is derived,

$$T^{ab}{}_{;b} = 0. \tag{B.20}$$

Appendix C

Brill-Hartle average

We show how to perform the spatial average over many reduced wavelength and the temporal average over many periods by introducing the averaging scheme used by Isaacson, which he called Brill-Hartle averaging. We consider averaging a tensor X_{ab} (second rank as an example). There will exist a unique geodesic of $\bar{g}_{ab}$ connecting any two points $\bar{\mathrm{P}}$ and P in the small region of size several times $\lambda\!\!\!^{-}$. Thus, if a tensor at $\bar{\mathrm{P}}$, $X(\bar{\mathrm{P}})$, is given, we can parallel transport it along the geodesic to P, and finally get a tensor at P, $X(\bar{\mathrm{P}} \to \mathrm{P})$. Let $f(\bar{\mathrm{P}}, \mathrm{P})$ be a weighting function that falls smoothly to zero when P and P' are separated by many wavelength, and that satisfies the following condition,

$$\int f(\bar{\mathrm{P}}, \mathrm{P})\sqrt{-\bar{g}(\bar{\mathrm{P}})}d^4\bar{x} = 1. \tag{C.1}$$

Then, the average of the tensor field X over several wavelengths at the point P is defined by

$$< X >_{\mathrm{P}} := \int X(\bar{\mathrm{P}} \to \mathrm{P}) f(\bar{\mathrm{P}}, \mathrm{P})\sqrt{-\bar{g}(\bar{\mathrm{P}})}d^4\bar{x}. \tag{C.2}$$

Here, we shall consider parallel propagation of arbitrary tensor along a geodesic $x(\tau)$ from $x(\tau_0) = y$ at $\bar{\mathrm{P}}$ to $x(\tau) = z$ at P,

$$t^a \nabla_a T^{\alpha_1 \ldots \alpha_k}{}_{\beta_1 \ldots \beta_l} = 0. \tag{C.3}$$

This parallel propagation equations lead to linear homogeneous set of first

order differential equations with respect to T,

$$t^a\{\partial_a T^{\alpha_1\cdots\alpha_k}{}_{\beta_1\cdots\beta_l} + \sum_i \Gamma^{\alpha_i}{}_{ad} T^{\alpha_1\cdots d\cdots\alpha_k}{}_{\beta_1\cdots\beta_l} - \sum_j \Gamma^{d}{}_{a\beta_j} T^{\alpha_1\cdots\alpha_k}{}_{\beta_1\cdots d\cdots\beta_l}\} = 0. \tag{C.4}$$

It is known that the solution of linear homogeneous set of first order differential equations can be expressed as linear homogeneous functions of initial values. Thus, from linear homogeneous character of the equations, we can express $T(\bar{\mathrm{P}} \to \mathrm{P})$ parallel propagated from $\bar{\mathrm{P}}$ as linear homogeneous functions of $T(\bar{\mathrm{P}})$

$$T^{\alpha_1\ldots\alpha_k}{}_{\beta_1\ldots\beta_l}(\bar{\mathrm{P}} \to \mathrm{P}) = P^{\alpha_1\ldots\alpha_k\bar{\beta}_1\ldots\bar{\beta}_l}_{\bar{\alpha}_1\ldots\bar{\alpha}_k\beta_1\ldots\beta_l}(\bar{\mathrm{P}} \to \mathrm{P}) T^{\bar{\alpha}_1\ldots\bar{\alpha}_k}{}_{\bar{\beta}_1\ldots\bar{\beta}_l}(\bar{\mathrm{P}}), \tag{C.5}$$

or

$$T^{\alpha_1\ldots\alpha_k}{}_{\beta_1\ldots\beta_l}(\tau) = P^{\alpha_1\ldots\alpha_k\bar{\beta}_1\ldots\bar{\beta}_l}_{\bar{\alpha}_1\ldots\bar{\alpha}_k\beta_1\ldots\beta_l}(\tau,\tau_0) T^{\bar{\alpha}_1\ldots\bar{\alpha}_k}{}_{\bar{\beta}_1\ldots\bar{\beta}_l}(\tau_0), \tag{C.6}$$

where $P^{\alpha_1\ldots\alpha_k\bar{\beta}_1\ldots\bar{\beta}_l}_{\bar{\alpha}_1\ldots\bar{\alpha}_k\beta_1\ldots\beta_l}(\bar{\mathrm{P}} \to \mathrm{P})$ or $P^{\alpha_1\ldots\alpha_k\bar{\beta}_1\ldots\bar{\beta}_l}_{\bar{\alpha}_1\ldots\bar{\alpha}_k\beta_1\ldots\beta_l}(\tau,\tau_0)$ is called parallel propagator and it depends on only two space-time points. Substituting this into the above parallel propagation equations, we get [1]

$$t^a \nabla_a P^{\alpha_1\ldots\alpha_k\bar{\beta}_1\ldots\bar{\beta}_l}_{\bar{\alpha}_1\ldots\bar{\alpha}_k\beta_1\ldots\beta_l}(\tau,\tau_0) = 0. \tag{C.7}$$

The coincide limits $\tau \to \tau_0$ give the initial conditions of the parallel propagator

$$P^{\alpha_1\ldots\alpha_k\bar{\beta}_1\ldots\bar{\beta}_l}_{\bar{\alpha}_1\ldots\bar{\alpha}_k\beta_1\ldots\beta_l}(\tau_0,\tau_0) = \delta^{\alpha_1}_{\bar{\alpha}_1}\cdots\delta^{\alpha_k}_{\bar{\alpha}_k}\delta^{\bar{\beta}_1}_{\beta_1}\cdots\delta^{\bar{\beta}_l}_{\beta_l} \tag{C.8}$$

We shall consider parallel propagation of a vector $\lambda^a(y)$ and a dual vector $\lambda_a(y)$ to obtain the general solution of parallel propagators $P^{\alpha_1\ldots\alpha_k\bar{\beta}_1\ldots\bar{\beta}_l}_{\bar{\alpha}_1\ldots\bar{\alpha}_k\beta_1\ldots\beta_l}(\tau,\tau_0)$. From Eq. (C.7), the parallel propagation equations for a vector $\lambda^a(y)$ and a dual vector $\lambda_a(y)$ are

$$\frac{d}{d\tau} P^{\mu}{}_{\bar{a}}(\tau,\tau_0) = A^{\mu}{}_{\nu}(\tau) P^{\nu}{}_{\bar{a}}(\tau,\tau_0), \quad A^{\mu}{}_{\nu}(\tau) := -\Gamma^{\mu}{}_{\lambda\nu}(\tau)\frac{dx^{\lambda}}{d\tau}(\tau), \tag{C.9}$$

[1] When we consider the differentiation with respect to τ or differential equations with respect to τ, we fix τ_0 at a point.

and

$$\frac{d}{d\tau}P_\mu{}^{\bar{a}}(\tau,\tau_0) = A_\mu{}^\nu(\tau)P_\nu{}^{\bar{a}}(\tau,\tau_0), \quad A_\nu{}^\mu(\tau) := +\Gamma^\mu{}_{\lambda\nu}(\tau)\frac{dx^\lambda}{d\tau}(\tau), \tag{C.10}$$

respectively [2] where $P^\mu{}_{\bar{a}}(\tau,\tau_0)$ and $P_\mu{}^{\bar{a}}(\tau,\tau_0)$ are parallel propagators for each vectors

$$\lambda^\mu(\tau) = P^\mu{}_{\bar{a}}(\tau,\tau_0)\lambda^{\bar{a}}(\tau_0), \tag{C.11}$$

and

$$\lambda_\mu(\tau) = P_\mu{}^{\bar{a}}(\tau,\tau_0)\lambda_{\bar{a}}(\tau_0), \tag{C.12}$$

in the coordinate. It is easily shown that parallel propagators are bi-vectors considering tensor transformation on both sides. By integrating both sides and substituting the result into the integrand repeatedly to solve these equations, we get

$$\begin{aligned} P^\mu{}_{\bar{a}}(\tau,\tau_0) &= \delta^\mu_{\bar{a}} + \int_{\tau_0}^{\tau} A^\mu{}_\nu(\eta)P^\nu{}_{\bar{a}}(\eta,\tau_0)d\eta \\ &= \delta^\mu_{\bar{a}} + \int_{\tau_0}^{\tau} A^\mu{}_{\bar{a}}(\eta)d\eta + \int_{\tau_0}^{\tau}\int_{\tau_0}^{\eta} A^\mu{}_\nu(\eta)A^\nu{}_{\bar{a}}(\eta')d\eta' d\eta + \cdots \\ &= \mathcal{P}\exp\left(-\int_{\tau_0}^{\tau}\Gamma^\mu{}_{\lambda\bar{a}}(\eta)\frac{dx^\lambda}{d\tau}(\eta)d\eta\right), \end{aligned} \tag{C.13}$$

and

$$P_\mu{}^{\bar{a}}(\tau,\tau_0) = \mathcal{P}\exp\left(+\int_{\tau_0}^{\tau}\Gamma^{\bar{a}}{}_{\lambda\mu}(\eta)\frac{dx^\lambda}{d\tau}(\eta)d\eta\right), \tag{C.14}$$

where $\mathcal{P}$ is path-ordering symbol.[3] In the same way, we can consider parallel propagator inversely from $\bar{\mathrm{P}}$ to P.

$$\lambda^{\bar{a}}(\tau_0) = P^{\bar{a}}{}_\mu(\tau_0,\tau)\lambda^\mu(\tau), \tag{C.15}$$

and

$$\lambda_{\bar{a}}(\tau_0) = P_{\bar{a}}{}^\mu(\tau_0,\tau)\lambda_\mu(\tau). \tag{C.16}$$

[2] Γ is a function of x^μ. Here we consider a geodesic $x^\mu(\tau)$. Thus, we can regard $\Gamma(x^\mu(\tau))$ as a function of τ.

[3] Path ordering symbol ensure the order of matrix product $\int_{\tau_0}^{\tau}\int_{\tau_0}^{\eta_n}\cdots\int_{\tau_0}^{\eta_2}A(\eta_n)\cdots A(\eta_1)d^n\eta = \frac{1}{n!}\int_{\tau_0}^{\tau}\int_{\tau_0}^{\tau}\cdots\int_{\tau_0}^{\tau}\mathcal{P}[A(\eta_n)\cdots A(\eta_1)]d^n\eta$

If we parallel propagate vectors and dual vectors $\mathrm{P} \to \bar{\mathrm{P}} \to \mathrm{P}$ and $\bar{\mathrm{P}} \to \mathrm{P} \to \bar{\mathrm{P}}$, we obtain

$$\begin{cases} P^{\mu}{}_{\bar{a}} P^{\bar{a}}{}_{\nu} = \delta^{\mu}_{\nu} \\ P_{\mu}{}^{\bar{a}} P_{\bar{a}}{}^{\nu} = \delta^{\nu}_{\mu}, \end{cases} \tag{C.17}$$

and

$$\begin{cases} P^{\bar{a}}{}_{\mu} P^{\nu}{}_{\bar{b}} = \delta^{\bar{a}}_{\bar{b}} \\ P_{\bar{a}}{}^{\mu} P_{\nu}{}^{\bar{b}} = \delta^{\bar{a}}_{\bar{b}}. \end{cases} \tag{C.18}$$

We can find general solutions of Eq. (C.7) with initial conditions Eq. (C.8) using these propagators for vector and dual vector

$$P^{\alpha_1 \ldots \alpha_k \bar{\beta}_1 \ldots \bar{\beta}_l}_{\bar{\alpha}_1 \ldots \bar{\alpha}_k \beta_1 \ldots \beta_l}(\tau_0, \tau_0) = P^{\alpha_1}{}_{\bar{\alpha}_1} \cdots P^{\alpha_k}{}_{\bar{\alpha}_k} P_{\beta_1}{}^{\bar{\beta}_1} \cdots P_{\beta_l}{}^{\bar{\beta}_l}. \tag{C.19}$$

Therefore, we can also express Brill-Hartle average in terms of components using parallel propagators.

Appendix D

Irreducible decomposition

Here, we provide the knowledge of the irreducible decomposition of tensor.

Our purpose is to decompose the tensor components into irreducible parts for the transformation. We consider pure spatial rotations represented by $R_j{}^k$. A vector field $A^j(\boldsymbol{x})$ can be always decomposed as

$$A^j = \partial^j A + A^j_T, \tag{D.1}$$

where $\partial^j A$ is the longitudinal piece and A^j_T is a transverse piece such that $\partial_j A^j_T$. The uniqueness of the decomposition is established by the uniqueness of the solution for the Poisson equation. A symmetric tensor field $B^{jk}(\boldsymbol{x})$ can be always decomposed as

$$B^{jk} = \frac{1}{3}\delta^{jk}B + (\partial^{jk} - \frac{1}{3}\delta^{jk}\nabla^2)C + \partial^{(j}C^{k)}_T + D^{jk}_{TT}, \tag{D.2}$$

where $\frac{1}{3}\delta^{jk}B$ is a trace piece, $(\partial^{jk} - \frac{1}{3}\delta^{jk}\nabla^2)C$ is a longitudinal-traceless piece, $\partial^{(j}C^{k)}_T$ is a longitudinal-transverse piece such that $\partial_j C^j_T = 0$, and D^{jk}_{TT} is a transverse-traceless piece such that $\partial_k C^{jk}_{TT} = 0 = \delta_{jk}C^{jk}_{TT}$. The uniqueness of the decomposition is also established by the uniqueness of the solution for the Poisson equation.

In terms of the Fourier components such as

$$A^j(\boldsymbol{x}) = \int d^3k \tilde{A}^j(\boldsymbol{k}) e^{ik^i x^i}, \tag{D.3}$$

and

$$B^{jk}(\boldsymbol{x}) = \int d^3k \tilde{B}^j(\boldsymbol{k}) e^{ik^i x^i}, \tag{D.4}$$

the above equations can be rewritten as

$$\tilde{A}^j(\boldsymbol{k}) = ik^j\tilde{A}(\boldsymbol{k}) + \tilde{A}^j_T(\boldsymbol{k}), \tag{D.5}$$

and

$$\tilde{B}^{jk} = \frac{1}{3}\delta^{jk}\tilde{B}(\boldsymbol{k}) + (-k^jk^k - \frac{1}{3}k^2)\tilde{C}(\boldsymbol{k}) + ik^{(j}\tilde{C}^{k)}_T(\boldsymbol{k}) + \tilde{D}^{jk}_{TT}(\boldsymbol{k}). \tag{D.6}$$

We consider spatial rotation $\Lambda_a{}^b$ with $\Lambda_0{}^b = \delta^b_0$ and $\Lambda_j{}^k = R_j{}^k$ in the four dimensional space-time. This transformation is a kind of Lorentz transformation and for some tensor X_{ab}, the X_{00} transform as a scalar, X_{0i} transform as a vector, and X_{jk} transform as a tensor under the transformation. Thus, we can apply the above discussion to this issue. When we decompose the metric on the four dimensional space-time, we need to deal with some tensors $X^{ab}(t_{\rm ret}, \boldsymbol{N})$ depending on the retarded time $t_{\rm ret}$ and the spatial unit vector $N^i := x^i/R, R := \sqrt{x^ix^i}$. The following relation for such a tensor is useful for the calculations[1]

$$\partial_j X^{ab}(t_{\rm ret}, \boldsymbol{N}) \simeq -\frac{\partial_\tau X^{ab}}{c}N^j. \tag{D.7}$$

Thus, the above decomposition at the time t can be rewritten as

$$A^j(\tau, \boldsymbol{x}) = N^j\frac{-\partial_\tau A}{c} + A^j_T, \tag{D.8}$$

and

$$B^{jk} = \frac{1}{3}\delta^{jk}B + (N^jN^k\frac{\partial_{\tau\tau}}{c^2} - \frac{1}{3}N^2\delta^{jk}\frac{\partial_{\tau\tau}}{c^2})C - N^{(j}\frac{\partial_\tau C^{k)}_T}{c} + D^{jk}_{TT}. \tag{D.9}$$

Finally, by re-defining

$$A := \frac{-\partial_\tau A}{c}, \tag{D.10}$$

$$C := \frac{\partial_{\tau\tau}}{c^2}C, \tag{D.11}$$

[1]Note that $\partial_0 = (\partial/\partial t)/c = (\partial/\partial\tau)/c$.

and

$$C_T^k := \frac{-\partial_\tau C_T^k}{c}, \tag{D.12}$$

then the decompositions are expressed as

$$A^j(\tau, \boldsymbol{x}) = N^j A + A_T^j, \tag{D.13}$$

and

$$B^{jk} = \frac{1}{3}\delta^{jk}B + (N^j N^k - \frac{1}{3}\delta^{jk})C - N^{(j}C_T^{k)} + D_{TT}^{jk}. \tag{D.14}$$

The conditions for each decomposed components still hold by replacement of N^i with the derivative in terms of ∂_j.

Appendix E

E(2) classification

Here, we summarize the $E(2)$ classification to classify the theories of gravity in terms of the physical degrees of freedom of GWs.

E.1 Newman-Penrose formalism

The physical degrees of freedom in the theory of gravity is the polarization modes of GWs. In this section, we present the polarization modes of GWs in metric theories of gravity. We can study the polarization modes of the null GWs by Newman-Penrose formalism transparently. In this section, I provide the Newman-Penrose formalism at first.

E.1.1 Spinorial Riemann tensor decomposition

In four dimensional space-time, the Riemann tensor can be divided into three irreducible parts, the Weyl tensor C_{abcd}, the traceless Riemann tensor $R_{ab} - \frac{1}{4}g_{ab}R$, and R. The Weyl tensor is defined by

$$C_{abcd} := R_{abcd} - \frac{1}{2}(g_{a[c}R_{d]b} - g_{b[c}R_{d]a}) - \frac{1}{3}Rg_{a[c}g_{d]b}. \tag{E.1}$$

In the Newman-Penrose formalism, the five complex Weyl-Newman-Penrose scalars are defined by

$$\Psi_0 := C_{abcd}k^a m^b k^c m^d, \tag{E.2}$$

$$\Psi_1 := C_{abcd}k^a k^b k^c m^d = C_{abcd}\bar{m}^a m^b k^c m^d, \tag{E.3}$$

$$\begin{aligned}\Psi_2 &:= C_{abcd}k^a m^b \bar{m}^c l^d \\ &= \frac{1}{2}(C_{abcd}k^a l^b k^c l^d + C_{abcd}k^a l^b \bar{m}^c m^d) \\ &= \frac{1}{2}(C_{abcd}\bar{m}^a m^b \bar{m}^c m^d + C_{abcd}k^a l^b \bar{m}^c m^d),\end{aligned} \tag{E.4}$$

$$\Psi_3 := C_{abcd}k^a l^b \bar{m}^c l^d = C_{abcd}\bar{m}^a m^b \bar{m}^c l^d, \tag{E.5}$$

$$\Psi_4 := C_{abcd}\bar{m}^a l^b \bar{m}^c l^d, \tag{E.6}$$

The ten Ricci-Newman-Penrose scalars are defined by

$$\Phi_{02} := \frac{1}{2}R_{ab}m^a m^b, \tag{E.7}$$

$$\Phi_{01} := \frac{1}{2}R_{ab}k^a m^b, \tag{E.8}$$

$$\Phi_{12} := \frac{1}{2}R_{ab}k^a k^b, \tag{E.9}$$

$$\Phi_{11} := \frac{1}{4}(R_{ab}k^a l^b + R_{ab}m^a \bar{m}^b), \tag{E.10}$$

$$\Phi_{22} := \frac{1}{2}R_{ab}l^a l^b, \tag{E.11}$$

$$\Phi_{10} := \frac{1}{2}R_{ab}k^a \bar{m}^b, \tag{E.12}$$

$$\Phi_{21} := \frac{1}{2}R_{ab}l^a \bar{m}^b, \tag{E.13}$$

$$\Phi_{20} := \frac{1}{2}R_{ab}\bar{m}^a \bar{m}^b, \tag{E.14}$$

$$\Lambda := \frac{R}{24}. \tag{E.15}$$

E.1.2 Lorentz transformations in Newman-Penrose formalism

Associated to the six parameters of the Lorentz group of transformations, there are six degrees of freedom corresponding rotations on the specific choice of the null tetrad basis. It is convenient to separate the rotations in three classes. Class I is null rotations (combination of boosts and rotations) that leave the

propagation direction k unchanged.

$$k \to k' = k,\ m \to m' = m+ak,\ \bar{m} \to \bar{m}' = \bar{m}+a^*k,\ l \to l' = l+a^*m+a\bar{m}+aa^*k. \tag{E.16}$$

with a complex function a. Class II is null rotations that leave the propagation direction l unchanged

$$l \to l' = l,\ m \to m' = m+bl,\ \bar{m} \to \bar{m}' = \bar{m}+b^*l,\ k \to k' = k+b^*m+b\bar{m}+bb^*l. \tag{E.17}$$

with a complex function b. Class III is boosts and rotations which leave the directions of k and l unchanged, while rotate m and $\bar{m}$ by an angle θ in their plane

$$k \to k' = Ak,\ m \to m' = e^{i\theta}m,\ \bar{m} \to \bar{m}' = e^{-i\theta}\bar{m},\ l \to l' = A^{-1}l. \tag{E.18}$$

with real functions A and θ.

E.1.3 $E(2)$ classification

We shall consider an experiment making use of matter of negligible self-gravity in a local region to measure the GWs from far-away sources.The Riemann tensor determines the relative accelerations between two points. A GW in a metric theory involves the metric field g_{ab} and any auxiliary gravitational fields in the theory. However, the Riemann tensor is the only locally observable quantity of gravity.

We shall consider a freely falling at any fiducial point P in the local region. We can always set an approximately Lorentz coordinate system

$$\{x^a\} = \{t, x^i\}, \tag{E.19}$$

with P as its origin. For sufficiently small $|x^i|$, the relative acceleration to P is

$$a_i = -R_{i0j0}x^j, \tag{E.20}$$

where R_{i0j0} is called electric components of R_{abcd}.

A weak, propagating, and vacuum GW in a metric theory is characterized

linearized Riemann tensor whose components depend only on a null retarded time $t_{\rm ret} := t - z/c$ [1] in some nearly Lorentz coordinate system,

$$R_{abcd} = R_{abcd}(t_{\rm ret}), \tag{E.21}$$

where the wave vector $k_a := \nabla_a t_{\rm ret}$ is null such that $g_{ab}k^a k^b = 0$ and the coordinate is oriented such that the propagation direction is $+z$. Here, two restrictions are encoded in this definition: (i) waves must propagate at the speed of light; (ii) waves must be plane.

A quasi-orthonormal null-tetrad basis is suitable to discuss the null GWs. See [68, 174, 175] for the details of Newman-Penrose formalism. Note that the approach is available for the null GW. When the massive modes appear, although the classification based on the above Newman-Penrsoe formalism is not available strictly, the approach can be applied to nearly null GWs approximately. In both cases massless and massive GWs, we can examine the polarization modes by solving the field equations and calculating the GW amplitudes h_A in Eq. (3.22) directly. Here, we provide the $E(2)$ classification based on the Newman-Penrose quantities. At any point P, the null tetrad $(k^a, l^a, m^a, \bar{m}^a)$ can be introduced, which are related to the basis of the local Lorentz system as

$$k^a = \frac{1}{\sqrt{2}}(\partial_t{}^a + \partial_z{}^a), \tag{E.22}$$

$$l^a = \frac{1}{\sqrt{2}}(\partial_t{}^a - \partial_z{}^a), \tag{E.23}$$

$$m^a = \frac{1}{\sqrt{2}}(\partial_x{}^a + i\partial_y{}^a), \tag{E.24}$$

$$\bar{m}^a = \frac{1}{\sqrt{2}}(\partial_x{}^a - i\partial_y{}^a). \tag{E.25}$$

Here, we choose one of the tetrads k^a proportional to the wave vector $k^a :=$

[1] For a plane wave, the phase in Eq. (2.30) can be written as $\theta = k^a x_a$ using some wave vector k^a. Thus, the wave vector should be defined by $k^a = \nabla^a\theta$. So, the k^a discussed here is different from the general wave vector, strictly speaking. $t_{\rm ret}$ has a dimension of time, while θ is a phase.

$\nabla^a t_{\rm ret}$[2]. The tetrad vectors satisfy the relation

$$-k_a l^a = m_a \bar{m}^a = 1, \tag{E.26}$$

while all other products vanish. For convenience, we introduce the tetrad notation.

$$z_{\boldsymbol{m}a} = (k_a, l_a, m_a, \bar{m}_a), \tag{E.27}$$

where $\boldsymbol{m}$ runs over $\mathbf{0}, \mathbf{1}, \mathbf{2}, \mathbf{3}$. [3]

We also adopt the notation such that the null-tetrad components of some tensor $X_{abc\cdots}$ can be written as

$$X_{\boldsymbol{abc}\cdots} := X_{abc\cdots} z^a_{\boldsymbol{a}} z^b_{\boldsymbol{b}} z^c_{\boldsymbol{c}} \cdots \tag{E.28}$$

The Bianchi identity in terms of the tetrad components can be expressed as [4]

$$R_{\boldsymbol{ab}[\boldsymbol{pq},\mathbf{2}]} = 0. \tag{E.29}$$

On the other hand, only their derivatives with respect to $t_{\rm ret}$ are non-vanishing [5]

$$R_{\boldsymbol{abcd},\boldsymbol{p}} = 0 \tag{E.30}$$

where $(\boldsymbol{a}, \boldsymbol{b}, \boldsymbol{c}, \boldsymbol{d})$ run over $(k, l, m, \bar{m})$, while $(\boldsymbol{p}, \boldsymbol{q}, \boldsymbol{r}, \cdots)$ run over $(k, m, \bar{m})$. So, we can re-express the Bianchi identity as

$$\frac{1}{3} R_{\boldsymbol{abpq},\mathbf{2}} = 0. \tag{E.31}$$

It leads

$$R_{\boldsymbol{abpq}} = 0, \tag{E.32}$$

except for a non-wavelike constant. As a result, $R_{\boldsymbol{abpq}}$ are all non-vaishing six independent components from the symmetry of the Riemann tensor.

Consequently, for the plane wave, the Newman-Penrose quantities can be

[2] $k^a = \partial^a t_{\rm ret} = (-\partial_0 t_{\rm ret}, \partial_i t_{\rm ret}) =$ with $t = \eta_{ab} k^a x^b$.

[3] Small latin $a, b, \cdots$ are tensor indices in the abstract index notation, and bold latin $\boldsymbol{a}, \boldsymbol{b}, \cdots$ are tetrad indices.

[4] The $\mathbf{2}$ corresponds to l_a in the tetrad notation.

[5] This can be derived by relations such as $\partial_k = 2^{-1/2}(\partial_t + \partial_z)$.

calculated as,

$$\Psi_0 = \Psi_1 = 0, \tag{E.33}$$

$$\Psi_2 = -\frac{1}{6}R_{\mathbf{1010}}, \tag{E.34}$$

$$\Psi_3 = -\frac{1}{2}R_{\mathbf{1013}}, \tag{E.35}$$

$$\Psi_4 = -R_{\mathbf{1313}}, \tag{E.36}$$

$$\Phi_{00} = \Phi_{01} = \Phi_{10} = \Phi_{02} = \Phi_{20} = 0, \tag{E.37}$$

$$\Phi_{22} = -R_{\mathbf{1213}}, \tag{E.38}$$

$$\Phi_{11} = \frac{3}{2}\Psi_2, \tag{E.39}$$

$$\Phi_{12} = \bar{\Phi}_{21} = \bar{\Psi}_3, \tag{E.40}$$

$$\Lambda = -\frac{1}{2}\Psi_2, \tag{E.41}$$

As a result, we can choose $\{\Psi_2,\ \Psi_3,\ \Psi_4,\ \Phi_{22}\}$ to describe the six independent components. Newman-Penrose quantities are defined in (13.2.25) in [2]. Please refer to Chapter 13 in [2] for spinor.

We consider the transformation of the Newman-Penrose quantities under the little group of the Lorentz transformation that leaves the wave vector k fixed. We consider two standard observers O and O', whose tetrads are $(k,\ l,\ m,\ \bar{m})$ and $(k',\ 'l,\ m',\ \bar{m}')$ with $k = k'$, respectively. Suppose that O measures $(\Psi_2, \Psi_3, \Psi_4, \Phi_{22})$ and O' measures $(\Psi'_2, \Psi'_3, \Psi'_4, \Phi'_{22})$. We obtain the $E(2)$ classification by investigating the properties of the quantities under the Lorentz transformation. Here, we are interested in the case in which $A = 1$ and the propagation direction k is unchanged.

$$k \to k' = k, \tag{E.42a}$$

$$m \to m' = e^{i\theta}(m + ak), \tag{E.42b}$$

$$\bar{m} \to \bar{m}' = e^{-i\theta}(\bar{m} + a^*k), \tag{E.42c}$$

$$l \to l' = l + a^*m + a\bar{m} + aa^*k. \tag{E.42d}$$

The transformations described by Eq. (E.42) form a subgroup of the Lorentz group, which is globally isomorphic to the abstract Lie group $E(2)$. Under the

transformations, $(\Psi_2, \Psi_3, \Psi_4, \Phi_{22})$ transform as

$$\Psi_2' = \Psi_2, \tag{E.43a}$$
$$\Psi_3' = e^{-i\theta}(\Psi_3 + 3a^*\Psi_2), \tag{E.43b}$$
$$\Psi_4' = e^{-2i\theta}(\Psi_4 + 4a^*\Psi_3 + 6a^{*2}\Psi_2), \tag{E.43c}$$
$$\Phi_{22}' = \Phi_{22} + 2a\Psi_3 + 2a^*\bar{\Psi}_3 + 6aa^*\Psi_2. \tag{E.43d}$$

Now, we shall consider rotations around z-axis by θ, so $a = 0$. Eq. (E.43) indicates that $(\Psi_2, \Psi_3, \Psi_4, \Phi_{22})$ are helicity eigenstates as follows [6]

$$\Psi_2 : s = 0, \tag{E.44a}$$
$$\Psi_3 : s = -1, \ \bar{\Psi}_3 : \ s = +1, \tag{E.44b}$$
$$\Psi_4 : s = -2, \ \bar{\Psi}_4 : \ s = +2, \tag{E.44c}$$
$$\Phi_{22} : s = 0. \tag{E.44d}$$

From Eq. (E.43), $(\Psi_2, \Psi_3, \Psi_4, \Phi_{22})$ can not be specified model independently. However, we can classify the GWs into some representation in a $E(2)$ invariant manner. The name of each class is named by the Petrov type of its nonvanishing Weyl tensor and the maximum number of nonvanishing amlitude $(\Psi_2, \Psi_3, \Psi_4, \Phi_{22})$ that is the dimension of representation, which are independent of observer. Invariant $E(2)$ classes are as follows.

Class II_6: $\Psi_2 \neq 0$. All observers measure the same nonzero Ψ_2, but the presence or absence of other modes is observer dependent.

Class III_5: $\Psi_2 = 0, \ \Psi_3 \neq 0$. All observers measure the absence of Ψ_2 and the presence of Ψ_3, but the presence or absence of Ψ_4 and Φ_{22} is observer dependent.

Class N_3: $\Psi_2 = 0, \ \Psi_3 = 0, \ \Psi_4 \neq 0, \Phi_{22} \neq 0$. Presence or absence of all modes is independent of observer.

Class N_2: $\Psi_2 = 0, \ \Psi_3 = 0, \ \Phi_{22} = 0, \Psi_4 \neq 0$. Presence or absence of all

[6] A quantity X that transforms under the rotation of θ as $X' = e^{is\theta}X$ is said to have helicity s.

modes is independent of observer.

Class O_1: $\Psi_2 = 0,\ \Psi_3 = 0,\ \Psi_4 = 0, \Phi_{22} \neq 0$. Presence or absence of all modes is independent of observer.

Class O_0: $\Psi_2 = 0,\ \Psi_3 = 0,\ \Psi_4 = 0, \Phi_{22} = 0$. Presence or absence of all modes is independent of observer. No wave.

II_6 and III_5 form reducible and indecomposable representations of $E(2)$. The invariant subspace is the space spanned by Ψ_4 and Φ_{22}. N_3, N_2, and O_1 form decomposable representations having invariant subspaces spanned by Ψ_4 and Φ_{22}, respectively.

Here, we apply the E(2) classification to some specific alternative theories of gravity that predict null or nearly null GWs and review the possible polarization modes in the alternative theories of gravity [7, 79].

General relativity

In GR, the far-field, linearized, vacuum field equation is given by

$$R_{ab} = 0, \tag{E.45}$$

From this field equation, we get

$$R_{\mathbf{1010}} = R_{\mathbf{1212}} = R_{\mathbf{1012}} = R_{\mathbf{1013}} = 0, \tag{E.46}$$

or

$$\Psi_2 = \Psi_3 = \Phi_{22} = 0 \neq \Psi_4. \tag{E.47}$$

Thus, the $E(2)$ classification of GR is N_2. The inspiral GW waveform in GR is calculated in the latter section Section 3.3.

Scalar-tensor theory

Scalar-tensor theories [176–179] have a scalar field ϕ in addition to the metric tensor and described by the action

$$S = \frac{1}{16\pi} \int \left[\phi R - \frac{\omega(\phi)}{\phi} \phi^{,\mu} \phi_{,\mu} + V(\phi) \right], \tag{E.48}$$

where $\omega(\phi)$ is the function and $V(\phi)$ is the self-interaction potential for ϕ. The variation gives the field equations

$$\begin{aligned} R_{ab} - \frac{1}{2}g_{ab}R = \frac{8\pi}{\phi}T_{ab} + \frac{1}{\phi}[\partial_a\partial_b - g_{ab}\Box]\phi \\ + \frac{\omega}{\phi^2}(\partial_a\phi\partial_b\phi - \frac{1}{2}g_{ab}(\partial\phi)^2) - g_{ab}\frac{V}{2\phi}, \end{aligned} \tag{E.49}$$

and

$$\frac{3+2\omega}{\phi}\Box\phi = \frac{8\pi}{\phi}T - \frac{\omega'(\phi)}{\phi}(\partial\phi)^2 + V'(\phi) - 2\frac{V}{\phi}. \tag{E.50}$$

Brans-Dicke theory [70] is a special case of scalar-tensor theories with

$$\omega(\phi) = \omega = const., \tag{E.51}$$

and we can set $V(\phi)$ to zero in the massless case

$$V(\phi) = 0. \tag{E.52}$$

In Brans-Dicke theory, the far-field, linearized, vacuum field equation is given by

$$\Box\phi = 0, \tag{E.53}$$

$$R_{ab} - \frac{1}{2}g_{ab}R = \omega\phi^{-2}(\phi_{,a}\phi_{,b} - \frac{1}{2}g_{ab}\phi_{,c}\phi^{,c}) + \phi^{-1}(\phi_{,ab} - g_{ab}g^{cd}\phi_{,cd}), \tag{E.54}$$

$$R = \omega\phi^{-2}\phi_{,c}\phi^{,c}. \tag{E.55}$$

From the wave solution

$$\phi = \phi_0 + \phi_1 e^{ik_e x^e}, \tag{E.56}$$

with constants ϕ_0 and ϕ_1 and Eq. (E.54), we get

$$R = 0, \tag{E.57}$$

and then we obtain

$$R_{ab} = -\phi_0^{-1}\phi_1 e^{ik_e x^e} q_a q_b. \tag{E.58}$$

From these relations, we get

$$R_{\mathbf{1010}} = R_{\mathbf{1012}} = R_{\mathbf{1013}} = 0 \neq R_{\mathbf{1213}}, \tag{E.59}$$

or

$$\Psi_2 = \Psi_3 = 0, \quad \Phi_{22} \neq 0 \neq \Psi_4. \tag{E.60}$$

Thus, the $E(2)$ classification of Brans-Dicke theory is N_3. The inspiral GW waveform in Brans-Dicke theory is calculated in the latter section Section 3.3.

Vector-tensor theory

Vector-tensor theories [7, 180, 181] have a time-like vector field K_a in addition to the metric tensor and are described by the action.

$$S = \frac{1}{16\pi}\int [R + \omega K_a K^a R + \eta K^a K^b R_{ab} - \epsilon F_{ab}F^{ab} + \tau K_{a;b}K^{a;b}], \tag{E.61}$$

where $\omega, \eta, \epsilon, \tau$ are constants and

$$F_{ab} := K_{b;a} - K_{a;b}. \tag{E.62}$$

The variation gives the field equations

$$R_{ab} - \frac{1}{2}g_{ab}R + \omega\Theta^{(\omega)}_{ab} + \eta\Theta^{(\eta)}_{ab} + \epsilon\Theta^{(\epsilon)}_{ab} + \tau\Theta^{(\tau)}_{ab} = 8\pi T_{ab}, \tag{E.63}$$

with

$$\Theta^{(\omega)}_{ab} = K_aK_bR + K^2R_{ab} - \frac{1}{2}K^2R - (K^2)_{;ab} + g_{ab}\Box_g K^2, \tag{E.64}$$

$$\begin{aligned}\Theta^{(\eta)}_{ab} =& 2K^cK_{(a}R_{b)c} - \frac{1}{2}K^cK^dR_{cd} - (K^cK_{(a})_{;b)c} \\ &+ \frac{1}{2}\Box_g(K_aK_b) + \frac{1}{2}g_{ab}(K^cK^d)_{;cd},\end{aligned} \tag{E.65}$$

$$\Theta^{(\epsilon)}_{ab} = -2(F^c_aF_{bc} - \frac{1}{4}g_{ab}F_{cd}F^{cd}), \tag{E.66}$$

$$\begin{aligned}\Theta^{(\tau)}_{ab} =& K_{a;c}K^{;c}_{b} + K_{c;a}K^{c}_{;b} - \frac{1}{2}g_{ab}K_{c;d}K^{c;d} \\ &+ (K^{c}K_{(a;b)} - K^{c}_{;(a}K_{b)} - K_{(a}K^{;c}_{b)})_{;c}\end{aligned} \tag{E.67}$$

Will-Nordtvedt theory [180] is a special case of vector-tensor theories with

$$\omega = \eta = \epsilon = 0, \quad \tau = 1. \tag{E.68}$$

In Will-Nordtvedt theory, the far-field, linearized, vacuum field equation is given by

$$\Box K_a = 0, \tag{E.69}$$

$$\begin{aligned}R_{ab} - \frac{1}{2}Rg_{ab} =& K_{a,c}K_{b}{}^{,c} + K_{c,a}K^{c}{}_{,b} - \frac{1}{2}g_{ab}K^{c}{}_{,d}K^{,d}_{c} \\ &+ \frac{1}{2}[2K^{c}K_{(a,b)} - K_{a}(K^{c}{}_{,b} + K_{b}{}^{,c}) - K_{b}(K^{c}{}_{,a} + K_{a}{}^{,c})]_{,c}.\end{aligned} \tag{E.70}$$

From the wave solution

$$K_a = A_a e^{ik_e x^e} + B_a, \tag{E.71}$$

with constants A_a and B_a and Eq. (E.70), we get

$$R = 0, \tag{E.72}$$

and

$$R_{ab} = e^{ik_e x^e}[(k_c A^c)k_{(a}B_{b)} - (B_c k^c)A_{(a}k_{b)}]. \tag{E.73}$$

From these relations, we get

$$R_{\mathbf{12}} \neq 0, R_{\mathbf{13}} \neq 0, R_{\mathbf{11}} \neq 0, \tag{E.74}$$

or

$$\Psi_2 = 0, \Psi_3 \neq 0, \Phi_{22} \neq 0. \tag{E.75}$$

Thus, the $E(2)$ classification of Will-Nordtvedt theory is III_5.

$f(R)$ gravity

$f(R)$ gravity [74] is a type of modified gravity theory and described by the action

$$S = \frac{1}{16\pi}\int f(R), \tag{E.76}$$

where $f(R)$ is the function of the Ricci scalar R. The $f(R)$ model with $R + \alpha R^2$ was first applied as an inflationary model by Starobinsky [182] and is consistent with the current observations [183]. The $f(R)$ gravity with $R+\alpha R^{-1}$ [184–187] was also modeled to explain the late time cosmic acceleration from the supernova observations [188, 189] although they are ruled out by the solar system tests [190,191]. More viable $f(R)$ models have been proposed [192–195]. The polarizations in $f(R)$ gravity was investigated in [196–203].

In $f(R)$ gravity, the far-field, linearized, vacuum field equation is given by

$$f'R_{ab} - \frac{1}{2}f g_{ab} - \nabla_a\nabla_b f' + g_{ab}\Box f' = 0, \tag{E.77}$$

where $f' = df/dR$. Here, we consider $f(R) = R + \alpha R^2$ and then obtain

$$\left(\Box - \frac{1}{6\alpha}\right) R = 0. \tag{E.78}$$

From the wave solution

$$R = R_0 e^{ik_e x^e}, \tag{E.79}$$

where R_0 is the constant, we get

$$R_{tt} = \frac{1}{2}(4\alpha k^2 + 1)R, \tag{E.80a}$$

$$R_{tz} = 2\alpha k\sqrt{k^2 + \frac{1}{6\alpha}R}, \tag{E.80b}$$

$$R_{zz} = \frac{1}{6}(-12\alpha k^2 + 1)R. \tag{E.80c}$$

From these relations, we get

$$R_{\mathbf{13}} = 0, R_{\mathbf{11}} \neq 0, R_{\mathbf{12}} \neq 0, \tag{E.81}$$

Table E.1: Possible polarization modes in alternative theories of gravity.

	+	×	x	y	b	l	reference
General relativity	✓	✓	–	–	–	–	[69]
Brans-Dicke theory	✓	✓	–	–	✓	✓	[204]
Will-Nordtvedt theory	✓	✓	✓	✓	✓	–	[68]
$f(R)$ gravity	✓	✓	–	–	✓	✓	[202]
Kaluza-Klein theory	✓	✓	✓	✓	✓	–	[205]
Bimetric theory	✓	✓	✓	✓	✓	✓	[96]
Horndeski theory	✓	✓	–	–	✓	✓	[77]
Einstein-æther theory	✓	✓	✓	✓	✓	✓	[173]

or

$$\Psi_3 = 0, \Psi_2 \neq 0, \Phi_{22} \neq 0, \Psi_4 \neq 0. \tag{E.82}$$

Thus, the $E(2)$ classification of $f(R)$ gravity is II_6.

The possible polarization modes have been reported in many alternative theories. We briefly summarize the possible polarizations and the references in Table E.1.

Appendix F

Inspiral waveforms in alternative theories

Here, we calculate the detector signal in several theories of gravity to construct the general parametrized inspiral waveforms so-called general parametrized post Einsteinian waveforms based on the derived specific waveforms.

General relativity

In GR, the trace-reversed metric perturbation for a quasi-circular binary system is given by the quadrupole formula

$$\bar{h}^{ij} = \frac{2}{d_L} Q^{ij}, \tag{F.1}$$

to leading PN order with the quadrupole moment

$$Q^{ij} = 2\mu \frac{m}{R_s} (\hat{v}^i \hat{v}^j - \hat{x}^i \hat{x}^j), \tag{F.2}$$

where $\mu := \eta m$ is the reduced mass and R_s is the orbital radius.

From Eq. (F.1), Eq. (3.24), and Eq. (3.23), we obtain

$$h_+ = \frac{2\mu m}{d_L R_s} \cos 2\Phi (1 + \cos^2 \iota), \tag{F.3a}$$

$$h_\times = \frac{4\mu m}{d_L R_s} \sin 2\Phi \cos \iota. \tag{F.3b}$$

From Eq. (3.38) and these polarization components, the time domain in-

spiral GW detector signal from the CBC in GR can be written as [110, 124],

$$h(t) \simeq \frac{2\mu m}{r(t)D_L}\mathscr{A}(t)\cos\left(\int^t f_{\rm GW}(t')dt' + \phi_p(t) + \phi_D(t)\right), \tag{F.4}$$

where the polarization amplitude $\mathscr{A}(t)$ and the polarization phase $\phi_p(t)$ are defined as

$$\mathscr{A}(t) := \sqrt{(1+\cos^2\iota)^2 F^+(t)^2 + 4\cos^2\iota F^\times(t)^2}, \tag{F.5}$$

$$\phi_p(t) := \arctan\left(\frac{2\cos\iota F^\times(t)}{(1+\cos^2\iota)F^+(t)}\right), \tag{F.6}$$

respectively, and $\phi_D(t)$ is so-called the doppler phase representing the arrival time difference between at the center of the Earth and at the GW detector.

We can evaluate the Fourier component of the observed signal by the SPA, since the factors such as $(2m_1m_2)/(r(t)D_L), \mathscr{A}(t), \phi_p$, and ϕ_D change in time slowly. From the Virial theorem, the binding energy of the binary system becomes

$$E_{\rm GR} = E_{\rm kinetic} + E_{\rm potential} = \frac{1}{2}\mu v^2 - \frac{\mu m}{r} = -\frac{\mu m}{2r}. \tag{F.7}$$

We find the radiated power per unit solid angle

$$\begin{aligned}\frac{dP}{d\Omega} &= \frac{d_L^2}{32\pi}\langle \dot{h}_{ij}^{TT}\dot{h}_{ij}^{TT}\rangle, \\ &= \frac{d_L^2}{16\pi}\langle \dot{h}_+^2 + \dot{h}_\times^2\rangle, \\ &= \frac{2\mu^2 m^2\Omega^2}{\pi r^2}\left\{\left(\frac{1+\cos^2\iota}{2}\right)^2 + \cos^2\iota\right\}.\end{aligned} \tag{F.8}$$

We then obtain he rate of change of the binding energy as the rate of change of the radiated GW energy

$$\dot{E}_{\rm GR} = \frac{32}{5}\frac{\mu^2 m^2\Omega^2}{r^2} = \frac{32}{5}(2\pi\mathcal{M}F)^{10/3}, \tag{F.9}$$

where we used the Kepler's law $\Omega^2 = m/r^3$. Equating the time derivative of $E_{\rm GR}$ and $\dot{E}_{\rm GR}$, we obtain the orbital frequency change rate

$$\frac{dF}{dt} = \frac{48}{5\pi\mathcal{M}^2}(2\pi\mathcal{M}F)^{11/3}. \tag{F.10}$$

Employing SPA, the Fourier transforms of the observed signal can be evaluated as [1, 123–126],

$$h_I(f) = \mathcal{A} f^{-7/6} e^{-i\Psi(f)} \left\{ \frac{5}{4} \mathscr{A}(t(f)) \right\} e^{-i(\phi_p(t(f)) + \phi_D(t(f)))}. \tag{F.11}$$

Here, we define the geometrical factor for tensor modes as

$$\mathcal{G}_{T,I} := \frac{5}{4} \{ (1 + \cos^2 \iota) F_{+,I}(t) + 2i \cos \iota F_{\times,I}(t) \} e^{i\phi_{D,I}(\theta_s, \phi_s, \theta_e, \phi_e)}, \tag{F.12}$$

where (θ_s, ϕ_s) are the the source direction angular parameters and (θ_e, ϕ_e) are detector position parameters. Here, the factor of $5/4$ is inserted for normalization of Eq. (F.12) over angular parameters. Then, we rewrite the detector signal as

$$h_I(f) = \mathcal{A} f^{-7/6} e^{-i\Psi(f)} \mathcal{G}_{T,I}(t(f)). \tag{F.13}$$

The GW amplitude $\mathcal{A}$ and the GW phase $\Psi(f)$ are given by

$$\mathcal{A} f^{-7/6} = \frac{1}{\sqrt{30}\pi^{2/3} d_L} \left(\frac{G\mathcal{M}}{c^3} \right)^{5/6} f^{-7/6}, \tag{F.14}$$

and

$$\Psi^{(l)}_{\rm GR}(f) = \frac{\pi}{4} + l\phi_c - 2\pi f t_c - \frac{3l}{256 u_l^5}. \tag{F.15}$$

up to leading order. Here, t_c is the coalescence time and ϕ_c is the phase at the coalescence time.

Note that $t(f)$ is given by integrating Eq. (F.10) and equating $f_{\rm GW} = F/l = f$

$$t(f) := t_* = t_c - \frac{5}{256} \mathcal{M}^{-5/3} (\pi f)^{-8/3}, \tag{F.16}$$

such that the condition for the stationary point

$$f = f_{\rm gw}(t_*), \tag{F.17}$$

is hold. Here, $\mathcal{M}$ is the source chirp mass and t_c is the coalescence time. In other words, $t(f)$ shows the relationship between the frequency of the GW

and the time to merger. Fig. 5.3 shows the time to merger as functions of the frequency of the GW for typical $1.4M_\odot - 1.4M_\odot$, $10M_\odot - 10M_\odot$, and $30M_\odot - 30M_\odot$ compact binary systems.

Post-Newtonian formalism Here, we briefly review the generation of the GWs beyond quadrupole formula for inspiral GWs. Some important approximations such as the post-Newtonian method (or non-linear $1/c$-expansion), the post-Minkowskian method or non-linear iteration (G-expansion), the far-zone expansion ($1/R$-expansion in the distance to the source), and the perturbation in the small mass limit (ν-expansion in the mass ratio of a binary system) are utilized in full theory of GR beyond linearized thory. The post-Minkowskian and the post-Newtonian formalism can approximately solve the Einstein equations and describe the GWs in the full theory of GR. For self gravitating systems, one can not assume that the background metric is independent of the source velocity, which is assumed in the linearized theory because $v/c \sim \sqrt{R_s/d}$ holds from the Virial theorem where $R_s = 2Gm/c^2$ is the Schwarzschild radius. The post-Minkowskian theory is an approximation to GR with a formal expansion in powers of G to measure the strength of the field. The post-Newtonian theory is an approximation to GR that combines an expansion in powers of G (to measure the strength of the field) with an expansion in powers of c^{-2} (to measure the velocity of the matter). The post-Minkowskian expansion is uniformly valid over all space-time when the source is weakly self-gravitating. On the other hand, the post-Newtonian approximation is valid under the assumptions of a weak gravitational field inside the source and of slow internal motions. In addition, for the post-Newtonian method the domain of validity is limited to the near zone of the source where the distance is much short with respect to the wavelength of the GWs. In a sense, the post-Minkowskian method is more fundamental than the post-Newtonian method and each coefficient of the post-Minkowskian series can in turn be re-expanded in a post Newtonian approach. However, even in the post-Minkowskian method, it is popular to assume that the fluid of the matter satisfy the slow motion condition because we consider the astrophysical systems in which the Virial theorem insist that (Potential energy) $\sim$ v^2 or that weak fields are naturally accompanied by slow motion, and any attempt

to keep the arbitrary velocities in the post-Minkowskian approach soon encounters the unmanageable calculations. Due to paper limitations, it is not possible to provide an exhaustive summary covering the post-Minkowskian and the post-Newtonian formalism, so please refer to [1, 69, 206] for details.

The space is divided into multiple regions corresponding to the range of application of the approximation method. The exterior near zone is the region

$$d < r << \lambda. \tag{F.18}$$

The far zone (or the wave zone) is the region

$$\lambda << r. \tag{F.19}$$

In computing GWs from a non-relativistic, self-gravitating, source with typical velocity v, there are two length scales: the typical source size d and an arbitrarily selected radius $\mathcal{R}$ that is placed for the boundary of the near zone and the far zone (having the same order of magnitude as λ). In other words, the exterior near zone is the region

$$d < r < \mathcal{R}. \tag{F.20}$$

The far zone (or the wave zone) is the region

$$\mathcal{R} < r. \tag{F.21}$$

In the near zone, the gravitational field can be calculated by the post-Newtonian formalism. However, the post-Newtonian approach becomes inapplicable at $r > \mathcal{R}$. On the other hand, the matter contribution to the stress-energy tensor vanishes outside the source at $r > d$ and the field will approach Minkowski space-time more and more as r increases. Thus, we can solve the Einstein vacuum equations over $d < r < \infty$ using a post-Minkowskian expansion that takes into account iteratively the deviation from flat space-time. In the post-Newtonian (PN) formalism, there are two formalism such as the Blanchet-Damour-Iyer (BDI) formalism [45] and another approach known as the Direct Integration of the Relaxed Einstein (DIRE) formalism, which can be shown to

be completely equivalent each other.

First, we define the tensor field denoted as the typographical symbol as

$$\mathsf{h}^{ab} := \sqrt{-g}g^{ab} - \eta^{ab}, \tag{F.22}$$

which reduces to $\bar{h}^{ab}$ in the linearized theory except for an overall sign when the metric g^{ab} can be written in the form $g_{ab} = \eta_{ab} + h_{ab} + O(h^2)$. Now, we impose the harmonic gauge condition

$$\partial_a(\sqrt{-g}g^{ab}) = \partial_a \mathsf{h}^{ab} = 0, \tag{F.23}$$

and then find the relaxed Einstein field equations

$$\Box \mathsf{h}^{ab} = \frac{16\pi G}{c^4}\tau^{ab}, \tag{F.24}$$

where

$$\tau^{ab} = (-g)T^{ab} + \frac{c^4}{16\pi G}\Lambda^{ab}, \tag{F.25}$$

with

$$\Lambda^{ab} := \frac{16\pi G}{c^4}(-g)t_{LL}^{ab} + (\partial_d \mathsf{h}^{ac}\partial_c \mathsf{h}^{bd} - \mathsf{h}^{cd}\partial_c\partial_d \mathsf{h}^{ab}), \tag{F.26}$$

where t_{LL}^{ab} is the Landau-Lifshitz energy momentum pseudotensor,

$$\begin{aligned}\frac{16\pi G}{c^4}(-g)t_{LL}^{ab} :=& g_{fc}g^{de}\partial_d \mathsf{h}^{af}\partial_e \mathsf{h}^{bc} + \frac{1}{2}g_{fc}g^{ab}\partial_e \mathsf{h}^{fd}\partial_d \mathsf{h}^{ec} \\ &- g_{cd}(g^{fa}\partial_e \mathsf{h}^{bd} + g^{fb}\partial_e \mathsf{h}^{ad})\partial_f \mathsf{h}^{ec} \\ &+ \frac{1}{8}(2g^{af}g^{bc} - g^{ab}g^{fc})(2g_{de}g_{gh} - g_{eg}g_{dh})\partial_f \mathsf{h}^{dh}\partial_c \mathsf{h}^{eg}.\end{aligned} \tag{F.27}$$

The solution to Eq. (F.24) can be obtained formally as

$$\mathsf{h}^{ab}(t, \boldsymbol{x}) = -\frac{4G}{c^4}\int d^3x' \frac{1}{|\boldsymbol{x} - \boldsymbol{x}'|}\tau^{ab}\left(t - \frac{|\boldsymbol{x} - \boldsymbol{x}'|}{c}, \boldsymbol{x}'\right). \tag{F.28}$$

Note that the τ^{ab} depends on h^{ab}, which is a manifestation of the nonlinear effect in GR. The strategy of the BDI formalism is to use the post-Newtonian expansion in the near zone and to use post-Minkowskian expansion outside the source for the relaxed Einstein field equations, and then to match them in the

overlap zone. The strategy of the DIRE formalism is to iterate the solution to the formal solution for the relaxed Einstein field equations.

Here, we apply the post-Newtonian approach to the GWs from the inspiraling compact binary. The post-Newtonian expansion of the gravitational field is formally expansion in powers of $1/c$, but physically in powers of a dimensionless quantity such as v/c where v is the typical velocity. There are many candidates as such expansion parameter. For example, it is useful to introduce

$$\beta := \left(\frac{Gm\Omega}{c^3}\right)^{1/3}, \tag{F.29}$$

where $m = m_1 + m_2$ is the total mass and Ω is the binary angular velocity. The another choice is $\sqrt{Gm/(rc^2)}$. Note that writing $\beta = [(Gm/r)(r\Omega/c^3)]^{2/3}$ and using $Gm/r \sim v^2$ and $r\Omega \sim v$ where r is the binary radius, we find $\beta = O(v^2/c^2)$. Note that also $\sqrt{Gm/(rc^2)} \sim O(v^2/c^2)$. Here, we adopt β as the PN parameter. The v/c corrections correspond to the corrections in powers of $\beta^{1/2}$. In the PN formalism, we say the nPN order for terms proportional to β^n.

In the context of the PN theory, the two tensor GW polarizations produced by a circular binary system have the general structure as

$$h_{+,\times} = \frac{2G\mu\beta}{c^2 r}\sum_{p\leq 0}\beta^{p/2}H^{(p/2)}_{+,\times} + O\left(\frac{1}{r^2}\right). \tag{F.30}$$

The leading terms are

$$H^{(0)}_{+} = -(1+C^2)\cos 2\psi, H^{(0)}_{\times} = -2C\sin 2\psi, \tag{F.31a}$$

where we use the short-notation $C := \cos\iota, S := \sin\iota$. The sign deference in this equations and Eq. (F.3b) comes from the sign difference in Eq. (F.22). Here, the auxiliary phase so-called tail-distorted phase is defined as

$$\psi(t) := \phi(t) - \frac{2Gm\Omega}{c^3}\log\left(\frac{\Omega}{\Omega_0}\right), \tag{F.32}$$

and Ω_0 is a constant frequency at which the signal enters the sensitive region of the detector where the phase ϕ receives a correction from the scattering of

the GW off the static curvature generated by the binary itself. The use of ψ instead of the actual phase ϕ for the source is useful because it allows us to collect the logarithmic terms for the tail effects.

The other polarizations up to 1.5PN order are

$$H_+^{(1/2)} = \Delta\left[-\frac{1}{8}S(5+C^2)\cos\psi + \frac{9}{8}S(1+C^2)\cos 3\psi\right], \tag{F.33a}$$

$$H_+^{(1)} = \frac{1}{6}[(19+9C^2-2C^4)-(19-11C^2-6C^4)\eta]\cos 2\psi - \frac{4}{3}(1-3\eta)S^2(1+C^2)\cos 4\psi, \tag{F.33b}$$

$$H_+^{(3/2)} = \Delta\left[\frac{1}{192}S[(57+60C^2-C^4)-2(49-12C^2-C^4)\eta]\cos\psi - \frac{9}{128}S[(73+40C^2-9C^4)-2(25-8C^2-9C^4)\eta]\cos 3\psi + \frac{625}{384}(1-2\eta)S^3(1+C^2)\cos 5\psi\right] - 2\pi(1+C^2)\cos 2\psi, \tag{F.33c}$$

and

$$H_\times^{(1/2)} = \Delta\left[-\frac{3}{4}SC\sin\psi + \frac{9}{4}SC\sin 3\psi\right], \tag{F.34a}$$

$$H_\times^{(1)} = \frac{1}{3}C[(17-4C^2)-(13-12C^2)\eta]\sin 2\psi - \frac{8}{3}(1-3\eta)S^2C\sin 4\psi, \tag{F.34b}$$

$$H_\times^{(3/2)} = \Delta\left[\frac{1}{96}SC[(63-5C^2)-2(23-5C^2)\eta]\sin\psi - \frac{9}{64}SC[(67-15C^2)-2(19-15C^2)\eta]\sin 3\psi + \frac{625}{192}(1-2\eta)S^3C\sin 5\psi\right], \tag{F.34c}$$

where $\Delta := (m_1-m_2)/m$. The higher polarizations are provided in [206,207].

The orbital phase ϕ is given by

$$\begin{aligned}\phi =& -\frac{\beta^{-5/2}}{32\eta}\left[1+\left(\frac{3715}{1008}+\frac{55}{12}\right)x-10\pi\beta^{3/2}\right.\\&+\left(\frac{15293365}{1016064}+\frac{27145}{1008}\eta+\frac{3085}{144}\eta^2\right)\beta^2+\left(\frac{38645}{1344}-\frac{65}{16}\eta\right)\pi\beta^{5/2}\ln\left(\frac{\beta}{\beta_0}\right)\\&+\left[\frac{12348611926451}{18776862720}-\frac{160}{3}\pi^2-\frac{1712}{21}\mathcal{C}-\frac{856}{21}\ln\left(16\beta\right)\right.\\&+\left(-\frac{15737765635}{12192768}+\frac{2255}{48}\pi^2\right)\eta+\frac{76055}{6912}\eta^2-\frac{127825}{5184}\eta^3\Big]\beta^3\\&\left.+\left(\frac{77096675}{2032128}+\frac{378515}{12096}\eta-\frac{74045}{6048}\eta^2\right)\pi\beta^{7/2}+O\left(\frac{1}{c^8}\right)\right].\end{aligned}\tag{F.35}$$

where $\mathcal{C}$ is the Euler-Mascheroni constant. We shall outline the procedure to find these expressions because a long calculation is required. To derive Eq. (F.30), we need calculate the generation expressions of the GWs, the equation of motion of the binary system, and the phase evolution of the binary system. The generation of the GWs can be derived by solving the relaxed Einstein equations. In the BDI formalism, the relaxed Einstein equations can be solved using the PM approximation and the PN approximation. In the external domain $d < r < \infty$, the metric is expanded as

$$\mathsf{h}^{\alpha\beta}=\sum_{n=1}^{\infty}G^n\mathsf{h}_n^{\alpha\beta}.\tag{F.36}$$

Substituting this into the relaxed Einstein equations, we find the n-th order equation

$$\Box\mathsf{h}_n^{\alpha\beta}=\Lambda_n^{\alpha\beta}[\mathsf{h}_1,\ldots,\mathsf{h}_{n-1}].\tag{F.37}$$

The solution becomes the form of

$$\mathsf{h}_n^{\alpha\beta}=u_n^{\alpha\beta}+v_n^{\alpha\beta}.\tag{F.38}$$

where $v_n^{\alpha\beta}$ is a solution of the homogeneous equation, chosen satisfying the harmonic gauge condition $\partial_\alpha v_n^{\alpha\beta}=-\partial_\alpha u_n^{\alpha\beta}$ and $u_n^{\alpha\beta}$ is a particular solution of the inhomogeneous solution. Next, we consider in the near zone $r < \mathcal{R}$. Similar

in the above PM expansion, we expand the metric and the stress-energy tensor as

$$\mathsf{h}^{\alpha\beta} = \sum_{n=2}^{\infty} \frac{1}{c^n} {}^{(n)}\mathsf{h}^{\alpha\beta}, \tag{F.39}$$

and

$$\tau^{\alpha\beta} = \sum_{n=-2}^{\infty} \frac{1}{c^n} {}^{(n)}\tau^{\alpha\beta}, \tag{F.40}$$

where we use $1/c^n$ to keep track of the small parameter. Substituting this into the relaxed Einstein equations and collecting the relevant powers of v/c, we find a set of recursive Poisson-like equations

$$\nabla^2[{}^{(n)}\mathsf{h}^{\alpha\beta}] = 16\pi[{}^{(n-4)}\tau^{\alpha\beta}] + \partial_t^2[{}^{(n-2)}\mathsf{h}^{\alpha\beta}]. \tag{F.41}$$

Similarly the solution becomes the form of

$$\mathsf{h}_n^{\alpha\beta} = u_n^{'\alpha\beta} + v_n^{'\alpha\beta}. \tag{F.42}$$

with the solution of the homogeneous equation $v_n^{'\alpha\beta}$ and a particular solution of the inhomogeneous solution $u_n^{'\alpha\beta}$.

The most general solution in the PM expansion is characterized by the set of multipole moments $\{I_L, J_L, W_L, X_L, Y_L, Z_L\}$, which are not unspecified and know nothing about the properties of the source and just most general solution. On the other hand, in the PN approximation, the gravitational field is expressed by the stress-energy tensor of the matter source. By matching the PM result to the PN result in the overlap region $d < r < \mathcal{R}$. Specifically, comparing the multipolar PN expansion with the PN re-expansion of the PM solution, we can specify the set of the multipole moments in terms of the stress-energy tensor of the source

$$\mathsf{N}(\mathsf{M}(\mathsf{h})) = \mathsf{M}(\mathsf{N}(\mathsf{h})), \tag{F.43}$$

where $\mathsf{N}(\mathsf{h})$ denotes the PN expansion of h and $\mathsf{M}(\mathsf{h})$ denotes the multipolar PM exterior metric. Here, the multipole expansion is an expansion in terms of d/r which is available outside the source. The multipole expansion is utilized for calculating the multipole expansions of $\mathsf{h}_n^{\alpha\beta}$, truncated to some finite order,

that depends on the order of the PN expansion that we want to compute, instead of the exact $\mathsf{h}_n^{\alpha\beta}$.

In the DIRE formalism, the relaxed Einstein equations can be solved directly and iteratively as

$$ {}^{(N+1)}\mathsf{h}^{\alpha\beta}(t,\boldsymbol{x}) = -\frac{4G}{c^4}\int d^4x' \frac{{}^{(N)}\tau^{\alpha\beta}(t',\boldsymbol{x}')\delta(t'-t+|\boldsymbol{x}-\boldsymbol{x}'|/c|)}{|\boldsymbol{x}-\boldsymbol{x}'|}, \tag{F.44} $$

where ${}^{(N+1)}\mathsf{h}^{\alpha\beta}$ denotes the result of the Nth iteration and ${}^{(N)}\tau^{\alpha\beta}$ denotes the value of $\tau^{\alpha\beta}$ when $h_{\alpha\beta} = {}^{(N)}\mathsf{h}^{\alpha\beta}$.

As a consequence, we find the generation expressions of $\mathsf{h}^{\alpha\beta}$ in terms of the stress-energy tensor of the source in both near and far zones by these procedure such as the BDI or DIRE formalism.

Next, in order to evaluate the various momentum depending on the stress-energy tensor appearing in the above expression of $\mathsf{h}^{\alpha\beta}$, we need the equations of motion of the system. The equations of motion are simply given by the geodesic equations associated with the regularized metric or by the geodesic equations together with the metric obtained from the PN formalism [208, 209]

$$ \frac{dv^i}{dt} = -\frac{Gm}{r^2}\left[(1+A)n^i + Bv^i\right] + O\left(\frac{1}{c^8}\right), \tag{F.45} $$

where n^i is the relative separation unit vector, v^i is the relative velocity, A and B are given in [206]. By the time the signals are detectable by Earth-based detectors, the orbit tends to be circularised by the radiation reaction. For circular orbits, the equations of motion reduce to

$$ \frac{dv^i}{dt} = \Omega^2 x^i - \zeta v^i, \tag{F.46} $$

where

$$ \begin{aligned} \Omega^2 =& \frac{Gm}{r^3}\{1+(-3+\eta)\gamma + (6+\frac{41}{4}\eta+\eta^2)\gamma^2 \\ &+ \left[-10+\left(22\log\frac{r}{r'_0} - \frac{75707}{840} + \frac{41}{64}\pi^2\right)\eta + \frac{19}{2}\eta^2 + \eta^3\right]\gamma^3\} + O\left(\frac{1}{c^8}\right), \end{aligned} \tag{F.47} $$

and

$$\zeta = \frac{32}{5}\frac{G^3 m^3 \eta}{c^5 r^4} + O\left(\frac{1}{c^7}\right). \tag{F.48}$$

where r_0 is a gauge-related constant coming from the binary radius r is the relative separation in harmonic coordinates and then not an invariant quantity. Eq. (F.47) is the PN generalization of Kepler's law. The second term in Eq. (F.46) describe the radiation reaction. From the equations of motion, we can compute the orbital energy of the circular orbit

$$\begin{aligned} E = &-\frac{\mu c^2 \beta}{2}\left\{1 + \left(-\frac{3}{4} - \frac{1}{12}\eta\right)\beta + \left(-\frac{27}{8} + \frac{19}{8}\eta - \frac{1}{24}\eta^2\right)\beta^2 + \right. \\ &\left.\left[-\frac{675}{64} + \left(\frac{34445}{576} - \frac{205}{96}\pi^2\right)\eta - \frac{155}{96}\eta^2 - \frac{35}{5184}\eta^3\right]\beta^3\right\} + O\left(\frac{1}{c^8}\right). \end{aligned} \tag{F.49}$$

in addition, the change of the binding energy or the total flux from GWs can be calculated from the binary ' s multipole moments, similar in the linearized theory,

$$\begin{aligned} P = &\frac{32c^5}{5G}\eta^2\beta^5\left\{1 + \left(-\frac{1247}{336} - \frac{35}{12}\eta\right)\beta + 4\pi\beta^{3/2}\right. \\ &+ \left(-\frac{44711}{9072} + \frac{9271}{504}\eta + \frac{65}{18}\eta^2\right)\beta^2 + \left(-\frac{8191}{672} - \frac{583}{24}\eta\right)\pi\beta^{5/2} + \\ &\left[\frac{6643739519}{69854400} + \frac{16}{3}\pi^2 - \frac{1712}{105}\mathcal{C} - \frac{856}{105}\ln(16\beta) + \left(-\frac{134543}{7776} + \frac{41}{48}\pi^2\right)\eta\right. \\ &\left.-\frac{94403}{3024}\eta^2 - \frac{775}{324}\eta^3\right]\beta^3 + \left(-\frac{16285}{504} + \frac{214745}{1728}\eta + \frac{193385}{3024}\eta^2\right)\pi\beta^{7/2} \\ &\left.+O\left(\frac{1}{c^8}\right)\right\}. \end{aligned} \tag{F.50}$$

The balance equation

$$\frac{dE}{dt} = -P, \tag{F.51}$$

can be used to compute the phase evolution as in the linearized theory.

GWs are basically analyzed by Bayesian estimation using a waveform model called a template. There are various templates depending on the approxima-

tion method and the nature of the system under consideration. For example, for the early inspiral of spinning and nonprecessing BBHs, TaylorT1, TaylorT2, TaylorT3, TaylorT4 and TaylorT5 approximants are known as the time-domain templates, and TaylorF1 and TeylorF2 approximants are known as the frequency-domain templates. In order to compute the phase function, in the calculation of these templates, it is the same to utilize the PN binding energy, PN energy fluxes, and the balance laws as discussed above. In the case of these templates, PN order terms are truncated differently. For a comparison of the template waveforms, please refer to [169, 210]. In this thesis, we will also deal with IMRPhenom templates that are the phenomenological inspiral-merger-ringdown waveforms or the frequency-domain models for compact binaries at comparable masses, tuned to numerical-relativity simulations. There are many types of IMRPhenom templates such as IMRPhenomA [211, 212], IMRPhenomB [213], IMRPhenomC [214], IMRPhenomD [127], IMRPhenomPv2 [215], IMRPhenomHM [216], IMRPhenomX [217–220], and so on. These have different properties of the binary (with/without spinning or with/without precessing), different physical phenomena and with/without higher modes. NRTidal approximant [156] is the numerical relativity (NR) based approximant for the tidal part of the phasing to describe the tidal deformation effect of the BNS.

Brans-Dicke theory

Brans-Dicke theory is described by the action in Jordan frame

$$S_{\rm BD} = \int \left[\phi R - \frac{\omega_{\rm BD}}{\phi} \phi^{,\mu} \phi_{,\mu} - \phi^2 V \right], \tag{F.52}$$

where ϕ is a dynamical scalar field, V is a potential for the scalar field, and $\omega_{\rm BD}$ is a coupling constant. Unless we are considering massive Brans-Dicke theory, we can set the potential V to zero. This is a subset of general scalar-tensor theories where the coupling is constant $\omega(\phi) = \omega_{\rm BD}$. Variation and linearization about a flat background metric of the action leads the evolution equations for h_{ab}. The solution of the trace-reversed metric perturbation for

the quasi-circular orbital binary inspiral phase is given by

$$\bar{h}^{ab} = \theta^{ab} + \frac{\phi}{\phi_0}\eta^{ab}, \tag{F.53}$$

with

$$\theta^{ij} = \frac{4\mu}{D_L}\left(1 - \frac{1}{2}\xi\right)\frac{Gm}{r}(\hat{v}^i\hat{v}^j - \hat{x}^i\hat{x}^j), \tag{F.54}$$

and

$$\frac{\phi}{\phi_0} = -\frac{4\mu}{D_L}\bar{S}, \tag{F.55}$$

where ϕ_0 is the asymptotic value of the scalar field at infinity, and

$$\bar{S} = -\frac{1}{4}\xi\left[\frac{\Gamma Gm}{r}[(\hat{N}\cdot\hat{v})^2 - (\hat{N}\cdot\hat{x})^2] - (G\Gamma + 2\Lambda)\frac{m}{r} - 2S\left(\frac{Gm}{r}\right)^{1/2}(\hat{N}\cdot\hat{v})\right], \tag{F.56}$$

with $\xi := (2+\omega_{\rm BD})^{-1}$, $G := 1 - \xi(s_1 + s_2 - 2s_1s_2)$, $S := s_1 - s_2$, $\Gamma := 1 - 2(m_1s_2 + m_2s_1)/m$, and $\Lambda := 1 - s_1 - s_2$. s_A is the sensitivity of the Ath object defined in Brans-Dicke theory.

From the trace-reversed metric perturbation, we can extract the waveform amplitude and then calculate the GW polarizations by Eq. (3.23) and Eq. (3.24)

$$h^b = \frac{-4\mu\bar{S}}{D_L}, \tag{F.57a}$$

$$h^+ = -\left(1 - \frac{1}{2}\xi\right)\frac{2G\mu m}{Dr}\cos 2\Phi(1+\cos^2\iota), \tag{F.57b}$$

$$h^\times = -\left(1 - \frac{1}{2}\xi\right)\frac{4G\mu m}{Dr}\sin 2\Phi\cos\iota, \tag{F.57c}$$

In Brans-Dicke theory, the Kepler's law is given by

$$2\pi F = \left(\frac{Gm}{r^3}\right)^{1/2} \tag{F.58}$$

the binding energy is given by

$$E = -\frac{Gm\mu}{r}, \tag{F.59}$$

and the change rate of the radiated energy is given by

$$\frac{dE}{dt} = -\frac{8}{15}\frac{\mu^2 m^2}{r^4}\left[12G^2\left(1-\frac{1}{2}\xi+\frac{1}{12}\xi\Gamma^2\right)v^2+\frac{5}{4}G^2\xi S^2\right] \tag{F.60}$$

Equating the time derivative of the binding energy and the change rate of the radiated energy, we find the frequency change rate

$$\begin{aligned}\frac{dF}{dt} =& \frac{48}{5\pi\mathcal{M}^2}(2\pi\mathcal{M}F)^{11/3}+\frac{S^2\eta^{2/5}}{\pi\mathcal{M}^2}\xi(2\pi\mathcal{M}F)^3 \\ &+\frac{48}{5\pi\mathcal{M}^2}(2\pi\mathcal{M}F)^{11/3}\left(\frac{1}{12}\Gamma^2-k_{\rm BD}\right).\end{aligned} \tag{F.61}$$

Finally, employing SPA, we find the Fourier transform of the detector signal in Brans-Dicke theory

$$\begin{aligned}\tilde{h}_{\rm BD}(f) =& \left[-\{F_+(1+\cos^2\iota)+2iF_\times\cos\iota\}\left\{1-\left(\frac{1}{24}\Gamma^2+\frac{k_{\rm BD}}{2}\right)\xi\right\}u_2^{-7/2}\right. \\ &\left.+F_b\sin^2\iota\frac{\Gamma}{2}\xi u_2^{-7/2}-\{F_+(1+\cos^2\iota)+2iF_\times\cos\iota\}\left(\frac{5}{96}\right)\eta^{2/5}\xi S^2 u_2^{-11/2}\right] \\ &\times\left(\frac{5\pi}{96}\right)^{1/2}\frac{\mathcal{M}^2}{D_L}e^{-i\Psi^{(2)}_{\rm BD}}-F_b\sin\iota S\xi\left(\frac{5\pi}{48}\right)^{1/2}\eta^{1/5}\frac{\mathcal{M}^2}{D_L}u_1^{-9/2}e^{-i\Psi^{(1)}_{\rm BD}}.\end{aligned} \tag{F.62}$$

with

$$\Psi^{(l)}_{\rm BD} = \frac{\pi}{4}+l\Phi_c-2\pi f t_c-\frac{3l}{256u_l^5}+\frac{5l}{7168}\xi\frac{S^2\eta^{2/5}}{u_l^7}. \tag{F.63}$$

Rosen's theory

Rosen theory is a bimetric theory of gravity described by the action

$$S_R = \frac{1}{32\pi G}\int_\eta \eta^{\mu\nu}g\alpha\beta g^{\gamma\delta}\bar{\nabla}_\mu g_{\alpha[\gamma}\bar{\nabla}_{|\nu|}g_{\beta[\delta}, \tag{F.64}$$

where $\eta_{\mu\nu}$ is the flat and non-dynamical metric, $\bar{\nabla}_\mu$ is a covariant derivative about $\eta_{\mu\nu}$. Variation and linearization about a flat background metric of the action leads the evolution equations for h_{ab}. The solution of the trace-reversed metric perturbation for the quasi-circular orbital binary inspiral phase is given

by

$$\bar{h}^{00} = \frac{4\mu}{D_L}\left\{\frac{m}{r}[(\hat{N}\cdot\hat{v})^2 - 1 - (\hat{N}\cdot\hat{x})^2] + \left(\frac{m}{r}\right)^{1/2}\mathcal{G}(\hat{N}\cdot\hat{v})\right\}, \tag{F.65a}$$

$$\bar{h}^{0j} = \frac{4\mu}{D_L}\left\{v^j\frac{m}{r}(\hat{N}\cdot\hat{v}) - x^j\frac{m}{r}(\hat{N}\cdot\hat{x}) + \frac{2}{3}\left(\frac{m}{r}\right)^{1/2}\mathcal{G}v^j\right\}, \tag{F.65b}$$

$$\bar{h}^{0j} = \frac{4\mu}{D_L}\left\{\frac{m}{r}v^iv^j - \frac{1}{3}\left(\frac{m}{r}\right)^{1/2}\mathcal{G}(\hat{N}\cdot\hat{v})\delta^{ij}\right\}, \tag{F.65c}$$

where $\mathcal{G} := s_1/m_1 - s_2/m_2$.

From the trace-reversed metric perturbation, we can extract the waveform amplitude and then calculate the GW polarizations by Eq. (3.23) and Eq. (3.24)

$$h^b = \frac{2\mu}{D_L}\left[\frac{m}{r}\sin^2\iota\sin^2\Phi + \frac{m}{r} - \frac{4}{3}\left(\frac{m}{r}\right)^{1/2}\mathcal{G}\sin\iota\cos\Phi\right], \tag{F.66a}$$

$$h^l = \frac{4\mu}{D_L}\left[\frac{m}{r}\sin^2\iota\sin^2\Phi - \frac{m}{r} - \frac{2}{3}\left(\frac{m}{r}\right)^{1/2}\mathcal{G}\sin\iota\cos\Phi\right], \tag{F.66b}$$

$$h^x = \frac{4\mu}{D_L}\left[-\frac{m}{r}\sin\iota\sin\Phi\cos\Phi - \frac{2}{3}\left(\frac{m}{r}\right)^{1/2}\mathcal{G}\sin\Phi\right], \tag{F.66c}$$

$$h^y = \frac{4\mu}{D_L}\left[\frac{m}{r}\sin\iota\cos\iota\sin^2\Phi - \frac{2}{3}\left(\frac{m}{r}\right)^{1/2}\mathcal{G}\sin\iota\cos\Phi\right], \tag{F.66d}$$

$$h^+ = \frac{2\mu m}{D_L r}(\sin^2\Phi - \cos^2\iota\cos^2\Phi), \tag{F.66e}$$

$$h^\times = -\frac{2\mu m}{D_L r}\cos\iota\sin 2\Phi. \tag{F.66f}$$

In Rosen theory, the Kepler's law is given by

$$2\pi F = \left(\frac{k_R m}{r^3}\right)^{1/2} \tag{F.67}$$

the binding energy is given by

$$E = -\frac{m\mu}{2r}, \tag{F.68}$$

and the change rate of the radiated energy is given by

$$\frac{dE}{dt} = \frac{84}{15}\frac{\mu^2 m^2}{r^4}v^2 + \frac{20}{9}\frac{\mu^2 m^2 \mathcal{G}^2}{r^4}. \tag{F.69}$$

where $k_R := 1 - 4s_1 s_2/3$.

Equating the time derivative of the binding energy and the change rate of the radiated energy, we find the frequency change rate

$$\frac{dF}{dt} = -\frac{42k_R^{-5/6}}{5\pi\mathcal{M}^2}(2\pi\mathcal{M}F)^{11/3} - \frac{10k_R^{-3/2}}{3\pi\mathcal{M}^2}\mathcal{G}^2\eta^{2/5}(2\pi\mathcal{M}F)^3. \tag{F.70}$$

Finally, employing SPA, we find the Fourier transform of the detector signal in Rosen theory

$$\begin{aligned}\tilde{h}_{\rm R}(f) =&[-F_+(1+\cos^2\iota) - 2iF_\times\cos\iota - F_b\sin^2\iota - 2F_l\sin^2\iota - 2F_x i\sin\iota \\ &- F_y\sin 2\iota]i\left(\frac{5\pi}{336}\right)^{1/2}k_{\rm R}^{-3/4}\frac{\mathcal{M}^2}{D_L}u_2^{-7/2}e^{-i\Psi_{\rm R}^{(2)}} + i(-F_b\sin\iota \\ &- F_l\sin\iota - F_x i - F_y\cos\iota)\mathcal{G}k_{\rm R}^{-7/12}\sqrt{\frac{40\pi}{189}}\eta^{1/5}\frac{\mathcal{M}^2}{D_L}u_1^{-9/2}e^{-i\Psi_{\rm R}^{(1)}}.\end{aligned} \tag{F.71}$$

with

$$\Psi_{\rm R}^{(l)} = \frac{\pi}{4} + l\Phi_c - 2\pi f t_c + \frac{3l}{224u_l^5}k_{\rm R}^{-5/6} + \frac{25l}{8232}\frac{k_{\rm R}^{-2/3}\mathcal{G}^2\eta^{2/5}}{u_l^7}. \tag{F.72}$$

Lightman-Lee theory

Lightman-Lee theory is a bimetric theory of gravity described by the action

$$S_{\rm LL} = -\frac{1}{16\pi}\int_{\bar{\eta}}\left(\frac{1}{4}B^{\mu\nu|\alpha}B_{\mu\nu|\alpha} - \frac{5}{64}B_{,\alpha}B^{,\alpha}\right), \tag{F.73}$$

where $B_{\mu\nu}$ is a dynamical gravitational tensor, $\bar{\eta}_{\mu\nu}$ is a background metric. They are related to the space-time metric and the perturbation metric as

$$g_{\mu\nu} = \left(1 - \frac{1}{16}B\right)^2\Delta_\mu{}^\alpha\Delta_{\alpha\nu}, \tag{F.74}$$

$$\delta^{\mu}{}_{\nu} = \Delta^{\alpha}{}_{\nu}\left(\delta_{\alpha}{}^{\mu} - \frac{1}{2}h_{\alpha}{}^{\mu}\right), \tag{F.75}$$

$$g_{\mu\nu} = \eta_{\mu\nu} + h_{\mu\nu}, \tag{F.76}$$

$$h_{\mu\nu} = B_{\mu\nu} - \frac{1}{8}B\eta_{\mu\nu}. \tag{F.77}$$

The solution of the trace-reversed metric perturbation $\bar{h}_{\mu\nu} = B_{\mu\nu} - \frac{3}{8}B\eta_{\mu\nu}$ for the quasi-circular orbital binary inspiral phase is given by

$$\bar{h}^{00} = \frac{\mu}{D_L}\left[\frac{m}{r}\{2(\hat{N}\cdot\hat{v})\}^2 - 8 - 2(\hat{N}\cdot\hat{x})^2] + 10\left(\frac{m}{r}\right)^{1/2}\mathcal{G}\hat{N}\cdot\hat{v}\right], \tag{F.78a}$$

$$\bar{h}^{0j} = \frac{4\mu}{D_L}\left[\frac{m}{r}v^j(\hat{N}\cdot\hat{v}) - x^j\frac{m}{r}\hat{N}\cdot\hat{x} + \frac{5}{3}\left(\frac{m}{r}\right)^{1/2}\mathcal{G}v^j\right], \tag{F.78b}$$

$$\bar{h}^{ij} = \frac{\mu}{D_L}\left[\frac{m}{r}\{4\hat{v}^i\hat{v}^j - (4 - 2(\hat{N}\cdot\hat{v})^2 + 2(\hat{N}\cdot\hat{x})^2)\delta^{ij}\} - \left(\frac{10}{3}\right)^{1/2}\mathcal{G}(\hat{N}\cdot\hat{v})\delta^{ij}\right]. \tag{F.78c}$$

From the trace-reversed metric perturbation, we can extract the waveform amplitude and then calculate the GW polarizations by Eq. (3.23) and Eq. (3.24)

$$h^b = \frac{\mu}{2D_L}\left[4\frac{m}{r}\sin^2\iota\cos^2\Phi - 4\frac{m}{r}\sin^2\iota\sin^2\Phi + 4\frac{m}{r} - \frac{50}{3}\left(\frac{m}{r}\right)^{1/2}\mathcal{G}\sin\iota\cos\Phi\right], \tag{F.79a}$$

$$h^l = \frac{\mu}{D_L}\left[4\frac{m}{r}\sin^2\iota\sin^2\Phi - 12\frac{m}{r} - \frac{20}{3}\left(\frac{m}{r}\right)^{1/2}\mathcal{G}\sin\iota\cos\Phi\right], \tag{F.79b}$$

$$h^x = \frac{\mu}{D_L}\left[-4\frac{m}{r}\sin\iota\sin\Phi\cos\Phi + \frac{20}{3}\left(\frac{m}{r}\right)^{1/2}\mathcal{G}\sin\Phi\right], \tag{F.79c}$$

$$h^y = \frac{\mu}{D_L}\left[4\frac{m}{r}\sin\iota\cos\iota\sin^2\Phi + \frac{20}{3}\left(\frac{m}{r}\right)^{1/2}\mathcal{G}\sin\iota\cos\Phi\right], \tag{F.79d}$$

$$h^+ = \frac{2\mu m}{D_L r}(\sin^2\Phi - \cos^2\iota\cos^2\Phi), \tag{F.79e}$$

$$h^\times = -\frac{2\mu m}{D_L r}\cos\iota\sin 2\Phi. \tag{F.79f}$$

In Lightman-Lee theory, the Kepler's law is given by

$$2\pi F = \left(\frac{m}{r^3}\right)^{1/2} \tag{F.80}$$

the binding energy is given by

$$E = -\frac{m\mu}{2r}, \tag{F.81}$$

and the change rate of the radiated energy is given by

$$\frac{dE}{dt} = \frac{84}{15}\frac{\mu^2 m^3}{r^5} + \frac{125}{9}\frac{\mu^2 m^2 \mathcal{G}^2}{r^4}. \tag{F.82}$$

Equating the time derivative of the binding energy and the change rate of the radiated energy, we find the frequency change rate

$$\frac{dF}{dt} = -\frac{42}{5\pi\mathcal{M}^2}(2\pi\mathcal{M}F)^{11/3} - \frac{125}{6\pi\mathcal{M}^2}\mathcal{G}^2\eta^{2/5}(2\pi\mathcal{M}F)^3. \tag{F.83}$$

Finally, employing SPA, we find the Fourier transform of the detector signal in Rosen theory

$$\begin{aligned}\tilde{h}_{\rm LL}(f) =&[-F_+(1+\cos^2\iota) - 2iF_\times\cos\iota + 3F_b\sin^2\iota - 2F_l\sin^2\iota - 2F_x i\sin\iota \\ &- F_y\sin 2\iota]i\left(\frac{5\pi}{336}\right)^{1/2}\frac{\mathcal{M}^2}{D_L}u_2^{-7/2}e^{-i\Psi^{(2)}_{\rm LL}} + i(\frac{5}{4}F_b\sin\iota \\ &- F_l\sin\iota + F_x + F_y\cos\iota)\mathcal{G}\sqrt{\frac{250\pi}{189}}\eta^{1/5}\frac{\mathcal{M}^2}{D_L}u_1^{-9/2}e^{-i\Psi^{(1)}_{\rm R}}.\end{aligned} \tag{F.84}$$

with

$$\Psi^{(l)}_{\rm LL} = \frac{\pi}{4} + l\Phi_c - 2\pi f t_c + \frac{3l}{224u_l^5} - \frac{625l}{16464}\frac{\mathcal{G}^2\eta^{2/5}}{u_l^7}. \tag{F.85}$$

Appendix G

Antenna pattern function

Here, we summarize the antenna pattern functions for interferometric detectors and the polarization angle of the GWs.

Suppose that a GW comes from a single distant source along with a unit vector $\hat{n}$ which points from the source to the observer. The GW can be written as

$$S_{ij}(t, \boldsymbol{x}) = e^A_{ij}(\hat{\boldsymbol{n}}) \int_{-\infty}^{\infty} df \tilde{h}_A(f) e^{-2\pi i f(t - \hat{\boldsymbol{n}} \cdot \boldsymbol{x})}, \tag{G.1}$$

where e^A_{ij} are the polarization basis tensors. We set the coordinate such that $\boldsymbol{x} = 0$ at the location of the detector. Since we consider a detector that is sensitive to only GWs with a reduced wavelength much larger than its size, we have $2\pi f \hat{\boldsymbol{n}} \cdot \boldsymbol{x} = \hat{\boldsymbol{n}} \cdot \boldsymbol{x}/\lambda << 1$ over the detector. We can simply write the GW,

$$\begin{aligned} S_{ij}(t, \boldsymbol{x}) &= e^A_{ij}(\hat{\boldsymbol{n}}) \int_{-\infty}^{\infty} df \tilde{h}_A(f) e^{-2\pi i f t} \\ &= e^A_{ij}(\hat{\boldsymbol{n}}) h_A(t). \end{aligned} \tag{G.2}$$

Consequently, the detector signal can be written as

$$h_I(t, \hat{\Omega}) = F^A_I(\hat{\Omega}) h_A(t). \tag{G.3}$$

F^A_I is the antenna pattern functions for the polarization "A" labeled with an index that identifies the detector,

$$F^A_I(\hat{\Omega}) := d^{ab}_I e^A_{ab}(\hat{\Omega}). \tag{G.4}$$

as explained in Section 3.2.

Then, we discuss about the transformation law of the polarization basis and the polarization components. Related to this, we also provide the polarization-angle dependence of the polarization components. The formulations of the detector signal are based on the fact that we have chosen a set of axes $(\hat{e}_x, \hat{e}_y)$ in the plane orthogonal to the propagation direction $\hat{e}_z = \hat{n}$, with respect to which the polarization modes h_+ and $h_\times$ are defined. We can change the basis of $(\hat{e}_x, \hat{e}_y)$ to $(\hat{e}'_x, \hat{e}'_y)$ by a rotation of ψ in the transverse plane.

$$\begin{aligned} \hat{e}'_x &= \cos\psi \hat{e}_x + \sin\psi \hat{e}_y, \\ \hat{e}'_y &= -\sin\psi \hat{e}_x + \cos\psi \hat{e}_y. \end{aligned} \tag{G.5}$$

The polarization basis tensors transform by the rotation as

$$\begin{aligned} e^{+\,\prime}_{ab} &= \hat{e}'_x \otimes \hat{e}'_x - \hat{e}'_y \otimes \hat{e}'_y \\ &= \cos 2\psi e^+_{ab} + \sin 2\psi e^\times_{ab}, \end{aligned} \tag{G.6}$$

$$\begin{aligned} e^{\times\,\prime}_{ab} &= \hat{e}'_x \otimes \hat{e}'_y + \hat{e}'_y \otimes \hat{e}'_x \\ &= -\sin 2\psi e^+_{ab} + \cos 2\psi e^\times_{ab}, \end{aligned} \tag{G.7}$$

$$\begin{aligned} e^{x\,\prime}_{ab} &= \hat{e}'_x \otimes \hat{e}'_z + \hat{e}'_z \otimes \hat{e}'_x \\ &= \cos\psi e^x_{ab} + \sin\psi e^y_{ab}, \end{aligned} \tag{G.8}$$

$$\begin{aligned} e^{y\,\prime}_{ab} &= \hat{e}'_y \otimes \hat{e}'_z + \hat{e}'_z \otimes \hat{e}'_y \\ &= -\sin\psi e^x_{ab} + \cos\psi e^y_{ab}, \end{aligned} \tag{G.9}$$

$$\begin{aligned} e^{b\,\prime}_{ab} &= \hat{e}'_x \otimes \hat{e}'_x + \hat{e}'_y \otimes \hat{e}'_y \\ &= \hat{e}_x \otimes \hat{e}_x + \hat{e}_y \otimes \hat{e}_y \\ &= e^b_{ab}, \end{aligned} \tag{G.10}$$

$$\begin{aligned} e^{l\,\prime}_{ab} &= \sqrt{2}\hat{e}'_z \otimes \hat{e}'_z \\ &= \sqrt{2}\hat{e}_z \otimes \hat{e}_z \\ &= e^l_{ab}. \end{aligned} \tag{G.11}$$

So, the components of the GW transform as

$$h^{+\prime} = \cos 2\psi h^+ + \sin 2\psi h^\times, \tag{G.12}$$

$$h^{\times\prime} = -\sin 2\psi h^{+} + \cos 2\psi h^{\times}, \tag{G.13}$$

$$h^{x\prime} = \cos\psi h^{x} + \sin\psi h^{y}, \tag{G.14}$$

$$h^{y\prime} = -\sin\psi h^{x} + \cos\psi h^{y}, \tag{G.15}$$

$$h^{b\prime} = h^{b}, \tag{G.16}$$

$$h^{l\prime} = h^{l}. \tag{G.17}$$

Since the antenna pattern functions are defined by the polarization basis tensor, the antenna pattern functions for the primed polarization basis tensor $F_I^{A\prime}(\hat{\Omega}) := d_I^{ab} e_{ab}^{A\,\prime}(\hat{\Omega})$ transform as

$$\begin{aligned} F_I^{+\prime} &= d_I^{ab} e_{ab}^{+\,\prime} \\ &= d_I^{ab}(\cos 2\psi e_{ab}^{+} + \sin 2\psi e_{ab}^{\times}) \\ &= \cos 2\psi F_I^{+} + \sin 2\psi F_I^{\times}, \end{aligned} \tag{G.18}$$

$$F_I^{\times\prime} = -\sin 2\psi F_I^{+} + \cos 2\psi F_I^{\times}, \tag{G.19}$$

$$F_I^{x\prime} = \cos\psi F_I^{x} + \sin\psi F_I^{y}, \tag{G.20}$$

$$F_I^{y\prime} = -\sin\psi F_I^{x} + \cos\psi F_I^{y}, \tag{G.21}$$

$$F_I^{b\prime} = F_I^{b}, \tag{G.22}$$

$$F_I^{l\prime} = F_I^{l}. \tag{G.23}$$

The detector signal can be written as

$$\begin{aligned} h_I(t,\hat{\Omega}) &= d_I^{ab} S_{ab}(t) \\ &= d_I^{ab} h'_A e_{ab}^{A\,\prime} \\ &= F_I^{A\prime} h'_A, \end{aligned} \tag{G.24}$$

in terms of the primed axes $\{\hat{e}'_x, \hat{e}'_y, \hat{e}'_z\}$. Of course, we can calculate the detector signal

$$\begin{aligned} h_I(t,\hat{\Omega}) &= d_I^{ab} S_{ab}(t) \\ &= d_I^{ab} h_A e_{ab}^{A} \\ &= F_I^{A} h_A, \end{aligned} \tag{G.25}$$

in terms of the non-primed axes $\{\hat{e}_x, \hat{e}_y, \hat{e}_z\}$. The detector signal is independent of the angle ψ because we discuss the change of the basis for the identical GW. Even if we change the basis, the physical effect of the GW does not change.

On the other hand, the detector signal for the GW should depend on an angle that is called the polarization angle ψ. The polarization angle is an angle parameter denoting the orientation of the source relative to the detector. We can introduce the polarization angle in analogy with the rotation of the polarization basis tensors, but in this case the angle ψ is introduced as a physical parameter identifying the orientation of the source relative to the detector. The polarization components h_A are usually calculated with respect to the preferred basis to the source. As with the case of the compact binary source, in which the orbit looks elliptical and the principal axes of the ellipse give a preferred basis set $\{\hat{e}'_x, \hat{e}'_y, \hat{e}'_z\}$,

$$\hat{e}'_x := -\frac{\hat{n} \times \hat{L}}{|\hat{n} \times \hat{L}|} \tag{G.26}$$

$$\hat{e}'_y := \frac{\hat{n} \times \hat{e}'_x}{|\hat{n} \times \hat{e}'_x|} \tag{G.27}$$

$$\hat{e}'_z := \hat{n} \tag{G.28}$$

where $\hat{L}$ is the unit vector in the direction of the orbital angular momentum of the binary, the system is generally characterized by a preferred basis set. The waveforms of the GW ${h_+}'$ and ${h_\times}'$ are usually calculated with respect to the preferred axes,

$$S_{ab} = {h_+}' {e^+_{ab}}' + {h_\times}' {e^\times_{ab}}'. \tag{G.29}$$

On the other hand, the antenna pattern functions are often defined with respect to the different reference basis $\{\hat{e}_x, \hat{e}_y, \hat{e}_z\}$,

$$F^A_I := d^{ab}_I e^A_{ab}. \tag{G.30}$$

For example, suppose that we specify the location of the source in equatorial coordinates in terms of its right ascension α and declination δ. This means that we specify the sky position $\hat{\Omega} = -\hat{n} =: -\hat{e}_z$ in its equatorial coordinates. Then, we require the reference axis $\hat{e}_x$ to be parallel to the celestial equator We

also require the reference axis $\hat{e}_y := \hat{e}_z \times \hat{e}_x$ to points into the Northern celestial hemisphere. We need to formulate the detector signal in terms of the above polarization components ${h_+}'$ and ${h_\times}'$ and the above antenna pattern functions with the basis e^A_{ab}. The preferred axes and the reference axes not necessarily correspond to each other. In general, $\{\hat{e}_x, \hat{e}_y\}$ are different from $\{\hat{e}'_x, \hat{e}'_y\}$ by an angle ψ. Thus, as a result we obtain the following detector signal that depends on the polarization angle, which denotes the relative difference between the preferred axes and the reference axes, or the orientation of the source relative to the GW source,

$$\begin{aligned}
h_I &= d^{ab}_I S_{ab} \\
&= d^{ab}_I h'_A {e^A_{ab}}' \\
&= h'_+(\cos 2\psi F^+_I + \sin 2\psi F^\times_I) + h'_\times(-\sin 2\psi F^+_I + \cos 2\psi F^\times_I) \\
&+ h'_x(\cos\psi F^x_I + \sin\psi F^y_I) + h'_y(-\sin\psi F^x_I + \cos\psi F^y_I) \\
&+ h'_b F^b_I + h'_l F^l_I \\
&= F^+_I(\cos 2\psi h'_+ - \sin 2\psi h'_\times) + F^\times_I(\sin 2\psi h'_+ + \cos 2\psi h'_\times) \\
&+ F^x_I(\cos\psi h'_x - \sin\psi h'_y) + F^y_I(\sin\psi h'_x + \cos\psi h'_y) \\
&+ h'_b F^b_I + h'_l F^l_I.
\end{aligned} \tag{G.31}$$

Here, we used the fact that ${e^A_{ab}}'$ can be written as the linear combinations of e^A_{ab} like Eq. (G.6) - Eq. (G.11) by considering a rotation of an angle ψ.

Finally, the concrete functions of the antenna pattern functions are given as follows.

$$F_b = -\frac{1}{2}\sin^2\theta\cos 2\phi, \tag{G.32}$$

$$F_l = \frac{1}{2}\sin^2\theta\cos 2\phi, \tag{G.33}$$

$$F_x = -\sin\theta(\cos\theta\cos 2\phi\cos\psi - \sin 2\phi\sin\psi), \tag{G.34}$$

$$F_y = -\sin\theta(\cos\theta\cos 2\phi\sin\psi + \sin 2\phi\cos\psi), \tag{G.35}$$

$$F_+ = \frac{1}{2}(1+\cos^2\theta)\cos 2\phi\cos 2\psi - \cos\theta\sin 2\phi\sin 2\psi, \tag{G.36}$$

$$F_\times = \frac{1}{2}(1+\cos^2\theta)\cos 2\phi\sin 2\psi + \cos\theta\sin 2\phi\cos 2\psi, \tag{G.37}$$

Appendix H

Probability, signal, and noise

The basics of probability, signal and noise are given here.

H.1 Probability

Probability can be abstractly defined by considering a set S representing a system formed by elementary events $i = 1, \ldots, \Omega \in S$. We can define probability p_i such that p_i satisfy the following conditions

$$\forall i,\ p_i > 0, \tag{H.1}$$

and

$$\sum_i p_i = 1. \tag{H.2}$$

We call p_i probability distribution.

Physical quantity (random variable) f is a map from the set of elementary events into $\mathbb{R}$.

We define an event as a map A from the set of elementary events into $\{\text{True}, \text{False}\}$[1], and for any $A \subset S$, we define the characteristic function as

$$\chi_i[A] := \begin{cases} 1, & \text{(When } A \text{ is true.)} \\ 0. & \text{(When } A \text{ is false.)} \end{cases} \tag{H.3}$$

[1] An event can be regarded as a subset $\{p_i \in S | A(p_i) = \text{True}\}$.

Then, we can define the probability of occurrence of A as

$$P[A] := \sum_i p_i \chi_i[A]. \tag{H.4}$$

So, for disjoint subsets $A \cap B = 0$, $P(A \cup B) = P(A) + P(B)$. In addition, we define the conditional probability $P(A|B)$, the probability of A given B, as

$$P(A|B) := \frac{P(A \cap B)}{P(B)}. \tag{H.5}$$

We also adopt the notation $P(A, B) := P(A \cap B)$ in some cases. The Bayes theorem can be derived by definition

$$P(A|B) = \frac{P(B|A)P(A)}{P(B)}. \tag{H.6}$$

Furthermore, for any B and A_i disjoints such that $\cup_i A_i = S$,

$$P(B) = \sum_i P(B|A_i)P(A_i). \tag{H.7}$$

Therefore,

$$P(A|B) = \frac{P(B|A)P(A)}{\sum_i P(B|A_i)P(A_i)}. \tag{H.8}$$

[2] When elementary elements are determined by real values $x_1, \ldots, x_\Omega$, the above discussion is naturally extended by replacing the probability with the real-valued probability distribution function $p(x_1, \ldots, x_\Omega)$. In this case, the summation is replaced by the integration.

In the frequentist approach, the events of the system are outcomes of a repeatable experiment. There should exist some parameters (or theories, or hypothesis) that are fixed in the system. The data is probabilistically obtained by the probability distribution having the fixed parameters (or the-

[2] $P(A|B,C) = P(A|B \cap C) = P(A \cap B \cap C)/P(B \cap C), P(B|A,C) = P(A \cap B \cap C)/P(A \cap C) \Rightarrow P(A|B,C)P(B \cap C) = P(B|A,C)P(A \cap C) \Rightarrow P(A|B,C)P(B|C)P(C) = P(B|A,C)P(A|C)P(C) \Rightarrow P(A|B,C) = P(B|A,C)P(A|C)/P(B|C) \Rightarrow P(A|B,C) = P(B|A,C)P(A|C)/P(B|C)$.

ories, or hypothesis). Thus, we can consider only P(data|hypothesis) and P(data|parameters) in the frequentist approach. However, we can not consider the probability such as P(hypothesis|data) and P(parameters|data) in the frequentist approach. In the Bayesian approach, by defining P(hypothesis|data) or P(parameters|data) through the Bayes theorem, we can consider the probability of a theory, or a hypothesis, or the probability that parameters take given values of data.

H.2 Signal and noise

As mentioned in the Chapter 3, we assume that the GW detector has a linear response to GWs and the output is a scalar. Thus, the detector signal $h(t)$ must be expressed as in Eq. (G.3). A whole detector can be modeled as a linear system with many stages labeled by i with each transfer function $T_i(f)$. The total transfer function is denoted by $T(f) = \Pi_i T_i(f)$ and noise should be added at each stage. So, it is useful to refer each noise to the detector input as a fictional noise by defining $n(t)$ as

$$n(f) = T^{-1}(f) n_{\rm out}(f). \tag{H.9}$$

We then write the input signal including the GWs as

$$s(t) = h(t) + n(t). \tag{H.10}$$

Thus, we will always refer to $s(t)$, which is the signal at the input of the detector, as the detector output and evaluate the signal of GWs and noise sources at the input stage of the detector. We consider a Gaussian, stochastic, and weak stationary process $n(t)$ hereafter. Thus, the values $n(t)$ are determined stochastically, the probability distribution is Gaussian, and the autocorrelation function depends only the time difference. We define the auto-correlation function as

$$R(\tau) := < n(t) n(t+\tau) >_E \, . \tag{H.11}$$

where $<>_E$ denotes the ensemble average. Then, the one-sided power spectral density $S_n(f)$ can be defined by its Fourier transform

$$\frac{1}{2}S_n(f) := \int_{-\infty}^{\infty} d\tau R(\tau) e^{i2\pi f\tau}. \tag{H.12}$$

This is the Wiener-Khintchin relation. The inverse transform is

$$R(\tau) = \frac{1}{2}\int_{-\infty}^{\infty} df S_n(f) e^{-i2\pi f\tau}. \tag{H.13}$$

Especially, the Parseval theorem holds [3]

$$< n^2(t) >_E = R(0) = \int_0^{\infty} df\ S_n(f) \tag{H.14}$$

We will give more intuitive discussion[4]. The detector noise is stationary. In other words, it is translated into an assumption that the different Fourier components are uncorrelated

$$< n^*(f)n(f') >_E = \frac{1}{2}S_n(f)\delta(f - f'). \tag{H.15}$$

This equation defines the function $S_n(f)$ known as the noise spectral density. As $f \to f'$,

$$\frac{1}{2}S_n(f) = < |n(f)|^2 >_E \Delta f, \tag{H.16}$$

with $\Delta f = 1/T$ where T is the duration of time for the data. Furthermore, the Parseval theorem also holds.

Finally, we list up the other properties of noise. The gaussian, random, and stationary noise is fully characterized by the mean $< n(t) >$ (=first order

[3] This $S_n(f)$ is called a single-sided spectral density, while a double-sided spectral density is defined as $S_n^{\rm double}(f) = (1/2)S_n(f)$. The parseval theorem is rewritten as $< n^2(t) >= \int_{-\infty}^{\infty} df\ S_n^{\rm double}(f)$.

[4] $n(f)$ can not be defined in general because it does not necessarily the condition $n(t) \to 0$ as $t \to \pm\infty$. If there exists $n(f)$, both definitions are consistent with each other.

moment) and its autocorrelation function $R(\tau)$ (that is related to the second order moment) in a sense that all higher-order moments above the third order are determined by moments up to the second order where k-th moment is defined by

$$m_k := \int x^k p(x) dx, \quad (k \in \mathbb{N}), \tag{H.17}$$

with the probability distribution $p(x)$ for the random variable x. White noise is the noise whose power spectral density does not depend on the frequency or is flat in frequency region. Ergodic noise is the noise satisfying the condition that the time average matches the ensemble average.

The detector noise spectrum can be characterized and evaluated by considering the transmission from the disturbance of the physical quantity such as light power, temperature, vibration, and so on to the detector output signal. Basically, the detector sensitivity or the detector noise spectrum in the lower-frequency region is limited by the vibration and the shot noise, and that in the higher-frequency region is limited by the radiation pressure noise for the ground-based detectors. The shot noise and the radiation pressure noise give the standard quantum limit of the detector sensitivity. The shot noise is the quantum photon counting noise at the interferometer readout. The radiation pressure noise is the quantum back-action noise of any phase-sensitive detection of the light reflected by a moving mirror. Please refer to [1, 110, 221–223] for more details of the detection principle and the detector noise.

Acknowledgement

This study was accomplished with the supports of many people. Finally, I would like to acknowledge my gratitude. I am so grateful to you.

First of all, I would like to thank my supervisor Masaki Ando for his great support. For five years, he helped me complete this study by giving me valuable advice based on his experience in all aspects of research and presentation. I appreciate him letting me research freely.

I also would like to thank Yuta Michimura for his support and insights. His interest in any field and willingness to discuss it is impressive. Thanks to his sound advice, I was able to improve the quality of this study.

I am really grateful to and respect Atsushi Nishizawa for his knowledge in gravity research and precise guidance. Thanks to him I could carry out this study. This study began with a discussion with him. The discussions with him were always very informative and enjoyable.

I also thank Kazuhiro Hayama for his supports. His work on the polarization tests of burst gravitational waves helped to advance this research.

I also thank Takahiro Tanaka for his advice. Meeting on the polarization tests with him helped to improve this study.

Kentaro Komori is not only well versed in gravitational wave experiments, but also bright in gravitational wave astronomy, and the daily discussions with him were exciting.

Koji Nagano is incredibly good at taking action and planning. His willingness to try to understand everything was very instructive. The discussions with him also encouraged me.

Soichiro Morisaki is a specialist in parameter estimation of neutron star binaries and his help was quick, accurate and helpful when testing the binary

neutron star in this study.

Thanks also to the other members of Ando Laboratory encouraging me. Tomofumi Shimoda is familiar with low-frequency gravitational wave detectors, and his advice helped me to consider the results of the analysis of the 3G detectors. Yutaro Enomoto is an expert on gravitational wave detectors, from control to quantum optics, and his ideas are unique and always provide an interesting discussion. Naoki Aritomi is also an experimentalist well experienced in quantum optics and detector. Ching Pin Ooi often corrected my English writing that was very helpful. Satoru Takano is knowledgeable about technical issues and a positive in everything and reliable person. Takuya Kawasaki is also familiar with quantum optics and discussed many interesting topics. Yuki Miyazaki and Naoki Kita were excellent juniors. Their growth encouraged me and chatting with them relaxed me. Hiroki Chiyoda helped me with other experiments. Yuka Oshima and Hiroki Fujimoto presented the latest interesting studies.

Mayuko Niwata helped me with the office work and supported me by talking with me friendly and so on.

I am more grateful to my parents and sister than anyone else, although I'm too embarrassed to express my gratitude in person. It is because of my family's support that I have become the person I am today. Since I can only say this here, I will write a secret note that I want to be born to this family again.

Finally, I would like to thank above all to my wife Shiori Izumikawa who married me on 17 December 2020. May you and I forever be happy.

Bibliography

[1] M. Maggiore, *Gravitational Waves* (Oxford University Press, 2007).

[2] R. M. Wald, *General Relativity* (The University of Chicago Press, 1984).

[3] I. Newton, *Philosophiæ Naturalis Principia Mathematica* (1687).

[4] A. Einstein, Annalen Phys. **49**, 769 (1916).

[5] C. W. Misner, K. S. Thorne, and J. A. Wheeler, *Gravitation* (W. H. Freeman, 1973).

[6] S. W. Hawking and G. F. R. Ellis, *The Large Scale Structure of Space-Time* (Cambridge University Press, 1973).

[7] C. M. Will, *Theory and Experiment in Gravitational Physics* (Cambridge University Press, 1993).

[8] C. M. Will, Living Reviews in Relativity **9**, 3 (2006), 0510072.

[9] J. G. Williams, S. G. Turyshev, and D. H. Boggs, Physical Review Letters **93**, 261101 (2004).

[10] I. Ciufolini and E. C. Pavlis, Nature **431**, 958 (2004).

[11] B. Bertotti, L. Iess, and P. Tortora, Nature **425**, 374 (2003).

[12] M. Burgay *et al.*, Nature **426**, 531 (2003).

[13] A. G. Lyne, Science **303**, 1153 (2004).

[14] M. Kramer *et al.*, Science **314**, 97 (2006).

[15] N. Yunes, K. Yagi, and F. Pretorius, Physical Review D **94**, 084002 (2016).

[16] B. P. Abbott *et al.*, Physical Review Letters **119**, 141101 (2017).

[17] B. P. Abbott *et al.*, Physical Review Letters **119**, 161101 (2017).

[18] J. Aasi *et al.*, Classical and Quantum Gravity **32**, 074001 (2015).

[19] B. P. Abbott *et al.*, Physical Review Letters **116**, 061102 (2016).

[20] É. É. Flanagan and S. A. Hughes, Physical Review D **57**, 4535 (1998).

[21] F. Pretorius, Binary black hole coalescence, (2007), 0710.1338.

[22] J. Centrella, J. G. Baker, B. J. Kelly, and J. R. van Meter, Annual Review of Nuclear and Particle Science **60**, 75 (2010).

[23] F. Acernese *et al.*, Classical and Quantum Gravity **32**, 024001 (2015).

[24] B. P. Abbott *et al.*, Physical Review Letters **9**, 031040, (2018), 1811.12907.

[25] R. Abbott *et al.*, Physical Review D **102**, 043015 (2020).

[26] R. Abbott *et al.*, The Astrophysical Journal **896**, L44 (2020).

[27] B. P. Abbott *et al.*, The Astrophysical Journal **892**, L3 (2020).

[28] R. Abbott *et al.*, Physical Review Letters **125**, 101102 (2020).

[29] R. Abbott *et al.*, Gwtc-2: Compact binary coalescences observed by LIGO and Virgo during the first half of the third observing run, (2020), 2010.14527.

[30] B. Abbott *et al.*, Physical Review D **100**, 104036 (2019).

[31] R. Abbott *et al.*, Tests of General Relativity with Binary Black Holes from the second LIGO-Virgo Gravitational-Wave Transient Catalog, (2020), 2010.14529.

[32] B. P. Abbott *et al.*, Physical Review Letters **116**, 221101 (2016).

[33] A. Ghosh *et al.*, Physical Review D **94**, 021101 (2016).

[34] A. Ghosh *et al.*, Classical and Quantum Gravity **35** (1), 014002, (2017), 1704.06784.

[35] K. G. Arun, B. R. Iyer, M. S. S. Qusailah, and B. S. Sathyaprakash, Physical Review D **74**, 024006 (2006).

[36] K. G. Arun, B. R. Iyer, M. S. S. Qusailah, and B. S. Sathyaprakash, Classical and Quantum Gravity **23**, L37 (2006).

[37] C. K. Mishra, K. G. Arun, B. R. Iyer, and B. S. Sathyaprakash, Physical Review D **82**, 064010 (2010).

[38] N. Yunes and F. Pretorius, Physical Review D **80**, 122003 (2009).

[39] T. G. F. Li *et al.*, Physical Review D **85**, 082003 (2012).

[40] T. G. F. Li *et al.*, Journal of Physics: Conference Series **363**, 012028 (2012).

[41] N. Cornish, L. Sampson, N. Yunes, and F. Pretorius, Physical Review D **84**, 062003 (2011).

[42] L. Sampson, N. Cornish, and N. Yunes, Physical Review D **89**, 064037 (2014).

[43] J. Meidam *et al.*, Physical Review D **97**, 044033 (2018).

[44] B. Abbott *et al.*, Physical Review Letters **123**, 011102 (2019).

[45] L. Blanchet, T. Damour, B. R. Iyer, C. M. Will, and A. G. Wiseman, Physical Review Letters **74**, 3515 (1995).

[46] L. Blanchet, T. Damour, G. Esposito-Farèse, and B. R. Iyer, Physical Review Letters **93**, 091101 (2004).

[47] L. Blanchet, Thibault Damour, Gilles Esposito-Farèse, and Bala R. Iyer, Physical Review D **71**, 124004 (2005).

[48] L. Blanchet, Living Reviews in Relativity **17**, 2 (2014).

[49] S. Mirshekari, N. Yunes, and C. M. Will, Physical Review D **85**, 024041 (2012).

[50] B. Abbott *et al.*, Physical Review Letters **118**, 221101 (2017).

[51] C. M. Will, Physical Review D **57**, 2061 (1998).

[52] G. Calcagni, Physical Review Letters **104**, 251301 (2010).

[53] G. Amelino-Camelia, Nature **418**, 34 (2002).

[54] P. Hořava, Physical Review D **79**, 084008 (2009).

[55] A. Sefiedgar, K. Nozari, and H. Sepangi, Physics Letters B **696**, 119 (2011).

[56] V. A. Kostelecký and M. Mewes, Physics Letters B **757**, 510 (2016).

[57] T. Baker *et al.*, Physical Review Letters **119**, 251301 (2017).

[58] P. Creminelli and F. Vernizzi, Physical Review Letters **119**, 251302 (2017).

[59] J. Sakstein and B. Jain, Physical Review Letters **119**, 251303 (2017).

[60] J. M. Ezquiaga and M. Zumalacárregui, Physical Review Letters **119**, 251304 (2017).

[61] S. Arai and A. Nishizawa, Physical Review D **97**, 104038 (2018).

[62] A. Emir Gümrükçüoğlu, M. Saravani, and T. P. Sotiriou, Physical Review D **97**, 024032 (2018).

[63] J. Oost, S. Mukohyama, and A. Wang, Physical Review D **97**, 124023 (2018).

[64] Y. Gong, S. Hou, D. Liang, and E. Papantonopoulos, Physical Review D **97**, 084040 (2018).

[65] Y. Gong, S. Hou, E. Papantonopoulos, and D. Tzortzis, Physical Review D **98**, 104017 (2018).

[66] C. de Rham and S. Melville, Physical Review Letters **121**, 221101 (2018).

[67] D. M. Eardley, D. L. Lee, A. P. Lightman, R. V. Wagoner, and C. M. Will, Physical Review Letters **30**, 884 (1973).

[68] D. M. Eardley", Physical Review D **8**, 3308 (1973).

[69] E. Poisson and C. M. Will, *Gravity: Newtonian, Post-Newtonian, Relativistic* (Cambridge University Press, 2014).

[70] C. Brans and R. H. Dicke, Physical Review **124**, 925 (1961).

[71] Y. Fujii and K.-i. Maeda, Classical and Quantum Gravity **20**, 4503 (2003).

[72] H. A. Buchdahl, Monthly Notices of the Royal Astronomical Society **150**, 1 (1970).

[73] A. De Felice and S. Tsujikawa, Living Reviews in Relativity **13**, 3 (2010).

[74] T. P. Sotiriou and V. Faraoni, Reviews of Modern Physics **82**, 451 (2010).

[75] S. Nojiri and S. D. Odintsov, Physics Reports **505**, 59 (2010), 1011.0544.

[76] S. Nojiri, S. D. Odintsov, and V. K. Oikonomou, Physics Reports **692**, 2 (2017), 1705.11098.

[77] S. Hou, Y. Gong, and Y. Liu, The European Physical Journal C **78**, 378 (2018).

[78] T. Katsuragawa, T. Nakamura, T. Ikeda, and S. Capozziello, Physical Review D **99**, 124050 (2019), 1902.02494.

[79] M. E. S. Alves, O. D. Miranda, and J. C. N. de Araujo, Classical and Quantum Gravity **27**, 145010 (2010).

[80] M. Visser, General Relativity and Gravitation **30** 1717 (1997), 9705051.

[81] S. F. Hassan and R. A. Rosen, Journal of High Energy Physics **2012**, 126 (2012), 1109.3515.

[82] C. de Rham, G. Gabadadze, and A. J. Tolley, Journal of High Energy Physics **2011**, 93 (2011).

[83] V. A. Rubakov and P. G. Tinyakov, Physics-Uspekhi **51**, 759 (2008).

[84] C. de Rham, G. Gabadadze, and A. J. Tolley, Physical Review Letters **106**, 231101 (2011), 1011.1232.

[85] G. Montani and F. Moretti, Physical Review D **100**, 024045 (2019).

[86] K. Hayama and A. Nishizawa, Physical Review D **87**, 062003 (2013).

[87] M. Isi, A. J. Weinstein, C. Mead, and M. Pitkin, Physical Review D **91**, 082002 (2015).

[88] M. Isi, M. Pitkin, and A. J. Weinstein, Physical Review D **96**, 042001 (2017), 1703.07530.

[89] A. Nishizawa, A. Taruya, K. Hayama, S. Kawamura, and M.-a. Sakagami, Physical Review D **79**, 082002 (2009).

[90] N. Christensen, Physical Review D **46**, 5250 (1992).

[91] E. E. Flanagan, Physical Review D **48**, 2389 (1993).

[92] B. Allen and J. D. Romano, Physical Review D **59**, 102001 (1999).

[93] T. Callister *et al.*, Physical Review X **7**, 041058 (2017).

[94] B. Abbott *et al.*, Physical Review Letters **120**, 201102 (2018).

[95] M. Isi and A. J. Weinstein, Probing gravitational wave polarizations with signals from compact binary coalescences, (2017), 1710.03794.

[96] K. Chatziioannou, N. Yunes, and N. Cornish, Physical Review D **86**, 022004 (2012).

[97] Y. Hagihara, N. Era, D. Iikawa, and H. Asada, Physical Review D **98**, 064035 (2018).

[98] Y. Hagihara, N. Era, D. Iikawa, A. Nishizawa, and H. Asada, Physical Review D **100**, 064010 (2019), 1904.02300.

[99] Y. Hagihara, N. Era, D. Iikawa, N. Takeda, and H. Asada, Physical Review D **101**, 041501 (2020).

[100] P. T. Pang, R. K. Lo, I. C. Wong, T. G. Li, and C. Van Den Broeck, Physical Review D **101**, 104055 (2020).

[101] L. O'Beirne, N. J. Cornish, S. J. Vigeland, and S. R. Taylor, Physical Review D **99**, 124039 (2019).

[102] C. Liu, W.-H. Ruan, and Z.-K. Guo, Constraining gravitational-wave polarizations with taiji, 2020, 2006.04413.

[103] S. Goyal, K. Haris, A. K. Mehta, and P. Ajith, Testing the nature of gravitational-wave polarizations using strongly lensed signals, (2020), 2008.07060.

[104] S. M. Carroll, Lecture Notes on General Relativity, (1997), gr-qc/9712019.

[105] W.-T. Ni and M. Zimmermann, Physical Review D **17**, 1473 (1978).

[106] P. J. Sutton *et al.*, New Journal of Physics **12**, 053034 (2010).

[107] R. E. Kass and A. E. Raftery, Journal of the American Statistical Association **90**, 773 (1995), https://www.tandfonline.com/doi/pdf/10.1080/01621459.1995.10476572.

[108] L. S. Finn, Physical Review D **46**, 5236 (1992).

[109] C. Cutler and É. E. Flanagan, Physical Review D **49**, 2658 (1994).

[110] J. D. E. Creighton and W. G. Anderson, *Gravitational-Wave Physics and Astronomy* (Wiley-VCH Verlag GmbH & Co. KGaA, Weinheim, Germany, 2011).

[111] T. Cokelaer, Classical and Quantum Gravity **25**, 184007 (2008).

[112] M. Vallisneri, Physical Review D **77**, 042001 (2008).

[113] C. L. Rodriguez, B. Farr, W. M. Farr, and I. Mandel, Physical Review D **88**, 084013 (2013).

[114] J. Skilling, Bayesian Analysis **1**, 833 (2006).

[115] J. S. Speagle, Monthly Notices of the Royal Astronomical Society **493**, 3132 (2020).

[116] T. G. F. Li, *Extracting Physics from Gravitational Waves: Testing the Strong-field Dynamics of General Relativity and Inferring the Large-scale Structure of the Universe*, PhD thesis, Vrije U., Amsterdam, 2013.

[117] H. Takeda *et al.*, Physical Review D **98**, 022008 (2018), 1806.02182.

[118] H. Takeda *et al.*, Physical Review D **100**, 042001 (2019).

[119] P. Amaro-Seoane *et al.*, Laser Interferometer Space Antenna, (2017), 1702.00786.

[120] M. Armano *et al.*, Physical Review Letters **120**, 061101 (2018).

[121] S. Kawamura *et al.*, Classical and Quantum Gravity **28**, 094011 (2011).

[122] J. Luo *et al.*, Classical and Quantum Gravity **33**, 035010 (2016).

[123] C. Cutler, Physical Review D **57**, 7089 (1998), 9703068.

[124] E. Berti, A. Buonanno, and C. M. Will, Physical Review D **71**, 084025 (2005).

[125] K. G. Arun, Physical Review D **74**, 024025 (2006), 0605021.

[126] W. Zhao and L. Wen, Physical Review D **97**, 064031 (2018), 1710.05325.

[127] S. Khan *et al.*, Physical Review D **93**, 044007 (2016).

[128] B. P. Abbott *et al.*, Living Reviews in Relativity **19**, 1 (2016).

[129] S. Vitale and M. Evans, Physical Review D **95**, 064052, (2016), 1610.06917.

[130] M. L. Chan, C. Messenger, I. S. Heng, and M. Hendry, Physical Review D **97**, 123014 (2018), 1803.09680.

[131] P. R. Saulson, Physical Review D **30**, 732 (1984).

[132] J. Harms, Living Reviews in Relativity **22**, 6 (2019), 1507.05850.

[133] S. Vitale and W. M. Farr, The Astrophysical Journal Letters **886** L1 (2019), 1808.00901.

[134] P. Madau and M. Dickinson, Annual Review of Astronomy and Astrophysics **52**, 415 (2014), 1403.0007.

[135] T. Regimbau and S. A. Hughes, Physical Review D **79**, 062002 (2009).

[136] B. P. Abbott *et al.*, The Astrophysical Journal Letters **882**, L24 (2019), 1811.12940.

[137] H. Yang *et al.*, Physical Review Letters **118**, 161101 (2017), 1701.05808.

[138] E. D. Hall and M. Evans, Classical and Quantum Gravity **36**, 225002 (2019), 1902.09485.

[139] C. L. Rodriguez *et al.*, Physical Review Letters **115**, 051101 (2015).

[140] M. Fujii, A. Tanikawa, and J. Makino, Publications of the Astronomical Society of Japan, **69**, 94 (2017), 1709.02058.

[141] G. Fragione and B. Kocsis, Physical Review Letters **121**, 161103 (2018).

[142] C. L. Rodriguez and A. Loeb, The Astrophysical Journal **866**, L5 (2018).

[143] T. Kinugawa, K. Inayoshi, K. Hotokezaka, D. Nakauchi, and T. Nakamura, Monthly Notices of the Royal Astronomical Society **442**, 2963 (2014).

[144] K. Belczynski *et al.*, Monthly Notices of the Royal Astronomical Society, **471**, 4702 (2017), 1612.01524.

[145] S. A. Hughes and K. S. Thorne, Physical Review D **58**, 122002 (1998).

[146] D. Fiorucci, J. Harms, M. Barsuglia, I. Fiori, and F. Paoletti, Physical Review D **97**, 062003 (2018).

[147] J. C. Driggers, J. Harms, and R. X. Adhikari, Physical Review D **86**, 102001 (2012).

[148] M. Coughlin *et al.*, Classical and Quantum Gravity **33**, 244001 (2016).

[149] J. Harms and K. Venkateswara, Classical and Quantum Gravity **33**, 234001 (2016).

[150] J. Harms and S. Hild, Classical and Quantum Gravity **31**, 185011 (2014).

[151] H. Takeda, S. Morisaki, and A. Nishizawa, Pure polarization test of GW170814 and GW170817 using waveforms consistent with modified theories of gravity, (2020), 2010.14538.

[152] LIGO Scientific Collaboration and Virgo Collaboration, B. P. Abbott *et al.*, Physical Review X **9**, 011001 (2019).

[153] G. Ashton *et al.*, The Astrophysical Journal Supplement Series **241**, 27 (2019).

[154] I. M. Romero-Shaw *et al.*, Monthly Notices of the Royal Astronomical Society **499**, 3295 (2020).

[155] J. Veitch, W. D. Pozzo, and C. M. Pitkin, https://doi.org/10.5281/zenodo.825456 (2017).

[156] T. Dietrich *et al.*, Physical Review D **99**, 024029 (2019).

[157] S. Morisaki and V. Raymond, Physical Review D **102**, 104020 (2020).

[158] P. Canizares *et al.*, Physical Review Letters **114**, 071104 (2015).

[159] R. Smith *et al.*, Physical Review D **94**, 044031 (2016).

[160] LIGO Scientific, Virgo, R. Abbott *et al.*, Open data from the first and second observing runs of Advanced LIGO and Advanced Virgo, (2019), 1912.11716.

[161] C. Cahillane *et al.*, Physical Review D **96**, 102001 (2017).

[162] D. A. Coulter *et al.*, Science **358**, 1556 (2017).

[163] N. R. Tanvir *et al.*, The Astrophysical Journal **848**, L27 (2017).

[164] B. P. Abbott *et al.*, The Astrophysical Journal **848**, L12 (2017).

[165] C. Meegan *et al.*, The Astrophysical Journal **702**, 791 (2009).

[166] A. von Kienlin *et al.*, Astronomy & Astrophysics **411**, L299 (2003).

[167] K. P. Mooley *et al.*, Nature **561**, 355 (2018).

[168] K. Hotokezaka *et al.*, Nature Astronomy **3**, 940 (2019).

[169] A. Buonanno, B. R. Iyer, E. Ochsner, Y. Pan, and B. S. Sathyaprakash, Physical Review D **80**, 084043 (2009).

[170] B. P. Abbott *et al.*, Living Reviews in Relativity **23**, 3 (2020).

[171] C. S. Unnikrishnan, International Journal of Modern Physics D **22**, 1341010 (2015), 1510.06059.

[172] W.-R. Hu and Y.-L. Wu, National Science Review **4**, 685 (2017).

[173] C. Zhang *et al.*, Physical Review D **101**, 044002 (2020).

[174] E. Newman and R. Penrose, Journal of Mathematical Physics **3**, 566 (1962).

[175] R. Penrose and W. Rindler, *Spinors and space-time* (Cambridge University Press, 1984).

[176] T. Clifton, P. G. Ferreira, A. Padilla, and C. Skordis, Physics Reports **513**, 1 (2012), Modified Gravity and Cosmology.

[177] P. G. Bergmann, International Journal of Theoretical Physics **1**, 25 (1968).

[178] J. Nordtvedt, Kenneth, The Astrophysical Journal **161**, 1059 (1970).

[179] R. V. Wagoner, Physical Review D **1**, 3209 (1970).

[180] C. M. Will and J. Nordtvedt, Kenneth, The Astrophysical Journal **177**, 757 (1972).

[181] R. W. Hellings and K. Nordtvedt, Physical Review D **7**, 3593 (1973).

[182] A. Starobinsky, Physics Letters B **91**, 99 (1980).

[183] P. A. R. Ade *et al.*, Astronomy & Astrophysics **594**, A20 (2016).

[184] S. M. Carroll, V. Duvvuri, M. Trodden, and M. S. Turner, Physical Review D **70**, 043528 (2004).

[185] D. N. Vollick, Physical Review D **68**, 063510 (2003).

[186] É. É. Flanagan, Physical Review Letters **92**, 071101 (2004).

[187] S. Nojiri and S. D. Odintsov, Physical Review D **68**, 123512 (2003).

[188] A. G. Riess *et al.*, The Astronomical Journal **116**, 1009 (1998).

[189] S. Perlmutter *et al.*, The Astrophysical Journal **517**, 565 (1999).

[190] T. Chiba, Physics Letters B **575**, 1 (2003).

[191] A. L. Erickcek, T. L. Smith, and M. Kamionkowski, Physical Review D **74**, 121501 (2006).

[192] W. Hu and I. Sawicki, Physical Review D **76**, 064004 (2007).

[193] A. A. Starobinsky, JETP Letters **86**, 157 (2007).

[194] G. Cognola *et al.*, Physical Review D **77**, 046009 (2008).

[195] R. Myrzakulov, L. Sebastiani, and S. Vagnozzi, The European Physical Journal C **75**, 444 (2015).

[196] P. Teyssandier and P. Tourrenc, Journal of Mathematical Physics **24**, 2793 (1983), https://doi.org/10.1063/1.525659.

[197] K. S. Stelle, General Relativity and Gravitation **9**, 353 (1978).

[198] C. Corda, Journal of Cosmology and Astroparticle Physics **2007**, 009 (2007).

[199] C. Corda, International Journal of Modern Physics A **23**, 1521 (2008).

[200] S. Capozziello, C. Corda, and M. F. De Laurentis, Physics Letters B **669**, 255 (2008).

[201] S. Capozziello, R. Cianci, M. De Laurentis, and S. Vignolo, The European Physical Journal C **70**, 341 (2010).

[202] M. Alves, O. Miranda, and J. de Araujo, Physics Letters B **679**, 401 (2009).

[203] H. R. Kausar, L. Philippoz, and P. Jetzer, Physical Review D **93**, 124071 (2016).

[204] M. Maggiore and A. Nicolis, Physical Review D **62**, 024004 (2000).

[205] E. ALESCI and G. MONTANI, International Journal of Modern Physics D **14**, 1 (2005).

[206] L. Blanchet, Living Reviews in Relativity **9**, 4 (2006).

[207] L. Blanchet, G. Faye, B. R. Iyer, and S. Sinha, Classical and Quantum Gravity **25**, 165003 (2008), 0802.1249, [Erratum: Classical and Quantum Gravity **29**, 239501 (2012)].

[208] L. Blanchet and G. Faye, Journal of Mathematical Physics **42**, 4391 (2001).

[209] L. Blanchet, G. Faye, and B. Ponsot, Physical Review D **58**, 124002 (1998).

[210] S. Isoyama, R. Sturani, and H. Nakano, Post-newtonian templates for gravitational waves from compact binary inspirals, (2020), 2012.01350.

[211] P. Ajith *et al.*, Physical Review D **77**, 104017 (2008).

[212] P. Ajith, Classical and Quantum Gravity **25**, 114033 (2008).

[213] P. Ajith *et al.*, Physical Review Letters **106**, 241101 (2011).

[214] L. Santamaría *et al.*, Physical Review D **82**, 064016 (2010).

[215] M. Hannam *et al.*, Physical Review Letters **113**, 151101 (2014).

[216] L. London *et al.*, Physical Review Letters **120**, 161102 (2018).

[217] C. García-Quirós *et al.*, Physical Review D **102**, 064002 (2020).

[218] C. García-Quirós, S. Husa, M. Mateu-Lucena, and A. Borchers, Accelerating the evaluation of inspiral-merger-ringdown waveforms with adapted grids, (2020), 2001.10897.

[219] G. Pratten *et al.*, Physical Review D **102**, 064001 (2020).

[220] G. Pratten *et al.*, Let's twist again: computationally efficient models for the dominant and sub-dominant harmonic modes of precessing binary black holes, (2020), 2004.06503.

[221] E. D. Black, American Journal of Physics **69**, 79 (2001), https://doi.org/10.1119/1.1286663.

[222] C. J. Moore, R. H. Cole, and C. P. L. Berry, Classical and Quantum Gravity **32**, 015014 (2014).

[223] C. Bond, D. Brown, A. Freise, and K. A. Strain, Living Reviews in Relativity **19**, 3 (2017).